

NAVSWC TR 90-683

AD-A247 191



2

SECOND-ORDER SHOCK-EXPANSION THEORY EXTENDED TO INCLUDE REAL GAS EFFECTS

BY FRANK G. MOORE MICHAEL A. ARMISTEAD STEVE H. ROWLES
WEAPONS SYSTEMS DEPARTMENT

FRED L. DeJARNETTE
NORTH CAROLINA STATE UNIVERSITY

FEBRUARY 1992

DTIC
ELECTE
MAR 05 1992
S. D.

Approved for public release; distribution is unlimited.

DESTRUCTION NOTICE — For unclassified, limited documents, destroy by any method that will prevent disclosure of contents or reconstruction of the document.



NAVAL SURFACE WARFARE CENTER

Dahlgren, Virginia 22448-5000 • Silver Spring, Maryland 20903-5000

92 2 26 030

92-05019



NAVSWC TR 90-683

**SECOND-ORDER SHOCK-EXPANSION THEORY
EXTENDED TO INCLUDE REAL GAS EFFECTS**

**BY FRANK G. MOORE MICHAEL A. ARMISTEAD
STEVE H. ROWLES
WEAPONS SYSTEMS DEPARTMENT**

**FRED R. DeJARNETTE
NORTH CAROLINA STATE UNIVERSITY**

FEBRUARY 1992

Approved for public release; distribution is unlimited

DESTRUCTION NOTICE -- For unclassified, limited documents,
destroy by any method that will prevent disclosure of contents
or reconstruction of the document

NAVAL SURFACE WARFARE CENTER

Dahlgren, Virginia 22448-5000 • Silver Spring, Maryland 20903-5000

FOREWORD

The effort described in this report is one part of the theoretical development necessary to make the last version of the Naval Surface Warfare Center (NAVSWC) aeroprediction code, published in 1981, more applicable to present and future weapon concepts. The particular theoretical development included in this report addresses the changes in skin temperatures and aerodynamics associated with real gas effects that occur at high Mach number flight.

Appreciation is given to Francis Priolo, who ran the ZEUS code to provide the exact computations with which to compare the present new engineering methods. Appreciation is also expressed to Dr. Roy McInville for consultation on heat transfer requirements and techniques.

The work described in this report was supported through the Office of Naval Research (Dave Siegel) and, more specifically, the Surface-launched Weapons Technology Block Program managed at NAVSWC by Robin Staton. Appreciation is expressed to these individuals for their support in this work.

Approved by:

Richard W. Dorsey

RICHARD W. DORSEY, Deputy Head
Weapons Systems Department



Accession For	
NTIS GRA&I	<input checked="" type="checkbox"/>
DTIC TAB	<input type="checkbox"/>
Unannounced	<input type="checkbox"/>
Justification	
By _____	
Distribution/	
Availability Codes	
Dist	Avail and/or Special
A-1	

ABSTRACT

New methods have been developed to compute inviscid surface pressures and temperatures for both perfect and equilibrium chemically reacting flows on both pointed and blunt bodies of revolution. These new methods include an improved Shock-expansion Theory, an improved Modified Newtonian Theory (MNT), and an improved method for angle-of-attack effects. Comparison of these approximate engineering techniques to exact inviscid computations using a full Euler code showed that these new methods gave very good agreement of surface temperature and pressures as well as forces and moments. Incorporation of this new technology into the NAVSWC aeroprediction code will allow the code to be used for engineering estimates of inviscid surface temperature at high Mach numbers. These approximate temperatures can then be used as inputs to perform heat transfer analysis.

CONTENTS

<u>Section</u>	<u>Page</u>
1 INTRODUCTION	1
2 ANALYSIS	2
2.1 PERFECT AND REAL GAS BACKGROUND	2
2.1.1 Definition	2
2.1.2 Importance of Real Gas Effects	3
2.1.3 Physical Phenomena That Cause Real Gas Effects	5
2.2 PERFECT GAS COMPUTATIONAL PROCEDURE	7
2.2.1 Modified Newtonian Theory	7
2.2.2 First-order Shock-expansion Theory	10
2.2.3 Second-order Shock-expansion Theory (SOSET)	14
2.3 REAL GAS COMPUTATIONAL PROCESS	19
2.3.1 Summary of Procedure for General Chemical Species Composition	19
2.3.2 Simplified Procedures for Air	24
2.3.3 Chemical Reaction Rates	29
2.3.4 Modified Newtonian Theory	30
2.3.5 Second-order Shock-expansion Theory (SOSET)	34
2.3.6 Angle-of-attack Solution for Body Alone	45
2.3.7 Wing and Interference Aerodynamics	53
2.3.8 Viscous Considerations	55
3 RESULTS AND DISCUSSION	59
3.1 STARTING SOLUTIONS	59
3.2 PRESSURE GRADIENT USED IN SOSET	67
3.3 CONFIGURATION RESULTS	70
4 SUMMARY	98
5 REFERENCES	99
6 SYMBOLS AND DEFINITIONS	103
APPENDIXES:	
A - DETERMINATION OF ANGLE δ USED IN NEWTONIAN THEORY	A-1
B - PRESSURE DISTRIBUTION ON A SPHERE IN HYPERSONIC FLOW	B-1
C - COMPUTATION OF PROPERTIES ACROSS SHOCK WAVES IN FROZEN AND EQUILIBRIUM CHEMICALLY REACTING FLOWS	C-1
D - COMPUTATION OF PROPERTIES ACROSS EXPANSION WAVES IN FROZEN AND EQUILIBRIUM CHEMICALLY REACTING FLOWS	D-1
E - DERIVATION OF CHARACTERISTIC COMPATIBILITY CONDITIONS IN STREAMLINE COORDINATES	E-1
DISTRIBUTION	(1)

ILLUSTRATIONS

<u>Figure</u>		<u>Page</u>
1	TEMPERATURE BEHIND A NORMAL SHOCK AS A FUNCTION OF FREESTREAM MACH NUMBER ($H = 170$ kft)	4
2	N_2 MOLECULE UNDERGOING TRANSLATION AND ROTATION	5
3	EQUILIBRIUM COMPOSITION OF AIR AT DENSITY OF 10^{-2} atm (FROM REFERENCE 11)	6
4	APPROXIMATION OF TRUE BODY BY ONE COMPOSED OF STRAIGHT LINE SEGMENTS TANGENT TO SURFACE	11
5	NOMENCLATURE FOR CONICAL SOLUTION	12
6	FLOW ABOUT A FRUSTUM ELEMENT	14
7	TYPICAL EQUIVALENT BODY SHAPES USED FOR COMPUTING LIFTING PROPERTIES WITH SECOND-ORDER SHOCK EXPANSION	16
8	SPECIFIC HEATS FOR AIR (NO DISSOCIATION OR IONIZATION)	22
9	CURVE FIT EQUATIONS (INTERNAL ENERGY RATIO)	27
10	CURVE FIT EQUATIONS (SPEED OF SOUND RATIO)	28
11	CURVE FIT EQUATIONS (TEMPERATURE RATIO)	28
12	CURVE FIT EQUATIONS (ENTHALPY RATIO)	29
13	STREAMLINE GEOMETRY	37
14(a)	APPROXIMATE PRESSURES ON A 20-PERCENT BLUNT VON KARMAN OGIVE USING ONLY EQUATION (138); ($M_\infty = 15, \alpha = 10^\circ$)	50
14(b)	COMPARISON OF APPROXIMATE (EQUATION 138) AND EXACT PRESSURES ON A 20-PERCENT BLUNT VON KARMAN OGIVE ($M_\infty = 15, \alpha = 10^\circ, \Phi = 180^\circ$)	50
14(c)	COMPARISON OF APPROXIMATE (EQUATION 138) AND EXACT PRESSURES ON A 20-PERCENT BLUNT VON KARMAN OGIVE ($M_\infty = 15, \alpha = 10^\circ, \Phi = 90^\circ$)	51
14(d)	COMPARISON OF APPROXIMATE (EQUATION 138) AND EXACT PRESSURES ON A 20-PERCENT BLUNT VON KARMAN OGIVE ($M_\infty = 15, \alpha = 10^\circ, \Phi = 0^\circ$)	51

ILLUSTRATIONS (CONTINUED)

<u>Figure</u>		<u>Page</u>
15(a)	APPROXIMATE PRESSURE PREDICTION ON A 20-PERCENT BLUNT VON KARMAN OGIVE (EQUATIONS 138 AND 142); ($M_\infty = 15, \alpha = 10^\circ$)	52
15(b)	APPROXIMATE TEMPERATURE PREDICTION ON A 20-PERCENT BLUNT VON KARMAN OGIVE ($M_\infty = 15, \alpha = 10^\circ$)	52
16	SUMMARY OF SOSET FOR REAL GASES ON BODIES AND WING BODY COMBINATIONS	54
17	PERFECT GAS COMPARISON OF EXACT AND PRESENT APPROXIMATE CONE SOLUTIONS	60
18	PERFECT GAS COMPARISON OF EXACT AND PRESENT APPROXIMATE CONE SOLUTIONS	61
19(a)	APPROXIMATE AND EXACT PRESSURE PREDICTION ON A CONE IN PERFECT AND EQUILIBRIUM CHEMICALLY REACTING FLOWS ($M_\infty = 15, \alpha = 10^\circ, h = 100k \text{ ft}, \theta_c = 15^\circ$)	62
19(B)	APPROXIMATE AND EXACT TEMPERATURE PREDICTION ON A CONE IN PERFECT AND EQUILIBRIUM CHEMICALLY REACTING FLOWS ($M_\infty = 15, \alpha = 10^\circ, h = 100k \text{ ft}, \theta_c = 15^\circ$)	62
20(a)	SURFACE PRESSURE DISTRIBUTION OVER A HEMISPHERICAL FOREBODY AT $M_\infty = 5$	63
20(b)	SURFACE PRESSURE DISTRIBUTION OVER A HEMISPHERICAL FOREBODY AT $M_\infty = 10$	64
20(c)	SURFACE PRESSURE DISTRIBUTION OVER A HEMISPHERICAL FOREBODY AT $M_\infty = 15$	65
20(d)	SURFACE PRESSURE DISTRIBUTION OVER A HEMISPHERICAL FOREBODY AT $M_\infty = 20$	65
21	BICONIC CONFIGURATION GEOMETRY FOR INVESTIGATING PRESSURE GRADIENT AROUND A CORNER	68
22	COMPARISON OF VARIOUS PRESSURE PREDICTION TECHNIQUES ON A 20-PERCENT BLUNT VON KARMAN OGIVE ($M_\infty = 15, \alpha = 0^\circ, h = 100k \text{ ft}$)	69

ILLUSTRATIONS (CONTINUED)

<u>Figure</u>		<u>Page</u>
23	COMPARISON OF VARIOUS PRESSURE PREDICTION TECHNIQUES ON A HEMISPHERE FOREBODY ($M_\infty = 15$, $\alpha = 0^\circ$, $h = 100k$ ft)	71
24	CONFIGURATIONS USED AS TEST CASES FOR NEW THEORY (DIMENSIONS IN CALIBERS)	72
25(a)	COMPARISON OF APPROXIMATE AND EXACT PRESSURE PREDICTION FOR A 20-PERCENT BLUNT VON KARMAN OGIVE ($M_\infty = 15$, $\alpha = 10^\circ$, $\Phi = 180^\circ$) ..	74
25(b)	COMPARISON OF APPROXIMATE AND EXACT TEMPERATURE PREDICTION FOR A 20-PERCENT BLUNT VON KARMAN OGIVE ($M_\infty = 15$, $\alpha = 10^\circ$, $\Phi = 180^\circ$ perfect gas)	75
26(a)	APPROXIMATE PRESSURE PREDICTION ON A 20-PERCENT BLUNT VON KARMAN OGIVE FOR A REAL GAS ($M_\infty = 15$, $\alpha = 10^\circ$, $h = 100k$ ft)	76
26(b)	APPROXIMATE TEMPERATURE PREDICTION ON A 20-PERCENT BLUNT VON KARMAN OGIVE FOR A REAL GAS ($M_\infty = 15$, $\alpha = 10^\circ$, $h = 100k$ ft)	77
26(c)	COMPARISON OF APPROXIMATE AND EXACT TEMPERATURE PREDICTION ON A 20-PERCENT BLUNT VON KARMAN OGIVE FOR A REAL GAS ($M_\infty = 15$, $\alpha = 10^\circ$, $h = 100k$ ft)	78
27(a)	COMPARISON OF APPROXIMATE AND EXACT PRESSURE COEFFICIENTS IN THE WINDWARD PLANE OF A 20-PERCENT BLUNT CONE ($M_\infty = 15$, $\alpha = 10^\circ$)	79
27(b)	COMPARISON OF APPROXIMATE AND EXACT TEMPERATURE IN THE WINDWARD PLANE OF A 20-PERCENT BLUNT CONE ($M_\infty = 15$, $\alpha = 10^\circ$) ...	80
27(c)	COMPARISON OF APPROXIMATE AND EXACT PRESSURE COEFFICIENTS ON A 20-PERCENT BLUNT CONE ($M_\infty = 15$, $\alpha = 10^\circ$, REAL GAS)	81
27(d)	COMPARISON OF APPROXIMATE AND EXACT TEMPERATURES ON A 20-PERCENT BLUNT CONE ($M_\infty = 15$, $\alpha = 10^\circ$, REAL GAS)	82
28(a)	PRESSURES PREDICTED BY APPROXIMATE METHOD ON A 20-PERCENT BLUNT CONE AS A FUNCTION OF MACH NUMBER ($\Phi = 180^\circ$, $x = 1.5$, $h = 100k$ ft)	83
28(b)	TEMPERATURES PREDICTED BY APPROXIMATE METHOD ON A 20-PERCENT BLUNT CONE AS A FUNCTION OF MACH NUMBER ($\Phi = 180^\circ$, $x = 1.5$, $h = 100k$ ft)	84

ILLUSTRATIONS (CONTINUED)

<u>Figure</u>		<u>Page</u>
29(a)	PRESSURE DISTRIBUTION ON A 10° CONE-CYLINDER-FLARE ($M_\infty = 15$, $\alpha = 10^\circ$, $\phi = 180^\circ$)	85
29(b)	TEMPERATURE DISTRIBUTION ON A 10° CONE-CYLINDER-FLARE ($M_\infty = 15$, $\alpha = 10^\circ$, $\phi = 180^\circ$)	86
29(c)	PRESSURE DISTRIBUTION ON A 10° CONE-CYLINDER-FLARE ($M_\infty = 15$, $\alpha = 10^\circ$, $x = 2, 4, 10$)	87
29(d)	TEMPERATURE DISTRIBUTION AROUND THE CONE OF A 10° CONE-CYLINDER-FLARE ($M_\infty = 15$, $\alpha = 10^\circ$, $x = 2$)	88
29(e)	TEMPERATURE DISTRIBUTION AROUND THE CYLINDER OF A 10° CONE-CYLINDER-FLARE ($M_\infty = 15$, $\alpha = 10^\circ$, $x = 4$)	89
29(f)	TEMPERATURE DISTRIBUTION AROUND THE FLARE OF A 10° CONE-CYLINDER-FLARE ($M_\infty = 10$, $\alpha = 10^\circ$, $x = 10$)	90
30(a)	COMPARISON OF PRESSURE COEFFICIENTS ON A 20-PERCENT BLUNT VON KARMAN OGIVE-CYLINDER-FIN CONFIGURATION ($M_\infty = 15$, $\alpha = 0^\circ$) .	87
30(b)	COMPARISON OF TEMPERATURE PREDICTIONS ON A 20-PERCENT BLUNT VON KARMAN OGIVE-CYLINDER-FIN CONFIGURATION ($M_\infty = 15$, $\alpha = 0^\circ$) .	88
31(a)	AXIAL WAVE DRAG OF A 20-PERCENT BLUNT VON KARMAN OGIVE-CYLINDER-FIN CONFIGURATION ($M_\infty = 15$)	93
31(b)	NORMAL FORCE COEFFICIENT OF A 20-PERCENT BLUNT VON KARMAN OGIVE-CYLINDER-FIN CONFIGURATION ($M_\infty = 15$)	94
31(c)	CENTER OF PRESSURE OF A 20-PERCENT BLUNT VON KARMAN OGIVE-CYLINDER-FIN CONFIGURATION ($M_\infty = 15$)	95
31(d)	AXIAL WAVE DRAG COEFFICIENT FOR A 20-PERCENT BLUNT VON KARMAN OGIVE-CYLINDER-FIN CONFIGURATION ($\alpha = 5^\circ$)	96
31(e)	NORMAL FORCE COEFFICIENT FOR A 20-PERCENT BLUNT VON KARMAN OGIVE-CYLINDER-FIN CONFIGURATION ($\alpha = 5^\circ$)	97

ILLUSTRATIONS (CONTINUED)

<u>Figure</u>		<u>Page</u>
A-1	NOMENCLATURE USED FOR DETERMINATION OF ANGLE δ_{eq}	A-3
B-1	PRESSURE ON A SPHERE	B-4
C-1	NORMAL SHOCK WAVE FLOW	C-4
C-2	INFLUENCE OF FREESTREAM PRESSURE AND VELOCITY ON NORMAL SHOCK TEMPERATURE FOR EQUILIBRIUM AIR ($T_1 = 225^\circ\text{K}$)	C-5
C-3	OBLIQUE SHOCK GEOMETRY FOR A WEDGE	C-7
C-4	DEFLECTION ANGLE/WAVE ANGLE VELOCITY DIAGRAM FOR OBLIQUE SHOCKS (ALTITUDE = 100k ft)	C-9
C-5	COMPARISON OF OBLIQUE SHOCK WAVES FOR A CALORICALLY PERFECT GAS VERSUS AN EQUILIBRIUM CHEMICALLY REACTING GAS	C-10
C-6	TEMPERATURE IN THE SHOCK LAYER FOR A WEDGE (ALTITUDE = 100k ft)	C-11
C-7	DENSITY IN THE SHOCK LAYER FOR A WEDGE (ALTITUDE = 100k ft)	C-11
C-8	PRESSURE IN THE SHOCK LAYER FOR A WEDGE (ALTITUDE = 100k ft) ...	C-12
C-9	OBLIQUE SHOCK GEOMETRY FOR A CONE (SPHERICAL COORDINATES)	C-13
C-10	EFFECT OF FREESTREAM VELOCITY AND CONE ANGLE ON CONE SHOCK WAVE ANGLE (H = 100k ft)	C-17
C-11	EFFECT OF FREESTREAM VELOCITY AND CONE HALF-ANGLE ON CONE SURFACE PRESSURE (H = 100k ft)	C-17
C-12	EFFECT OF FREESTREAM VELOCITY AND CONE ANGLE ON CONE SURFACE TEMPERATURE (H = 100k ft)	C-18
C-13	EFFECT OF FREESTREAM VELOCITY AND CONE ANGLE ON CONE SURFACE DENSITY (H = 100k ft)	C-18

ILLUSTRATIONS (CONTINUED)

<u>Figure</u>		<u>Page</u>
C-14	ENTROPY VERSUS ENERGY FOR CONSTANT VALUES OF DENSITY	C-19
C-15	COMPARISON OF DENSITY AT THE CONE SURFACE USING VARIOUS WAYS OF UPDATING DENSITY IN FLOW FIELD SOLUTION ($h = 100k$ ft) ..	C-20
C-16	CONE SURFACE PRESSURE COMPUTED WITH VARIOUS WAYS OF IMPLEMENTING REAL GAS EFFECTS ($h = 100k$ ft)	C-21
C-17	CONE SURFACE TEMPERATURE COMPUTED WITH VARIOUS WAYS OF IMPLEMENTING REAL GAS EFFECTS ($h = 100k$ ft)	C-21
C-18	CONE SURFACE DENSITY COMPUTED WITH VARIOUS WAYS OF IMPLEMENTING REAL GAS EFFECTS ($h = 100k$ ft)	C-22
D-1	PRANDTL-MEYER EXPANSION (PME) PROCESS	D-3
D-2	GEOMETRY USED IN DERIVATION OF PRANDTL-MEYER EQUATION	D-5
D-3	PRESSURE COMPARISON OF INTEGRATION TECHNIQUES FOR PME OF EQUILIBRIUM FLOW ($M_1 = 1.0$, $T_1 = 6140^\circ K$, $\rho_1 = 1.2$ atm)	D-11
D-4	TEMPERATURE COMPARISON OF INTEGRATION TECHNIQUES FOR PME OF EQUILIBRIUM FLOW ($M_1 = 1.0$, $T_1 = 6140^\circ K$, $\rho_1 = 1.2$ atm)	D-11
D-5	PERFECT, FROZEN, EQUILIBRIUM PME: PRESSURE VERSUS FLOW DEFLECTION ANGLE ($M_1 = 1.0$, $T_1 = 6140^\circ K$, $\rho_1 = 1.2$ atm)	D-12
D-6	PERFECT, FROZEN, EQUILIBRIUM PME: TEMPERATURE VERSUS FLOW DEFLECTION ANGLE ($M_1 = 1.0$, $T_1 = 6140^\circ K$, $\rho_1 = 1.2$ atm)	D-12
D-7	PERFECT, FROZEN, EQUILIBRIUM PME: DENSITY VERSUS FLOW DEFLECTION ANGLE ($M_1 = 1.0$, $T_1 = 6140^\circ K$, $\rho_1 = 1.2$ atm)	D-13
D-8	PERFECT, FROZEN, EQUILIBRIUM PME: MACH NUMBER VERSUS FLOW DEFLECTION ANGLE ($M_1 = 1.0$, $T_1 = 6140^\circ K$, $\rho_1 = 1.2$ atm)	D-13

1. INTRODUCTION

For the past 20 years, the Naval Surface Warfare Center (NAVSWC) has been involved in developing codes to calculate aerodynamics on tactical weapons. These codes have attempted to meet the changing needs of the Tactical Weapons Community and keep pace with aerodynamic requirements. A recent effort¹ was undertaken to look at where we have been, where we are, and where we need to go in the future with respect to aerodynamic codes. This effort identified three needs: (1) an improved aerodynamic prediction code that allows Mach numbers to 20, has improved low aspect ratio wing lifting capabilities, and allows improved base drag prediction; (2) an improved full Euler code that has real gas effects included, improved low supersonic Mach number ability, and an integral boundary layer code to compute viscous effects; (3) a Navier Stokes code to provide aeroheating and high-angle-of-attack aerodynamics on a limited number of high-value projects. This report is concerned with partially meeting the number 1 need above; that is, including real gas effects into the computations so that higher Mach numbers can be considered.

The latest version of the aeroprediction code²⁻⁴ calculates aerodynamics up to Mach 8. The main reason for limiting the code to this Mach number is that real gas effects start becoming important around Mach 6, and at Mach 8 can still be neglected for most applications. However, as Mach number increases substantially above Mach 6, the requirement to have real gas effects included in the aeroprediction code increases. Over the past 5 years, tactical weapon concepts have been investigated that fly at Mach numbers up to 20. For this reason, it is believed that real gas effects need to be included in the aeroprediction code.

The theoretical methodology used to predict aerodynamics above about Mach 3 is Second-order Shock-expansion Theory (SOSET) combined with Modified Newtonian Theory (MNT). A brief search of the literature revealed no present second-order accurate theoretical techniques for including real gas effects into aerodynamic computations. The only approaches available were either incorporation of real gas effects into the full inviscid Euler equations of motion or first-order local slope techniques. The first approach is beyond the computational complexity desired for an approximate engineering code, whereas the latter approach does not yield accurate axial force calculations. Hence, extending SOSET to include real gas effects will meet an immediate need for the aeroprediction code and will also fill a gap in the external literature.

2. ANALYSIS

This section is written at a level that covers the high-speed fluid flow phenomena discussed in the Introduction from a *first principles* viewpoint. The intent is to acquaint the reader who has no prior background in Real Gas effects with the importance and the physics and chemistry of these effects as well as how one mathematically goes about solving for the flow field.

2.1 PERFECT AND REAL GAS BACKGROUND

2.1.1 Definition

Usually when one thinks of a definition, one thinks in terms of a clear and concise answer. Such is not necessarily the case with real and perfect or ideal gases. This is because there are several definitions of perfect gases and real gases depending on which reference one uses⁵⁻¹⁰ and whether one uses the chemist's or aerodynamicist's definition. To define a real gas, we must first define a perfect gas. Once we have defined a perfect gas, a real gas will be defined to cover all other cases.

Some references define a perfect gas as one that follows the equation of state identically

$$p = \rho RT \quad (1)$$

and has constant specific heats

$$\bar{C}_p, \bar{C}_v = \text{const} \quad (2)$$

(NOTE: Here a bar is placed over the C_p, C_v to distinguish the specific heats from pressure coefficient C_p , used throughout the report.)

Others break down the definition of perfect gas into a calorically-perfect gas, which is defined by Equations (1) and (2), and a thermally perfect gas where Equation (1) is still satisfied but the specific heats are functions of temperature. That is

$$\begin{aligned} \bar{C}_p &= f(T) \\ \bar{C}_v &= f(T) \end{aligned} \quad (3)$$

Finally, one author⁸ allowed a perfect gas to include cases where the specific heats were functions of pressure and temperature, i.e.

$$\begin{aligned} \bar{C}_p &= f(T, p) \\ \bar{C}_v &= f(T, p) \end{aligned} \quad (4)$$

and Equation (1) was not required to be satisfied. The only requirement for a perfect gas was that the intermolecular attractive or repulsive forces between atoms or molecules be neglected (this is the original definition by the chemist).

For purposes of this report, the most strict definition for a perfect gas is taken (which is sometimes referred to as a calorically-perfect gas). That is, Equations (1) and (2) must be satisfied. A real gas is, therefore, one where either intermolecular forces cannot be neglected (low temperature and high pressure) or one where the temperature is high enough to excite the internal energy modes of vibration, electronic excitation, or cause chemical reactions and dissociation of molecules or ionizations of atoms. In some cases, Equation (3) is valid (computation of additional internal energy from vibration) whereas, in other cases, chemical reactions are occurring or the intermolecular forces are not small and Equation (4) applies and Equation (1) is no longer valid.

In summary, a perfect gas is defined here as one that obeys Equations (1) and (2) exactly, and a real gas is defined as one that violates either Equation (1) or (2) or both. This definition is consistent with most of the aerodynamics literature.

2.1.2 Importance of Real Gas Effects

One may ask: Why be concerned about real gas effects for tactical weapons (since they have been neglected up to this point in time, to the author's knowledge, for aerodynamic computations)? A good illustration for the importance is given by Anderson.⁸ He showed the results of static temperature behind a normal shock where the perfect gas assumption was made and then these results were compared to a real gas. For a perfect gas, the static temperature ratio across a normal shock is

$$\frac{T_2}{T_\infty} = 1 + \frac{2(\gamma - 1)}{(\gamma + 1)^2} \frac{(\gamma M_\infty^2 + 1)}{M_\infty^2} (M_\infty^2 - 1) \quad (5)$$

where T_2 is temperature behind the shock and subscript ∞ represents conditions in the freestream ahead of the shock. Figure 1 plots these results as a function of Mach number for an altitude of 170,000 ft. At this altitude, the speed of sound is approximately 1100 ft/sec and the freestream air temperature is approximately 283°K. The normal shock would occur in the vicinity immediately ahead of the blunted portion of a seeker or the missile nose. Note that the temperatures of interest to tactical weapons aerodynamicists can be very high for high Mach number conditions assuming a perfect gas. Also shown on the figure are the real gas results taken from Reference 8. Note, in particular, the plot of T_R/T_p , the ratio of the real gas to perfect gas temperature. For Mach numbers of 6 or less, this ratio is unity or near unity. This is the reason that aerodynamic computations below $M_\infty = 6$ could neglect real gas effects with little error. However, as one goes above $M_\infty = 6$, the error in temperature using the real gas assumption can be quite large. This is of particular importance to materials and structures engineers who must design the system to

withstand these temperatures. Also shown in Figure 1 is the melting point of typical structural materials used in present-day missile design. The actual-use temperature is less than the melting-point temperature. For missiles that fly at any appreciable time above the maximum-use temperature of a given material, some form of active cooling or insulation would be required. This means additional dead weight and, hence, less performance for the missile. It is therefore obvious that a reasonably accurate estimate of temperature is essential for the design of the seeker and the structure of the weapon. The reasons for this drastic effect on the temperature will be discussed in the next section on fundamental phenomena.

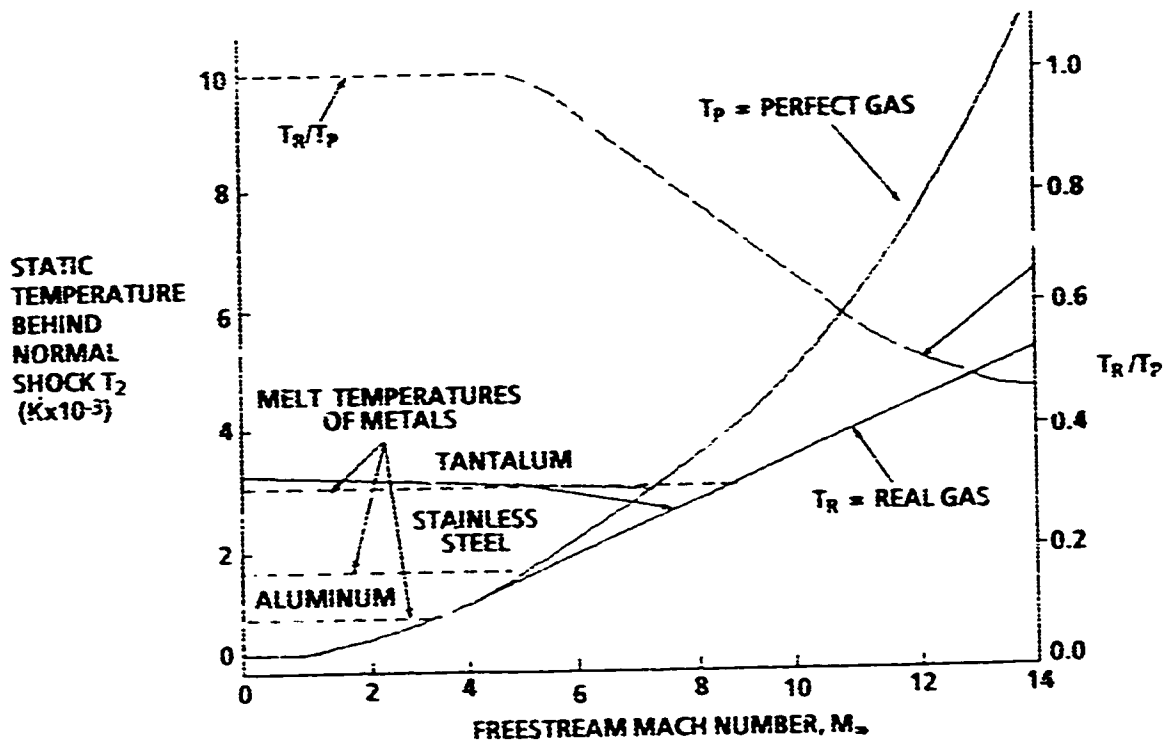


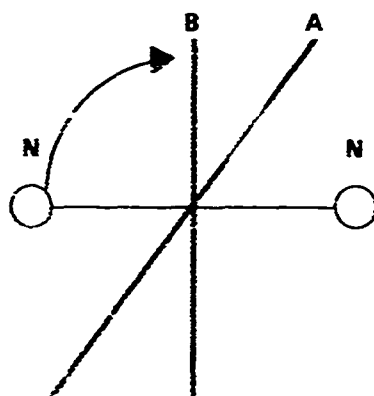
FIGURE 1. TEMPERATURE BEHIND A NORMAL SHOCK AS A FUNCTION OF FREESTREAM MACH NUMBER ($H = 170 \text{ km}$)

Before we finish the discussion on the importance of real gases, it should be noted that pressure is also affected but to a much less extent than temperature. This leads one to the conclusion that if temperature is not of concern and aerodynamic forces and moments are the major interest, the assumption of a perfect gas can be made with reasonable validity for Mach numbers much higher than 6. The reason for this is that pressure is mainly governed by the kinetic energy of the flow and not the potential energy. On the other hand, the temperature is a function of both and, therefore, varies considerably due to the real gas effects. In fact, many of the hypersonic flow assumptions are based on the assumption of a thin shock layer and $M_\infty \gg 1$, and reasonable results for aerodynamic forces can be obtained.

2.1.3 Physical Phenomena That Cause Real Gas Effects

A gas, like any other substance, is composed of atomic structures either in singular form (monatomic) or joined together (diatomic or polyatomic). Air at room temperature is composed primarily of nitrogen (N_2) and oxygen (O_2) with minute traces of carbon dioxide (CO_2), argon (Ar), and nitrogen oxide (NO). The total amount of these trace elements is less than 2 percent of the mass of a given volume of air, whereas the N_2 is about 78 percent and O_2 about 20 percent. Hence, for engineering purposes, air at low to moderate temperatures ($T < 2500^\circ K$) can be assumed to be composed of N_2 and O_2 .

These diatomic molecules are in continuous motion and can translate in three directions (x, y, z) and can rotate in two directions about axes A and B as shown in Figure 2. (Note that rotational energy about an axis going through both N atoms can be neglected in comparison to that about the transverse axis.)



$$\text{TRANSLATION VELOCITY} = \sqrt{V_x^2 + V_y^2 + V_z^2}$$

$$\text{ROTATION VELOCITY} = \omega_A, \omega_B$$

FIGURE 2. N_2 MOLECULE UNDERGOING TRANSLATION AND ROTATION

So as air stays below about $600^\circ K$, the only energy it contains is the rotation and translation of the diatomic N_2 and O_2 . This is what allows us to make the assumptions of a perfect gas that must follow Equations (1) and (2). However, as the air is heated further, an additional energy mode enters into the physical model of the N_2 , O_2 molecules. This mode is vibration. That is, referring to Figure 2, one could imagine a spring-mass system with a spring that allows additional internal energy to be generated between the nitrogen or oxygen atoms. At temperatures above $2500^\circ K$, the molecule has acquired about 90 percent of the internal energy possible from vibration of the molecules.

As the air is heated above $2000^\circ K$, the diatomic molecules of N_2 , O_2 begin to dissociate and chemically react. Air then begins to contain significant amounts of O_2 , O , N_2 , N , and NO as the temperature is increased. Finally, as the air is heated above $8000^\circ K$, significant ionization occurs (an electron leaving one atom and being picked up by another atom), which gives rise to an additional mode of internal energy (the

gain or loss of electrons) as well as additional chemical reactions. An example of the species composition of air as a function of temperature is shown in Figure 3, which is taken from Reference 11. Figure 3 shows how the O_2 , N_2 go to N , O , NO , N^+ , O^+ , and e (free electrons) as temperature is increased.

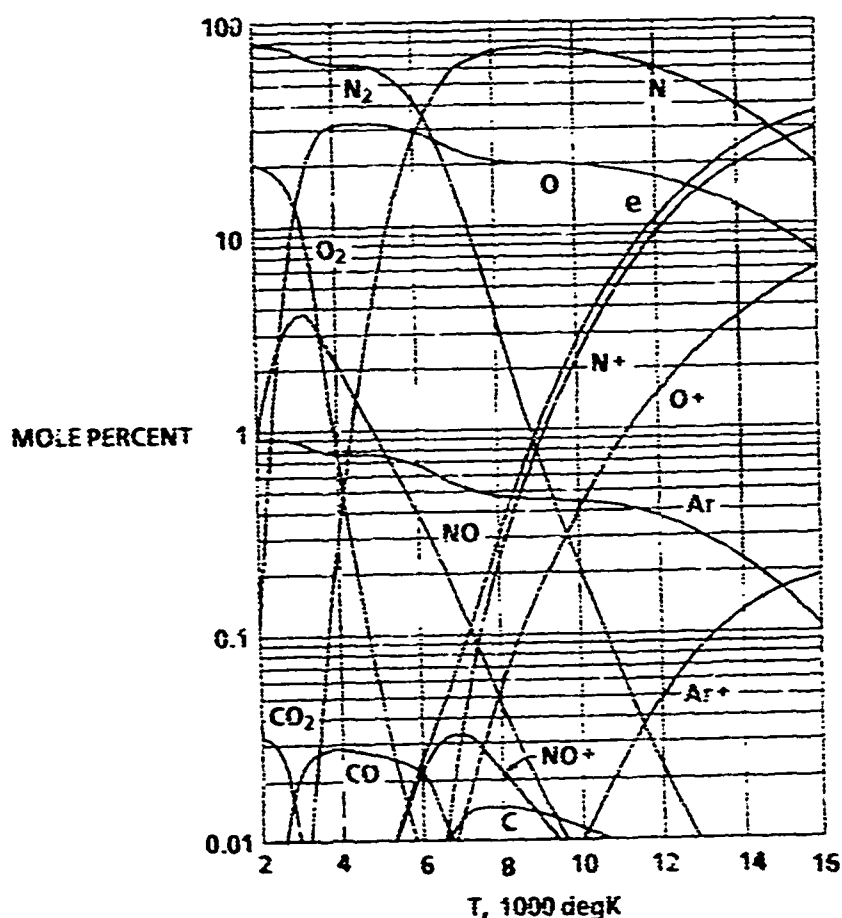


FIGURE 3. EQUILIBRIUM COMPOSITION OF AIR AT DENSITY OF 10^{-2} atm
(FROM REFERENCE 11)

The fundamental physical phenomenon that occurs as air is heated (or as Mach number of a vehicle is increased) is that the additional energy modes of vibration and ionization are added and the air molecules break down and chemically react to form other species. It is this transfer of energy to vibration and the dissociation process that accounts for the fact that the temperature is much lower for a real gas than for a perfect gas at high Mach numbers. That is, the translational and rotational energy that accounts for the high temperatures in a perfect gas is shared by other forms of energy and the chemical reactions in a real gas. It is this sharing of energy across

energy modes and the conservation of energy that require the temperature for a real gas to be lower than that for a perfect gas. How one treats the computation of real gas effects from a computational standpoint is discussed later in the Real Gas Computational Process section.

2.2 PERFECT GAS COMPUTATIONAL PROCEDURE

Before getting into the mathematics of real gas computations, it is instructive to briefly discuss perfect gas computations on a missile-like body using a combination of Newtonian Theory and SOSET. Here it is assumed that the missile has a blunt nose where Modified Newtonian Theory (MNT) would be used for flow computations and SOSET would be used past some match point (between the pressures predicted by the two theories). If the nose is sharp or pointed, SOSET can be used directly.

2.2.1 Modified Newtonian Theory

Newtonian Impact Theory assumes that, in the limit of high Mach number, the shock lies on the body. This means that the disturbed flow field lies in an infinitely-thin layer between the shock and body. Applying the laws of conservation of mass and momentum across the shock yields the result that density behind the shock approaches infinite values and the ratio of specific heats approaches unity. The pressure coefficient on the surface becomes¹²

$$C_p = 2 \sin^2 \delta_{eq} \quad (6)$$

where δ_{eq} is the angle between the velocity vector and a tangent to the body at the point in question (see Appendix A).

Lees¹² noted that a much more accurate prediction of pressure on the blunt-nosed body could be obtained by replacing the constant "2" in Equation (6) with the stagnation pressure coefficient C_{p0} . C_{p0} can be found from

$$C_{p0} = \frac{2}{\gamma M_\infty^2} \left| \left(\frac{p_2}{p_\infty} \right) \left(\frac{p_{O_2}}{p_2} \right) - 1 \right| \quad (7)$$

where p_2/p_∞ and p_{O_2}/p_2 are given by¹³

$$\frac{p_2}{p_\infty} = \frac{2\gamma M_\infty^2 - (\gamma - 1)}{\gamma + 1} \quad (8)$$

$$\frac{p_{O_2}}{p_2} = \left(1 + \frac{\gamma - 1}{2} M_2^2 \right)^{\frac{\gamma}{\gamma - 1}} \quad (9)$$

Also

$$M_2^2 = \frac{(\gamma - 1)M_\infty^2 + 2}{2\gamma M_\infty^2 - (\gamma - 1)} \quad (10)$$

so that Equation (9) can be related to M_∞ and γ only by substitution of Equation (10) into (9) to obtain

$$\frac{p_{O_2}}{p_2} = \left[\frac{4\gamma M_\infty^2 - 2(\gamma - 1)}{(\gamma + 1)^2 M_\infty^2} \right]^{\frac{\gamma}{\gamma - 1}} \quad (11)$$

Equations (8) and (10) hold only for a perfect gas. They are the relationships taken from Reference 13 for flow across a normal shock wave. Combining Equations (11) and (8) into Equation (6), we obtain

$$C_{pO} = \frac{2}{\gamma M_\infty^2} \left\{ \left[\frac{(\gamma + 1)M_\infty^2}{2} \right]^{\frac{\gamma}{\gamma - 1}} \left[\frac{\gamma + 1}{2\gamma M_\infty^2 - (\gamma - 1)} \right]^{\frac{1}{\gamma - 1}} - 1 \right\} \quad (12)$$

and

$$C_p = C_{pO} \sin^2 \delta_{eq} \quad (13)$$

Equation (13) allows the calculation of the pressure coefficient all along the blunt surface of a missile nose or wing leading edge for a perfect gas where C_{pO} is given by Equation (12) and $\sin \delta_{eq}$ from Appendix A.

We also must derive an expression for static temperature along the surface. To do this recall that, for an adiabatic flow, total temperature is constant. This means that

$$T_{O_2} = T_{O_1} = T_\infty \left(1 + \frac{\gamma - 1}{2} M_\infty^2 \right) \quad (14)$$

Also recall that the total pressure and density relationships are constant only for isentropic flow. This means that these relationships do not apply across a shock but they are constant along a streamline for a perfect gas, frozen flow, or equilibrium flow. Since the stagnation streamline wets the body, we can apply these relationships along the body to compute local Mach number and then apply Equation (14) to compute local temperature. The total pressure is given by Equation (9) and the total density is

$$\frac{p_{O_2}}{\rho_2} = \left(1 + \frac{\gamma - 1}{2} M_2^2 \right)^{\frac{1}{\gamma - 1}} \quad (15)$$

Now from Equation (13)

$$C_p = \frac{p_L - p_\infty}{\frac{1}{2} \rho_\infty V_\infty^2}$$

or

$$p_L = \left(\frac{1}{2} \rho_\infty V_\infty^2 \right) C_p + p_\infty \quad (16)$$

Also

$$p_{O_2} = p_L$$

at the stagnation point. Thus

$$p_{O_2} = \frac{1}{2} \rho_\infty V_\infty^2 C_{p_O} + p_\infty \quad (17)$$

Equation (17) gives p_{O_2} as a function of freestream conditions only so it is a known number. Since Equation (16) is also known all along the surface, then from Equation (9) local Mach number can be computed by

$$M_L = \left\{ \left(\frac{2}{\gamma - 1} \right) \left[\left(\frac{p_{O_2}}{p_L} \right)^{\frac{\gamma - 1}{\gamma}} - 1 \right] \right\}^{\frac{1}{2}} \quad (18)$$

Then from Equation (14)

$$T_L = T_{O_2} \left[1 + \frac{\gamma - 1}{2} M_L^2 \right]^{-1} \quad (19)$$

Also from the equation of state for a perfect gas

$$\rho_L = \frac{p_L}{R T_L} \quad (20)$$

Other properties such as internal energy, enthalpy, and entropy could also be computed, if desired, at each point. That is

$$e_L = \bar{C}_v T_L = \left(\frac{R}{\gamma - 1} \right) T_L \quad (21)$$

$$h_L = \bar{C}_P T_L = \left(\frac{\gamma R}{\gamma - 1} \right) T_L \quad (22)$$

$$H = \bar{C}_P T_{O_1} = \left(\frac{\gamma R}{\gamma - 1} \right) T_{O_1} \quad (25)$$

The change in entropy across the shock is

$$\frac{\Delta S}{C_v} = -(\gamma - 1) \ln \left(\frac{p_{O_2}}{p_{O_1}} \right) \quad (24)$$

Since the flow is isentropic along a streamline (which can include the body surface), ΔS along the body is zero.

2.2.2 First-order Shock-expansion Theory

First-order Expansion Theory was first proposed by Eggers et al.¹⁴⁻¹⁷ for bodies of revolution flying at high supersonic speeds. Basically, the Shock-expansion Theory computes the flow parameters at the leading edge of a two-dimensional (2-D) surface with the oblique shock wave relations and with the solution for a cone at the tip of a three-dimensional (3-D) body. Standard Prandtl-Meyer Expansion (PME) is then applied along the surface behind the leading edge or tip solution to get the complete pressure distribution over the body surface. Referring to Figure 4, this theory inherently assumes that the expansion waves created by the change in curvature around the body are entirely absorbed by the shock and do not reflect back to the body surface. Since the theory assumes constant pressure along one of the conical tangent elements of the surface, fairly slender surfaces must be assumed or many points along the surface assumed to obtain a fairly accurate pressure distribution. Another way of stating this is to minimize the strength of the disturbance created by Mach waves emanating from the expansion corner and intersecting the shock, the degree of turn should be small.

For the 2-D starting solution, the equations for a perfect gas across an oblique shock are¹³

$$\frac{p_2}{p_1} = \frac{2 \gamma M_1^2 \sin^2 \sigma - (\gamma - 1)}{\gamma + 1} \quad (25)$$

$$\frac{\rho_2}{\rho_1} = \frac{(\gamma + 1) M_1^2 \sin^2 \sigma}{(\gamma - 1) M_1^2 \sin^2 \sigma + 2} \quad (26)$$

$$\frac{T_2}{T_\infty} = \frac{[2\gamma M_\infty^2 \sin^2 \sigma - (\gamma - 1)][(\gamma - 1)M_\infty^2 \sin^2 \sigma + 2]}{(\gamma + 1)^2 M_\infty^2 \sin^2 \sigma} \quad (27)$$

$$M_2^2 = \frac{(\gamma + 1)^2 M_\infty^2 \sin^2 \sigma - 4(M_\infty^2 \sin^2 \sigma - 1)(\gamma M_\infty^2 \sin^2 \sigma + 1)}{[2\gamma M_\infty^2 \sin^2 \sigma - (\gamma - 1)][(\gamma - 1)M_\infty^2 \sin^2 \sigma + 2]} \quad (28)$$

σ in Equations (25) through (28) is the shock angle for a 2-D body with initial angle θ . This angle may be determined by the numerical solution of Equation (29)

$$\sin^6 \sigma + b \sin^4 \sigma + c \sin^2 \sigma + d = 0 \quad (29)$$

where

$$b = -\frac{M_\infty^2 + 2}{M_\infty^2} - \gamma \sin^2 \theta$$

$$c = \frac{2M_\infty^2 + 1}{M_\infty^4} + \left[\frac{(\gamma + 1)^2}{4} + \frac{\gamma - 1}{M_\infty^2} \right] \sin^2 \theta$$

$$d = -\frac{\cos^2 \theta}{M_\infty^4}$$

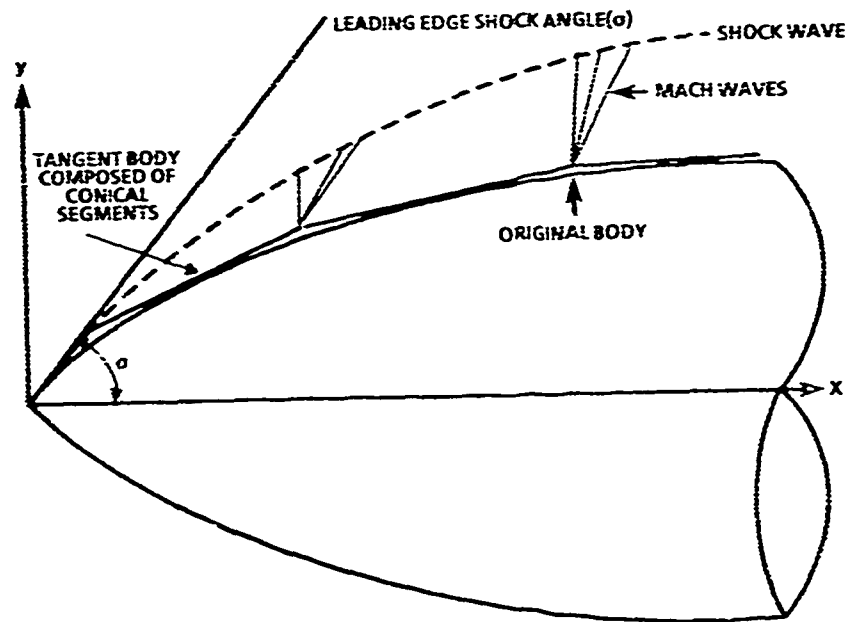


FIGURE 4. APPROXIMATION OF TRUE BODY BY ONE COMPOSED OF STRAIGHT LINE SEGMENTS TANGENT TO SURFACE

Here the weak shock solution is taken as physically more correct (intermediate value of $\sin^2 \sigma$). For a wedge flow, conditions behind the shock are constant so Equations (25) through (28) determine the conditions at the surface as well. Total conditions can be determined by Equations (9), (14), and (15) and energy, enthalpy, and entropy change by Equations (21) through (24). The 2-D starting solution would be used for the leading edge portion of the lifting surface on missile configurations.

For the 3-D starting solution, the tip is approximated by a cone where the initial cone angle is defined by a tangent to the surface at the tip as shown in Figure 4. Properties immediately behind the shock are also calculated by the oblique shock relations given by Equations (25) through (28). However, the flow between the shock and body is not constant throughout the flow field, as in the case with the wedge solution, but is constant along rays emanating from the cone tip. This requires solution of a differential equation to define the shock wave angle and properties at the body surface. This was done by Taylor and McCall.¹⁸ Without going through the derivation of the differential equation, it is repeated here for reference.

$$\frac{\gamma-1}{2} \left[V_{\max}^2 - V_r^2 - \left(\frac{dV_r}{d\theta} \right)^2 \right] \left[2V_r + \frac{dV_r}{d\theta} \cos^2 \theta + \frac{d^2 V_r}{d\theta^2} \right] - \frac{dV_r}{d\theta} \left[V_r \frac{dV_r}{d\theta} + \frac{dV_r}{d\theta} \left(\frac{d^2 V_r}{d\theta^2} \right) \right] = 0 \quad (30)$$

where

$$V_{\max}^2 = 2H = \text{Const}$$

Refer to Figure 5 for the nomenclature.

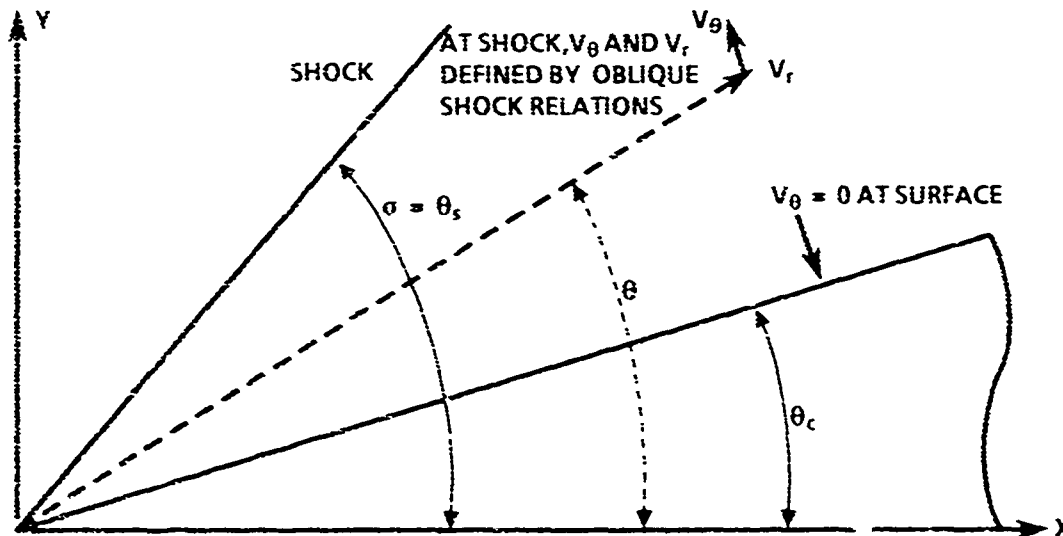


FIGURE 5. NOMENCLATURE FOR CONICAL SOLUTION

To solve this equation, we assume a shock angle σ . With this, the conditions behind the shock can be computed for a given freestream Mach number by Equations (25) through (28), and the initial velocity components V_r and V_θ behind the shock can be computed. Equation (30) is integrated until $V_\theta = 0$. If the angle θ_c is not correct, a new value of shock angle is guessed and an iteration occurs until the correct value of θ_c is found for $V_\theta = 0$.

The Mach number at the surface is then related to the total enthalpy as follows:

$$V_{\max}^2 = a^2 / (\gamma - 1) + V^2$$

or

$$\frac{V_{\max}^2}{V^2} = 1 + \frac{1}{(\gamma - 1)M^2} \quad (31)$$

Solving for M^2 , there is obtained

$$M^2 = \left[\frac{(V/V_{\max})^2}{1 - (V/V_{\max})^2} \right] \frac{1}{(\gamma - 1)} \quad (32)$$

The temperature at the surface can then be determined from Equation (14) since T_0 is constant throughout the flow. Knowing the total pressure and density behind the shock (where the flow field is isentropic) also allows one to then compute the local p and ρ throughout the flow and, in particular, at the surface from Equations (11) and (15).

Once the starting solution and the various flow properties are known at the surface of a 2-D or 3-D body, the PME Theory is applied for points downstream.

For a perfect gas, one can write⁷

$$v(M) = \sqrt{\frac{\gamma + 1}{\gamma - 1}} \tan^{-1} \sqrt{\frac{\gamma - 1}{\gamma + 1}} (M^2 - 1) - \tan^{-1} \sqrt{M^2 - 1} \quad (33)$$

If $\Delta\theta$ is the change in the local surface slope in going from one tangent segment of the body or airfoil to another tangent surface (see Figure 4), then

$$v_2(M_2) = \Delta\theta + v_1(M_1) \quad (34)$$

This means that one calculates the Prandtl-Meyer angle for the first surface with Equation (33), using M_1 from Equation (32), then must solve Equation (33) numerically for M_2 based on some value of v_2 from Equation (34). Knowing M_2 , we can compute T_2 , p_2 , ρ_2 from Equations (11), (14), and (15). Thus for $\alpha = 0$, sharp-nosed bodies, or airfoils in a perfect gas, we now have expressions for pressure and temperature all along the surface of the body or airfoil.

2.2.3 Second-order Shock-expansion Theory (SOSET)

Syverson (et al.) extended the generalized Shock-expansion Theory on pointed bodies and sharp airfoils to what he called a second-order theory.¹⁹ He defined the pressure along a conical frustum by

$$p = p_C - (p_C - p_2)e^{-\eta} \quad (35)$$

instead of a constant on each segment as was the case in the generalized theory. Here p_C is the pressure on a cone with the given cone half angle equal to the slope of the conical segment with respect to the axis of symmetry. p_2 is the pressure just aft of a conical segment (see Figure 6), which is calculated from the PME, Equations (33) and (34).

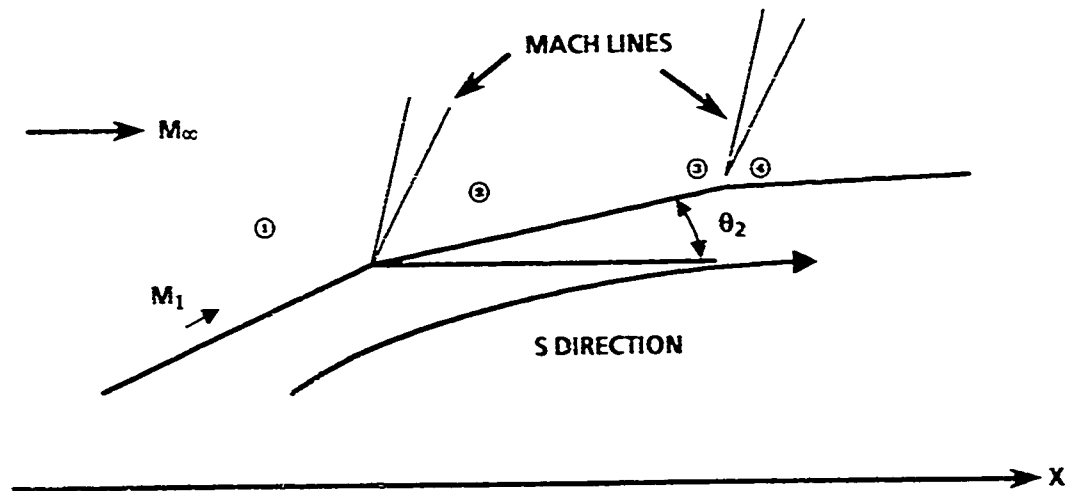


FIGURE 6. FLOW ABOUT A FRUSTUM ELEMENT

Also

$$\eta = \frac{\left(\frac{\partial p}{\partial s} \right)_2 (s - s_2)}{p_C - p_2} \quad (36)$$

Thus examining p from the equation, it can be seen, for example, on the frustum element 2-3 that the pressure varies from the pressure of the generalized theory at

point 2 to that of a cone of angle θ_2 and Mach number M_2 as s gets large. Reference 19 approximated the pressure gradient as

$$\left(\frac{\partial p}{\partial s}\right)_2 = \frac{B_2}{r} \left(\frac{\Omega_1}{\Omega_2} \sin \theta_2 - \sin \theta_2 \right) + \frac{B_2}{B_1} \frac{\Omega_1}{\Omega_2} \left(\frac{\partial p}{\partial s}\right)_1 \quad (37)$$

where

$$B_{1,2} = \frac{\gamma p M_{1,2}^2}{2(M_{1,2}^2 - 1)}$$

$$\Omega_{1,2} = \frac{1}{M_{1,2}} \left[\frac{1 + \frac{\gamma-1}{2} M_{1,2}^2}{\frac{\gamma+1}{2}} \right]^{\frac{\gamma+1}{2\gamma-1}}$$

Finally, for negative angles such as would occur on a boattailed configuration, p_c was replaced by p_w . No discussion was given for blunt bodies. It should be noted that if η of Equation (36) becomes negative, the SOSET reverts to the generalized or First-order Shock-expansion Theory of section 2.2.2. This is because (35) will not give the correct asymptotic cone solution for negative values of η .

Jackson et al.²⁰ combined SOSET with MNT to treat blunt-nosed configurations with or without flares. They, like the authors of Reference 18, assumed that the lifting properties could be predicted by assuming that the original body is made up of several equivalent bodies of revolution represented by the various meridians (see Figure 7). They assumed the match point between the MNT and second-order shock pressure prediction to be the angle that corresponds to shock detachment on a wedge with the given freestream Mach number.

DeJarnette et al.²¹⁻²³ made significant improvements to the work of Jackson et al.²⁰ and Syvertson.¹⁹ These new improvements included the following:

1. A new empirical equation for calculating pressures on blunt noses.
2. A new matching point to match the blunt-nose pressures with those of SOSET.
3. An exact (as opposed to an approximate) expression for the pressure gradient downstream of a corner.
4. A new expression for pointed-cone pressures at angle of attack which improves the initial pressure prediction over that of tangent cone theory.
5. A new technique for calculating pressures on bodies at incidence.

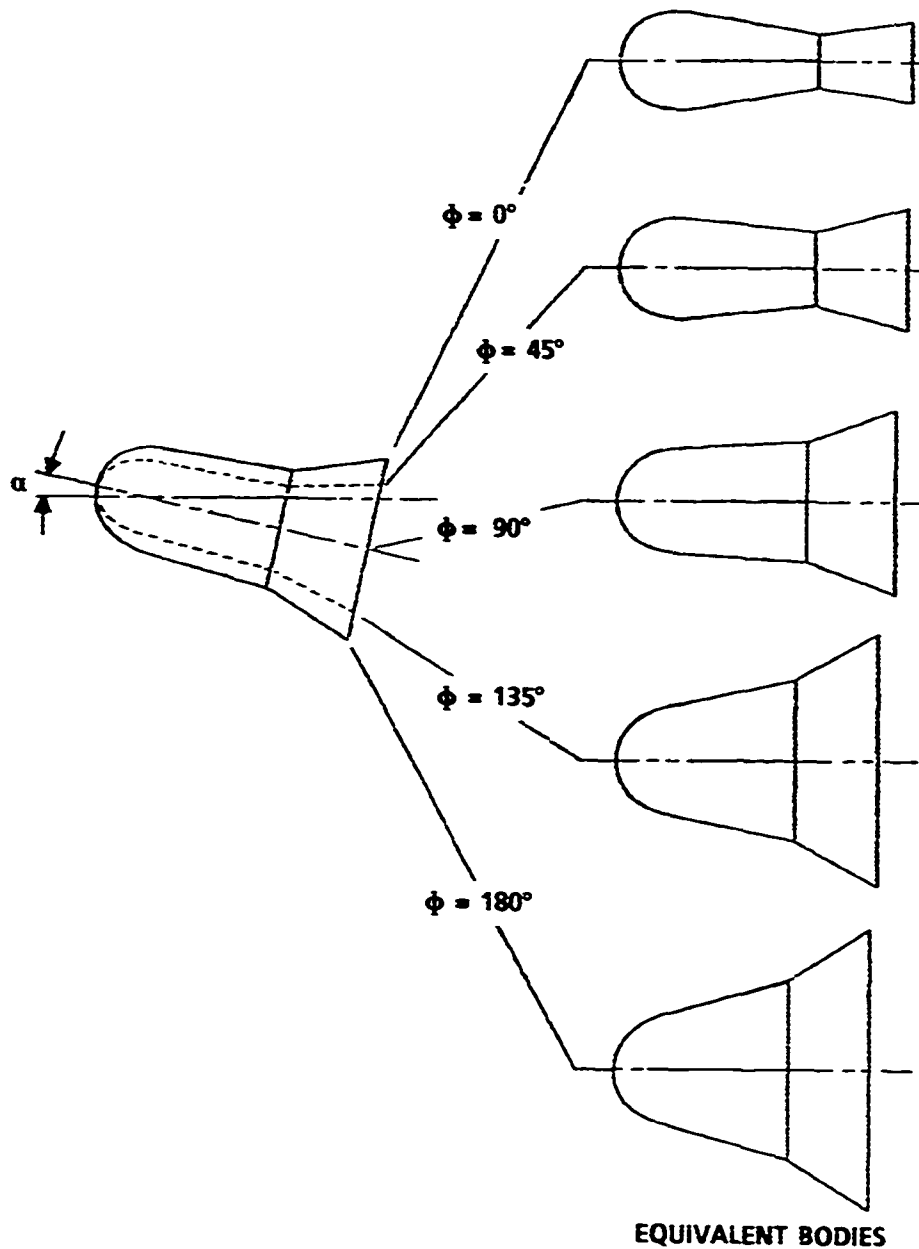


FIGURE 7. TYPICAL EQUIVALENT BODY SHAPES USED FOR COMPUTING LIFTING PROPERTIES WITH SECOND-ORDER SHOCK EXPANSION

The pressure gradient after a corner was calculated exactly through a numerical integration of the equation

$$-\left(\frac{\partial G}{\partial s}\right) \frac{\gamma+1}{2} \frac{\Omega M^4}{(M^2-1)} = \frac{d}{d\theta} \left[\Omega \left\{ \left(\sqrt{M^2-1} \right) 2 \left(\frac{\partial G}{\partial s} \right) + \frac{\sin \theta}{r} \right\} \right] \quad (38)$$

Integration of this equation gives $\partial G/\partial s$, and $\partial p/\partial s$ is then computed from

$$\frac{\partial p}{\partial s} = \left(\frac{\partial G}{\partial s} + \frac{\partial \theta}{\partial s} \right) \lambda \quad (39)$$

where

$$\lambda = \frac{2\gamma p}{\sin 2\mu}$$

and $\partial\theta/\partial s$ is the curvature of the body at a given point.

The exact pressure prediction gives much more accurate results than does the approximate method given by Equation (37), particularly for large jumps $\Delta\theta$. As noted by DeJarnette, it is important to get an accurate initial pressure to accurately predict the pressures over the rest of the body profile. Similar expressions were derived for

$$\frac{\partial p}{\partial s} \text{ when } \alpha > 0$$

but are not repeated here.

Finally, the expression for the pointed-core pressure at $\alpha > 0$ was estimated by combining Slender Body Theory, Newtonian Theory, and an approximate expression for $C_{p_{\alpha=0}}$ to give

$$C_p(\alpha, \theta, \phi, M) = C_{p_{\alpha=0}} + \Delta C_p \quad (40)$$

where

$$\Delta C_p = -\sin 2\alpha \sin 2\theta \cos \phi + \sin^2 \alpha \cos^2 \theta \left[\left(2 - \frac{1}{\beta} \right) (1 - \tan^2 \theta) - \left(2 + \frac{2}{\beta} \right) \sin^2 \phi \right] \quad (40a)$$

$$C_{p_{\alpha=0}} = \sin^2 \theta_c \left[1 + \frac{(\gamma+1)K^2+2}{(\gamma-1)K^2+2} \ln \left(\frac{\gamma+1}{2} + \frac{1}{K^2} \right) \right] \quad (40b)$$

$$K^2 = (M_\infty^2 - 1) \sin^2 \theta_c \quad (40c)$$

Note that $\phi=0$ is the leeward plane in this report versus the windward plane in Reference 23.

As shown in Reference 23, the addition of these improvements gave a significant improvement in pressure and force and moment prediction over a limited range of configurations for which computations were performed. Reference 2, which used the techniques of Reference 23 to conduct more extensive comparisons with experiment, found that improvements in MNT were minimal and, therefore, the standard MNT was used with a match point occurring where the local Mach number was 1.1. Hence, the latest version of the NAVSWC Aeroprediction Code (References 3 and 4) contains the last three improvements by DeJarnette et al. but does not contain the first two.

In more recent, unpublished research, DeJarnette was able to derive expressions for improving the Modified Newtonian Theory on blunt-nosed bodies compared to present usage. The derivation of this new methodology is given in Appendix B. This new methodology is given by

$$C_p = C_{p_{MN}} - k \cos^m \delta_{eq} \left| \cos \delta_{eq} - \cos(\delta_{eq})_m \right| \quad (41)$$

where $m = 2.78$, $(\delta_{eq})_m = 25.95^\circ$, and

$$k = \frac{-\left(\frac{dC_p}{d\delta_{eq}}\right)_{MN} + 1.5 \left| \left(C_p + \frac{2}{\gamma M_\infty^2}\right) \left(\frac{dC_p}{d\delta_{eq}}\right) \right|_{MN}^{\frac{1}{2}}}{\sin(\delta_{eq})_m \cos^m(\delta_{eq})_m}$$

Here

$$\left(\frac{dC_p}{d\delta_{eq}}\right)_{MN} = C_{p_o} \sin(2\delta_{eq}) \quad (42)$$

Thus, the theory that will be extended to $M_\infty = 20$ and to calculate the effects of equilibrium chemically reacting flow behind the shock is given by Equations (38) through (42).

Note that making the above extensions and modifications will require several changes to the existing Shock-expansion Theory combined with MNT for blunt bodies. These include the following:

1. Calculation of real gas effects behind a normal shock.
2. Calculation of real gas effects across an oblique shock attached to a cone and wedge.
3. Calculation of PME for chemical equilibrium flows.
4. Extension of the exact pressure gradient formula for $\alpha = 0$ and $\alpha \neq 0$ to include frozen and chemical equilibrium flows.
5. Modified Newtonian Theory extended to real gases.
6. Definition of match point up to $M_\infty = 20$.
7. Computation of temperature along body surface (in addition to pressure).
8. Modification of any empirical formulas as necessary for frozen and equilibrium flows.

These changes will be discussed later in this report. It should be noted that, while the first three changes are state of the art,²⁴⁻²⁷ the last five have never been presented before to the author's knowledge.

2.3 REAL GAS COMPUTATIONAL PROCESS

2.3.1 Summary of Procedure for General Chemical Species Composition

To put real gas computations in proper perspective, consider the mathematical model of an inviscid flow field. These equations are standard in the literature⁵⁻¹⁰ and are sometimes referred to as Euler's equations. They will be stated here in vector form without derivation.

Continuity Equation

$$\frac{\partial \rho}{\partial t} + \nabla \cdot \rho \vec{V} = 0 \quad (43)$$

(one equation, four unknowns)

Momentum Equation

$$\frac{D}{Dt} \vec{V} = \frac{-1}{\rho} \nabla p \quad (44)$$

(three equations, one additional unknown)

Energy Equation

$$\rho \frac{D(h + V^2/2)}{Dt} = \frac{\partial p}{\partial t} + \rho \mathbf{q} + \rho(\vec{f} \cdot \vec{V}) \quad (45)$$

(one equation, three additional unknowns)

Equation of State

$$h = h(p, \rho) \quad (46)$$

(one equation, zero additional unknowns)

These equations have few assumptions. They assume inviscid flow with no sources or sinks present and the potential energy of the air mass due to gravity is negligible. There is a total of six equations and eight unknowns. If we make the assumption of no body forces (i.e., $\mathbf{f} = 0$) and no heat added to the system from the outside (radiation, etc. so that $\mathbf{q} = 0$), then the system reduces to six equations and six unknowns. For a perfect gas, Equation (46) is

$$h = \bar{C}_p T \quad (47)$$

and from the equation of state for a perfect gas:

$$T = \frac{p}{\rho R} \quad (48)$$

Here \bar{C}_p is a constant. Equation (48) along with Equations (43) through (47) form a deterministic mathematical model for general 3-D computation of inviscid flows over configurations in a Mach number range where these equations are valid. They are solved in finite difference form such as References 28 and 29 or in various approximate forms such as References 3, 4, or 30-32 (among others). If viscous flows are of interest, the viscous stress terms can be added to Equation (44), and the set of equations then becomes the Navier Stokes equations. Also, they can be solved numerically or by approximations of a thin layer near the body (boundary layer).

The question we must answer is how we calculate the enthalpy (or internal energy since $h = e + p/\rho$) when the gas is at a temperature such that the perfect gas law is no longer valid. Numerous efforts are reported in the literature going back to the 1940s and 1950s when high-speed flight was really becoming a practical problem. Again, a rederivation of results will not be repeated here—only a summary computation process. The process draws heavily on the kinetic theory of gases and Quantum Mechanics.

The internal energy of an atom (O, N, O+, N+) or molecule (NO, O₂, N₂) is comprised of

$$e = e_t + e_r + e_v + e_e + e_d \quad (49)$$

where subscripts t, r, v, e, d stand for translation, rotation, vibration, electronic excitation, and dissociation. For a single atom, only e_t and e_e are important since the rotational energy is small compared to translational energy. From the kinetic theory of gases⁵

$$e_t = \frac{3}{2} RT \quad (50)$$

for both atoms and molecules. Also

$$e_r = 0 \text{ for atoms}$$

$$e_r = RT \text{ for molecules} \quad (51)$$

The vibration energy is somewhat more difficult to compute. The vibration energy is

$$e_v = 0 \text{ for atoms}$$

$$e_v = \frac{R\theta_v}{\exp\left(\frac{\theta_v}{T}\right) - 1} \quad (52)$$

where θ_v is 2270°K for O₂, 3390°K for N₂, or approximately 3160°K for air up to the point of dissociation. Also, exp has been used to denote exponential to distinguish the normal terminology of e for exp from the total internal energy e.

Combining Equations (49) through (52), for air up to approximately 2000°K

$$e = e_t + e_r + e_v$$

$$e = \frac{5}{2} RT + \frac{R\theta_v}{\exp\left(\frac{\theta_v}{T}\right) - 1} \quad (53)$$

Equation (53) is for molecules only as we assume air is about 80 percent N₂ and 20 percent O₂ and, therefore, no atomic species are present. Note that Equation (53) is a function of several fixed constants and temperature only. Hence, Equation (1) or (46)

holds identically, and one can replace Equation (48) with Equation (53) for temperatures in the range of 600°K to 2000°K. Figure 8 is a plot of the specific heats and the ratio of specific heats where only the rotation, translation, and vibration modes of energy are accounted for (see References 6 and 8).

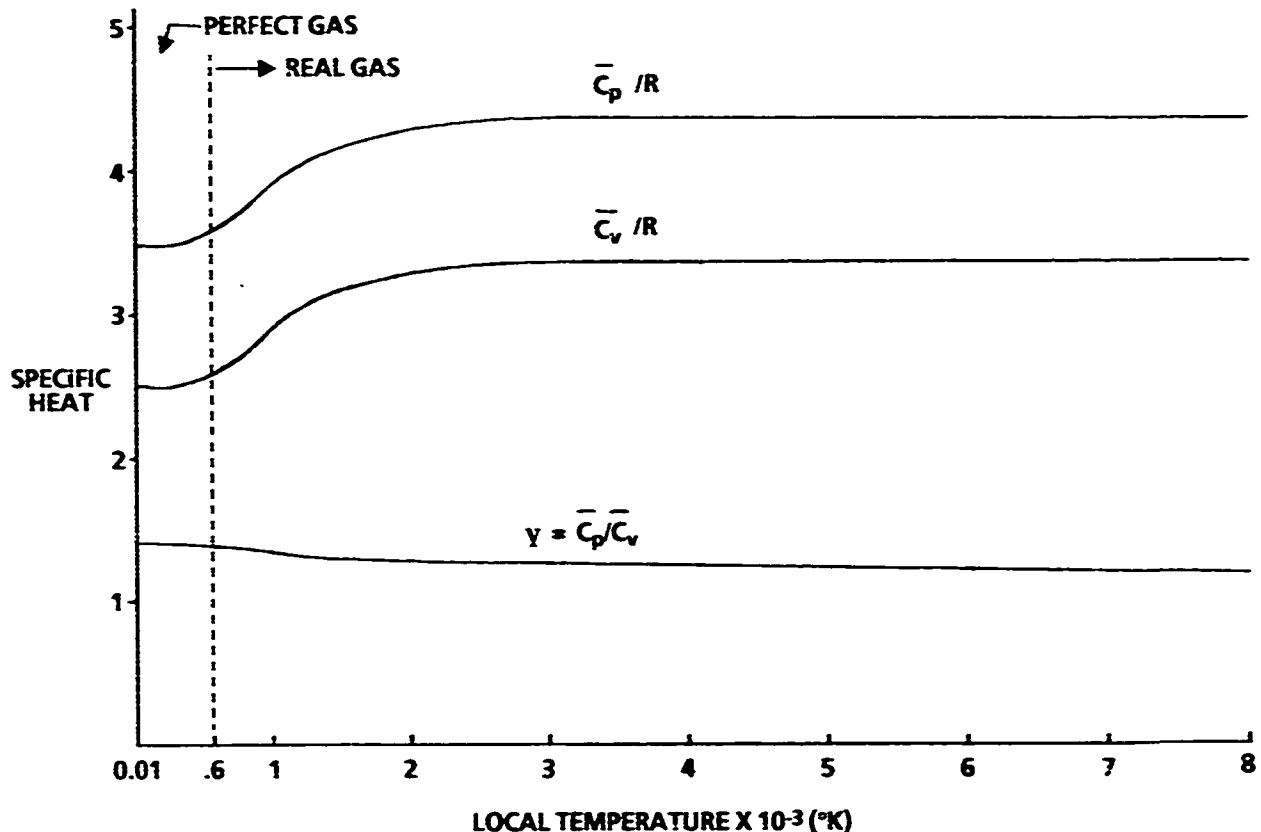


FIGURE 8. SPECIFIC HEATS FOR AIR (NO DISSOCIATION OR IONIZATION)

As air is heated above 2000°K, it begins to dissociate into N, O, and NO atoms and molecules in addition to the N₂, O₂ already prevalent. Initially, the O₂ begins to dissociate, but at temperatures of about 4000°K, the N₂ dissociation also becomes appreciable. Finally, above temperatures of 9000°K, the oxygen and nitrogen atoms and molecules begin to give up electrons (ionize). This dissociation and ionization of the air molecules creates additional internal energy that must be accounted for to accurately predict the thermodynamic and transport properties in the flow. To compute these thermodynamic properties, we first must determine the species concentrations at the given T and p of the mixture. Then enthalpy, internal energy,

and values of specific heats, ratio of specific heats, and gas constant can be computed. Some typical chemical reactions for air are



Reference 11 shows there is a total of 22 chemical reactions that occur for temperatures up to 15000°K, resulting in a set of 28 nonlinear equations. Each of these reactions will have an equilibrium constant. These equilibrium constants are known functions of temperature from either measurements or statistical mechanics computations. These equilibrium constants are related to the partial pressures of the individual constituents by the Law of Mass Action.⁵ Here the partial pressures can be thought of (for example, p_{O}) as the pressure that would result if a container of given volume were filled with only oxygen atoms. As an example, for Equations (54) through (57), the equilibrium constants are related to the partial pressures of individual constituents as follows:

$$\frac{(p_{\text{O}})^2}{p_{\text{O}_2}} = K_{\text{P, O}_2}(T) \quad (58)$$

$$\frac{(p_{\text{N}})^2}{p_{\text{N}_2}} = K_{\text{P, N}_2}(T) \quad (59)$$

$$\frac{p_{\text{NO}}}{p_{\text{N}} p_{\text{O}}} = K_{\text{P, NO}}(T) \quad (60)$$

$$\frac{p_{\text{NO}} p_{\text{e}}}{p_{\text{N}} p_{\text{O}}} = K_{\text{P, NO}^+}(T) \quad (61)$$

There, of course, would be a single equation corresponding to each significant chemical reaction. For temperatures below about 9000°K, Equations (58) through (61) are the most important reactions. In addition to Equations (58) through (61), we have Dalton's Law of Partial Pressures, which states that the total pressure of the mixture is the sum of the partial pressures. Mathematically, for the constituents of Equations (58) through (61), this can be written as follows:

$$p = p_{\text{O}_2} + p_{\text{O}} + p_{\text{N}_2} + p_{\text{N}} + p_{\text{NO}} + p_{\text{NO}^+} + p_{\text{e}^-} \quad (62)$$

Of course, if the temperature is higher than 9000°K and other chemical reactions occur, the other species must be added to Equation (62), just as the chemical reaction equations are included in the set (58) through (61). Note that there are seven unknowns in Equation (62) and five equations so far. The remaining two equations come from a chemical balance of the number of O and N atoms and the fact that electric charge must be conserved. These facts, in equation form, may be written as

$$\frac{N_O}{N_N} = \frac{0.2}{0.8} = 0.25 = \frac{2p_{O_2} + p_O + p_{NO} + p_{NO}}{2p_{N_2} + p_N + p_{NO} + p_{NO}} \quad (63)$$

and

$$p_{NO^-} = p_{e^-} \quad (64)$$

Again, if more reaction equations are included, then Equations (63) and (64) will change to include other species. The fundamental principle of correct balance of O₂, N₂ and electric charge will not change, however. For a given temperature and pressure, Equations (58) through (64) give a unique set of seven partial pressures for the seven species (Reference 5, of course, has 22 species). This is a nonlinear set of algebraic equations that must be solved for each given T, p to determine the species content once temperatures are high enough for dissociation to occur. Knowing the partial pressures of the species present allows one to uniquely determine the other properties of the system. The details will not be repeated here but can be found in References 5, 9, or 33. Figure 3 is an example of an equilibrium composition of air as a function of temperature at a given density.

2.3.2 Simplified Procedures for Air

This discussion, thus far, has focused on how to compute the thermodynamic and flow field properties of a chemically reacting gas. For general chemical reactions, this is the process that must be used. However, for air other alternatives are available. For example, Reference 11 has produced tables of the properties of air as a function of p and ρ. These could be used in a table look-up mode in the computation process. A more simplified approach was produced by Tannehill and Mugge³⁴ and later extended to other thermodynamic variables by Srinivasan et al.³⁵ They produced curve fits from algebraic equations for p = p(e, ρ), a = a(e, ρ), T = T(e, ρ), h = h(p, ρ), and T = T(p, ρ). These fits are valid up to temperatures of 25000°K. Since this is by far the most computationally efficient method and since we will only be dealing with air, this is the technique used in this report. Since it is the technique used, a brief discussion of the equations relevant to the work herein will be given.

Appendix B shows the iteration process to determine properties behind a normal or oblique shock wave, which involves assuming a value of p₁/p₂ behind the shock, computing p₂ and h₂ from this assumed value, and then recomputing a new

value of p_2 based on these values of p_2 and h_2 from the thermodynamic properties of equilibrium air. An example of the algebraic equation contained in Reference 34 is shown here. From Reference 34, an effective γ as a function of p and ρ is defined by

$$\bar{\gamma} = C_1 + C_2 Y + C_3 Z + C_4 YZ + \frac{C_5 + C_6 Y + C_7 Z + C_8 YZ}{1 + \exp[(C_9(X + C_{10}Y + C_{11}))]} \quad (65)$$

where

$$Y = \log_{10} \left(\frac{p}{1.292} \right)$$

$$X = \log_{10} \left(\frac{p}{1.013 \times 10^5} \right)$$

$$Z = X - Y$$

The coefficients $C_1, C_2, C_3, C_4, C_5, C_6, C_7, C_8, C_9, C_{10}, C_{11}$ are tabulated in Table 1 of Reference 34. This allows one to compute enthalpy from the relation

$$h = \frac{p}{\rho} \left[\frac{\bar{\gamma}}{\bar{\gamma} - 1} \right] \quad (66)$$

and energy from

$$e = h - \frac{p}{\rho} \quad (67)$$

Also, from values of p and ρ , the temperature can be determined from

$$\log_{10}(T/T_\infty) = d_1 + d_2 Y + d_3 Z + d_4 YZ + d_5 Z^2 + \frac{d_6 + d_7 Y + d_8 Z + d_9 YZ + d_{10} Z^2}{1 + \exp[d_{11}(Z + d_{12})]} \quad (68)$$

Here

$$Y = \log_{10} \left(\frac{p}{1.225} \right)$$

$$X = \log_{10} \left(\frac{p}{1.0134 \times 10^5} \right)$$

$$Z = X - Y$$

and $d_1, d_2, d_3, d_4, d_5, d_6, d_7, d_8, d_9, d_{10}, d_{11}, d_{12}$ are given in Table 2 of Reference 34. Knowing $\rho, p, T, h, \bar{\gamma}, e$, the only quantities remaining are velocity and compressibility factor. These can be determined from the constancy of total enthalpy relation and the equation of state

$$H = \text{Const} = h_1 + \frac{U_1^2}{2} = h_2 + \frac{U_2^2}{2} \quad (69)$$

$$\bar{Z} = \frac{p}{\rho RT} \quad (70)$$

Knowing H from freestream conditions and a new h_2 allows one to compute the local U_2 . It should be noted here that the relationship

$$\frac{\bar{\gamma} p}{\rho}$$

does not yield the true speed of sound as in the case of a perfect gas. This is because $\bar{\gamma}$ is h/e as defined by Reference 34 and $\bar{\gamma} = \gamma$ only if no dissociation of air molecules occurs. Tannehill³⁴ gave an expression for the approximate speed of sound if e and p were known. That is

$$a = \left[e \left\{ k_1 + (\bar{\gamma} - 1) \left[\bar{\gamma} + k_2 \left(\frac{\partial \bar{\gamma}}{\partial \log e} \right)_p \right] + k_3 \left(\frac{\partial \bar{\gamma}}{\partial \log p} \right)_e \right\} \right]^{\frac{1}{2}} \quad (71)$$

This is also provided in curve fit form by Tannehill

$$a = a(e, p)$$

The correct local Mach number is then

$$M = \frac{V}{a} \quad (72)$$

Srinivasan³⁵ produced additional curve fits of various thermodynamic variables. These included

$$\left. \begin{aligned} \rho &= \rho(h, p) \\ \rho &= \rho(p, T) \\ S &= S(e, p) \\ \rho &= \rho(p, S) \\ a &= a(p, S) \\ e &= e(p, S) \end{aligned} \right\} \quad (73)$$

Having curve fits available for thermodynamic variables means that the computational time for real gas flow fields has been reduced considerably over what it would be if the chemistry of the gas had to be computed at each point in the flow field.

Some results of the Reference 34 curve fit procedure are given in Figures 9 through 12 in terms of various thermodynamic properties. In each of the figures, the thermodynamic properties are referenced to some set of standard conditions that could be the sea level standard atmosphere for example.

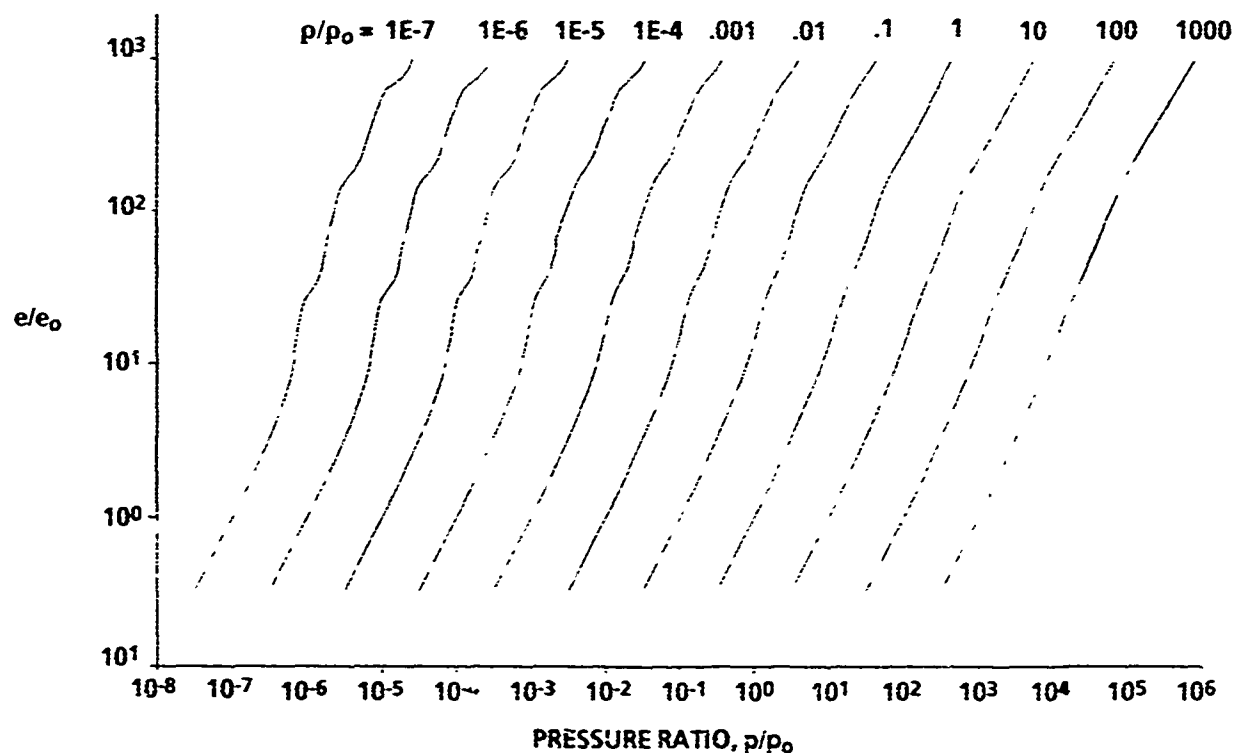


FIGURE 9. CURVE FIT EQUATIONS (INTERNAL ENERGY RATIO)

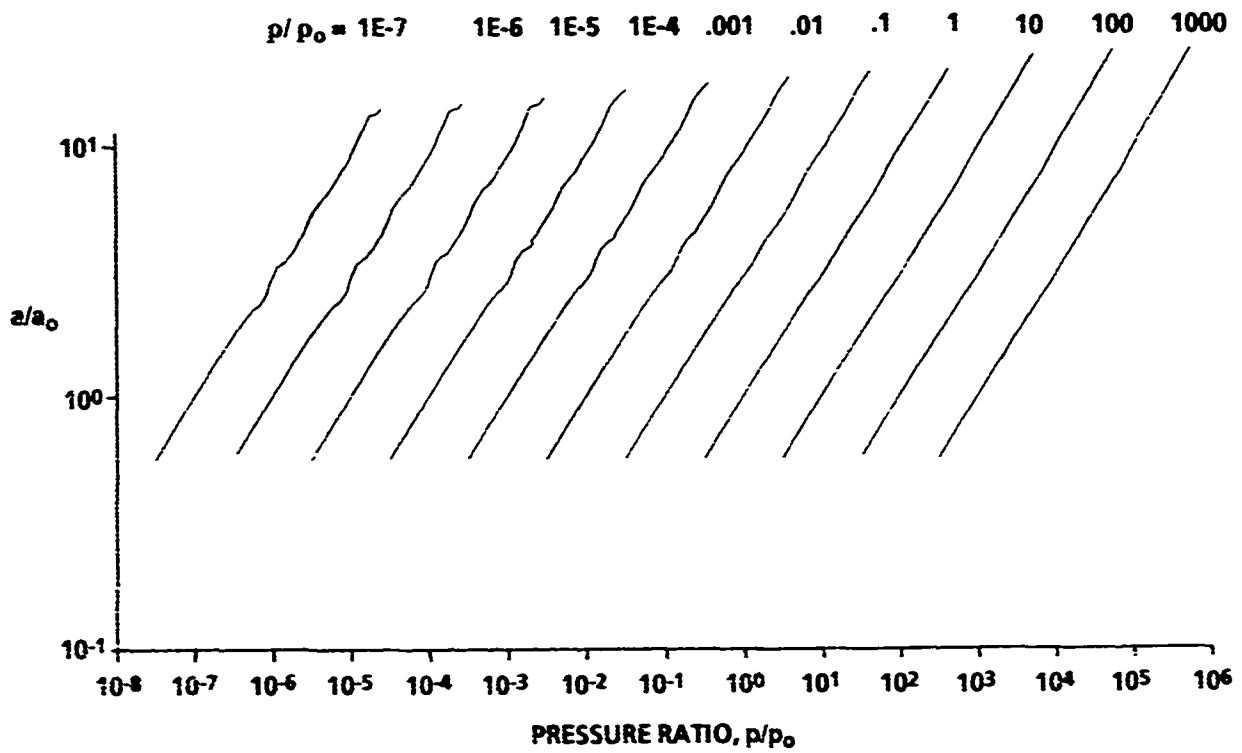


FIGURE 10. CURVE FIT EQUATIONS (SPEED OF SOUND RATIO)

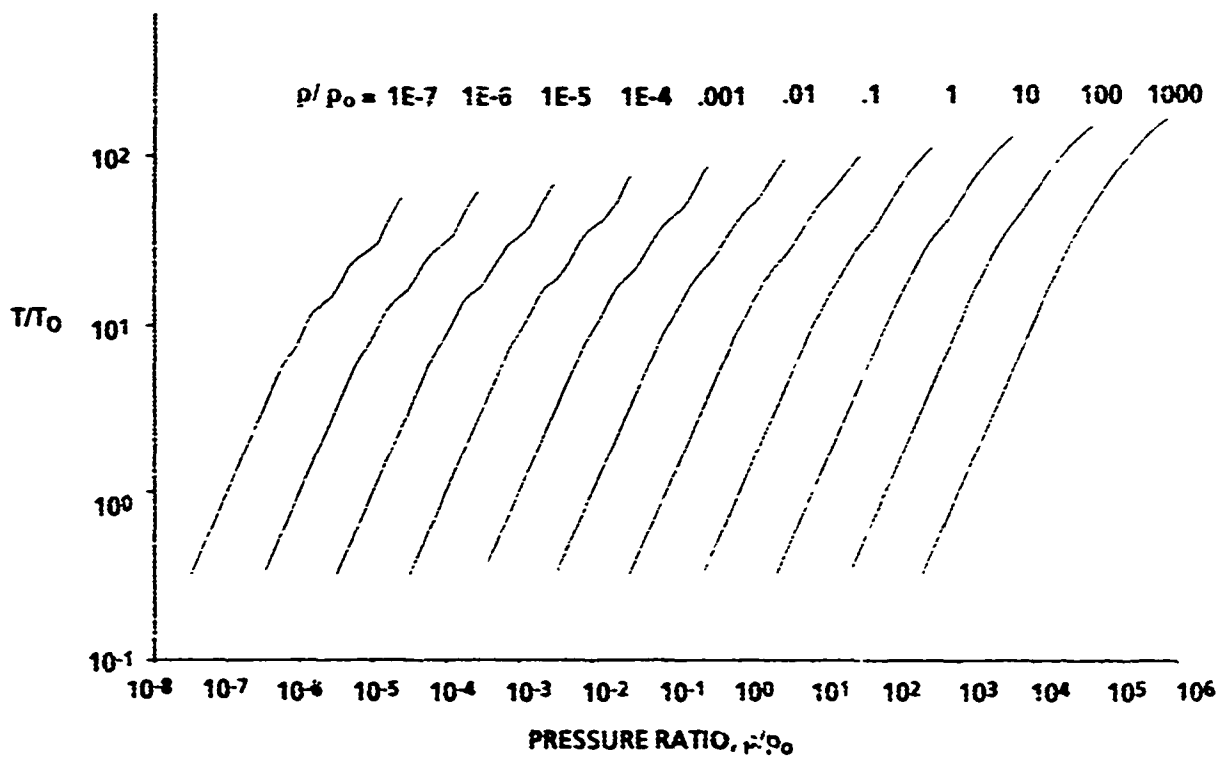


FIGURE 11. CURVE FIT EQUATIONS (TEMPERATURE RATIO)

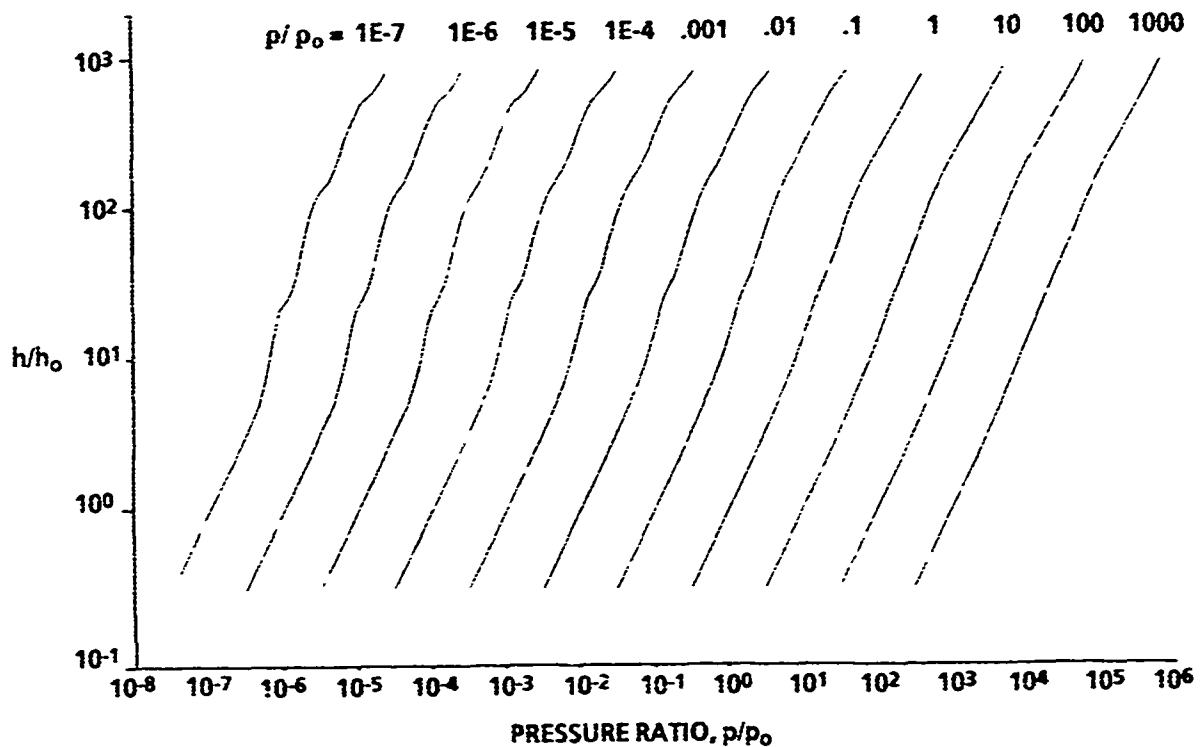


FIGURE 12. CURVE FIT EQUATIONS (ENTHALPY RATIO)

2.3.3 Chemical Reaction Rates

In the preceding discussion, it was assumed that the reaction rates of the chemical processes were infinitely fast so that the flow could be assumed to be in chemical equilibrium at all points in the flow field. If one defines the characteristic length of the flow field to be the body length, then the time it takes for a fluid element to traverse the shock wave and full body length is

$$t_1 = l_B / V \quad (74)$$

Defining the time it takes for a chemical reaction to come into equilibrium as t_2 , then if

$$t_1 \gg t_2 \quad (75)$$

the flow is truly in chemical equilibrium for all practical purposes. On the other hand, if

$$t_2 \gg t_1 \quad (76)$$

we may assume that the flow is "frozen" at the chemistry that exists just behind the shock. That is, we can compute the flow as if it were a perfect gas except we have a different value of $\gamma = \gamma_f$ behind the shock. Finally, if

$$t_1 \approx t_2 \quad (77)$$

we have nonequilibrium flow, which means that the chemical processes are occurring and changing significantly along the body. This results in an order of magnitude more difficulty in making real gas computations. What can be done, however, from a more practical standpoint is to compute the local conditions assuming "frozen" and "equilibrium" flows and assume that the nonequilibrium case falls in between these two. That is, generally the equilibrium and frozen flow cases present boundaries for flow properties and the nonequilibrium case falls in between.

Since the focus of the present work is to incorporate real gas effects into SOSET, only equilibrium and frozen flows will be considered. The computations involved with a nonequilibrium flow are inconsistent with an approximate mathematical model of the flow field and are more consistent with solution of the full Euler or Navier Stokes equations.

2.3.4 Modified Newtonian Theory

Recall from Section 2.2.1, that the MNT pressure coefficient is given by

$$C_p = C_{p_0} \sin^2 \delta_{eq} \quad (78)$$

where δ_{eq} is evaluated according to Appendix A. (Note that even though Equations (41) and (42) are the relations used to calculate pressures around the blunt portion, they are both functions of modified Newtonian pressures.) For the perfect gas computations, C_{p_0} was evaluated according to Equation (12). However, Equation (12) no longer holds for real gas computations across normal or oblique shock waves (see Appendix C). The conditions behind the shock wave can no longer be solved for in closed form, as in Section 2.2.1, because the specific heats and compressibility factor are no longer constant. This means that an iteration takes place to determine the properties immediately behind the shock. Appendix C thus is the process for defining conditions behind the shock, i.e.

$$Y_2, P_2, \rho_2, h_2, s_2, V_2, M_2, T_2, Z_2, S_2$$

The question that must be addressed is twofold:

1. How do these parameters vary along the stagnation streamline between the body and shock?
2. How do these properties vary from the stagnation point around the body to the point where shock expansion theory is applied?

This section of the report will address these questions for both frozen flow and equilibrium chemically reacting flows where MNT is used on the blunt portion of a configuration for pressure, temperature, force, and moment computations.

2.3.4.1 Frozen Flow. For frozen flow, it is assumed that the γ and compressibility factor are fixed at the values they have just behind the shock (i.e., $\gamma = \gamma_f$, $Z = Z_f$). It is also known that, along the stagnation streamline, the flow is isentropic for equilibrium flow conditions. Furthermore, it is known from many previous works (see, for example, References 10, 13, and 24) that the Mach number behind a normal shock is much less than 1 for high freestream Mach numbers. Also, this Mach number must go to 0 at the stagnation point which is only a slight distance away from the shock. This has led to approximate theories in the stagnation region based on constant density, temperature, and pressure which, in effect, is the Newtonian assumption in the shock layer. That is, the shock is assumed to lie on the body and the conditions behind the shock are the same as those on the body surface. The physics of the flow between the shock and body is what allows one to assume γ_f and Z_f are in fact approximately constant for both equilibrium and frozen flow between the shock and body and along the stagnation streamline. Reference 24 indicates a maximum 2.3 percent error in making this assumption, and in most cases the error was much less.

A second assumption will also be made. This assumption will allow the use of Equations (9), (14), and (15) in a local sense along the body where $\gamma = \gamma_f$ and M is the local value. Strictly speaking, these equations relating total to static conditions are derived based on perfect gas assumptions and with constant $\gamma = 1.4$. The accuracy of this assumption (combined with others) can be assessed in comparison with exact calculations over a blunt-nosed body by solution of the full Euler equations. This will be done in the Results section of this report.

Returning now to Equation (78) and recognizing the fact that all the properties behind the shock are known from the real gas computations of the flow across a normal shock (Appendix C), one can write

$$C_{pO} = \frac{p_{O_2} - p_\infty}{\frac{1}{2} \rho_\infty V_\infty^2} = \frac{2}{\gamma M_\infty^2} \left(\frac{p_{O_2}}{p_\infty} - 1 \right) = \text{Const} \quad (79)$$

where

$$p_{O_2} = p_2 \left(1 + \frac{\gamma_f - 1}{2} M_2^2 \right)^{\frac{\gamma_f}{\gamma_f - 1}} = \text{Const} \quad (80)$$

along the stagnation streamline. Here p_2 , p_2 , h_2 , V_2 , z_2 , M_2 , γ_f , z_f etc. are the values calculated immediately behind the shock from Appendix B. Also

$$H = h_2 + \frac{V_2^2}{2} \quad (81)$$

$$T_{O_2} = T_2 \left(1 + \frac{\gamma_f - 1}{2} M_2^2 \right) \quad (82)$$

$$p_{O_2} = p_2 \left(1 + \frac{\gamma_f - 1}{2} M_2^2 \right)^{\frac{1}{\gamma_f - 1}} \quad (83)$$

Now, since at the stagnation point local velocity and Mach number are zero, the static pressure, temperature, density, and enthalpy at the stagnation point are simply the total values behind the shock given by Equations (80) through (83). Thus, at the stagnation point, for frozen flow

$$\left. \begin{aligned} p_S &= p_{O_2} \\ T_S &= T_{O_2} \\ h_S &= H \\ p_S &= p_{O_2} \\ M_S &= V_S = 0 \\ \gamma &= \gamma_f = \text{Const} \\ \bar{C}_p &= \bar{C}_{p_f} = \text{Const} \\ \bar{C}_v &= \bar{C}_{v_f} = \text{Const} \\ Z_S &= Z_f = \text{Const} \\ S &= S_2 = \text{Const along body} \end{aligned} \right\} \quad (84)$$

To continue the computations around the blunt surface, an isentropic expansion is assumed and Equation (78) is applied at each point on the surface where δ is given by

Appendix A and C_{p0} is constant at the value given by Equation (79). Knowing δ_{eq} , C_{p0} , and C_p allows one to calculate the local pressure at a given point. That is

$$p_L = p_\infty \left[1 + \frac{\gamma_\infty M_\infty^2}{2} C_p \right] \quad (85)$$

Since the flow is frozen, we can treat it just like a perfect gas except that the values of $\gamma = \gamma_f$ and $R_f = RZ_f$. Hence, knowing local pressure from Equation (85), total pressure, temperature, density, and other flow properties behind the normal shock [Equations (80) - (84)], the fact that total conditions are constant along a streamline, the local conditions at any point on the blunt body can be calculated by

$$M_L = \left\{ \left[\left(\frac{p_{02}}{p_L} \right)^{\frac{\gamma_f-1}{\gamma_f}} - 1 \right] \left(\frac{2}{\gamma_f-1} \right) \right\}^{\frac{1}{2}} \quad (86)$$

$$T_L = T_{02} / \left(1 + \frac{\gamma_f-1}{2} M_L^2 \right) \quad (87)$$

$$\rho_L = \rho_{02} / \left(1 + \frac{\gamma_f-1}{2} M_L^2 \right)^{\frac{1}{\gamma_f-1}} \quad (88)$$

$$a_L = \left(\frac{\gamma_f p_L}{\rho_L} \right)^{\frac{1}{2}} \quad (89)$$

$$V_L = M_L a_L \quad (90)$$

$$h_L = H - \frac{V_L^2}{2} \text{ and } e_L = h_L - p_L / \rho_L \quad (91)$$

2.3.4.2 Equilibrium Flow. Equilibrium chemically reacting flow properties at the stagnation point are computed just like the frozen flow case. This is based on the rationale discussed previously of only slight changes in the specific heats and compressibility factor between the body and shock. However, for the isentropic expansion around the body, γ and Z are allowed to vary from the values at the stagnation point in contrast to the frozen flow case where these parameters are frozen at values behind the shock. Hence, for equilibrium chemically reacting flows, Equation (84) defines the stagnation point conditions. Also, Equation (85) defines the pressure at the next point around the body. To get the remaining properties, recourse is once again made to the real gas curve fits of Section 2.3.2. To obtain p , we know local pressure and entropy so that

$$\rho_L = \rho(p, S) \quad (92)$$

Then, knowing pressure and density

$$h_L = h(p, \rho), T_L = T(p, \rho), a_L = a(p, \rho) \quad (93)$$

The remaining quantities can be computed from thermodynamic relations as follows:

$$V_L = \sqrt{2(H_O - h_L)} \quad (94)$$

$$M_L = V_L / a_L \quad (95)$$

$$\gamma_L = a_L^2 \rho_L / p_L \quad (96)$$

$$e_L = h_L - p_L / \rho_L \quad (97)$$

$$Z_L = p_L / (\rho_L R T_L) \quad (98)$$

This process is continued around the body surface to the point where shock expansion begins. Again, Equations (85), (86), and (92) through (98) provide initial conditions for the shock expansion process.

2.3.5 Second-order Shock-expansion Theory (SOSET)

2.3.5.1 Zero Angle-of-Attack Solution

Recall that SOSET was given by Equations (35) and (36), repeated here for convenience.

$$p = p_C - (p_C - p_2)e^{-\eta} \quad (35)$$

$$\eta = \frac{\left(\frac{\partial p}{\partial s}\right)_2 (s - s_2)}{p_C - p_2} \quad (36)$$

We desire to develop the theory to allow computations to proceed around the body using modified versions of Equations (35) and (36) for real gas effects. To do this requires pressures on wedges and cones calculated based on real gases (see Appendix C) and pressures behind an expansion corner computed by the PME for real gases (see

Appendix D). Note some of the results of wedge, cone, and expansion flows of real versus perfect gases shown in Appendixes C and D. The pressures in compression processes are almost identical for perfect and real gases, whereas the temperatures show significant differences as the Mach number and compression angle increase. On the other hand, expansion processes show differences for both pressure and temperature of real versus perfect gas computations.

If one were only interested in applying generalized Shock-expansion Theory for equilibrium or frozen flows over wing body configurations in a local sense at near-zero angle of attack, one would stop at this point. Appendixes C and D give the results for pressures and temperatures that are used for points around the 2-D or axisymmetric body. One would simply compute the pressure and temperature on the blunt portion of the body using section 2.3.4, determine a match point, use the PME of Appendix D to march around the surface where the pressure and other properties are constant on each straight-line segment of Figure 6. For a sharp conical tip or wedge, results of Appendix C could be used for the initial solution, and the solution could proceed along the body or wing surface again using the PME results of Appendix D. However, experience has shown that a first-order solution is unacceptable for pressure on most bodies of revolution at lower supersonic Mach numbers, so a second-order accurate pressure scheme is necessary for good force and moment predictions. Since this is the case, a comparable second-order technique for real gas pressures and temperatures at the surface to be available for inputs to heat transfer and force and moment computations is also desirable.

The crux of the problem in addressing second-order solutions for inclusion of real gas effects is to successfully address the pressure gradient of Equation 36

$$\left(\frac{\partial p}{\partial s} \right)_2$$

behind the corner and to find simple but accurate ways of addressing angle-of-attack computations for values of p_c in Equation (35) and temperature along the surface. The pressure gradient change behind a corner will be investigated first. To do this will require several steps:

1. Conversion of the equations of motion [Equations (43 and (44)] from rectangular to streamline coordinates and derivation of the characteristic equations.
2. Derivation of the pressure change along a left running characteristic (or Mach line) since this is the mechanism for differential pressure change along the surface.
3. For angle-of-attack computations, a method for accurately computing Δp and ΔT due to α .

4. An algebraic approximation as a solution to an ordinary differential equation (ODE).

While the labor and math are fairly involved to get to step 4, the solution of the equation in step 4 is the only thing the computer sees and it is very fast. Most of the details of the derivation of steps 1-2 will be indicated in the following discussion and will be included either in the text or an appendix. Angle-of-attack effects are discussed in section 2.3.6. The theoretical methodology follows the approach of Reference 23 for perfect gases and modifies the mathematical model as necessary or states assumptions made to allow real gas computations.

Appendix E converts the continuity and momentum equations from rectangular to streamline coordinates and then derives the characteristic compatibility relations. These equations for axisymmetric bodies at zero angle of attack, repeated here, are

$$\frac{\beta}{\rho V^2} \frac{dp}{dC_1} + \frac{d\theta}{dC_1} = \frac{-\sin \theta \sin \mu}{r} \quad (99)$$

$$\frac{\beta}{\rho V^2} \frac{dp}{dC_2} - \frac{d\theta}{dC_2} = \frac{-\sin \theta \sin \mu}{r} \quad (100)$$

Since we are looking for $\partial p / \partial s$ downstream of an isentropic turn, information away from the body surface must be obtained. To do this, we must relate the change in flow variables along the left running characteristic to the change of these variables along a streamline. In general, one can write

$$s = s(C_1, C_2)$$

where s , C_1 , and C_2 are all curvilinear coordinates. By the chain rule

$$\frac{\partial}{\partial s} = \frac{\partial C_1}{\partial s} \frac{\partial}{\partial C_1} + \frac{\partial C_2}{\partial s} \frac{\partial}{\partial C_2} \quad (101)$$

Also, the differential ds is

$$ds = \frac{\partial s}{\partial C_1} dC_1 + \frac{\partial s}{\partial C_2} dC_2 \quad (102)$$

And, since $ds = dC_1 \cos \mu + dC_2 \cos \mu$ and along a streamline $dC_1 = dC_2$, then

$$\frac{\partial C_1}{\partial s} = \frac{\partial C_2}{\partial s} = \frac{1}{2 \cos \mu}$$

Thus Equation (101) becomes

$$\frac{\partial}{\partial s} = \frac{1}{2 \cos \mu} \left[\frac{\partial}{\partial C_1} + \frac{\partial}{\partial C_2} \right] \quad (103)$$

or

$$\frac{\partial}{\partial C_1} = 2 \cos \mu \frac{\partial}{\partial s} - \frac{\partial}{\partial C_2} \quad (104)$$

Now adding Equations (99) and (100), using the relation (104), there is obtained (where $\lambda = \rho V^2 / \beta$)

$$\frac{\partial \theta}{\partial C_1} = \frac{-\sin \mu \sin \theta}{r} - \frac{\cos \mu}{\lambda} \left[\frac{\partial p}{\partial s} - \lambda \frac{\partial \theta}{\partial s} \right] \quad (105)$$

Likewise, subtracting Equation (99) from (100), the relationship for pressure along the left running characteristic is obtained as

$$\frac{\partial p}{\partial C_1} = \cos \mu \left[\frac{\partial p}{\partial s} - \lambda \frac{\partial \theta}{\partial s} \right] \quad (106)$$

Equations (105) and (106) are the two relations we will use to provide information to allow computation of

$$\left(\frac{\partial p}{\partial s} \right)_2$$

To do this, consider a streamline very near the body surface that will form a streamtube between the body and the streamline (see Figure 13). Referring to Figure 13, the distance along a Mach line to the streamline is b , which again is assumed to be very small compared to the body radius. The thickness of the streamtube is $b_1 \sin \mu_1$ ahead of the turn and $b_2 \sin \mu_2$ after the turn.

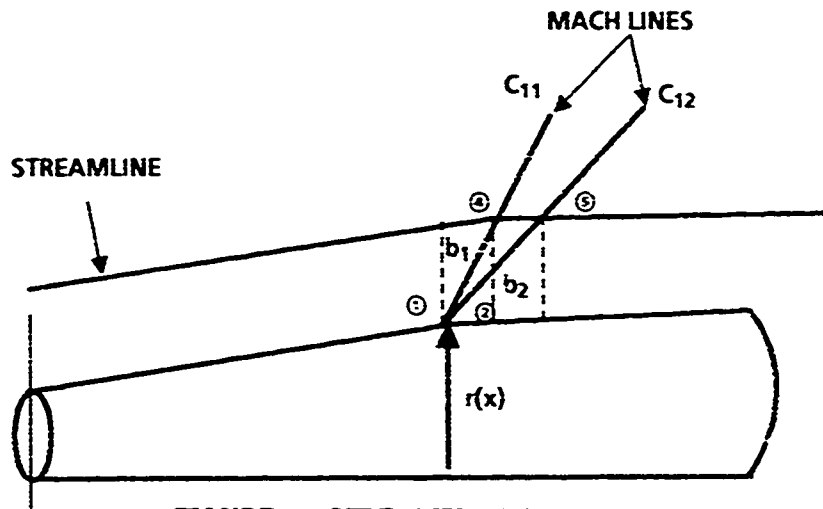


FIGURE 13. STREAMTUBE GEOMETRY

Applying Equation (106) along the streamline near the body between points ③ and ⑤, which correspond to the beginning and end of the expansion turn, there is obtained

$$\int_{p_4}^{p_5} \frac{dp}{\lambda} = \int_4^5 \frac{1}{\lambda \cos \mu} \frac{\partial p}{\partial C_1} ds + \int_4^5 \frac{\partial \theta}{\partial s} ds \quad (107)$$

The left side of Equation (107) may be expanded as

$$\int_{p_4}^{p_5} \frac{dp}{\lambda} = \int_4^1 \frac{1}{\lambda} \frac{\partial p}{\partial C_1} dC_1 + \int_1^2 \frac{dp}{\lambda} + \int_2^5 \frac{1}{\lambda} \frac{\partial p}{\partial C_1} dC_1 \quad (108)$$

The first and third integrals on the right side of Equation (108) can be approximated by

$$\left(\frac{1}{\lambda} \frac{\partial p}{\partial C_1} \right)_{1-4} (-b_1) \text{ and } \left(\frac{1}{\lambda} \frac{\partial p}{\partial C_1} \right)_{5-2} (b_2) \quad (109)$$

Here 1-4 and 5-2 refer to the average values of these parameters between these points. The differential dC_1 between 1-4 and 5-2 is simply the distance along the left running characteristics, which we defined as b_1 and b_2 . Note that since the first integral goes from 4 to 1, the integral of dC_1 is negative so it integrates to $-b_1$.

The second integral on the right side can be integrated directly using the Prandtl-Meyer Expansion. Referring to Appendix C, where

$$\frac{dp}{d\theta} = + \frac{\rho V^2}{\sqrt{M^2 - 1}} = + \lambda$$

then

$$\int_1^2 \frac{dp}{\lambda} = + \int_1^2 d\theta = \theta_2 - \theta_1 \quad (110)$$

Substituting Equations (109) and (110) into (108) there is obtained for the left side of Equation (107)

$$\int_{p_4}^{p_5} \frac{dp}{\lambda} = -b_1 \left(\frac{1}{\lambda} \frac{\partial p}{\partial C_1} \right)_{1-4} + \theta_2 - \theta_1 + b_2 \left(\frac{1}{\lambda} \frac{\partial p}{\partial C_1} \right)_{5-2} \quad (111)$$

Assuming that the streamline is close to the body surface so that the Mach lines μ_1 and μ_2 are basically straight and the pressure varies linearly along the left running characteristic, then the second integral of Equation (107) may be approximated by use of the trapezoidal rule as

$$\int_4^5 \frac{1}{\lambda \cos \mu} \frac{\partial p}{\partial C_1} ds = \left[\frac{1}{\lambda_1 \cos \mu_1} \left(\frac{\partial p}{\partial C_1} \right)_1 + \frac{1}{\lambda_2 \cos \mu_2} \left(\frac{\partial p}{\partial C_1} \right)_2 \right] \frac{(s_5 - s_4)}{2} \quad (112)$$

The last integral, of course, integrates directly to

$$\int_4^5 d\theta = \theta_5 - \theta_4$$

Again expanding in a Taylor series expansion yields

$$\theta_5 = \theta_2 + b_2 \left(\frac{\partial \theta}{\partial C_1} \right)_2 + \dots$$

$$\theta_4 = \theta_1 + b_1 \left(\frac{\partial \theta}{\partial C_1} \right)_1 + \dots$$

or

$$\theta_5 - \theta_4 = \theta_2 - \theta_1 + b_2 \left(\frac{\partial \theta}{\partial C_1} \right)_2 - b_1 \left(\frac{\partial \theta}{\partial C_1} \right)_1 \quad (113)$$

Substituting (111), (112), and (113) into (107) one obtains

$$\begin{aligned} -b_1 \left(\frac{1}{\lambda} \frac{\partial p}{\partial C_1} \right)_{1-4} + b_2 \left[\frac{1}{\lambda} \left(\frac{\partial p}{\partial C_1} \right) \right]_{5-2} &= \left[\frac{1}{\lambda_1 \cos \mu_1} \left(\frac{\partial p}{\partial C_1} \right)_1 \right. \\ &\quad \left. + \frac{1}{\lambda_2 \cos \mu_2} \left(\frac{\partial p}{\partial C_1} \right)_2 \right] \frac{(s_5 - s_4)}{2} + b_2 \left(\frac{\partial \theta}{\partial C_1} \right)_2 - b_1 \left(\frac{\partial \theta}{\partial C_1} \right)_1 \end{aligned} \quad (114)$$

Note that $\theta_2 - \theta_1$ cancels on each side of Equation (114). Now divide through by b_1 and take the limit as $b_1 \rightarrow 0$ to obtain

$$\begin{aligned} -\left(\frac{1}{\lambda} \frac{\partial p}{\partial C_1} \right)_1 + \left(\frac{b_2}{b_1} \right) \left(\frac{1}{\lambda} \frac{\partial p}{\partial C_1} \right)_2 &= \left[\frac{1}{\lambda_1 \cos \mu_1} \left(\frac{\partial p}{\partial C_1} \right)_1 \right. \\ &\quad \left. + \frac{1}{\lambda_2 \cos \mu_2} \left(\frac{\partial p}{\partial C_1} \right)_2 \right] \frac{s_5 - s_4}{2 b_1} + \frac{b_2}{b_1} \left(\frac{\partial \theta}{\partial C_1} \right)_2 - \left(\frac{\partial \theta}{\partial C_1} \right)_1 \end{aligned} \quad (115)$$

Note that b_2/b_1 and $(s_5 - s_4)/b_1$ are not infinite but in fact are finite as will be shown shortly. Now Equations (105) and (106) can be used to evaluate

$$\left(\frac{\partial p}{\partial C_1} \right) \text{ and } \left(\frac{\partial \theta}{\partial C_1} \right)$$

Substituting for these relations and carrying out the algebra, Equation (115) becomes

$$\begin{aligned} & - \frac{2 \cos \mu_1}{\lambda_1} \left[\frac{\partial p}{\partial s} - \lambda \frac{\partial \theta}{\partial s} \right]_1 - \frac{\sin(\mu_1) \sin(\theta_1)}{r} \\ & + \frac{b_2}{b_1} \left\{ \frac{2 \cos \mu_2}{\lambda_2} \left[\frac{\partial p}{\partial s} - \lambda \frac{\partial \theta}{\partial s} \right]_2 + \frac{\sin(\mu_2) \sin(\theta_2)}{r} \right\} \\ & = \left\{ \frac{1}{\lambda_1 \cos(\mu_1)} \left[\cos(\mu_1) \left(\frac{\partial p}{\partial s} - \lambda \frac{\partial \theta}{\partial s} \right)_1 \right] \right. \\ & \quad \left. + \frac{1}{\lambda_2 \cos(\mu_2)} \left[\cos(\mu_2) \left(\frac{\partial p}{\partial s} - \lambda \frac{\partial \theta}{\partial s} \right)_2 \right] \right\} \frac{s_5 - s_4}{2 b_1} \end{aligned} \quad (116)$$

Now except for the matchpoint between a blunt nose and a conical frustrum

$$\left(\frac{\partial \theta}{\partial s} \right)_1 = \left(\frac{\partial \theta}{\partial s} \right)_2 = 0 \quad (117)$$

since θ is constant along conical segments. At the matchpoint

$$\left(\frac{\partial \theta}{\partial s} \right)_1 = - \frac{1}{R_N}$$

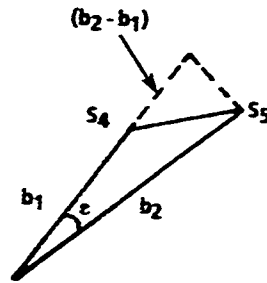
where R_N is the radius of the spherical nose tip. Using the relation (117) and solving for

$$\left(\frac{\partial p}{\partial s} \right)_2$$

one obtains for Equation (116)

$$\left(\frac{\partial p}{\partial s} \right)_2 = \frac{\left(\frac{1}{2 \lambda} \frac{\partial p}{\partial s} \right)_1 \left[\frac{s_5 - s_4}{b_1} + 4 \cos(\mu_1) \right] + \frac{1}{r} \left[\sin(\mu_1) \sin(\theta_1) - \left(\frac{b_2}{b_1} \right) \sin(\mu_2) \sin(\theta_2) \right]}{\left(\frac{b_2}{b_1} \right) \frac{2 \cos(\mu_2)}{\lambda_2} - \frac{s_5 - s_4}{2 \lambda_2 b_1}} \quad (118)$$

From geometry, referring to Figure 13 and the sketch below, one can write approximately for small angles ϵ



$$\epsilon = \mu_1 + \theta_1 - \mu_2 - \theta_2$$

$$(s_5 - s_4)^2 = (b_2 - b_1)^2 + \epsilon^2 b_2^2$$

This can be written as

$$\frac{s_5 - s_4}{b_1} = \left[\left(\frac{b_2}{b_1} - 1 \right)^2 + \left(\frac{b_2}{b_1} \right)^2 \epsilon^2 \right]^{\frac{1}{2}} \quad (119)$$

From conservation of mass, one can write

$$\rho_1 V_1 b_1 \sin(\mu_1) = \rho_2 V_2 b_2 \sin(\mu_2)$$

or

$$\frac{b_2}{b_1} = \frac{\rho_1 V_1 \sin(\mu_1)}{\rho_2 V_2 \sin(\mu_2)} \quad (120)$$

Using (120) in (119) there is obtained

$$\frac{s_5 - s_4}{b_1} = \left[\left(\frac{\rho_1 V_1 \sin(\mu_1)}{\rho_2 V_2 \sin(\mu_2)} - 1 \right)^2 + \left(\mu_1 + \theta_1 - \mu_2 - \theta_2 \right)^2 \left(\frac{\rho_1 V_1 \sin(\mu_1)}{\rho_2 V_2 \sin(\mu_2)} \right)^2 \right]^{\frac{1}{2}} \quad (121)$$

Note that with Equations (120) and (121), Equation (118) can be calculated independent of the distances b_1 and b_2 . The only distance that enters the equation is r , which is the local body radius at a point in question. Defining

$$F_1 = \frac{s_5 - s_4}{b_1} \quad \text{and} \quad F_2 = b_2 / b_1$$

where these expressions are determined by Equations (120) and (121), and

$$F_3 = \frac{1}{2\lambda_1} \left(\frac{\partial p}{\partial s} \right)_1 \left[F_1 + 4 \cos(\mu_1) \right]$$

$$F_4 = \frac{1}{r} \left[\sin(\mu_1) \sin(\theta_1) - F_2 \sin(\mu_2) \sin(\theta_2) \right]$$

$$F_5 = F_2 \left[\frac{2 \cos(\mu_2)}{\lambda_2} \right]$$

allows Equation (118) to be written in an abbreviated form as

$$\left(\frac{\partial p}{\partial s} \right)_2 = \frac{F_3 + F_4}{F_5 - F_1 / 2\lambda_2} \quad (122)$$

This is our final expression we desired to relate the pressure gradient behind an expansion point for use in the SOSET.

Note that Equation (122) gives a first-order estimate for

$$\left(\frac{\partial p}{\partial s}\right)_2$$

based on all known quantities once the Prandtl-Meyer integration of Appendix D has taken place through each turn. This equation is valid for real gases since no perfect gas assumption has been made.

Returning now to Equations (35) and (36), use of Equation (122) in conjunction with the Prandtl-Meyer solution of Appendix D now allows one to estimate the pressure all along the body surface to second-order accuracy for real gases. With entropy constant along the body surface, other thermodynamic and flow field quantities can be calculated from Equations (D-27) and (D-28) along with

$$T = T(p, S)$$

$$M = V/a$$

(123)

$$\gamma = \frac{a^2 p}{p}$$

$$Z = \frac{p}{\rho RT}$$

Previous applications of SOSET have applied the pressure computed from Equation (35) at the midpoint of all body sections (see Figure 6) for force and moment computations. While this is the correct location for 2-D surfaces and cylindrical portions of the body, it is not the most appropriate location for conical frustums. For conical frustums, both on the nose and tail, the centroid of the surface area is

$$\bar{X} = \frac{2}{3} \frac{(x_{i+1} - x_i)(r_{i+1}^3 - r_i^3)}{(r_{i+1} - r_i)^2(r_{i+1} + r_i)} \quad (124)$$

Here x_{i+1} , r_{i+1} are the x and r coordinates of the aft portion of the frustum and x_i , r_i the x and r coordinates of the forward portion. Hence, for cylindrical segments and two-dimensional sections (such as wings), the pressure computed from the Shock Expansion is applied at the midpoint, whereas for conical frustums, it is applied at the point given by Equation (124).

2.3.5.2 Matching Point Between MNT and SOSET

Several alternatives have been used in past literature to match the MNT to SOSET on the blunt nose part of the body. The first alternative was that of Jackson, et al.²⁰ where the body slope was assumed to be that for the maximum wedge angle allowed for an attached shock wave. Their results showed good agreement with experimental data for $2.3 \leq M_\infty$ but only fair agreement for lower supersonic Mach numbers. DeJarnette, et al.³⁵ developed an empirical equation for the Mach number to match MNT to SOSET. This approach gave improved results over Reference 20, particularly at low supersonic Mach numbers. Reference 2 found that using a constant value of $M_M = 1.1$ was about as good as the results of Reference 20.

Appendix B, which contains a derivation of the new methodology by DeJarnette for pressures on spheres in hypersonic flows found a constant value of a match point of $\theta_m = 25.95^\circ$. The pressure at this point is defined by

$$p_1/p_\infty = 1 + \frac{\gamma_\infty M_\infty^2}{2} C_{p_1} \quad (125)$$

where C_{p_1} is given by Equation (41). Differentiating Equation (125) there is obtained

$$\frac{dp_1}{ds} = \frac{\gamma_\infty M_\infty^2 p_\infty}{2} \frac{dC_{p_1}}{d\delta_{eq}} \frac{d\delta_{eq}}{ds} \quad (126)$$

But, for a sphere

$$\frac{d\delta_{eq}}{ds} = -1/R_N \quad (127)$$

Also, from Appendix B

$$\frac{dC_{p_1}}{d\delta_{eq}} = 1.5 \left[\left(C_p + \frac{2}{\gamma M_\infty^2} \right) \frac{dC_p}{d\delta_{eq}} \right]_{MN}^{\frac{1}{2}} \quad (128)$$

$$C_p = C_{p_0} \sin^2 \delta_{eq} \quad (129)$$

Using the relations (126) through (129) and recognizing that $\delta_{eq} = 25.95^\circ$ at the match point, Equation (116) just past the match point becomes

$$\left(\frac{\partial p}{\partial s}\right)_2 = \left(\frac{\partial p}{\partial s}\right)_1 + \frac{A_1}{R_N} = \frac{1}{R_N} \left[\frac{p_1 V_1^2}{\sqrt{M_1^2 - 1}} - 1.05 M_\infty^2 p_\infty \left(0.1676 C_{p_o}^2 + 1.251 C_{p_o} \right)^{\frac{1}{2}} \right] \quad (130)$$

p_1 , V_1 , M_1 , and C_{p_o} of Equation (130) are computed from Equation (79) and the MNT of section 2.3.4.2.

Thus, in summary, at the match point the pressure is computed from Equation (41). Downstream of this point, the solution is continued by use of Equations (35), (36), (122), and (130) where p_c is the value of pressure computed by a tangent cone approach (given freestream Mach number and local slope, given entropy along the surface, compute the value of p_c by the approach of Appendix C). The value of p_2 comes from the Prandtl-Meyer integration in Appendix D.

2.3.6 Angle-of-attack Solution for Body Alone

The angle-of-attack solution will follow the general approach of References 2 and 23 for including angle-of-attack effects in the pressure distribution. However, those references were not concerned with real gas effects or with estimating temperatures for aeroheating and thermostructural analyses. Hence, while the general approach of References 2 and 23 will be used, modifications and additions will be added to make the approach more relevant to the problems at hand.

2.3.6.1 Pointed-cone Pressure Distribution at $\alpha > 0$

To start SOSET on a pointed body or to compute the local properties on a conical frustum, a pointed-cone solution for $\alpha > 0$ is needed. One would desire an approximate solution, if good accuracy can be obtained, as opposed to a numerical solution of partial differential equations³⁶ modified to include real gas effects. The approach of Reference 23 for perfect gases is given by Equation (40). Equation (40a) is independent of the type of gas and is therefore appropriate in its present form for computing the $\Delta C_p(\alpha, \theta, \phi, M_\infty)$ for a real gas as well. However, the approximate relation (40b), for the pressure coefficient on cones at zero angle of attack, is replaced by the pressure computed in Appendix C for cones in real gas flow. Hudgins³⁷ presents an approximate formula for the cone surface pressure for real gas computations based on a fairly broad range of parameters including freestream velocity, altitude, and cone half-angles. The pressure formula is

$$\frac{p_c}{p_\infty} = 1.4932 (M_\infty \sin \theta_c)^{1.965} + 1.3017 \quad \text{for } M_\infty \sin \theta_c > 1.5 \quad (131)$$

or since

$$C_{p_{\alpha=0}} = \frac{2}{\gamma_\infty M_\infty^2} \left| \frac{p}{p_\infty} - 1 \right|$$

then

$$(C_p)_{\alpha=0} = \frac{2}{\gamma_\infty M_\infty^2} \left| 1.4932 \left(M_\infty \sin \theta_c \right)^{1.9534} + 0.3017 \right| \quad (132)$$

Reference 37 indicates accuracies of better than 1.5 percent for Equation (131). It should be pointed out that for values of $M_\infty \sin \theta_c \leq 1.5$, real gas effects on pressure are negligible and Equation (49b) can be used instead of Equation (132). For values of $M_\infty \sin \theta_c > 1.5$, Equation (132) replaces Equation (40b).

Reference 23 used Equations (40) and (40a) to estimate angle-of-attack effects on the cone. A slightly more accurate method will be used here. The method uses the Equations (40) and (40a) but combines these relations in a Taylor series expansion in angle of attack.

Assume small angles of attack so that the pressure coefficient can be written in a Taylor Series Expansion about $\alpha = 0$ as follows:

$$\begin{aligned} C_p \left[r, \theta(x, r), \phi \right] &= \left[C_p(\theta) \right]_{\alpha=0} + \left[\frac{\partial C_p}{\partial \alpha} \right]_{\alpha=0} \alpha + \left[\frac{\partial^2 C_p}{\partial \alpha^2} \right]_{\alpha=0} \frac{\alpha^2}{2!} \\ &+ \left[\frac{\partial^3 C_p}{\partial \alpha^3} \right]_{\alpha=0} \frac{\alpha^3}{3!} + \dots \end{aligned} \quad (133)$$

Now, if we use the methodology for the cone at angle of attack to evaluate the derivatives of Equation (133), then referring to Equations (40) and (40a)

$$\begin{aligned} C_p(r, \phi) &= \left[C_p(\theta_c) \right]_{\alpha=0} - \sin 2\alpha \sin 2\theta_c \cos \phi \\ &+ \sin^2 \alpha \cos^2 \theta_c \left[\left(2 - \frac{1}{\beta} \right) \left(1 - \tan^2 \theta_c \right) - \left(2 + \frac{2}{\beta} \right) \sin^2 \phi \right] \end{aligned} \quad (134)$$

Differentiating Equation (134) and evaluating at $\alpha=0$, one obtains

$$\left[\frac{\partial C_p}{\partial \alpha} \right]_{\alpha=0} = -2 \sin(2\theta) \cos \phi \quad (135)$$

Here, the value of θ is taken to be that that exists on the conical segment in question. In essence, use of Equations (133) and (134) allows an analogous but more accurate technique than a tangent cone approach to solve for the pressure coefficient on a body at angle of attack without recomputing local cone solutions for each point around and along the body. Differentiating Equation (134) a second and third time, and evaluating at $\alpha = 0$, one obtains

$$\left| \frac{\partial^2 C_p}{\partial \alpha^2} \right|_{\alpha=0} = 2F \cos^2 \theta \quad (136)$$

where

$$F = \left(2 - \frac{1}{\beta} \right) (1 - \tan^2 \theta) - \left(2 + \frac{2}{\beta} \right) \sin^2 \phi$$

and

$$\left| \frac{\partial^3 C_p}{\partial \alpha^3} \right|_{\alpha=0} = +8 \sin(2\theta) \cos \phi \quad (137)$$

Substituting (135), (136), (147) into (133), one obtains

$$\begin{aligned} C_p(u, \theta(x, r), \phi) = & \left| C_p(\theta) \right|_{\alpha=0} - 2\alpha \sin(2\theta) \cos \phi \\ & + (F \cos^2 \theta) \alpha^2 + \left(\frac{4}{3} \sin 2\theta \cos \phi \right) \alpha^3 \end{aligned} \quad (138)$$

Equation (138) indicates that the local angle-of-attack effects of pressure can be estimated with the zero angle-of-attack solution already computed, the local value of body slope and roll position, and the freestream Mach number and angle of attack.

The other question is how does one compute other flow properties at the cone surface? Consider two cases. First is the case where the cone solution is being used as the starting solution for the pointed body. For that case, since entropy behind the shock is not known, the flow field for the cone at $\alpha = 0$ must be computed as in Appendix B. Since the flow properties are computed numerically to the accuracy of the thermodynamic curve fits of Reference 35, the pressure on the cone surface is also given by this solution rather than Equation (132) or (40b). Now, since Equation (138) gives the C_p due to α for various values of ϕ , θ , M , then a new C_p for $\phi = 180^\circ$ (windward plane) is computed with this equation. A new value of an effective cone angle corresponding to the windward plane is then given by solving Equation (132) for $\sin \theta$ with C_n replaced by the value of p corresponding to $C_{p\phi = 180^\circ}$. Then the cone solution of Appendix B is repeated with a new cone angle. This gives the value of entropy, temperature, and other properties as well. Since the flow between the body and shock is isentropic, this value of entropy is held constant for the rest of the

computations downstream. Once the value of entropy is known and C_p at other positions around the body is computed from Equation (138), then

$$T(\theta, \phi, \alpha) = T \left[p(\theta, \phi, \alpha), S \right] \quad (139)$$

can be determined from the thermofit equations.

Other flow properties can be computed from the thermofit equations or energy equations as follows:

$$\left. \begin{aligned} p(\theta, \phi, \alpha) &= p \left[p(\theta, \phi, \alpha), S \right] \\ a(\theta, \phi, \alpha) &= a \left[p(\theta, \phi, \alpha), S \right] \\ e(\theta, \phi, \alpha) &= e \left[p(\theta, \phi, \alpha), S \right] \end{aligned} \right\} \quad (140)$$

$$\left. \begin{aligned} h &= e + p/\rho \\ V &= \left[2(H - h) \right]^{\frac{1}{2}} \\ M &= V/a \\ \gamma &= \frac{a^2 \rho}{p} \\ Z &= p/(\rho RT) \end{aligned} \right\} \quad (141)$$

The second case of interest is when we desire to compute the flow properties for a cone at angle of attack for use in a tangent cone approach where entropy has been defined by the properties across either a pointed body or blunt body. In both of these cases, the entropy is fixed at either the value in the windward plane of the starting cone solution or that on the stagnation streamline behind a normal shock. For this case, since entropy is known, the local value of p can be determined directly from Equations (138), (40), (40a), and (40b) if $M_\infty \sin \theta_C \leq 1.5$. Then, the values of temperature, density, speed of sound, and internal energy can be computed via Equations (139) and (140) as previously discussed.

2.3.6.2 Body Angle-of-attack Effects

References 2 and 23 used so-called loading functions to include angle-of-attack effects at a given point along the body. The essence of this approach was Equations (40) and (40a). A similar approach will be used here except the slightly improved pressure prediction method given by Equation (138) will be used. In essence, Equation (138) can be used in a tangent cone approach to compute pressure at any point on the body surface given an accurate value of pressure on the given body at zero angle of attack. That is, at a given angle of attack, local body slope, position around the body, and freestream Mach number, pressures all around the body can be computed from Equation (138). Knowing pressure and the correct value of entropy, Equations (139) through (141) can be used to determine other flow properties at the body surface.

In using Equation (138), it was found that for blunt bodies at moderate angles of attack, results in the leeward plane were not as good as desired. To illustrate this point, consider Figure 14, which shows the perfect gas pressure computations on a 20-percent blunt Von Karman ogive at $M_\infty = 15$ and $\alpha = 10^\circ$. Figure 14(a) shows the pressure coefficients predicted by Equation (138) in several planes around the body, and Figures 14(b) through (d) compare the results in the $\phi = 180^\circ$, 90° , and 0° planes to the exact Euler code, ZEUS.^{41,47} In examining Figures 14(a) through (d), two points are worth noting: (1) the present method agrees reasonably well with ZEUS computations in the $\phi = 180^\circ$ and 90° planes, and (2) while Equation (138) works well in the windward plane area for cones, it exhibits unacceptable behavior in the leeward plane for blunted ogives.

The unacceptable behavior exhibited by Equation (138) in the leeward plane of configurations other than cones comes from two phenomena: (1) for a blunt body, the angle θ is fairly large in the nose tip region causing the second term of Equation (138) to be larger than desired in this region, and (2) on ogives as θ goes to zero near the shoulder, the second and fourth terms of Equation (138) go to zero whereas the third term reaches its maximum positive value. This causes the increase in pressure past $x = 1$ seen in Figures 14(a) and 14(d). It was found that a way to remedy both of these problems in the $\phi \leq 30^\circ$ planes was to modify Equation (138) as follows:

$$C_p(\alpha, \theta, \phi) = \left[C_p(\theta) \right]_{\alpha=0} - \frac{2\alpha \sin(2\theta) \cos \phi}{3} \quad (142)$$

Equation (142) is used for configurations other than sharp cones in the leeward plane area. The results of this modification are shown in Figure 15(a) for pressure and Figure 15(b) for temperature. Note that significant improvement in pressure coefficient compared to the ZEUS code is obtained. The ZEUS code data in the various planes are not shown on Figure 15 for clarification purposes. To show the improved comparison, one can simply use the leeward plane curve ($\phi = 0^\circ$) of Figure 15 and compare this to Figure 14(d). Since Equation (138) is still used in the $\phi = 180^\circ$ and $\phi = 90^\circ$ planes, Figures 14(b) and (c) remain the same. Also, use of

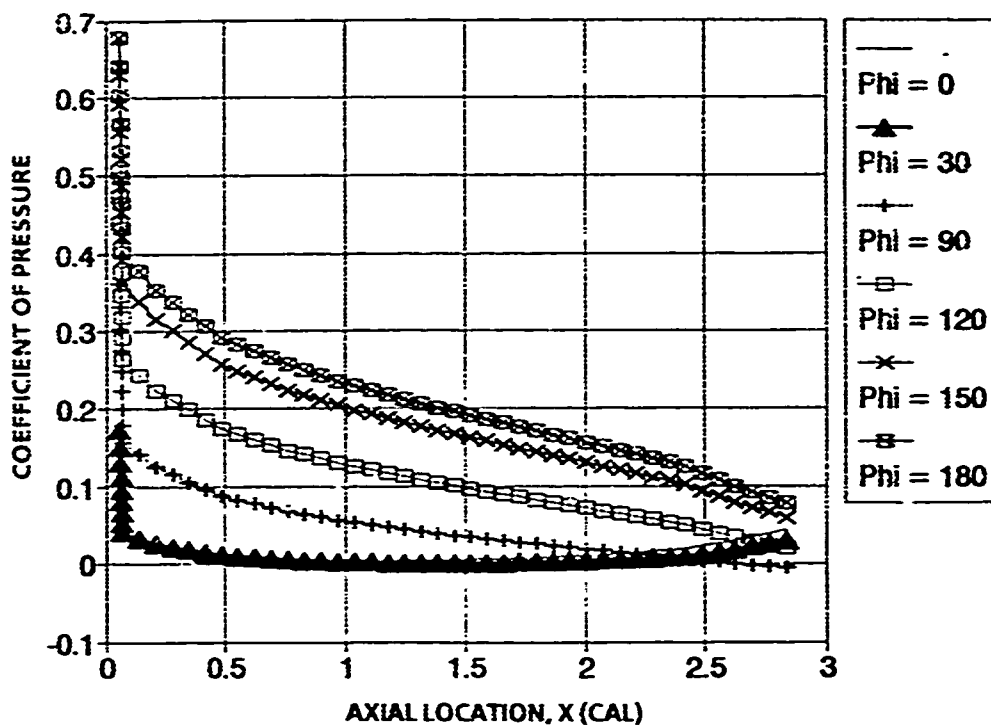


FIGURE 14(a). APPROXIMATE PRESSURES ON A 20-PERCENT BLUNT VON KARMAN OGIVE USING ONLY EQUATION (138); ($M_\infty = 15$, $\alpha = 10^\circ$)

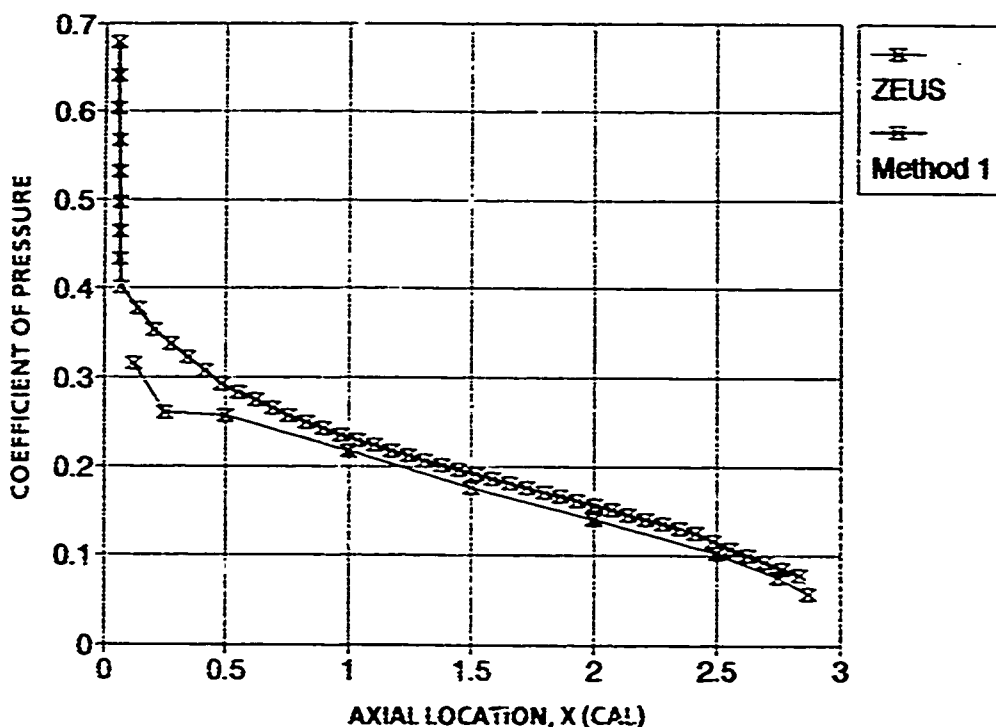


FIGURE 14(b). COMPARISON OF APPROXIMATE (EQUATION 138) AND EXACT PRESSURES ON A 20-PERCENT BLUNT VON KARMAN OGIVE ($M_\infty = 15$, $\alpha = 10^\circ$, $\phi = 180^\circ$)

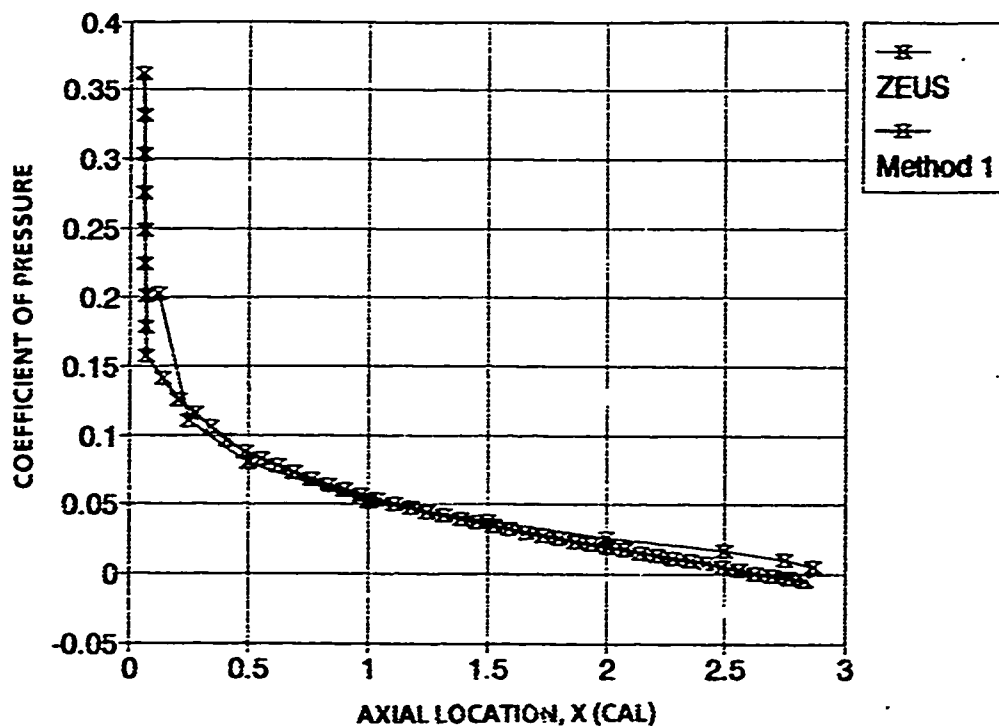


FIGURE 14(c). COMPARISON OF APPROXIMATE (EQUATION 138) AND EXACT PRESSURES ON A 20-PERCENT BLUNT VON KARMAN OGIVE ($M_\infty = 15$, $\alpha = 10^\circ$, $\phi = 90^\circ$)

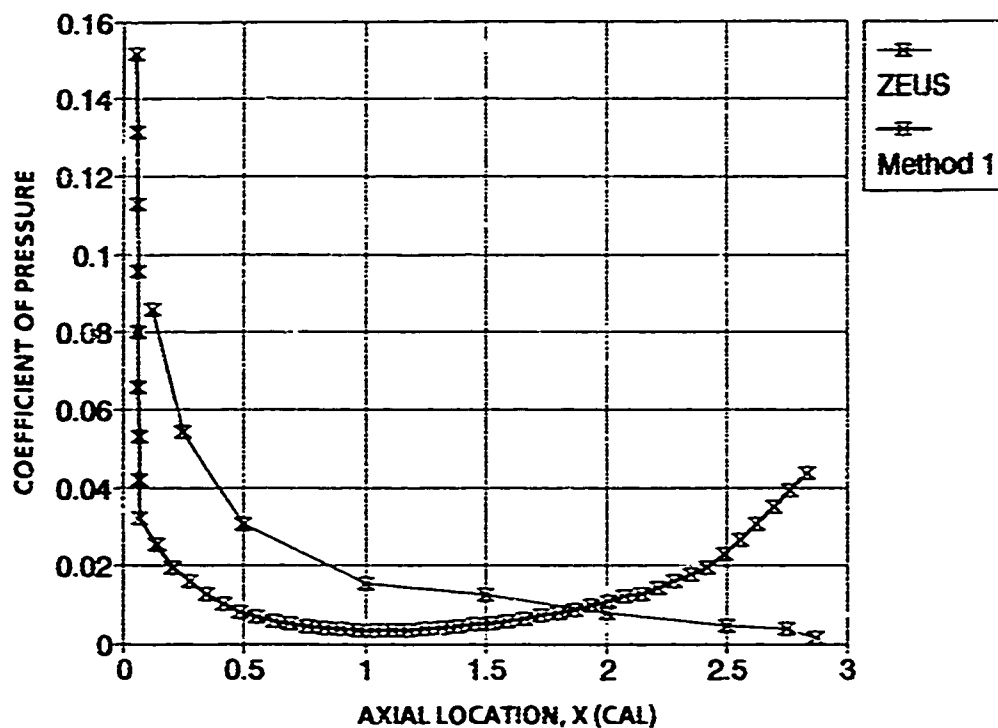


FIGURE 14(d). COMPARISON OF APPROXIMATE (EQUATION 138) AND EXACT PRESSURES ON A 20-PERCENT BLUNT VON KARMAN OGIVE ($M_\infty = 15$, $\alpha = 10^\circ$, $\phi = 0^\circ$)

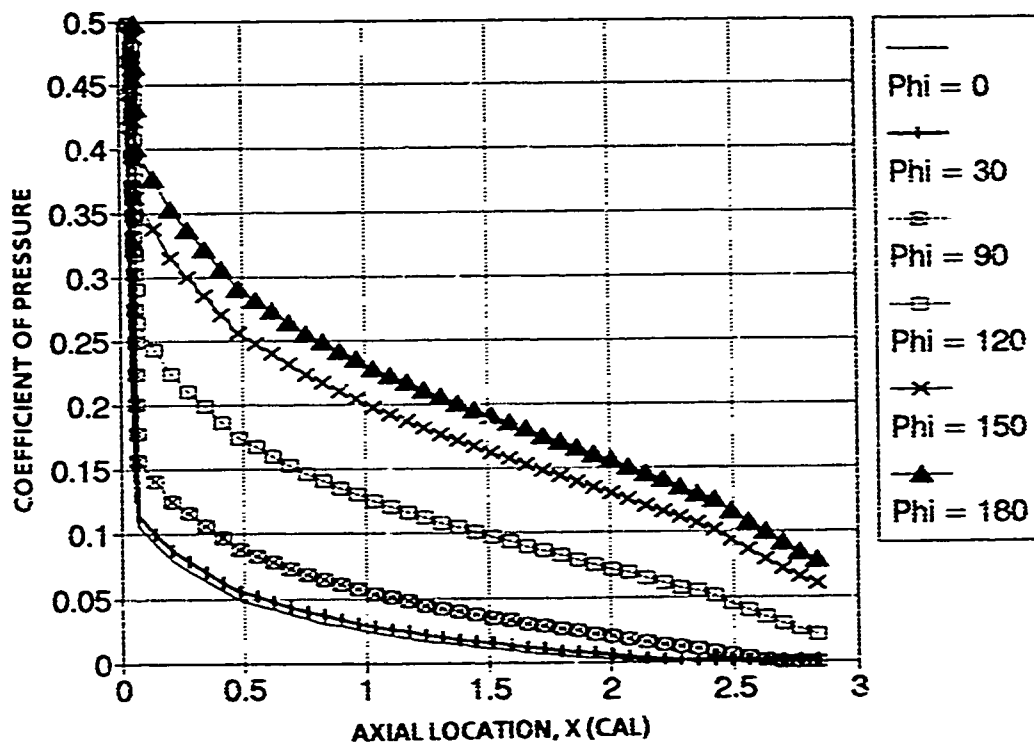


FIGURE 15(a). APPROXIMATE PRESSURE PREDICTION ON A 20-PERCENT BLUNT VON KARMAN OGIVE (EQUATIONS 138 AND 142); ($M_\infty = 15$, $\alpha = 10^\circ$)

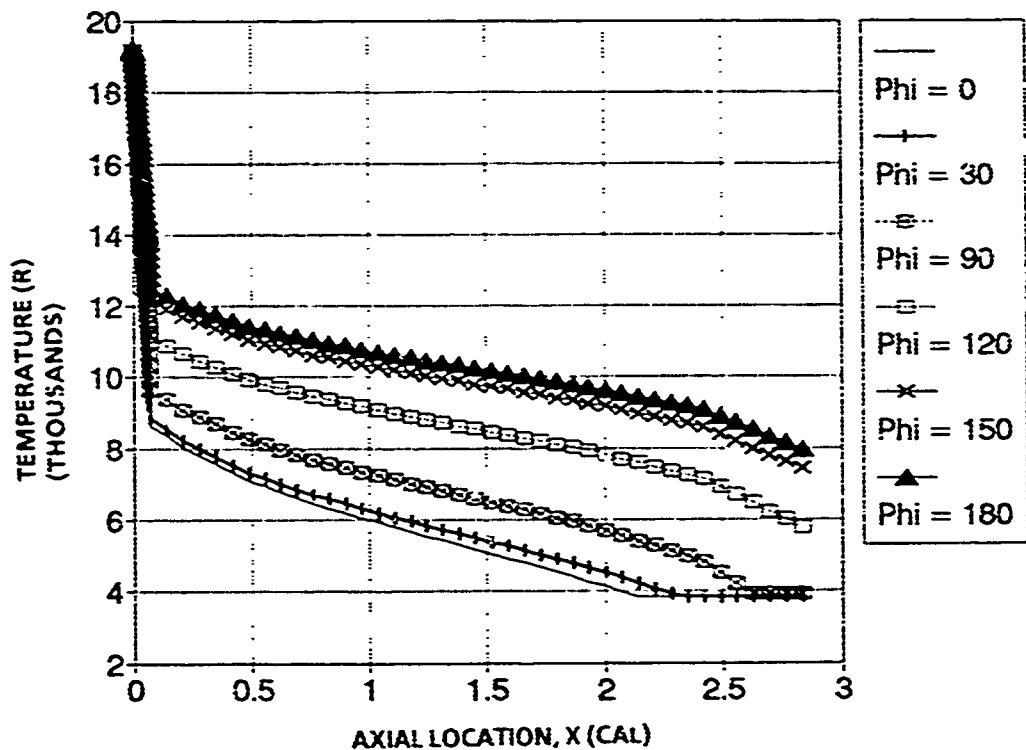


FIGURE 15(b). APPROXIMATE TEMPERATURE PREDICTION ON A 20-PERCENT BLUNT VON KARMAN OGIVE ($M_\infty = 15$, $\alpha = 10^\circ$)

Equation (142) versus (138) in the leeward plane area presents little change to the axial force but improves the normal force and center-of-pressure predictions by about 5 and 6 percent, respectively. Compared to ZEUS computations, the errors in the aerodynamic coefficients for wave drag, normal force, and center of pressure using the present approach of Equations (138) and (142) is 5, 11, and 4 percent, respectively. This is considered to be quite acceptable for an engineering type aeroprediction code.

Past the nose portion of the body, standard Modified Newtonian Theory is used to predict the pressures with the pressure coefficient assumed to be zero in the shadowed region. That is

$$\begin{aligned} C_p &= C_{p_0} \sin^2(\delta_{eq}) \quad \text{for } \delta_{eq} \geq 0 \\ C_p &= 0 \quad \quad \quad \text{for } \delta_{eq} < 0 \end{aligned} \quad (143)$$

Since entropy is constant on the body surface, values of temperature and other local properties are computed with Equations (139) through (141) as before.

2.3.7 Wing and Interference Aerodynamics

For high Mach numbers (M_∞ typically greater than 6), the method of References 2 and 21 will be used for real gas computations except that the pressures and other properties will be computed using real gas as opposed to perfect gas computations. References 2 and 21 used local slope techniques for the wing aerodynamic computations. That is, MNT on the leading edge of the wing, tangent wedge from the match point rearward on a compression surface, and PME on expansion surfaces. The methods of section 2.3.4, Appendix C, and Appendix D, respectively, are used to compute the local pressure coefficient and temperature at the outer edge of the boundary layer. The match point between MNT and the tangent wedge is taken to be $\theta_M = 25.95^\circ$. Since this is a first-order as opposed to a second-order approach, there could be a slight discontinuity in the pressure coefficient. This is due to the fact that there is no pressure derivative to blend the pressure coefficients together as with SOSET.

Use of a first-order as opposed to a second-order solution for the wings and other lifting surfaces can be justified by the fact that these surfaces generally contribute less than 25 percent of the axial force. Experience³⁰ has shown that the axial force is where second-order accuracy is required for pressure coefficients. On the other hand, lift can be reasonably well estimated by a first-order theory. Since the wings contribute significantly to the lift force, a first-order theory is acceptable.

It was found in References 2 and 21 that when local slope techniques were used in a 2-D "strip theory" approach (wing is considered to be made up of several

streamwise 2-D surfaces and total forces and moments summed from these surfaces), no interference aerodynamics were needed. This was due to the fortuitous cancellation of errors and the fact that 2-D pressures were higher than 3-D pressures on most wings. At the wing root, the pressure was underpredicted due to use of freestream versus local conditions, and at the wing tip the pressure was overpredicted due to the same reason. The two effects canceled each other in an approximate sense. A summary of the approaches for computing real gas properties on bodies and wing bodies using SOSET is given in Figure 16.

i. BODY AT $\alpha = 0$

1. For pointed body, use cone solution for real gases of Appendix C to start solution. For blunt bodies, use MNT of section 2.3.4 to start solution.
2. Use Equations (35), (36), and (122) to calculate pressure on conical segments along body downstream of tip.
3. Use Equations (139), (140), (141) to calculate other flow properties on each conical segment given the entropy from step 1 and pressure from step 2.

ii. POINTED BODY AT $\alpha > 0$

1. Compute $(C_p)_\alpha$ from Equation (138) and $(C_p)_{\alpha=0}$ from Equation (132) (or Equation (40b) if $M_\infty \sin \theta_c \leq 1.5$). This gives C_p on cone at $\alpha > 0$.
2. Compute effective θ_c from Equation (131) where p_c of Equation (131) is replaced by that for $\phi = 180^\circ$ of step 1.
3. Use this value of θ to obtain the cone solution for real gases and obtain the value of entropy between the shock and body.
4. Compute $T, a, e, h, V, M, \gamma, Z$ from Equations (133), (134), and (135) around conical tip.
5. Use Equations (138), (142), (143), and Appendix D to compute pressures downstream on body at $\alpha > 0$.
6. Using $C_p(\alpha, \theta, \phi)$ from step 5, the value of entropy from step 3, compute other flow properties from Equations (139), (140), and (141) at desired points along and around body.

FIGURE 16. SUMMARY OF SOSET FOR REAL GASES ON BODIES
AND WING BODY COMBINATIONS

III. BLUNT BODY AT $\alpha > 0$

1. Compute conditions across normal shock and at stagnation point from Appendix C and section 2.3.4.
2. Compute conditions up to match point from section 2.3.4.
3. Compute body solution at $\alpha = 0$ as described above
4. Compute $C_p(\alpha, \theta, \phi)$ from Equations (138), (142), and (143).
5. Using the value of entropy from step 1, pressure from step 4, compute other properties from Equations (139), (140), and (141).

IV. WING

1. For blunt leading edge, compute flow properties at each point based on section 2.3.4. For sharp leading edges, use wedge solution for real gases of Appendix C. Angles used are local angles that include angle of attack, local slope, and sweepback.
2. Use PME and tangent wedge aft of the leading edge using local slopes and freestream conditions. This gives all flow properties directly based on the entropy of step 1 and the pressure of PME and tangent wedge.

FIGURE 16. SUMMARY OF SOSET FOR REAL GASES ON BODIES
AND WING BODY COMBINATIONS (CONTINUED)

If one is most interested in correct values of wing lift and axial force and not as concerned with high temperature effects, the 3-D thin wing theory of Reference 31 combined with interference factors is more accurate. This approach is still allowed as an option to the user in the aeroprediction code.²⁻⁴

2.3.8 Viscous Considerations

The main intent of this report was to extend SOSET to include real gas effects and hence allow computation of forces, moments, and surface temperatures at Mach numbers above about 6. With the exception of surface temperature, these objectives have now been accomplished. However, some additional comments are in order as to how to include the viscous effects that occur on the wing and body. Ultimately, the current technique will be transitioned into the latest version of the NAVSWC aeroprediction code²⁻⁴ and an updated version will be generated.

The skin friction and body base pressure drag can be estimated by the same techniques of Reference 30, Van Driest II,³⁹ and empirical methods, respectively. The 2-D base pressure drag on the rear of wing surfaces is again empirical and the same approach as that of Reference 31 can be used. The nonlinear effects of lift and drag that occur due to higher angles of attack can be accounted for by the Allen-Perkins Viscous Crossflow Theory.⁴⁰

The other viscous consideration is that of temperature. Recall that one of the main objectives of the present work was to calculate real gas temperatures at the wall for use in heat transfer analysis. The temperatures calculated by the present analysis are those that exist at the outer edge of the boundary layer and thus must be carried to the wall and heat transfer analysis performed to get the true wall temperature. This can be done with one of several state-of-the-art⁴⁴ engineering techniques. However, without the more accurate real gas versus perfect gas temperatures computed at the outer edge of the boundary layer, these estimates of wall temperature will be considerably in error at higher Mach numbers. This in turn could cause costly and possibly unnecessary design decisions. Hence, while the present report is primarily focused on providing improved estimates of temperatures at the outer edge of the boundary layer, those temperatures will make local wall temperature and heat transfer computations (which are dependent on material properties, insulation assumptions, etc.) much more accurate.

The present inviscid analysis gives values of all the properties at the outer edge of the boundary layer. They could thus be input to a boundary layer code and surface properties calculated for heat transfer analysis. To aid in heat transfer analysis, an approximate technique will be given for estimating two of the parameters needed as inputs; the adiabatic wall temperature or enthalpy and heat transfer coefficients. While the technique is not as elaborate as a numerical solution of the axisymmetric or three-dimensional boundary layer equations, it does give an engineering approximation. The results can then be compared to more accurate computations.

The aerodynamic heating to the wall is defined by

$$q_w = \rho_L V_L C_h (h_{a_w} - h_w) \quad (144)$$

Here the subscript L refers to inviscid computations at the outer edge of the boundary layer so these quantities are known. Thus, by computing the heat transfer coefficient C_h and adiabatic wall enthalpy, the heat transfer to the wall for a given wall enthalpy can be computed.

The adiabatic wall enthalpy means the change in enthalpy normal to the wall is zero. That is

$$\left(\frac{\partial h}{\partial y} \right)_w = 0 \quad (145)$$

where y is normal to the wall. Solution of the boundary layer equations with this boundary condition will give the true adiabatic wall enthalpy. However, most engineering computations are performed with h_{a_w} related to the recovery factor r_c as⁴⁴

$$h_{a_w} = h_L + r_c \frac{V_L^2}{2} \quad (146)$$

For a turbulent boundary layer, r has been shown to be

$$r_c = P_r^{1/3}$$

For a real gas, Prandtl number is a function of other thermodynamic properties and must be found from the thermodynamic fit equations of References 34 and 35. That is

$$P_r = P_r(\rho_L, T_L) \quad (147)$$

Thus, since ρ_L , T_L , h_L , V_L are all known from the inviscid computations, h_{a_w} can be computed from Equation (146). The adiabatic wall temperature is also defined in many references by

$$T_{a_w} = \left[1 + r_c \frac{(\gamma_L - 1)}{2} M_L^2 \right] T_L \quad (148)$$

The perfect gas assumption can be somewhat compensated for in Equation (152) by using the local value of γ_L as opposed to 1.4.

To compute the heat transfer coefficient, resort will be made to the reference temperature method^{45,46} and Reynolds analogy.³³ The reference temperature, T^* , is given by¹¹³

$$\frac{T^*}{T_L} = 1 + 0.032 M_L^2 + 0.58 \left(\frac{T_w}{T_L} - 1 \right) \quad (149)$$

Then the local skin friction coefficient is³³

$$C_{f_w} = \frac{0.0592}{(R_N^*)^{0.2}} \quad (150)$$

Here

$$R_N^* = \frac{\rho^* V_L s}{\mu_1^*} \quad (151)$$

ρ^* and μ_1^* are evaluated at the local pressure and reference temperature defined by Equation (149) from the real gas thermofit equations.^{34,35} That is

$$\rho^* = \rho^*(T^*, p_L) \quad (152)$$

$$\mu_1^* = \mu_1^*(T^*, \rho^*) \quad (153)$$

Reynolds analogy then gives

$$C_{h_w} = \frac{C_{f_w}}{2} (p_r^*)^{-\frac{2}{3}} \quad (154)$$

p_r^* is also evaluated from the thermofit equations where

$$p_r^* = p_r^*(T^*, \rho^*) \quad (155)$$

Finally, if one desires enthalpy as opposed to, or in addition to, temperature, then

$$h = h(p_L, T_L) \quad (156a)$$

$$h^* = h^*(p_L, T^*) \quad (156b)$$

can be computed once again from the thermofit equations since pressure is assumed constant across the boundary layer. That is

$$\left(\frac{\partial p}{\partial y} = 0 \right)$$

Equations (150) and (154) are valid for flat plates in a turbulent compressible boundary layer. They are thus the appropriate equations for the wings and other lifting surfaces on the configuration of interest. For the body, Reference 33 indicates that Equations (150) and (154) should be multiplied by the Mangler fraction, $\sqrt{3}$. Hence

$$C_{f_b} = \frac{0.103}{(R_N^*)^{0.2}} \quad (157)$$

$$C_{L_b} = \frac{C_{f_b}}{2} (p_r^*)^{-\frac{2}{3}} \quad (158)$$

Again it should be emphasized that the reference enthalpy or temperature and Reynolds analogy are approximate engineering techniques. They have been used extensively and have a theoretical foundation. The more rigorous alternative of using the inviscid properties as inputs to a chemically reacting turbulent boundary layer computation is considered beyond the scope of the present work.

3. RESULTS AND DISCUSSION

3.1 STARTING SOLUTIONS

It is of interest first to check the validity and accuracy of the starting solutions for both the pointed and blunt body cases. Figures 17 and 18 compare the perfect gas pressure and temperature predicted by the present method to the exact cone solution of Jones⁵³ for several conditions. The first of these conditions, $M_\infty = 10.6$, $\theta_c = 15^\circ$, $\alpha = 10^\circ$, is the only one of interest as far as real gas effects are concerned. However, the other lower Mach number and higher angle-of-attack cases are shown to indicate the robustness of the present method for computing pressure and temperature. Note that for all four conditions of Figures 17 and 18, good agreement on pressure and temperature is obtained compared to the exact solution. In most cases, accuracies of 3 percent or better are found for the conditions investigated to date. An exception is the pressure prediction at the bottom of Figure 18 where errors in pressure of up to 15 percent are encountered. Comparing Figures 17 and 18 shows that the method gives slightly improved accuracy at the higher Mach numbers.

Figure 19 compares the present conical starting solution with the exact results from the ZEUS code⁴⁷ for $M_\infty = 15$, $\alpha = 10^\circ$, $\theta_c = 15^\circ$. Both real and perfect gas results are shown. Note that the approximate and ZEUS, real and perfect gas pressures are nearly identical (Figure 19(a)). This is as anticipated from knowledge of compression processes with respect to real gas effects. On the other hand, Figure 19(b) shows the large differences in temperature that can occur due to real gas effects. In comparing approximate and exact temperature calculations in Figure 19(b), it is seen that the perfect gas results are within a couple of percent whereas the real gas deviates by up to 10 percent. The ZEUS real gas temperatures are actually higher than the perfect gas results in the leeward plane, which is not correct. The reason for this is that the ZEUS code uses the real gas thermofit equations to obtain entropy directly. On the other hand, referring to Figure C-15 and the discussion that goes with the figure, it is seen that obtaining entropy in this manner gives temperatures about 250° too high for cone angles of 15° and 25°. Referring to Figure 19(b), this is

the approximate value of the difference between the ZEUS code and the present computations. This 250° reduction would apply all around the body since this incorrect value of entropy is held constant. This explains why there is a crossover of the real and perfect gas temperatures with the ZEUS computations in Figure 19(b).

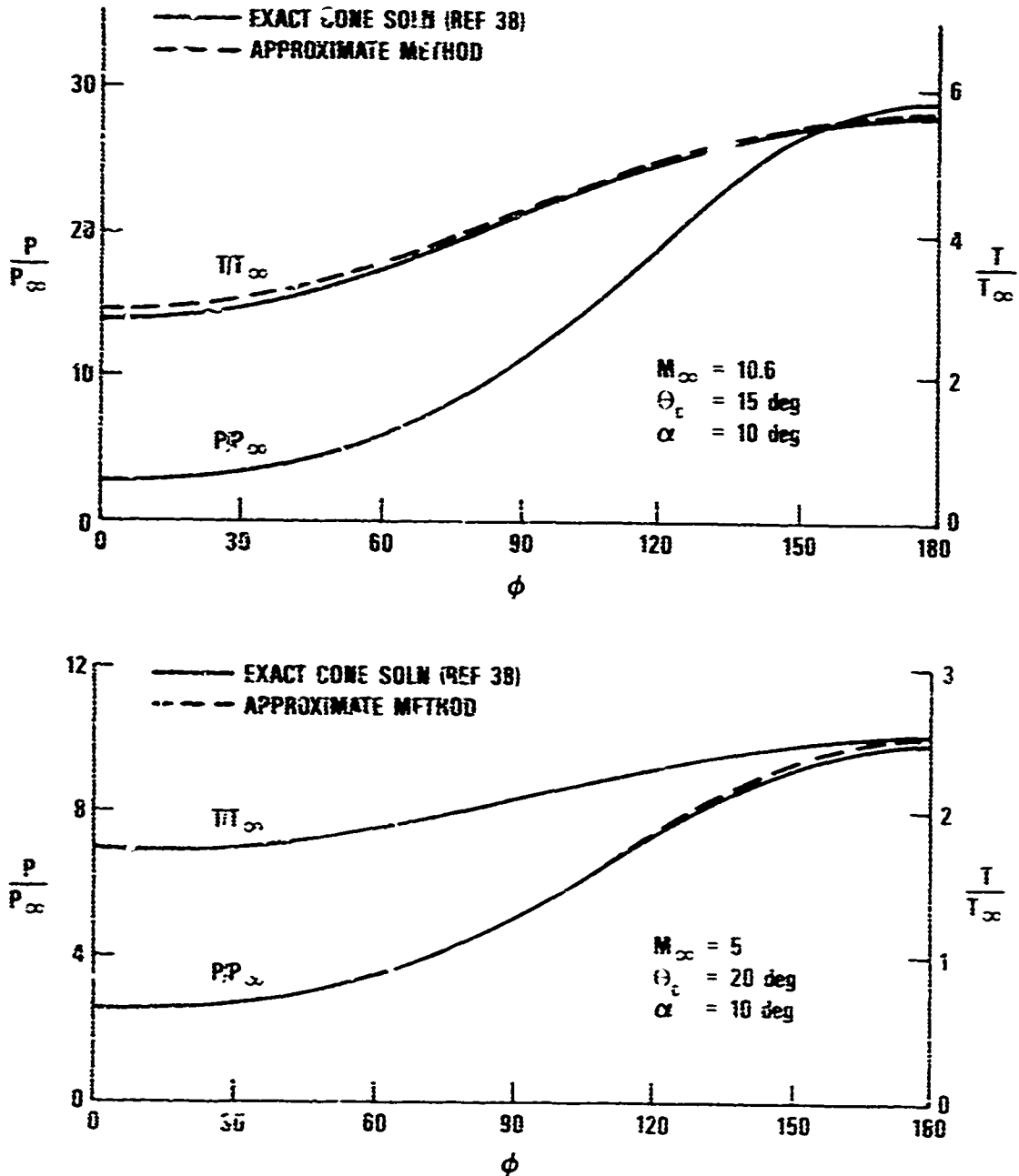


FIGURE 17. PERFECT GAS COMPARISON OF EXACT AND PRESENT APPROXIMATE CONE SOLUTIONS

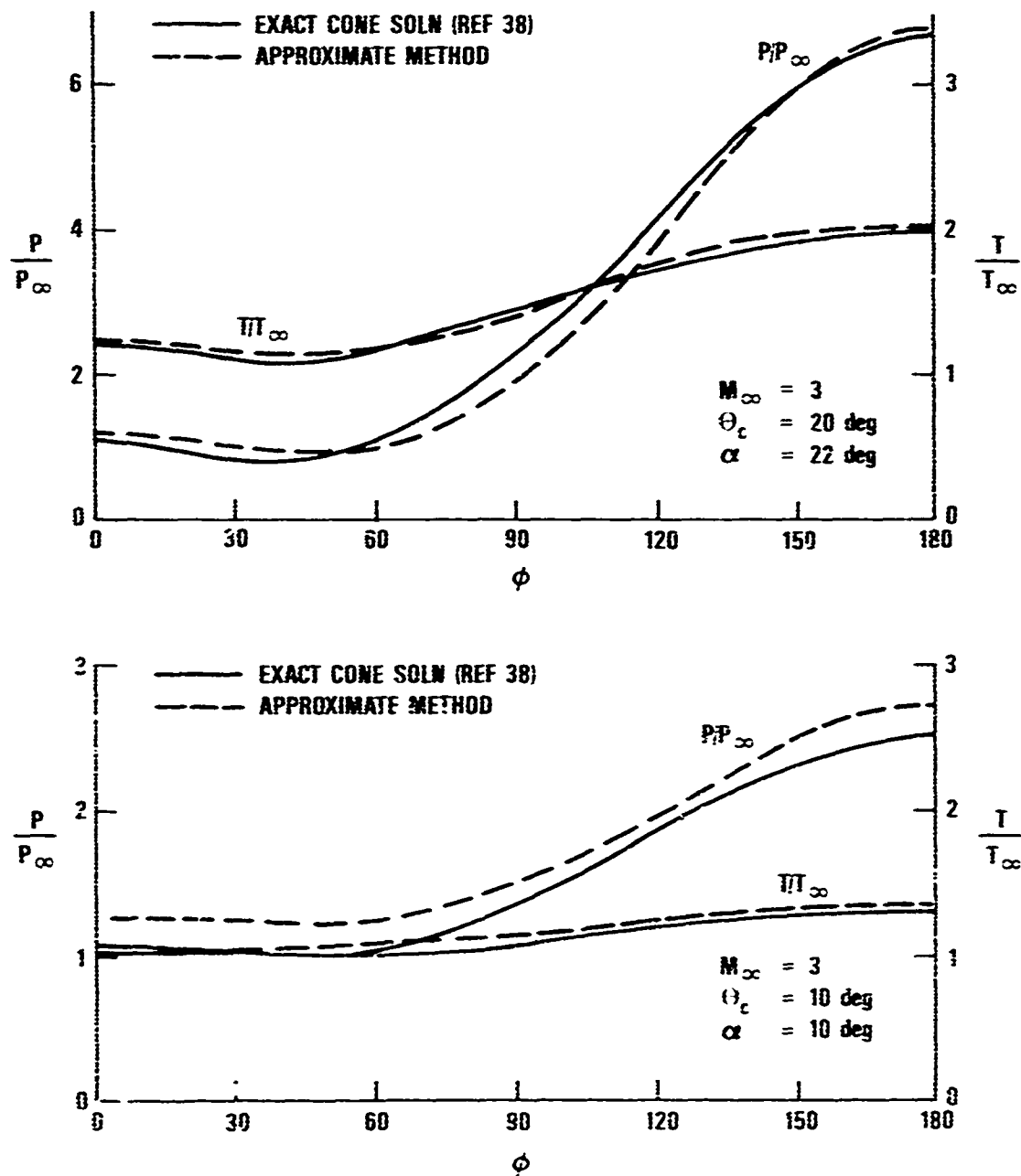


FIGURE 18. PERFECT GAS COMPARISON OF EXACT AND PRESENT APPROXIMATE CONE SOLUTIONS

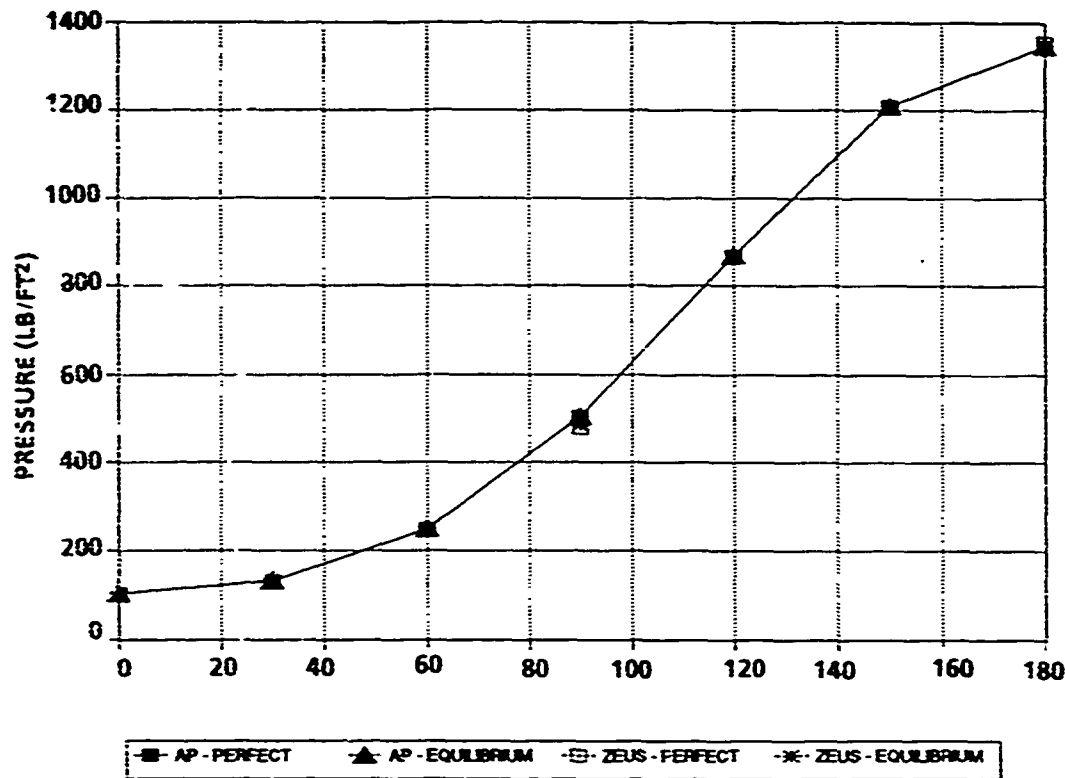


FIGURE 19(a). APPROXIMATE AND EXACT PRESSURE PREDICTION ON A CONE IN PERFECT AND EQUILIBRIUM CHEMICALLY REACTING FLOWS ($M_\infty = 15$, $\alpha = 10^\circ$, $h = 100k$ ft, $\theta_c = 15^\circ$)

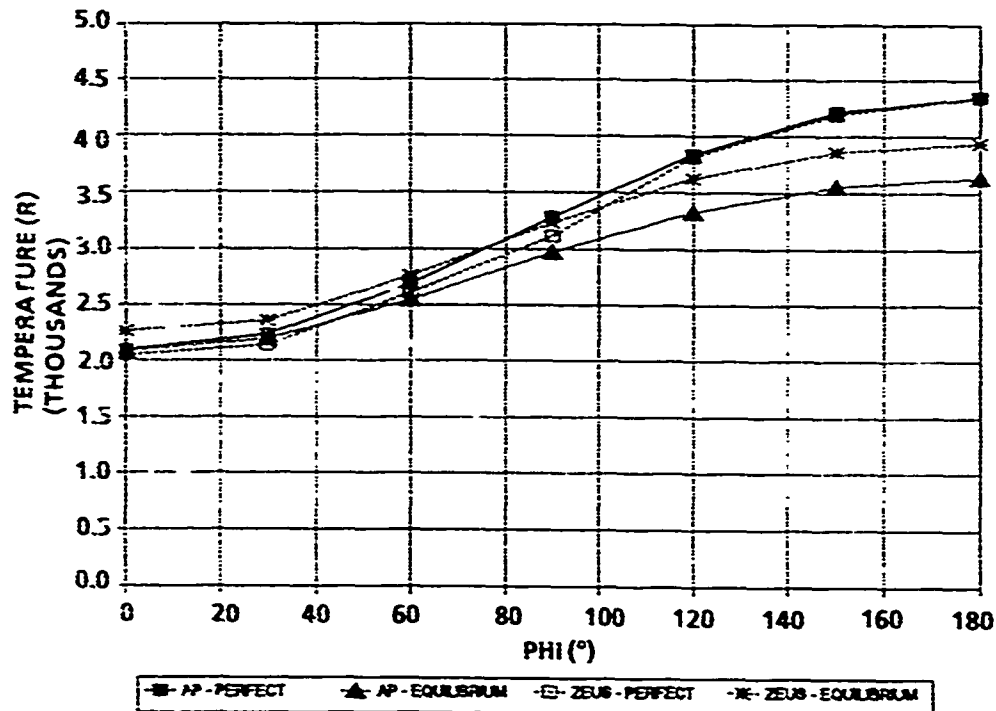


FIGURE 19(b). APPROXIMATE AND EXACT TEMPERATURE PREDICTION ON A CONE IN PERFECT AND EQUILIBRIUM CHEMICALLY REACTING FLOWS ($M_\infty = 15$, $\alpha = 10^\circ$, $h = 100k$ ft, $\theta_c = 15^\circ$)

Figures 20(a) through (d) illustrate the accuracy of the Improved Modified Newtonian Theory (IMNT) over MNT. The figures show the IMNT, MNT, and the exact results from Reference 48. Note that the IMNT gives virtually identical results to the exact computations. Although not shown, this excellent agreement in pressure prediction holds true all the way to $M_\infty = 30$. In the present method, the match point between SOSET and IMNT is at $\delta_{eq} = 25.95^\circ$ so that IMNT is used for $\delta_{eq} \geq 25.95^\circ$ and SOSET for values of $\delta_{eq} < 25.95^\circ$. Knowing accurate values of pressure and a good estimate of entropy should allow good estimates of other properties at the body surface.

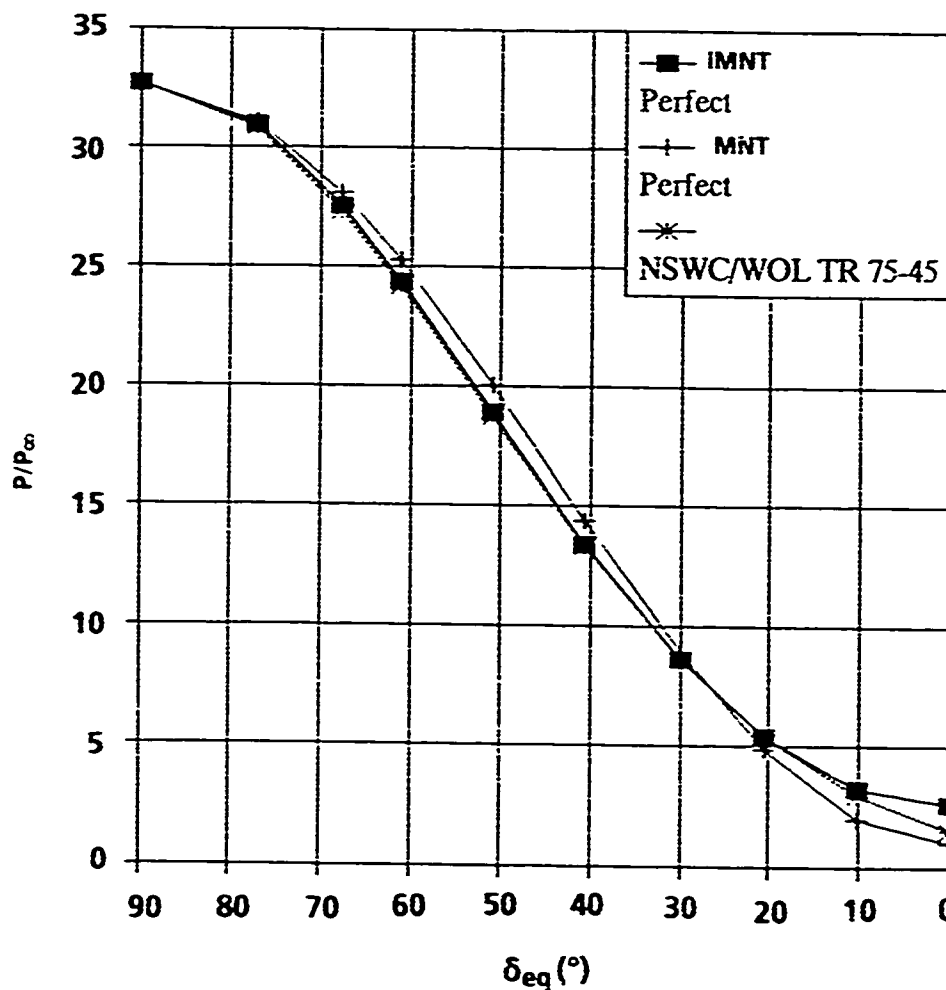


FIGURE 20(a). SURFACE PRESSURE DISTRIBUTION OVER A HEMISPHERICAL FOREBODY AT $M_\infty = 5$

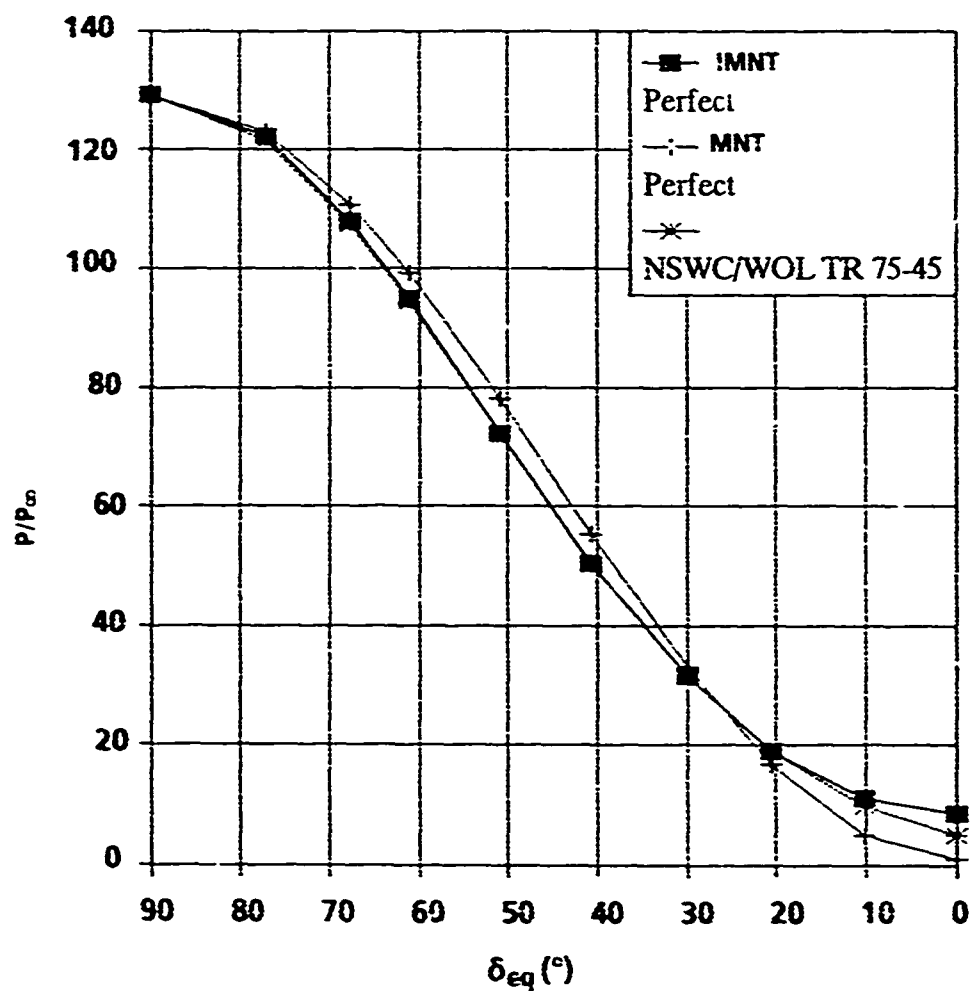


FIGURE 20(b). SURFACE PRESSURE DISTRIBUTION OVER A HEMISPHERICAL FOREBODY AT $M_\infty = 10$

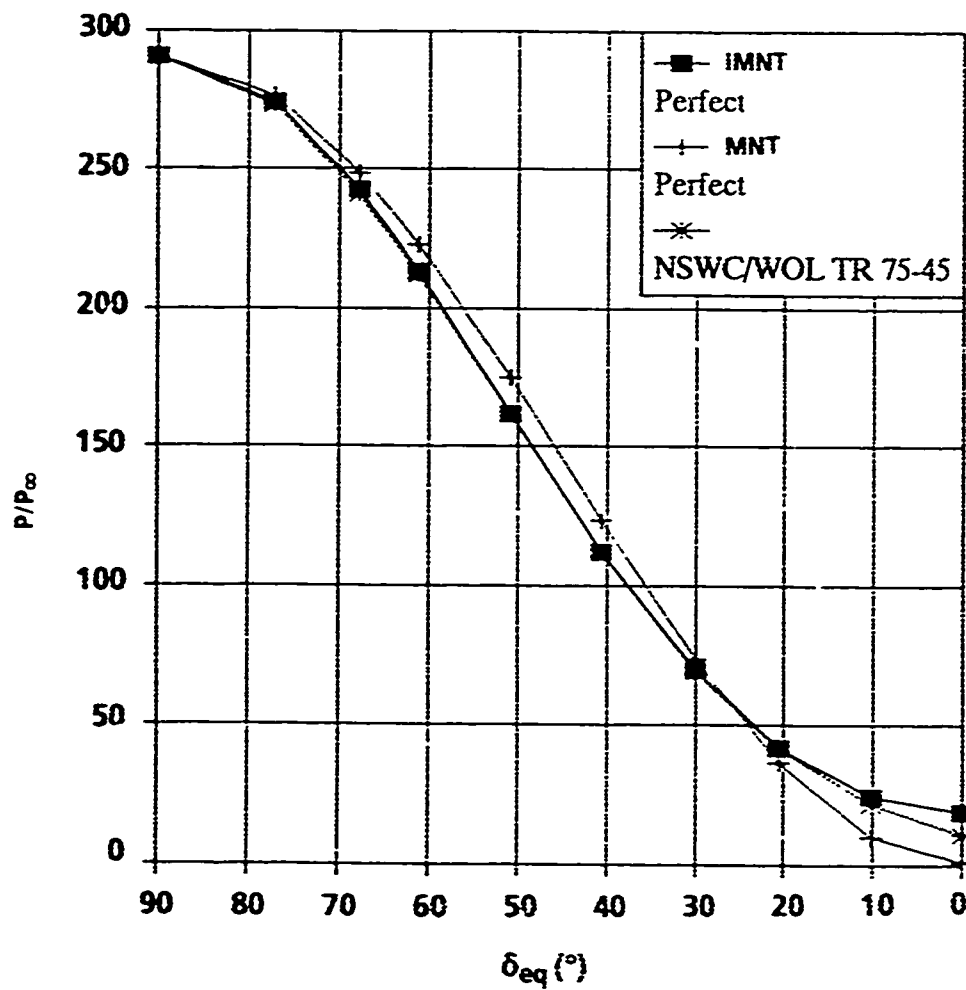


FIGURE 20(c). SURFACE PRESSURE DISTRIBUTION OVER A HEMISPHERICAL FOREBODY AT $M_\infty = 15$

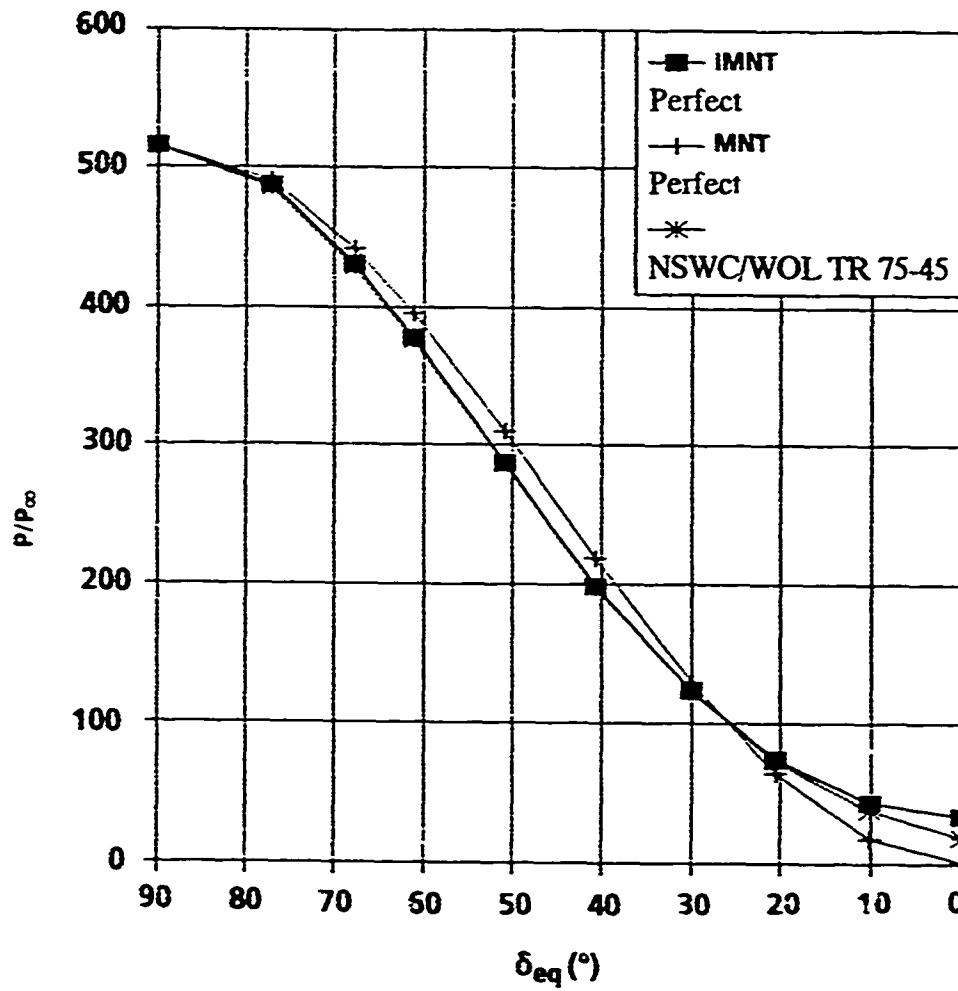


FIGURE 20(d). SURFACE PRESSURE DISTRIBUTION OVER A HEMISPHERICAL FOREBODY AT $M_\infty = 20$

3.2 PRESSURE GRADIENT USED IN SOSET

Before computing pressures and temperatures on general body shapes using the section 3.1 starting solutions combined with SOSET, it is of interest to examine Equation (36), which defines η . Recall that η is the exponent containing

$$\left(\frac{\partial p}{\partial s} \right)_2$$

which is used in Equation (35) in the SOSET to determine the blend of Tangent Cone Theory (TCT) and Generalized Shock Expansion Theory (GSET). To do this, a simple biconic nose shape was considered as indicated in Figure 21. This allowed a simple starting solution and then a computation of the properties around a turn of a given $\Delta\theta = \theta_2 - \theta_1$ as shown in Figure 1. Results were obtained for the parameter

$$\left(\frac{r}{p_\infty} \frac{\partial p}{\partial s} \right)_2$$

under various conditions using the approximate method of Syvertson and Dennis,¹⁹ the exact prediction by DeJarnette,²³ and the approximate present technique given by Equation (122). Since the Reference 19 and 23 results were for perfect gas only, the cases considered for comparison were for perfect gas. The results of this study are presented in Table 1, which shows M_∞ varying from 3 to 15, cone half angle from 5 to 20, and $\Delta\theta$ 2° and 5°. Note first of all that the present approximation for

$$\left(\frac{r}{p_\infty} \frac{\partial p}{\partial s} \right)_2$$

agrees very closely with the exact integration of Reference 23. The only difference between the two techniques is the fact that the present method approximates the integral of Equation (112) using the Trapezoidal Rule whereas Reference 23 integrates the entire equation numerically. On the other hand, the Reference 19 results neglect the integral of Equation (112) altogether. As seen in Table 1, neglecting the integral gives reasonable results (within 10 percent) in most cases shown where $\Delta\theta$ is small.

The most important aspect of the Table 1 results is the fact that η becomes negative quite often for Mach numbers of 5 and greater. This means that η must be defined and SOSET of Equation (35) reverts back to GSET or TCT; that is, $p = p_2$ or $p = p_c$. As a result of this dilemma, we investigated a different approach that would allow us to take advantage of both p_c and p_2 . This approach defined p in the SOSET as

$$p = p_c - (p_c - p_2) \eta_1 \quad (159)$$

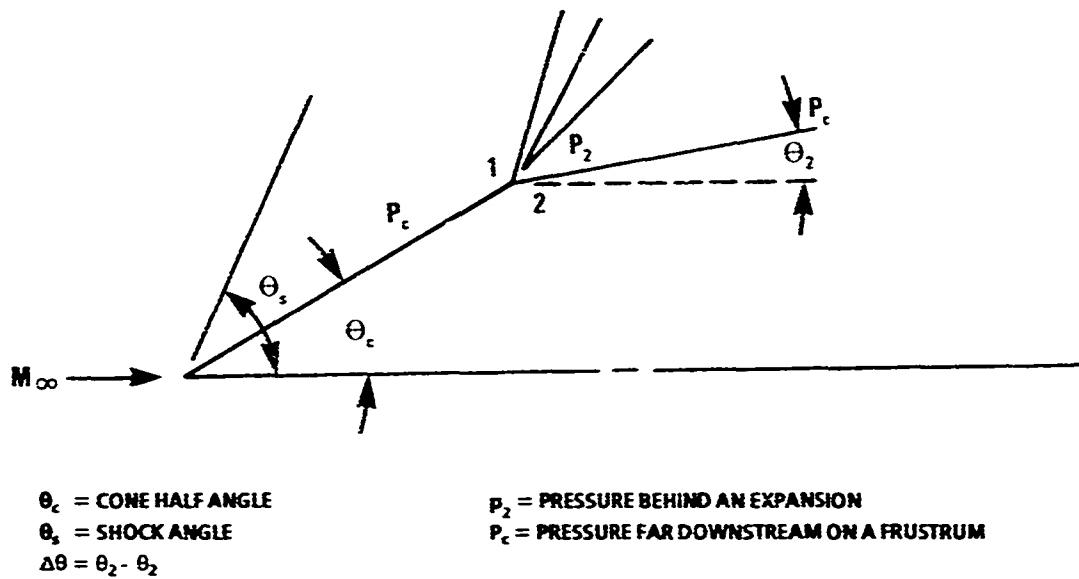


FIGURE 21. BICONIC CONFIGURATION GEOMETRY FOR INVESTIGATING PRESSURE GRADIENT AROUND A CORNER (see Table 1)

TABLE 1. ESTIMATES OF $(r_2/p_x) (\partial p/\partial s)_2$ FOR VARIOUS CONDITIONS

M_∞	θ_c (deg)	$\Delta\theta$	Exact ²³	Syv & Dennis ¹⁹	Present	$(r_2/p_\infty) (\partial p / \partial s)_2 /$ $(p_c - p_2)$	P_2	P_c
3	15	2	0.0216	0.0209	0.0216	0.657	1.86	1.89
		5	0.0478	0.0441	0.0478	0.622	1.50	1.58
5	20	2	-0.0148	-0.0142	-0.0147	-0.143	4.68	4.78
		5	-0.0129	-0.0109	-0.0120	-0.077	3.56	3.73
5	10	2	0.0153	0.0147	0.0154	0.389	1.88	1.92
		5	0.0341	0.0306	0.0341	0.359	1.34	1.43
10	15	2	-0.0879	-0.0822	-0.0872	-0.209	8.29	8.71
		5	-0.0952	-0.0785	-0.0896	-0.188	5.20	5.71
10	10	2	-0.0144	-0.0131	-0.0141	-0.097	3.96	4.11
		5	0.0014	0.0033	0.0034	0.010	2.20	2.35
15	15	2	-0.2602	-0.2415	-0.2580	-0.206	16.73	17.99
		5	-0.2840	-0.2310	-0.2672	-0.193	9.77	11.24
15	10	2	-0.0719	-0.0649	-0.0706	-0.141	7.17	7.68
		5	-0.0420	-0.0294	-0.0351	-0.122	3.43	3.77
15	5	2	0.0061	0.0056	0.0063	0.068	2.04	2.13
		5	0.0165	0.0135	0.0167	0.051	0.72	1.0

where $\eta_1 = 0$ gives $p = p_c$ and $\eta_1 = 1$ gives $p = p_2$ and $0 < \eta_1 < 1$ gives a blend of the two. This approach would allow a direct input of η_1 as opposed to a computation as done in the past.

To investigate the Equation (159) approach, two cases were considered. The first of these is a 20-percent blunt Von Karman ogive at $M_\infty = 15$. Results of the pressure computation are shown in Figure 22. In Figure 22, IMNT + p_2 is when $\eta_1 = 1$, IMNT + p_c is where $\eta_1 = 0$, old AP is the current aeroprediction code, and ZEUS is the exact computation. In the current aeroprediction code, SOSET is implemented with Equation (35) and when η becomes negative, p is set to p_c . As a result, note in Figure 20 that the present results for $\eta_1 = 1$ are slightly better than the old AP compared to the ZEUS computations. This is due solely to the IMNT. However, if one were to use $\eta_1 = 1$, significantly worse results would be obtained.

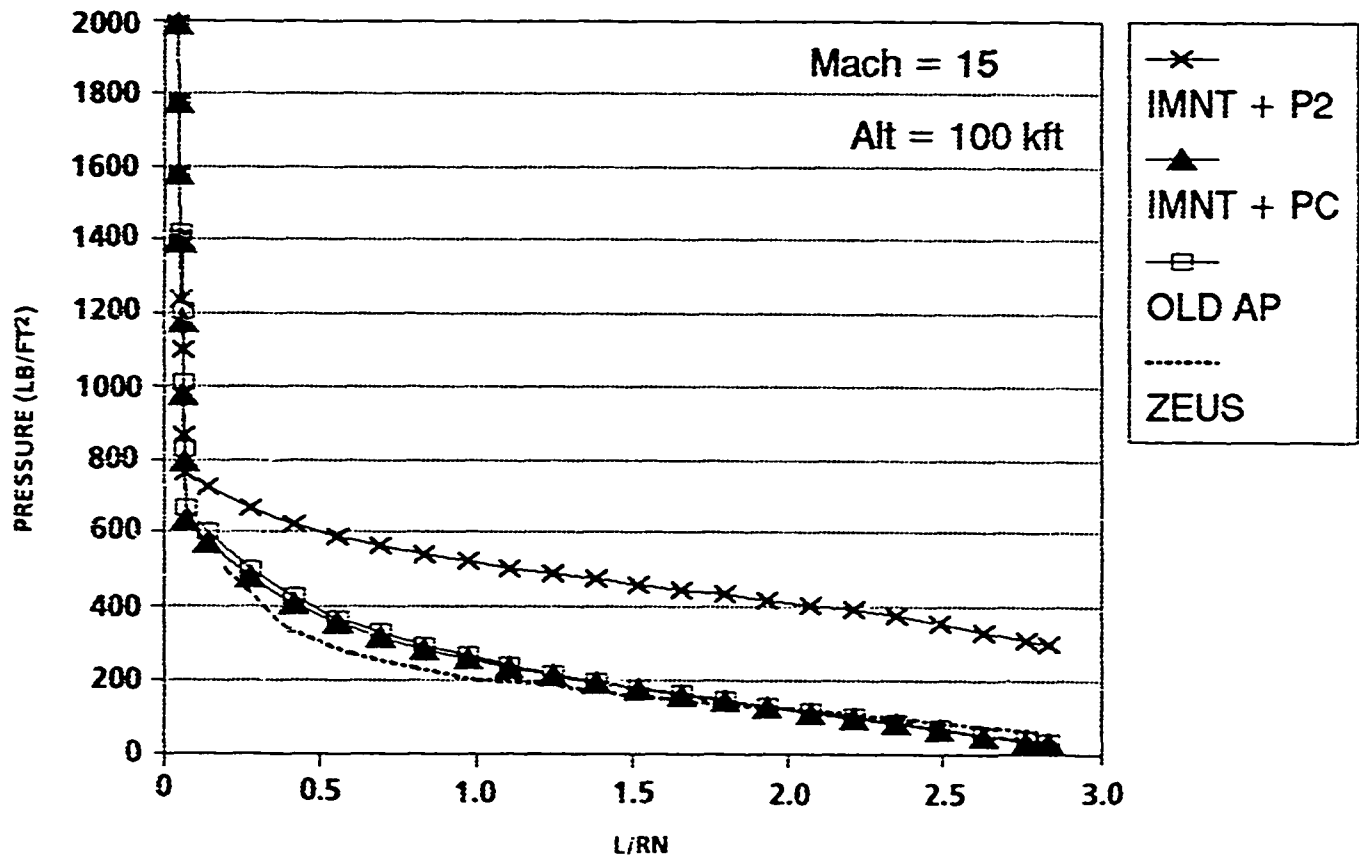


FIGURE 22. COMPARISON OF VARIOUS PRESSURE PREDICTION TECHNIQUES ON A 20-PERCENT BLUNT VON KARMAN OGIVE ($M_\infty = 15$, $\alpha = 0^\circ$, $h = 100$ k ft)

The second case investigated to examine the Equation (159) approach is a simple hemisphere forebody. These results are shown in Figure 23. Note here that the $IMNT + p_c$ and old AP results are inferior to the $IMNT + p_2$ results compared to ZEUS. This is even more reason for allowing η_1 to be input as opposed to computed.

To summarize the pressure prediction using SOSET, it was found that for Mach numbers greater than 5, η becomes negative quite often requiring one to revert back to either TCT or GSET. Since this is the case, it is believed that the Equation (159) approach is a better way to implement SOSET. A value of $\eta_1 = 0$ is recommended for hemispheres or near hemispheres. For other configurations, a value of $\eta_1 = 1.0$ is recommended. This is the approach that is being implemented in the aeroprediction code for Mach numbers greater than about 6. For Mach numbers between about 2.5 and 6, conventional SOSET is used, and for Mach numbers 1.2 to about 2.5, second-order Van Dyke Theory³⁰ is used.

3.3 CONFIGURATION RESULTS

To thoroughly investigate the current new methods for calculating real gas effects, several configurations were selected that covered the typical range of missile-type configurations. These include a 20-percent blunt Von Karman ogive, a 20-percent blunt Von Karman ogive-cylinder, a blunt cone nose shape, and a sharp cone-cylinder-flare configuration (see Figure 24). Exact solutions were also generated as a basis for comparison of the present approximate engineering methods.

Figure 15 showed the results of using the $IMNT + SOSET$ for the zero angle-of-attack solution, applying Equations (138) and (142) to get angle-of-attack pressure effects, and knowing entropy, applying Equation (139) to get temperature. Figure 16 was for perfect gas. Figure 25 further illustrates the present methodology for the Von Karman ogive by comparing the pressure and temperature in the windward plane (perfect gas) to conventional TCT and ZEUS results. Conventional TCT is where one computes pressure at a given point on a body surface with the freestream Mach number and the local slope with respect to the freestream velocity vector. The standard Taylor McCall¹⁸ cone solution can be solved for perfect gases, Hudgins³⁷ solution for real gases or approximations to these solutions such as Equations (40b) or (132). The $IMNT$ was used on the blunt nose portion. Note that in comparing the three theoretical approaches for both pressure and temperature, the present method agrees closer with the exact solution than does the TCT.

Figure 26 presents the results for the same case as Figure 25 except here the gas is equilibrium chemically reacting. Note that in comparing Figure 26(a) to 25(a), little difference in pressure is noted (and indeed in the aerodynamic coefficients); however, comparing Figure 26(b) to Figure 25(b), real gas temperatures are lower by as much as a factor of 2. Figure 26(c) compares the present predictions to those of the ZEUS code in three planes. Agreement on temperature in the critical windward plane is within 4 percent.

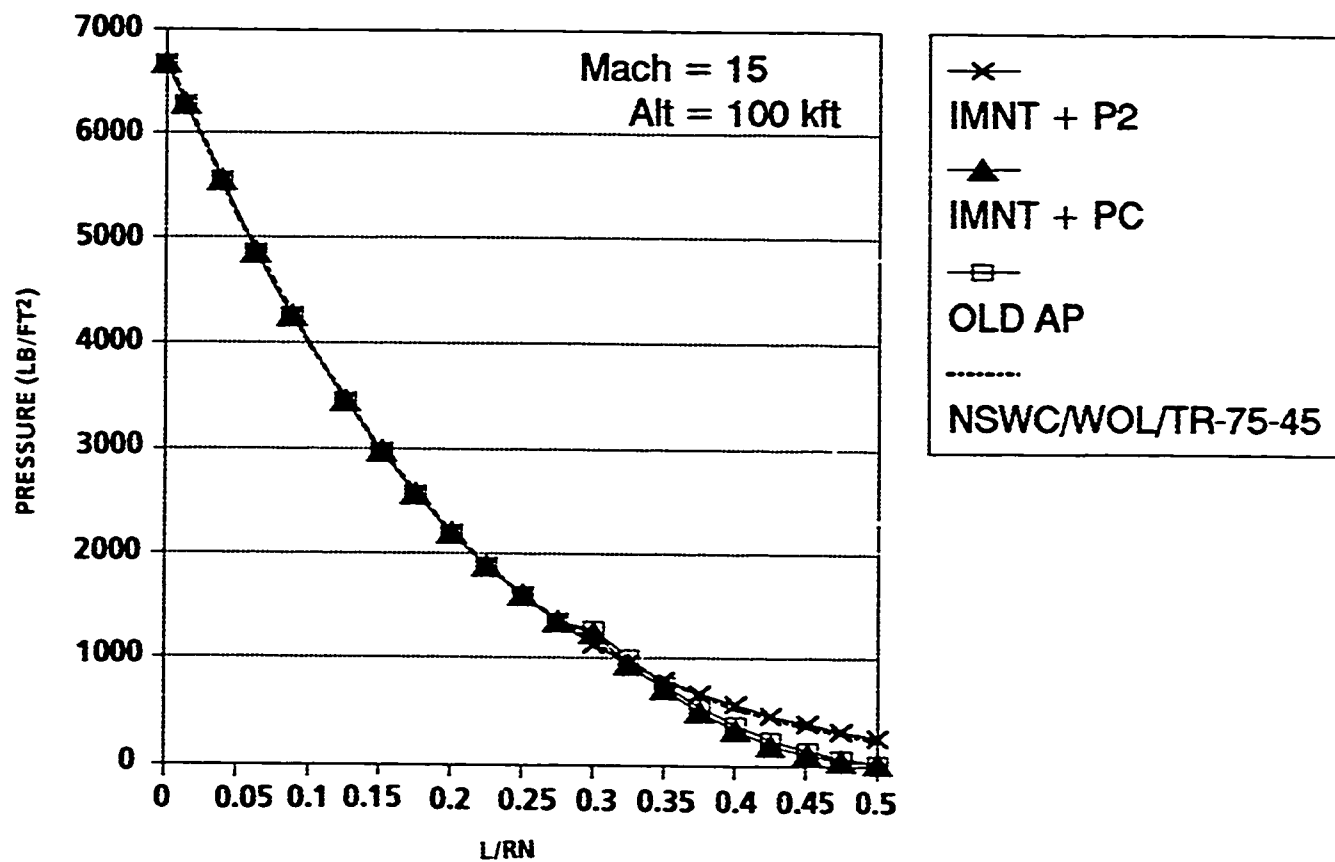
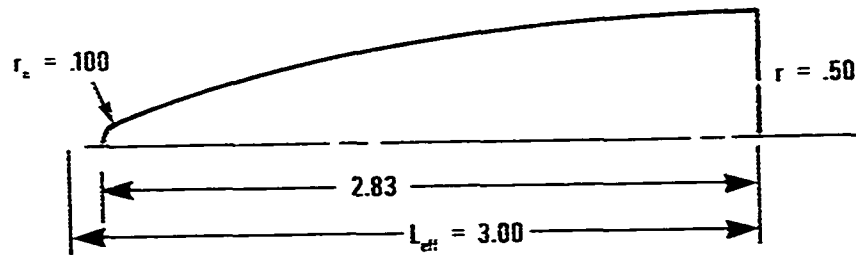
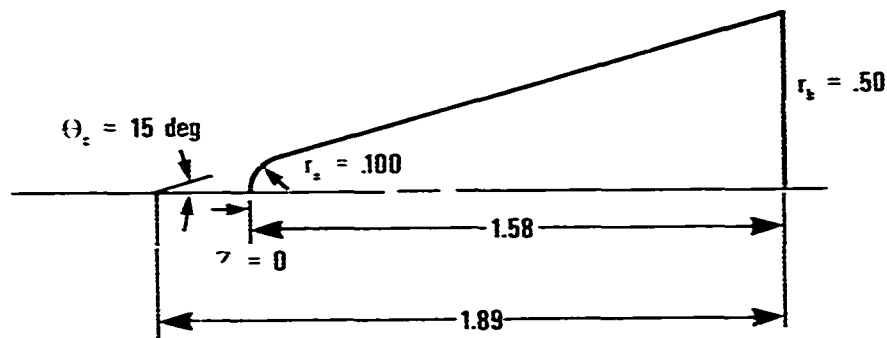


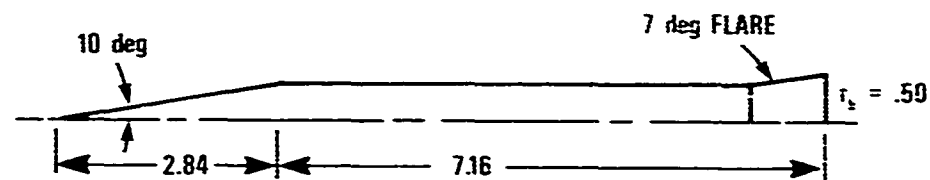
FIGURE 23. COMPARISON OF VARIOUS PRESSURE PREDICTION TECHNIQUES
ON A HEMISPHERE FOREBODY ($M_\infty = 15$, $\alpha = 0^\circ$, $h = 100$ k ft)



TEST CASE 1: 20-PERCENT BLUNT VON KARMAN OGIVE

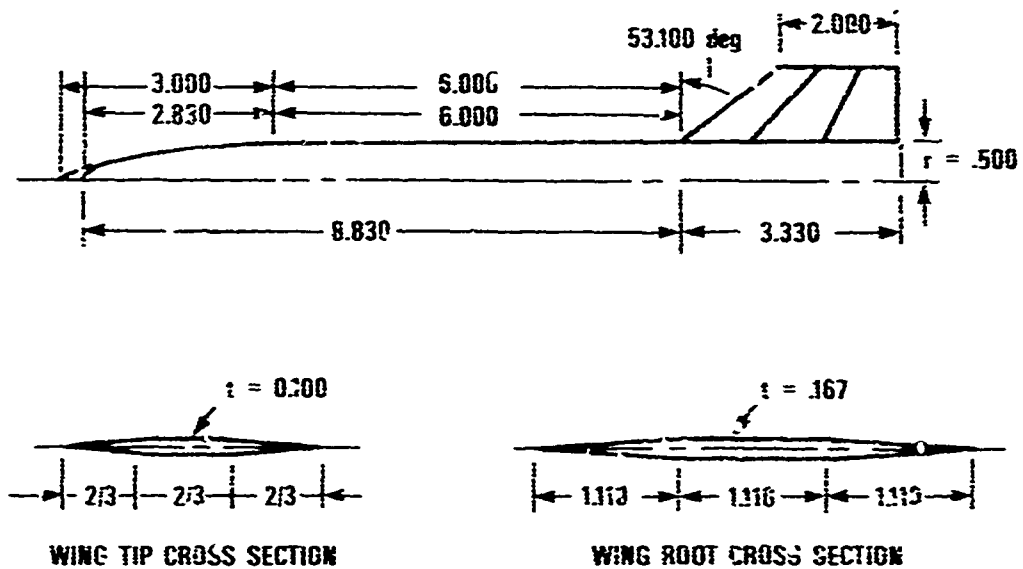


TEST CASE 2: 20-PERCENT BLUNT CONE



TEST CASE 3: CONE-CYLINDER-FLARE

FIGURE 24. CONFIGURATIONS USED AS TEST CASES FOR NEW THEORY (DIMENSIONS IN CALIBERS)



TEST CASE 4: 20-PERCENT BLUNT VON KARMAN
OGIVE—CYLINDER WITH CRUCIFORM TAILS

FIGURE 24. CONFIGURATIONS USED AS TEST CASES FOR NEW THEORY
(DIMENSIONS IN CALIBERS) (CONTINUED)

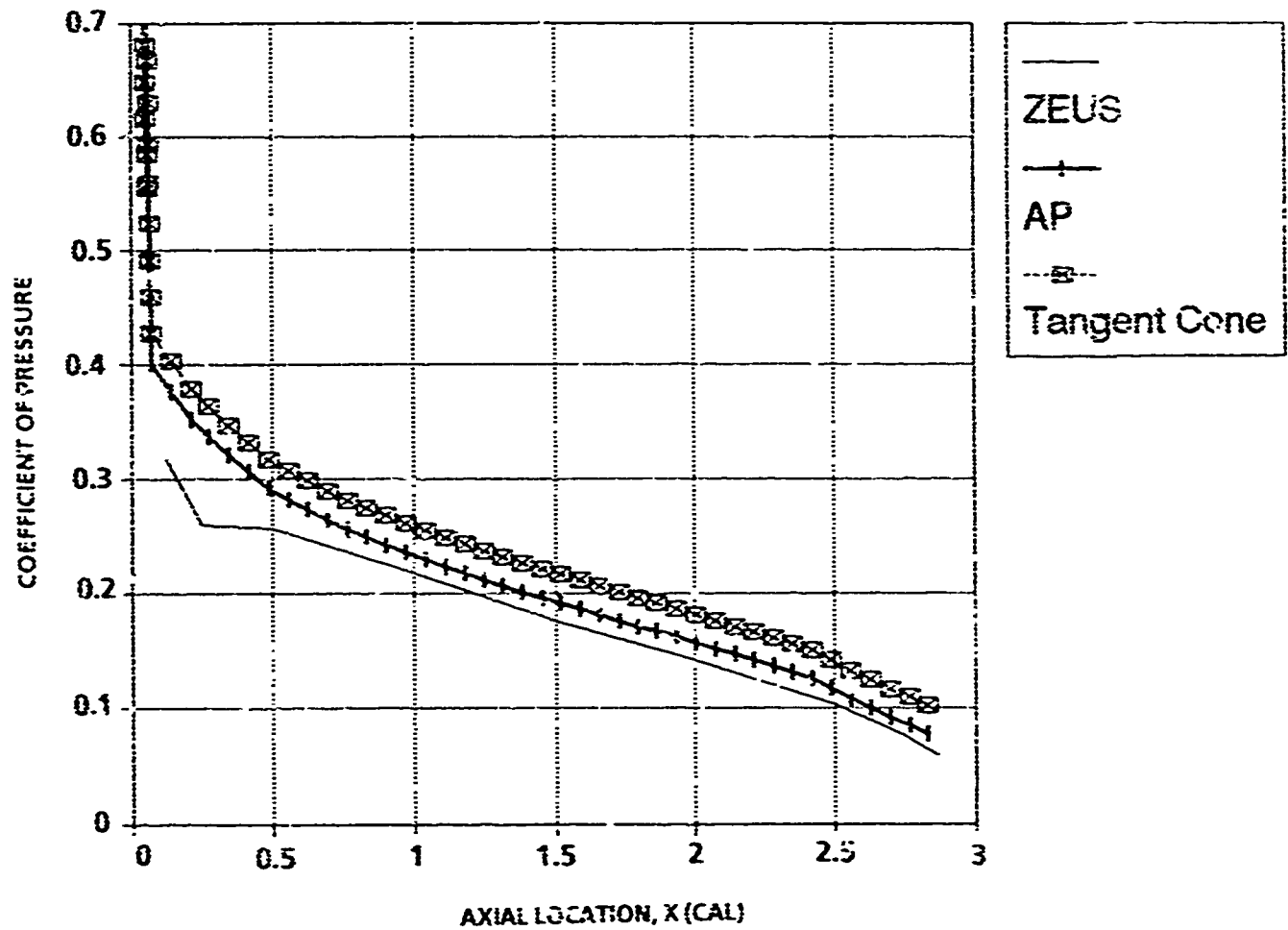


FIGURE 25(a). COMPARISON OF APPROXIMATE AND EXACT PRESSURE PREDICTION FOR A 20-PERCENT BLUNT VON KARMAN OGIVE ($M_\infty = 15$, $\alpha = 10^\circ$, $\Phi = 180^\circ$, perfect gas)

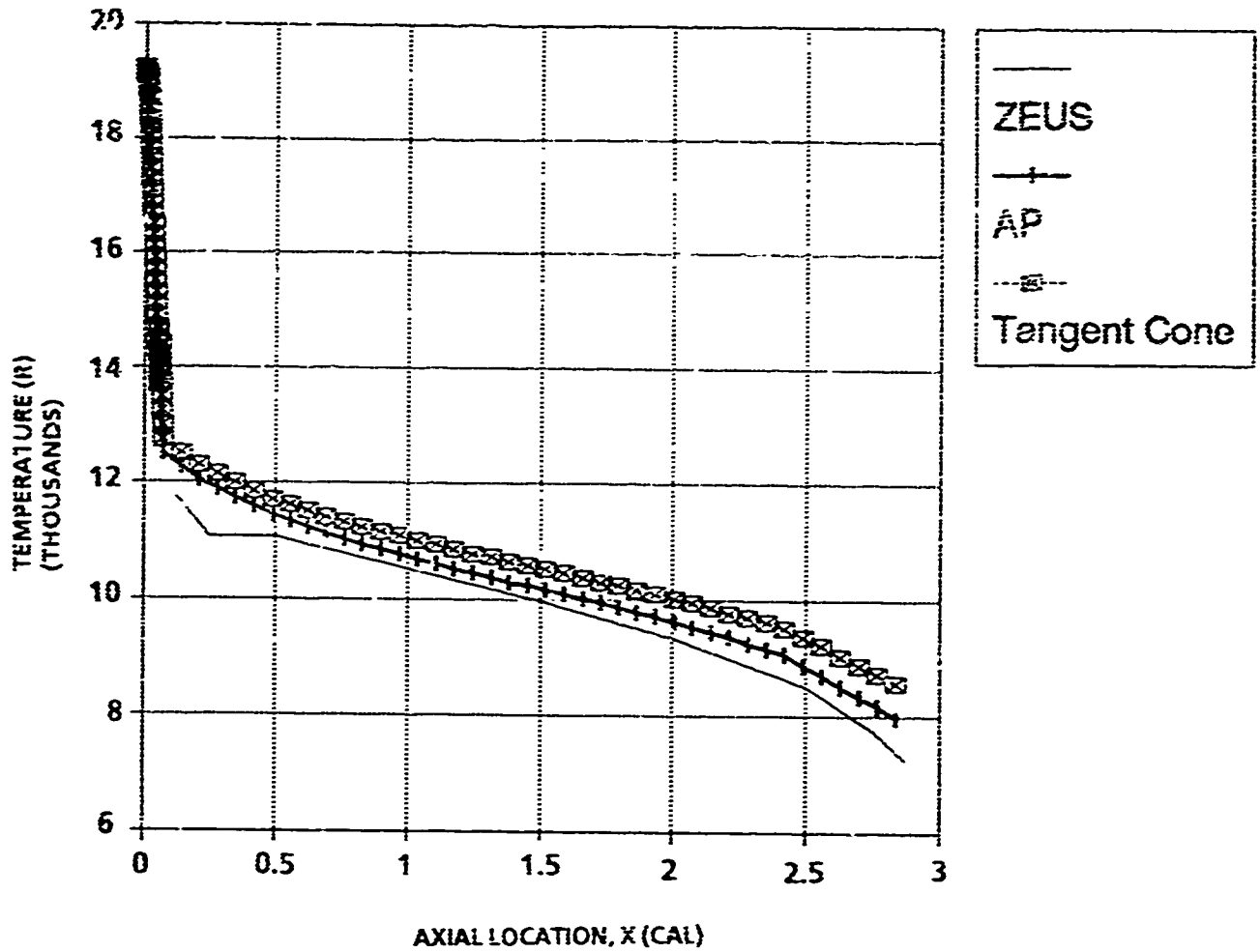


FIGURE 25(b). COMPARISON OF APPROXIMATE AND EXACT TEMPERATURE PREDICTION FOR A 20-PERCENT BLUNT VON KARMAN OGIVE ($M_\infty = 15$, $\alpha = 10^\circ$, $\Phi = 180^\circ$, perfect gas)

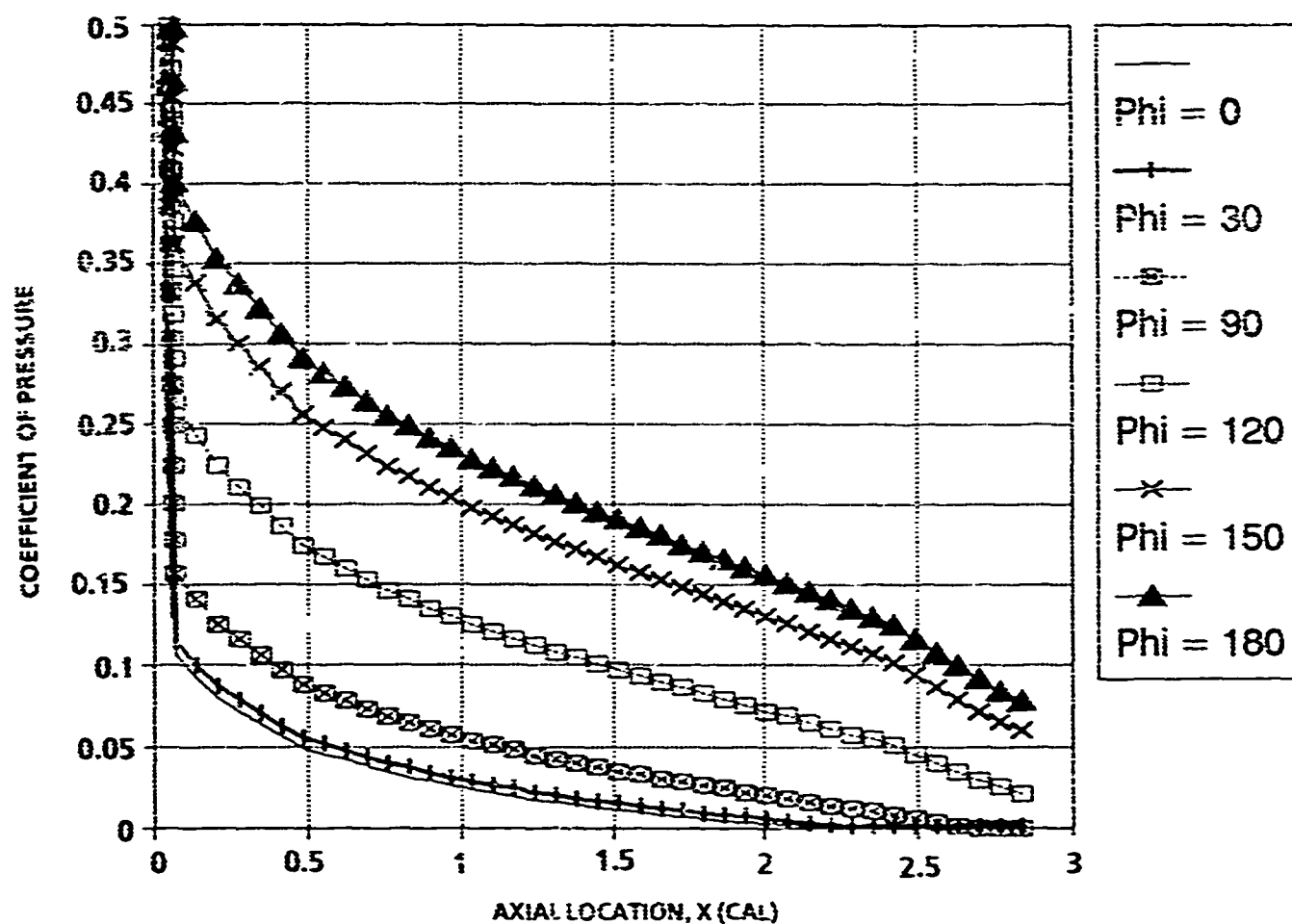


FIGURE 26(a). APPROXIMATE PRESSURE PREDICTION ON A 20-PERCENT BLUNT VON KARMAN OGIVE FOR A REAL GAS ($M_\infty = 15$, $\alpha = 10^\circ$, $h = 100k$ ft)

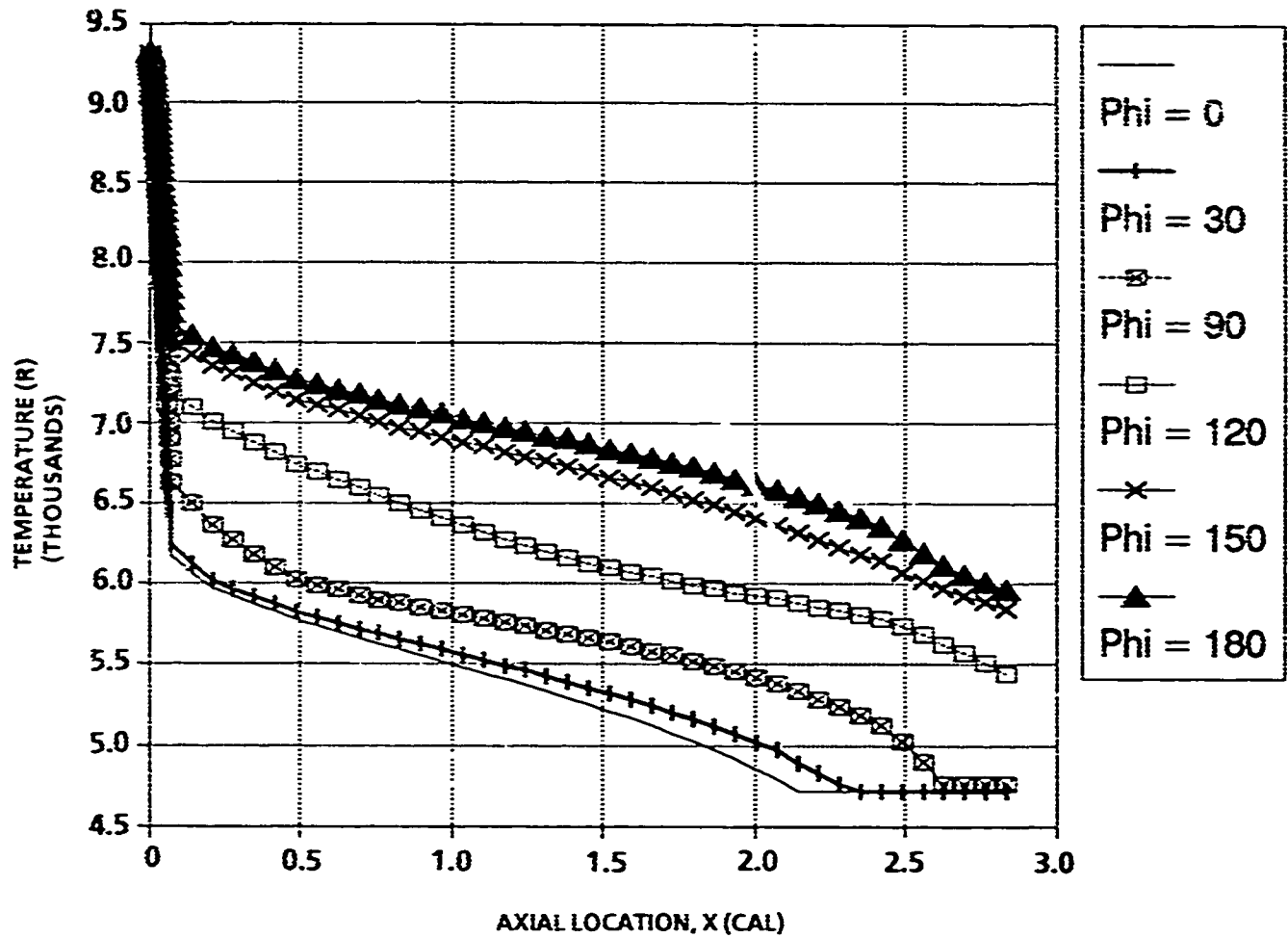


FIGURE 26(b). APPROXIMATE TEMPERATURE PREDICTION ON A 20-PERCENT BLUNT VON KARMAN OGIVE FOR A REAL GAS ($M_\infty = 15$, $\alpha = 10^\circ$, $h = 100k$ ft)

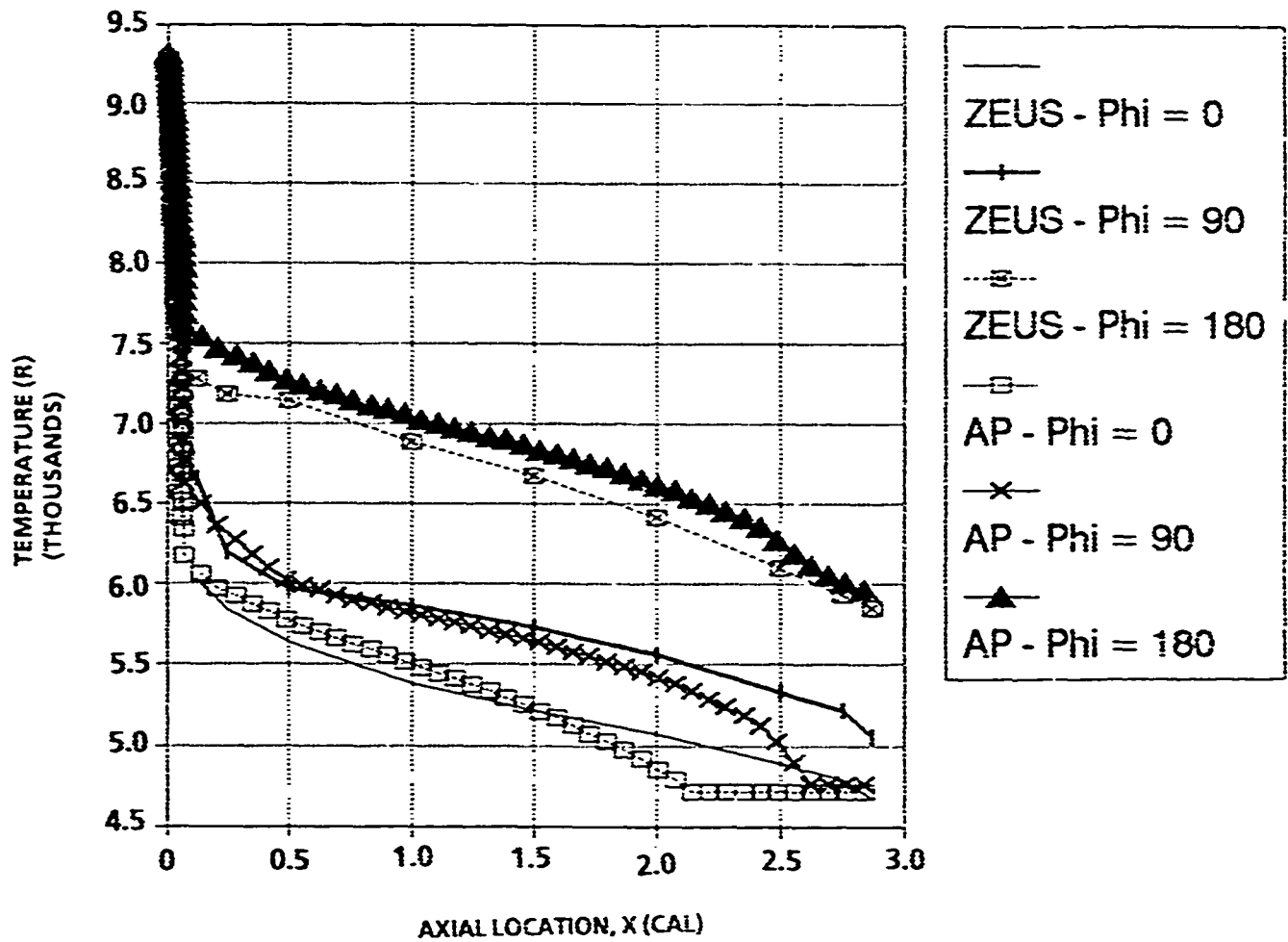


FIGURE 26(c). COMPARISON OF APPROXIMATE AND EXACT TEMPERATURE PREDICTION
ON A 20-PERCENT BLUNT VON KARMAN OGIVE FOR A REAL GAS
($M_\infty = 15$, $\alpha = 10^\circ$, $h = 100k ft$)

The second test case considered is the blunt cone shown in Figure 24. While the bluntness is the same as the Von Karman ogive, the aft part of the nose has a constant angle so it is of interest to see how the results of the approximate method compare with ZEUS computations. These comparisons are presented in Figure 27. Figures 27(a) and 27(b) present the windward plane pressure coefficient and temperature comparisons between the ZEUS and approximate computations. In examining Figure 27(a), ZEUS computations do show some slight differences in pressure coefficient between real and perfect gas on the overexpansion region of the blunt nose whereas the approximate results give basically identical pressures. Also note that good agreement between the exact and approximate technique is evident except in the overexpansion region. In examining Figure 27(b), good agreement in temperature predictions between the two theoretical methods is noted. Even in the overexpansion region where the disagreement is largest, the maximum deviation from the exact results is only about 8 percent. On the maximum temperature portions of the nose, the deviation is less than 2 percent. Also worthy of note is the almost 5000° R lower temperature of real versus perfect gas computations.

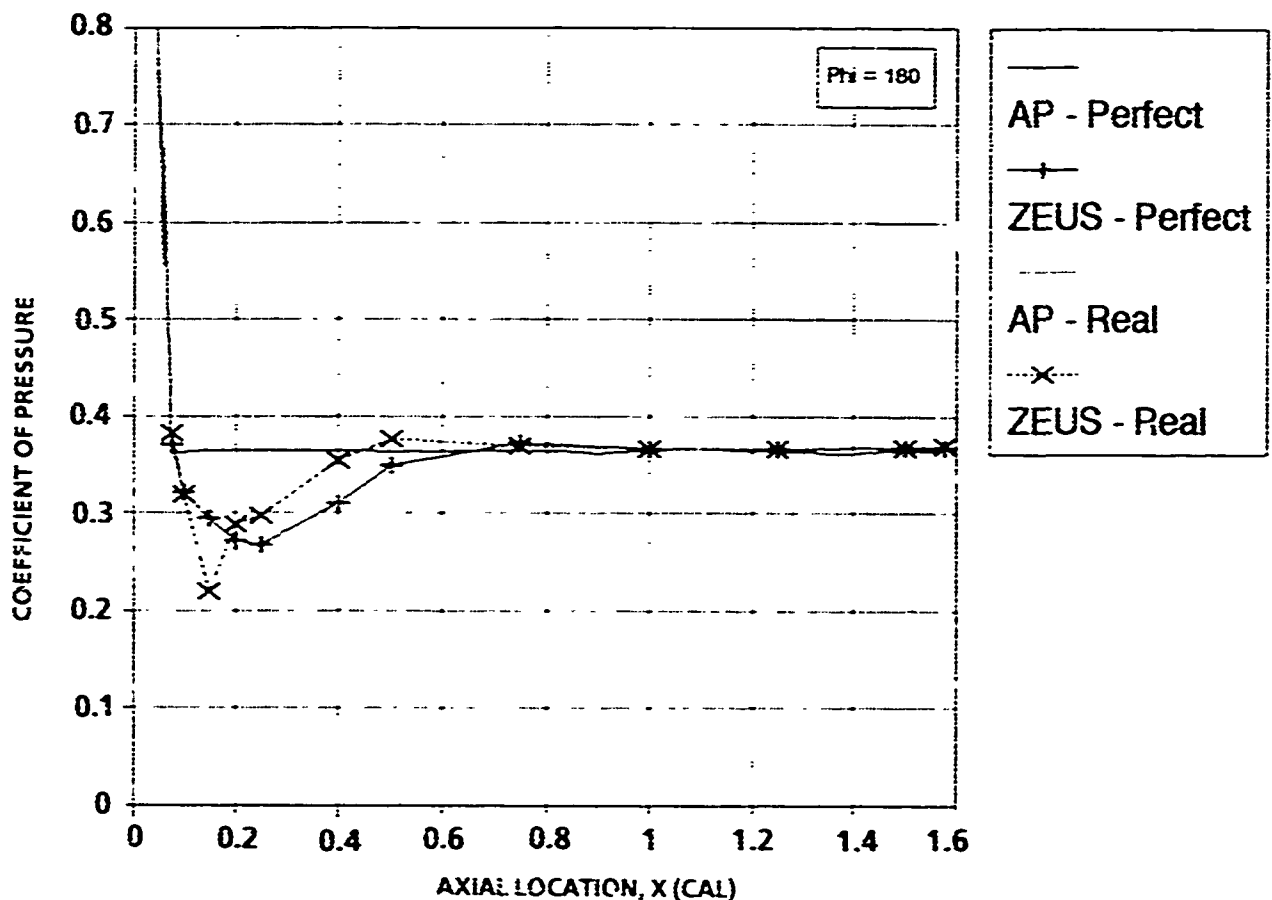


FIGURE 27(a) COMPARISON OF APPROXIMATE AND EXACT PRESSURE COEFFICIENTS IN THE WINDWARD PLANE OF A 20-PERCENT BLUNT CONE ($M_\infty = 15$, $\alpha = 10^\circ$)

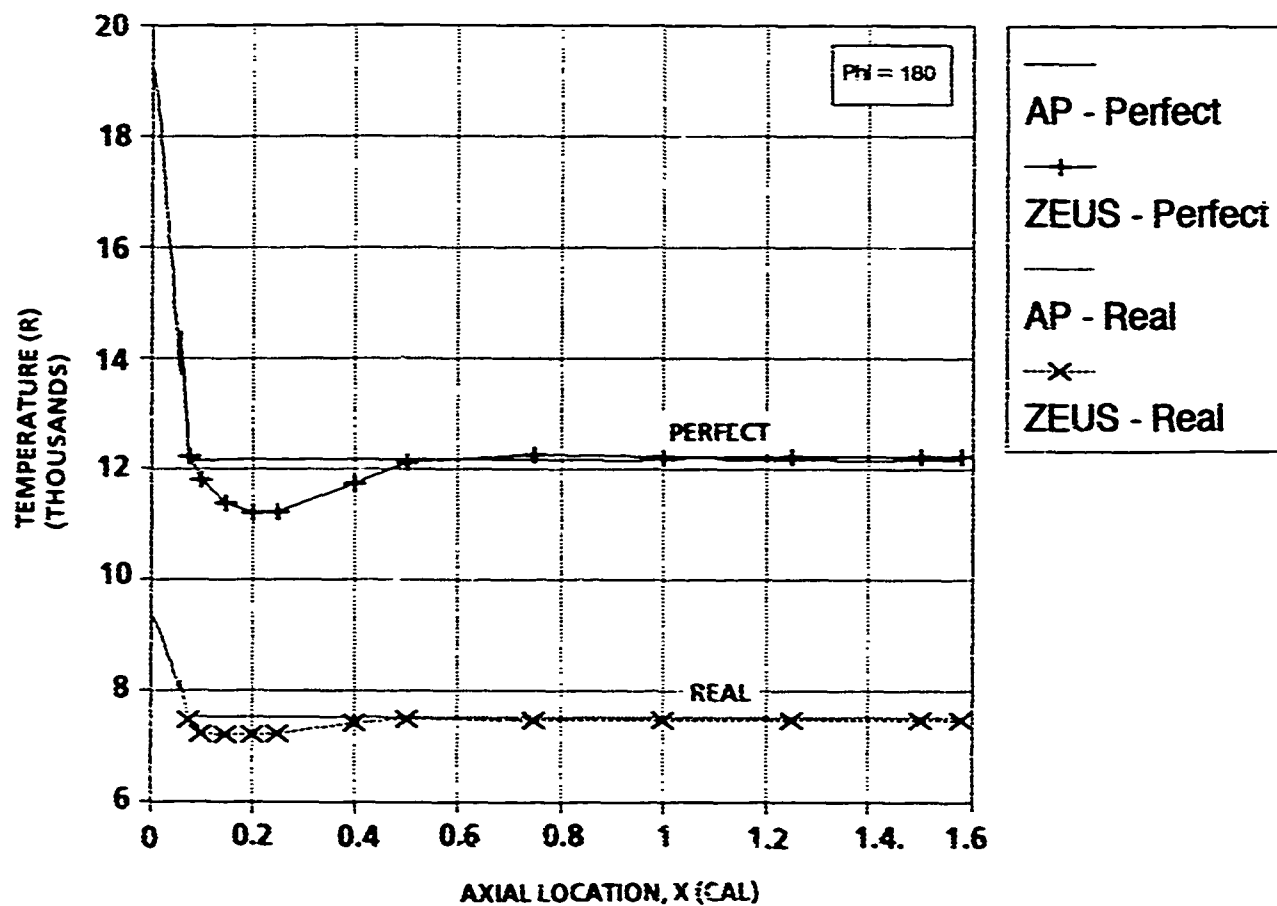


FIGURE 27(b). COMPARISON OF APPROXIMATE AND EXACT TEMPERATURE IN THE WINDWARD PLANE OF A 20-PERCENT BLUNT CONE ($M_\infty = 15$, $\alpha = 10^\circ$)

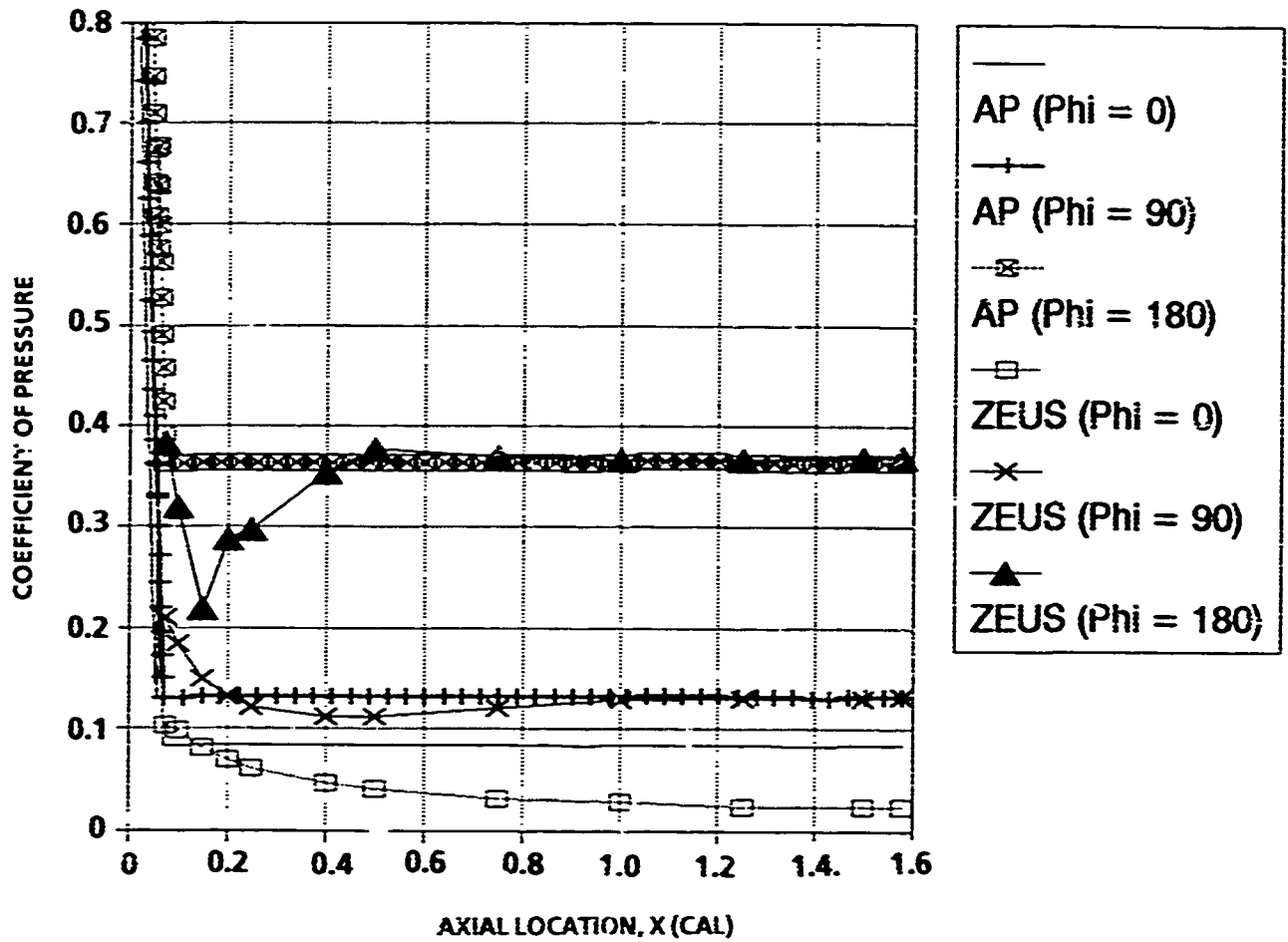


FIGURE 27(c). COMPARISON OF APPROXIMATE AND EXACT PRESSURE COEFFICIENTS ON A 20-PERCENT BLUNT CONE ($M_\infty = 15$, $\alpha = 10^\circ$, REAL GAS)

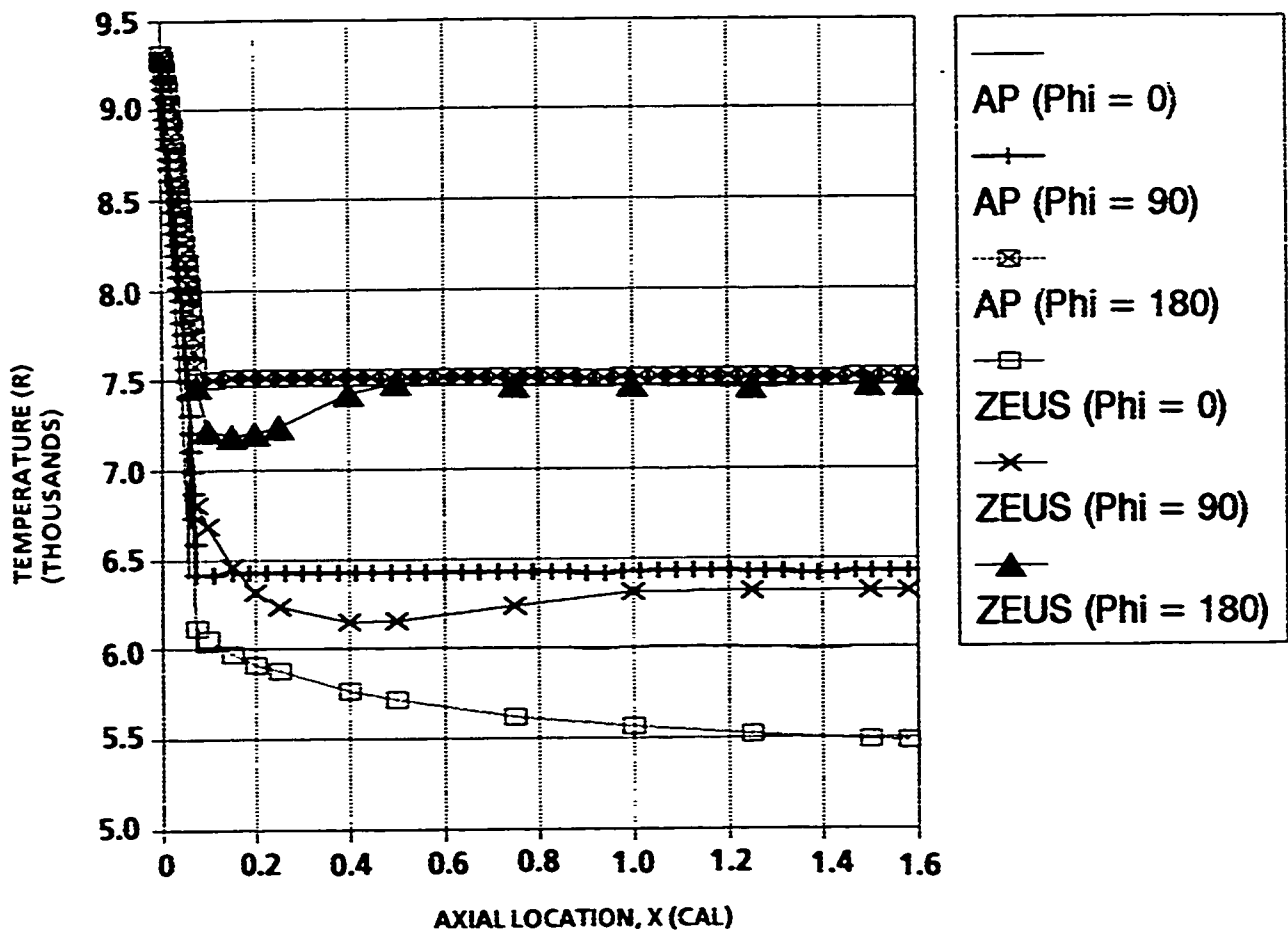


FIGURE 27(d). COMPARISON OF APPROXIMATE AND EXACT TEMPERATURES ON A 20-PERCENT BLUNT CONE ($M_\infty = 15$, $\alpha = 10^\circ$, REAL GAS)

Figures 27(c) and 27(d) present the real gas pressure coefficient and temperature comparisons in the $\phi = 180^\circ$, 90° , and 0° planes. The worst case comparisons on temperature are in the leeward plane where the deviation is as high as 10 percent. However, as already noted, the windward plane maximum temperature deviation is only 2 percent or less. Figures 28(a) and 28(b) present the blunt cone real and perfect gas pressures and temperatures, respectively, as a function of Mach number for $\alpha = 0$ and 15° using the approximate method. The results presented are those near the base of the cone, $x = 1.5$, and in the windward plane. Several points are worthy of note. First of all, Figure 28(a) reiterates the negligible effect of real gas conditions on pressure at all Mach numbers. It also illustrates the strong pressure increase as a function of angle of attack and Mach number. Figure 28(b) illustrates how the real gas affects temperature as Mach number increases. It is also interesting to note that while temperature differs by up to several thousands of degrees due to angle-of-attack effects for a perfect gas, the real gas difference is a maximum of 1500° at $M_\infty = 20$ and $\alpha = 15^\circ$ and $\alpha = 0^\circ$. Finally, as already discussed, the present approximate code gives very good agreement for inviscid surface properties with the exact Euler solver, ZEUS.

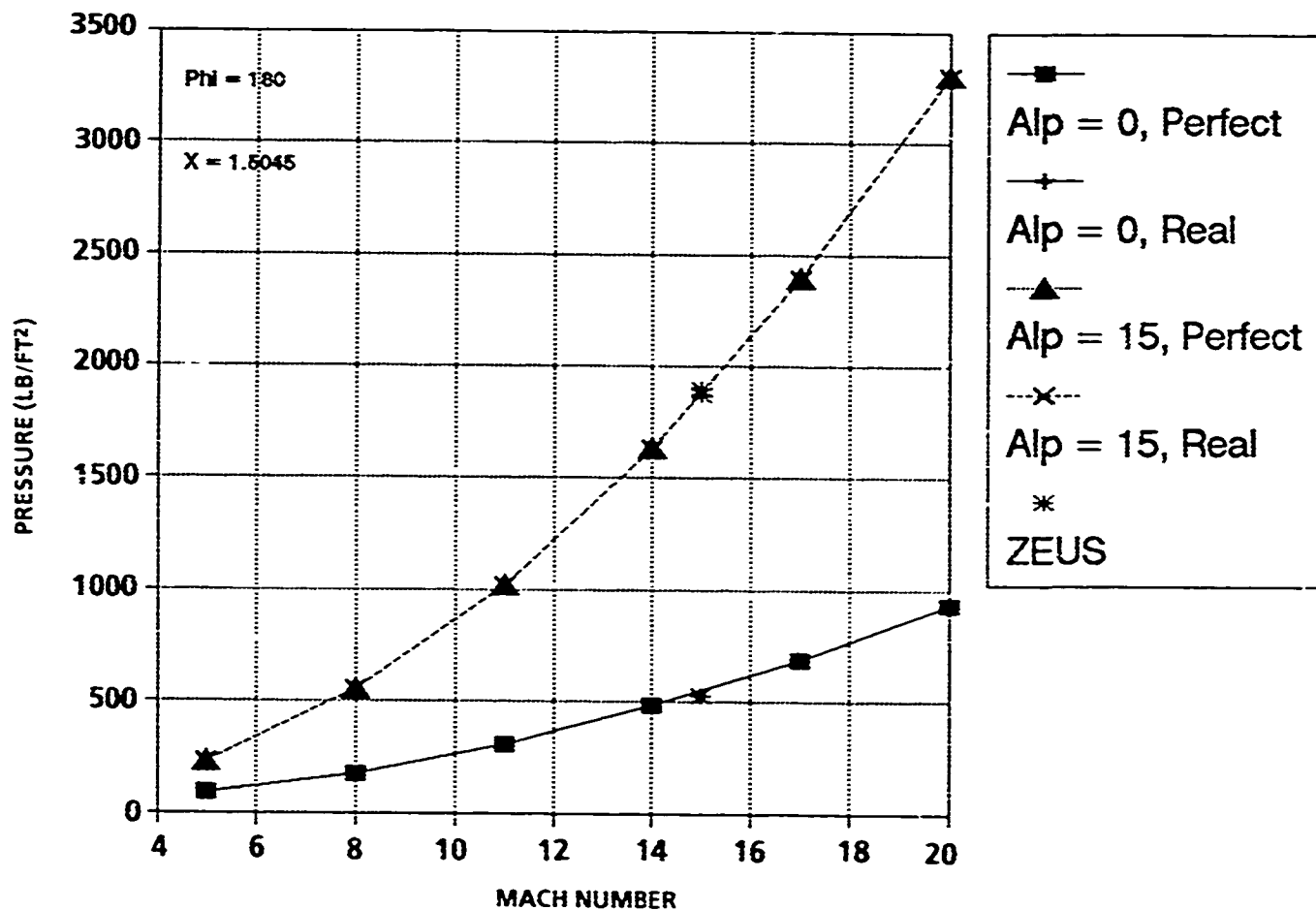


FIGURE 28(a). PRESSURES PREDICTED BY APPROXIMATE METHOD ON A 20-PERCENT BLUNT CONE AS A FUNCTION OF MACH NUMBER ($\Phi = 180^\circ$, $x = 1.5$, $h = 100$ k ft)

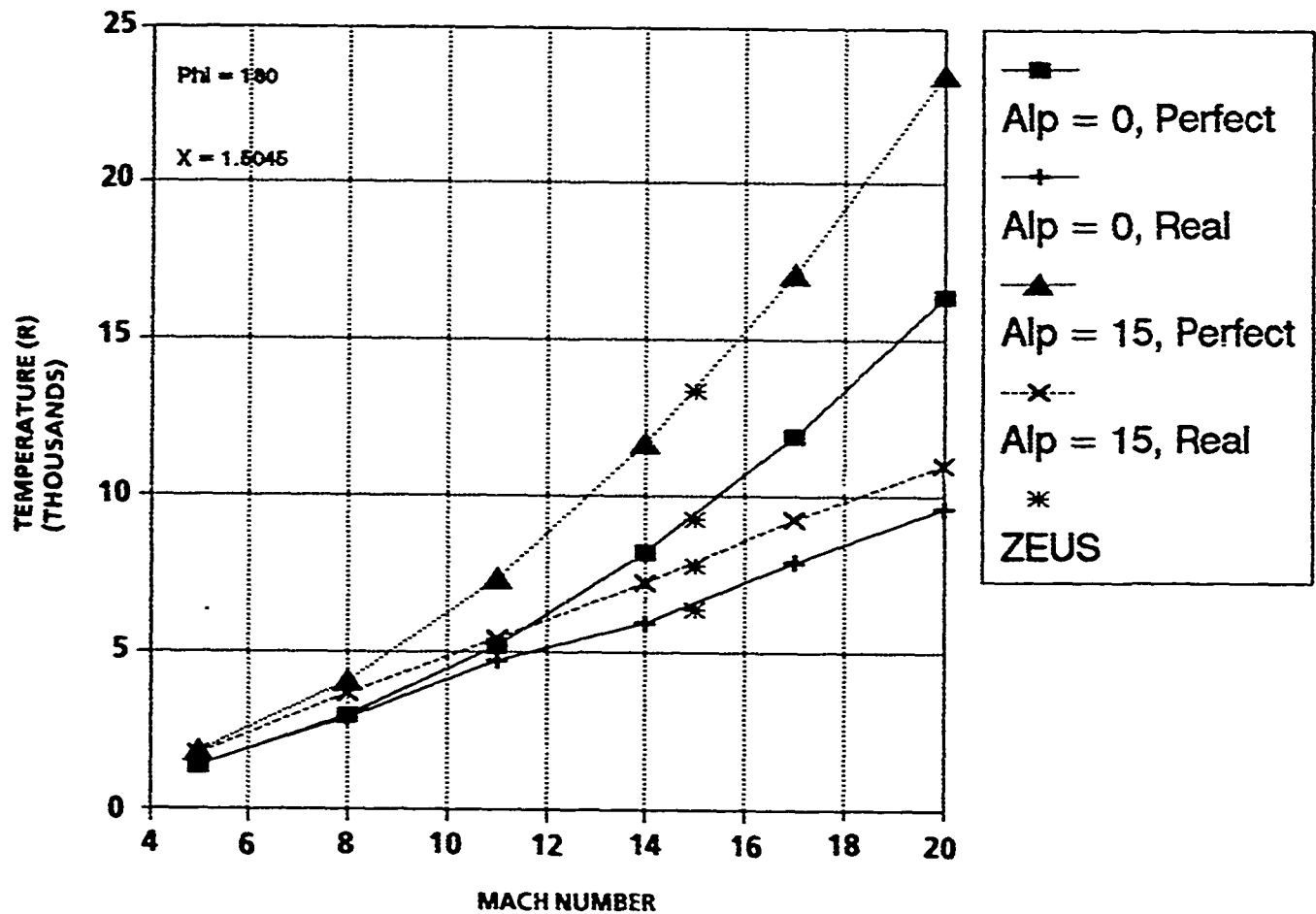


FIGURE 28(b). TEMPERATURES PREDICTED BY APPROXIMATE METHOD
ON A 20-PERCENT BLUNT CONE AS A FUNCTION OF MACH NUMBER
($\Phi = 180^\circ$, $x = 1.5$, $h = 100k$ ft)

The third case considered is a cone-cylinder-flare (see Figure 24). Results of the pressures and temperatures on this configuration are shown in Figures 29. Figures 29(a) and 29(b) present the pressure and temperature in the windward plane respectively as a function of distance along the body surface. Note the present theory shows no overexpansion behind the shoulder due to the fact that MNT is used to estimate pressures around the surface. Also note in Figure 29(b) that for the conical surfaces, real gas temperatures are lower by only about 10 to 15 percent, whereas on blunt nose configurations at the same Mach number, temperatures can be as much as a factor of 2 lower for real compared to perfect gases. Figure 29(c) presents the pressures around the cone-cylinder-flare configuration at three x stations corresponding to a point on the cone, cylinder, and flare. Figures 29(d), (e), and (f) present the temperature comparisons for the same x stations of Figure 29(c). Note that in Figures 29(e) and 29(f), values of temperature are constant in the leeward plane area due to the Newtonian assumption that $c_p = 0$ in shadowed regions.

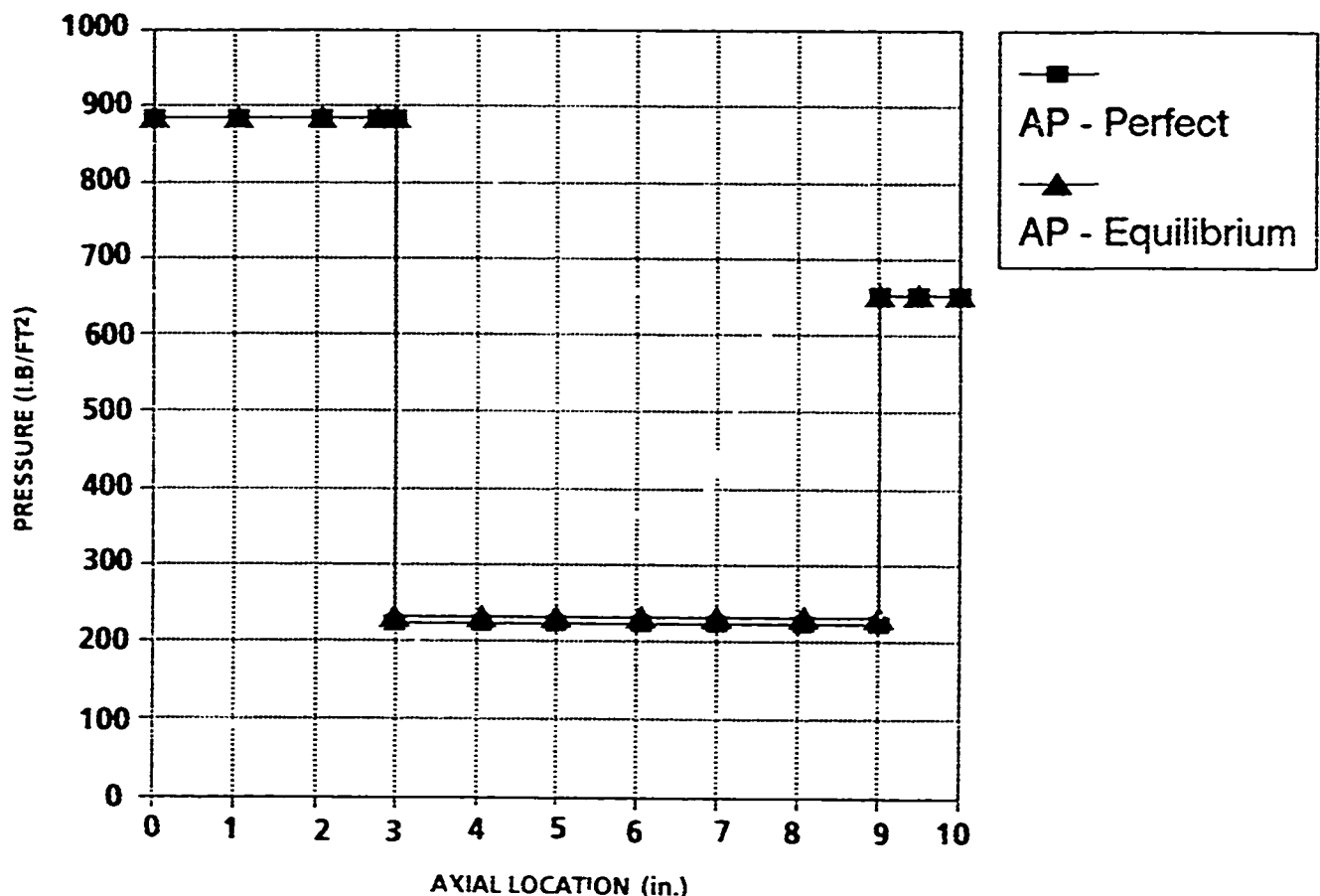


FIGURE 29(a). PRESSURE DISTRIBUTION ON A 10° CONE-CYLINDER-FLARE
($M_\infty = 15$, $\alpha = 10^\circ$, $\phi = 180^\circ$)

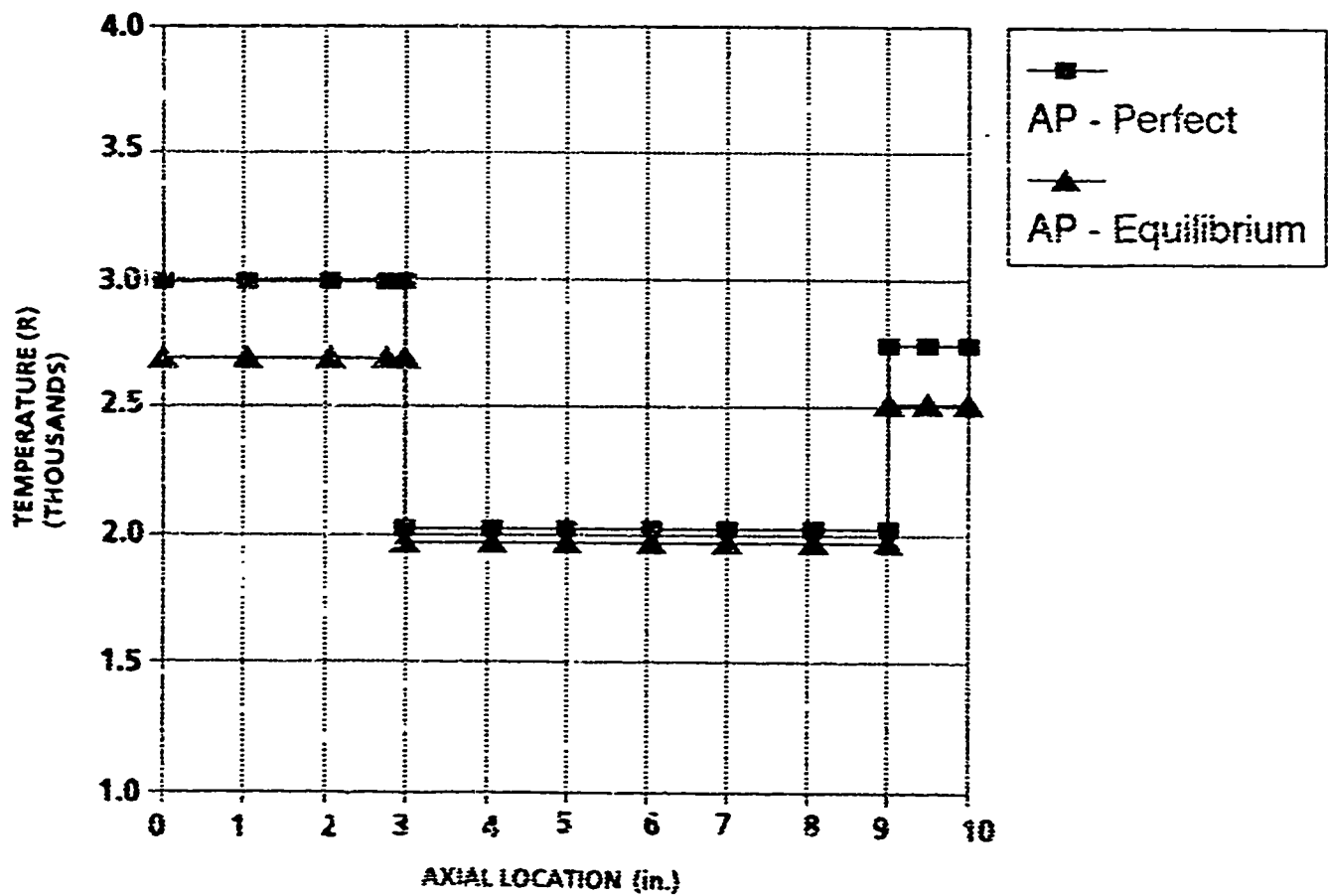


FIGURE 29(b). TEMPERATURE DISTRIBUTION ON A 10° CONE-CYLINDER-FLARE
 $(M_\infty = 15, \alpha = 10^\circ, \phi = 180^\circ)$

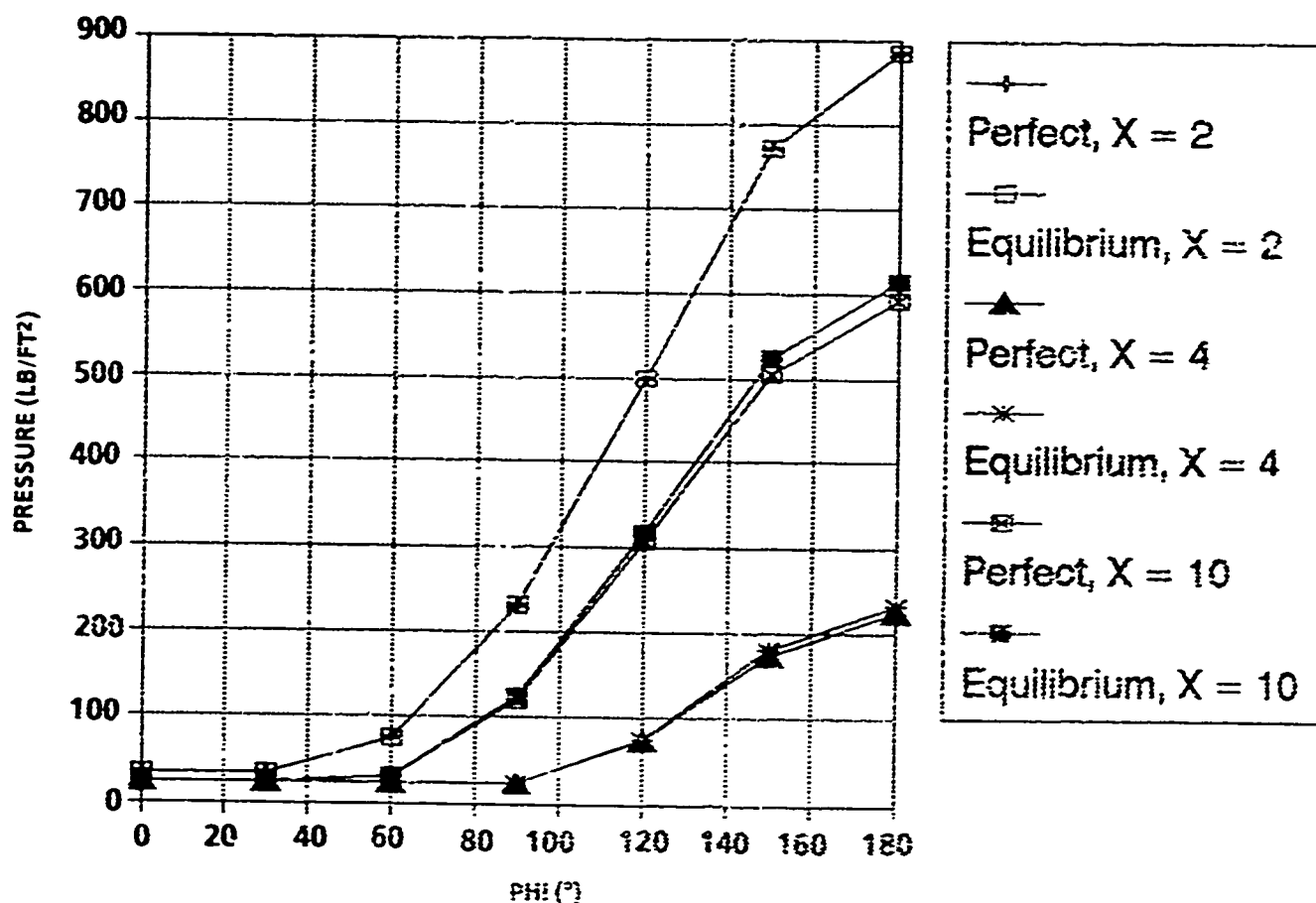


FIGURE 29(c). PRESSURE DISTRIBUTION ON A 10° CONE-CYLINDER-FLARE
($M_\infty = 15$, $\alpha = 10^\circ$, $x = 2, 4, 10$)

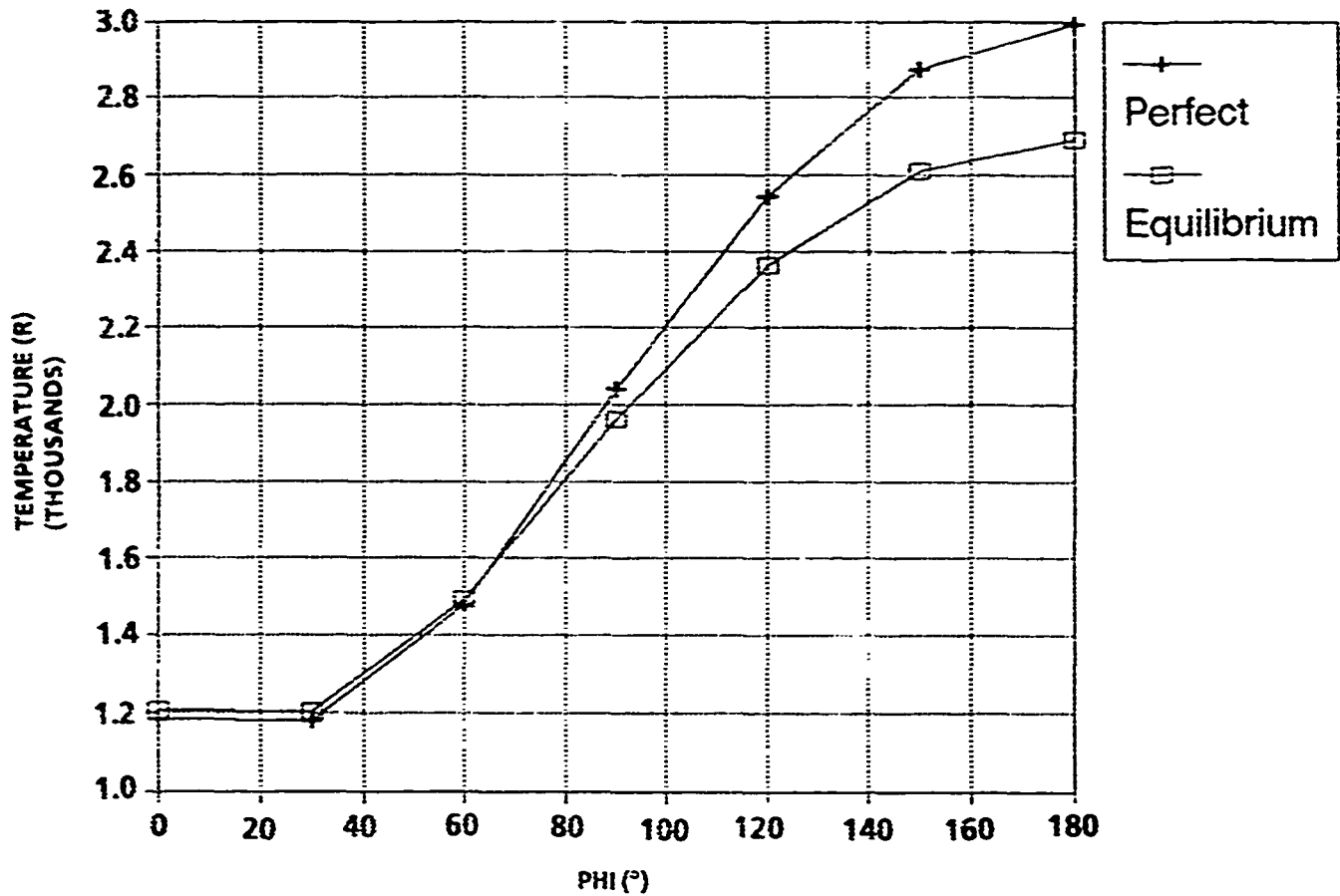


FIGURE 29(d). TEMPERATURE DISTRIBUTION AROUND THE CONE
OF A 10° CONE-CYLINDER-FLARE
($M_\infty = 15$, $\alpha = 10^\circ$, $x = 2$)

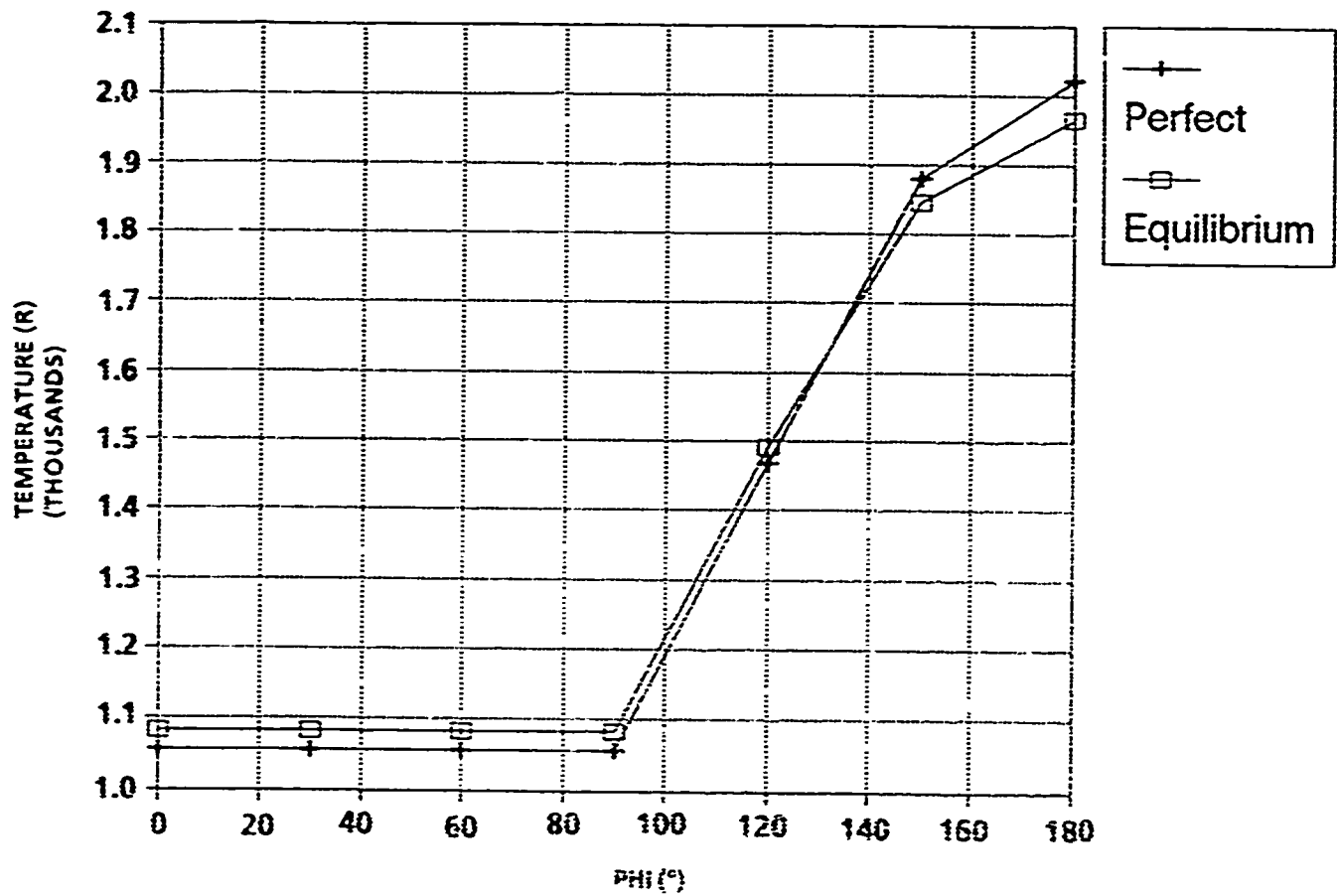


FIGURE 29(e). TEMPERATURE DISTRIBUTION AROUND THE CYLINDER
OF A 10° CONE-CYLINDER-FLARE
($M_\infty = 15$, $\alpha = 10^\circ$, $x = 4$)

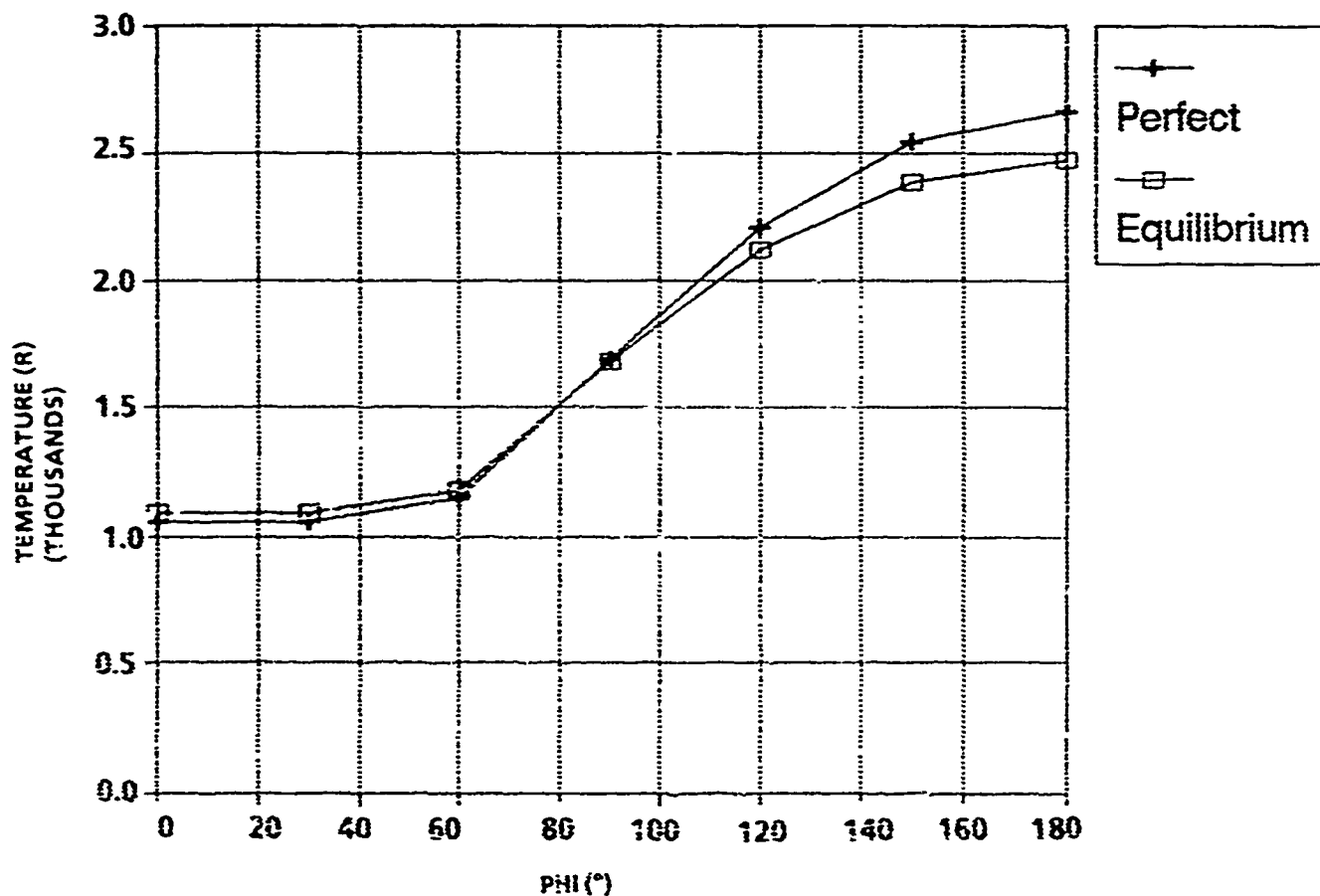


FIGURE 29(C). TEMPERATURE DISTRIBUTION AROUND THE FLARE
OF A 16° CONE-CYLINDER-FLARE
($M_\infty = 10$, $\alpha = 10^\circ$, $x = 10$)

The final case considered is the 20-percent blunt Von Karman ogive-cylinder-fin configuration shown in Figure 24. The angle-of-attack 0° pressure coefficient and temperature for real and perfect gases are shown in Figure 30 for $M_\infty = 15$. Note again the excellent agreement up to the location of the tail fins. This figure was primarily shown to indicate that while the present approximate engineering code is quite applicable for preliminary design, it does not have the physics included for detailed interaction effects. These effects could include bow shock waves intersecting fins, or fin shock waves intersecting the body. These interaction effects can cause local "hot" spots and more detailed analysis codes such as ZEUS or Navier Stokes solvers are required. The fin interaction effects are shown by the ZEUS results at $x = 9$ calibers to the end of the body.

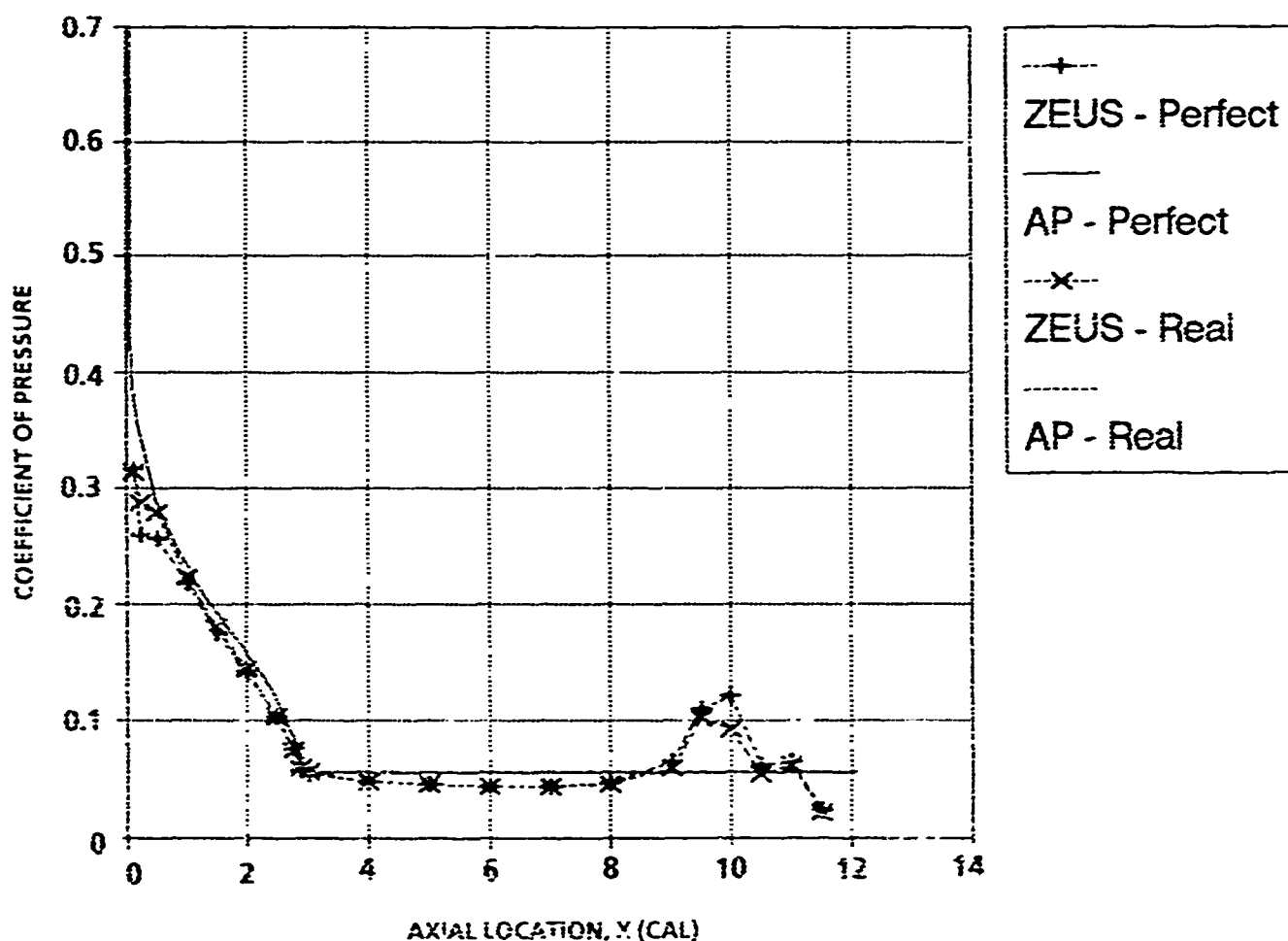


FIGURE 30(a). COMPARISON OF PRESSURE COEFFICIENTS ON A 20-PERCENT BLUNT VON KARMAN OGIVE-CYLINDER-FIN CONFIGURATION ($M_\infty = 15$, $\alpha = 0^\circ$)

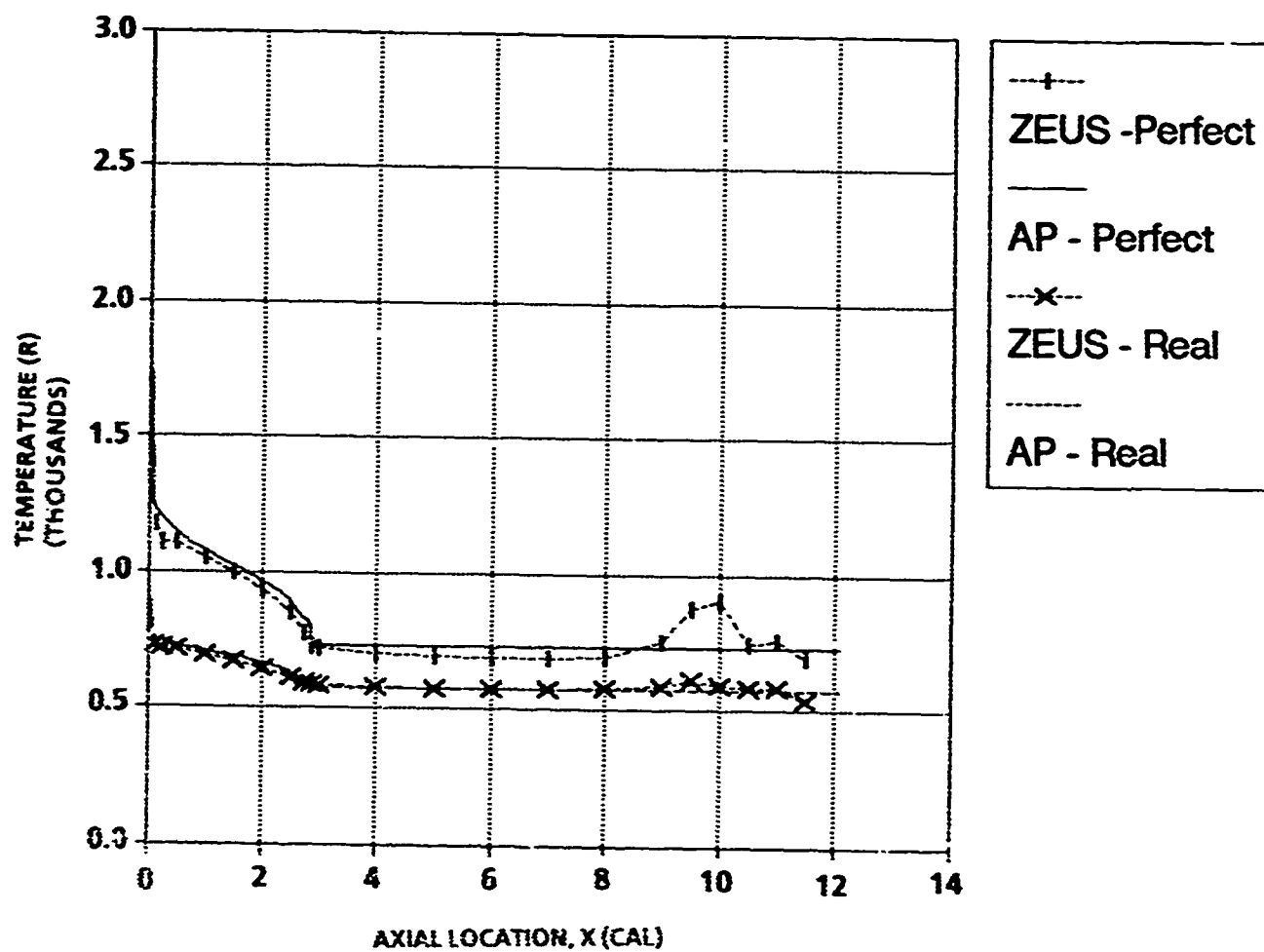


FIGURE 30(b). COMPARISON OF TEMPERATURE PREDICTIONS ON A 20-PERCENT BLUNT VON KARMAN OGIVE-CYLINDER-FIN CONFIGURATION ($M_\infty = 15$, $\alpha = 0^\circ$)

The emphasis to this point has been on accurate values of inviscid surface temperature to allow accurate heat transfer analysis. In getting accurate values of heat transfer, accurate values of pressure prediction were required. These accurate values of pressure prediction also give good force and moment predictions. The final Figure 31 illustrates force and moment predictions as a function of Mach number and angle of attack compared to the ZEUS code. Note that the axial force only includes wave drag since ZEUS at present is an inviscid code. Accuracies on wave drag and normal force are within 10 percent, and center of pressure near angle of attack zero within 8 percent of the body length compared to the full Euler code. About half of the error in wave drag is due to the high fin alone predictions using the present strip theory approach, Figure 31(a). Note that the theory does predict some slight changes in forces and moments due to real gas effects. However, except for very specialized problems, it is believed that these effects can be neglected, particularly in an engineering code such as the aeroprediction. However, as already noted many times, heat transfer analysis definitely needs to consider the real gas effects when flying at any appreciable time above $M_\infty = 6$ to 8.

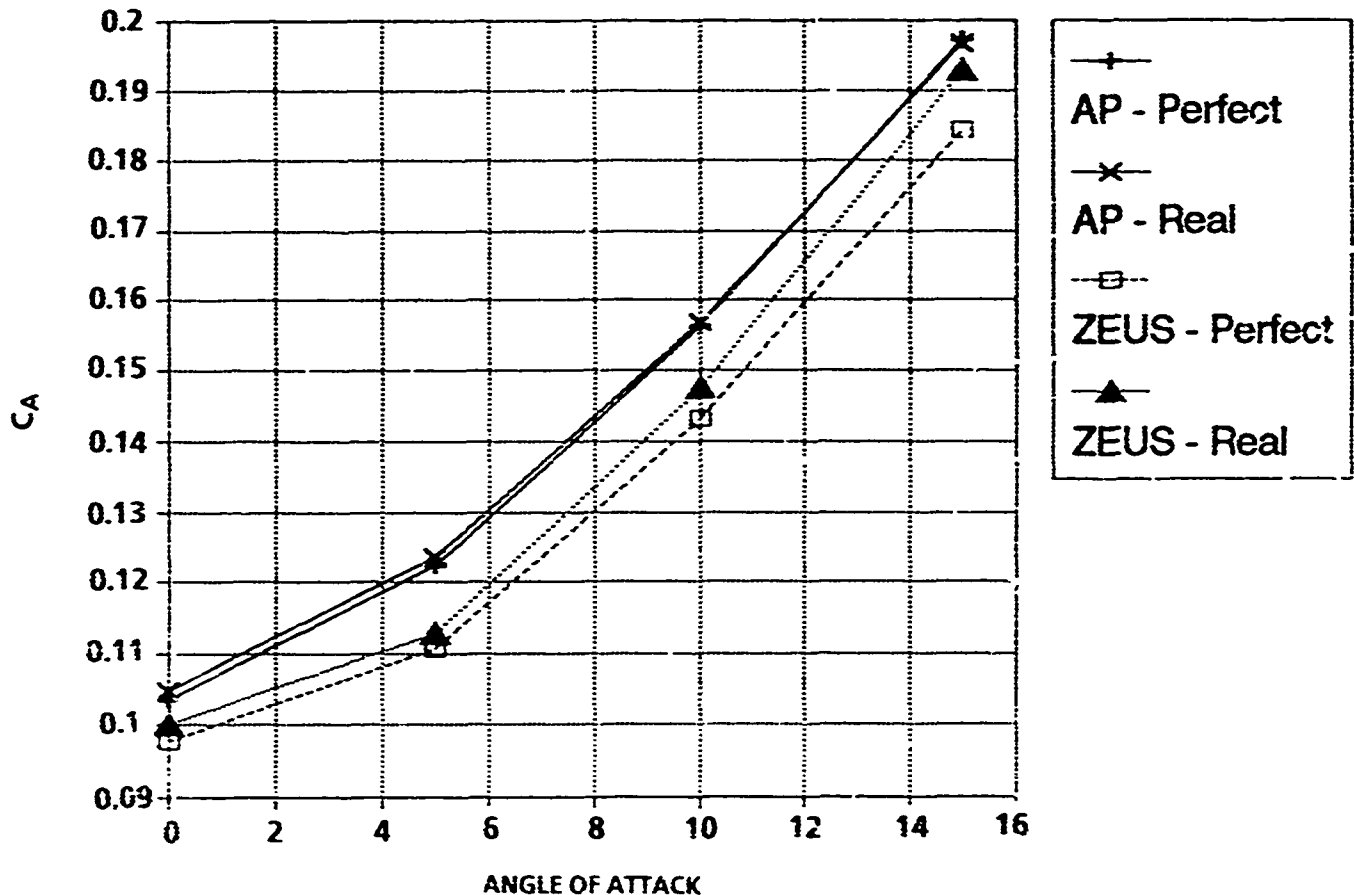


FIGURE 31(a). AXIAL WAVE DRAG OF A 20-PERCENT BLUNT VON KARMAN OGIVE-CYLINDER-FIN CONFIGURATION ($M_\infty = 15$)

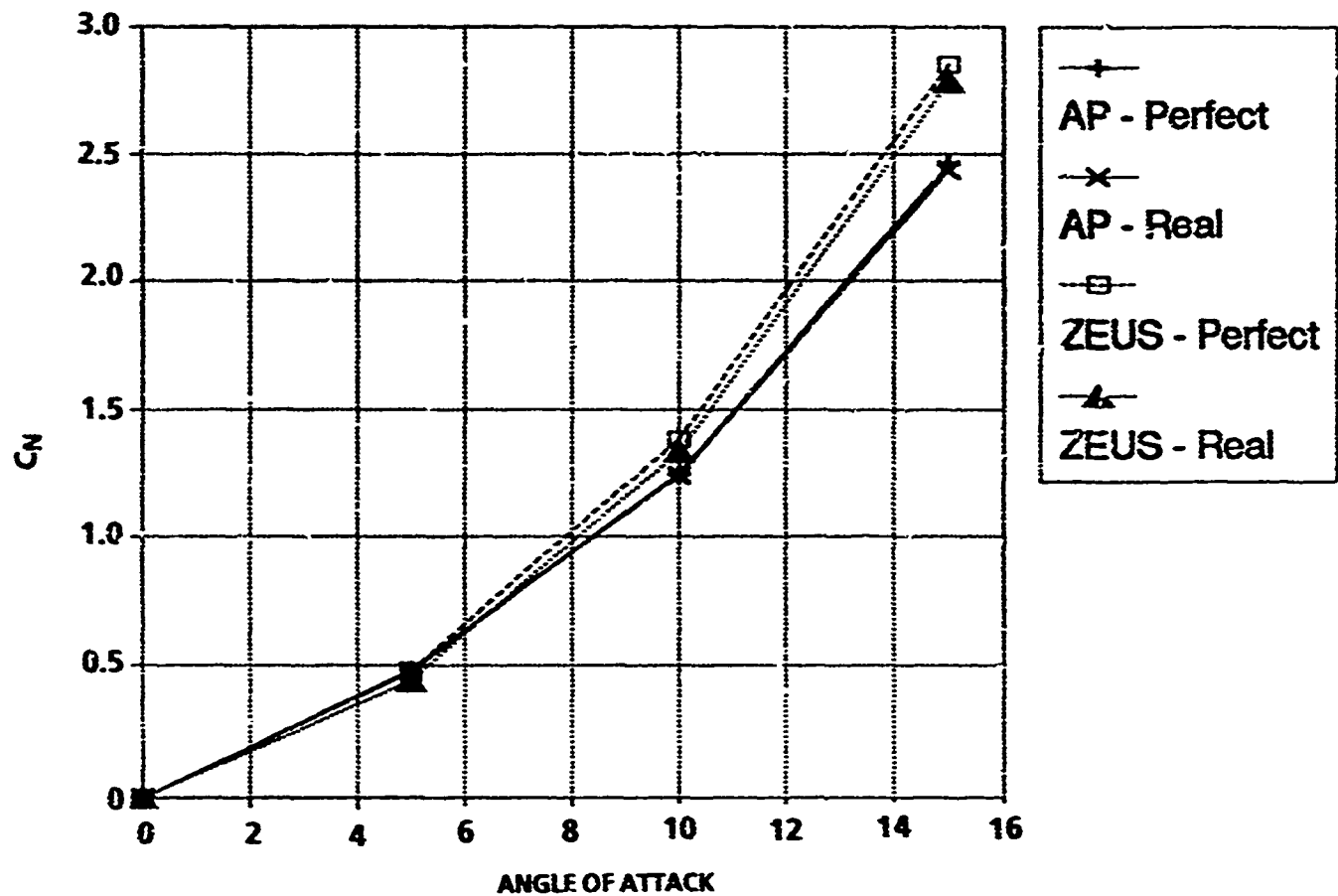


FIGURE 31(b). NORMAL FORCE COEFFICIENT OF A 20-PERCENT BLUNT VON KARMAN OGIVE-CYLINDER-FIN CONFIGURATION ($M_\infty = 15$)

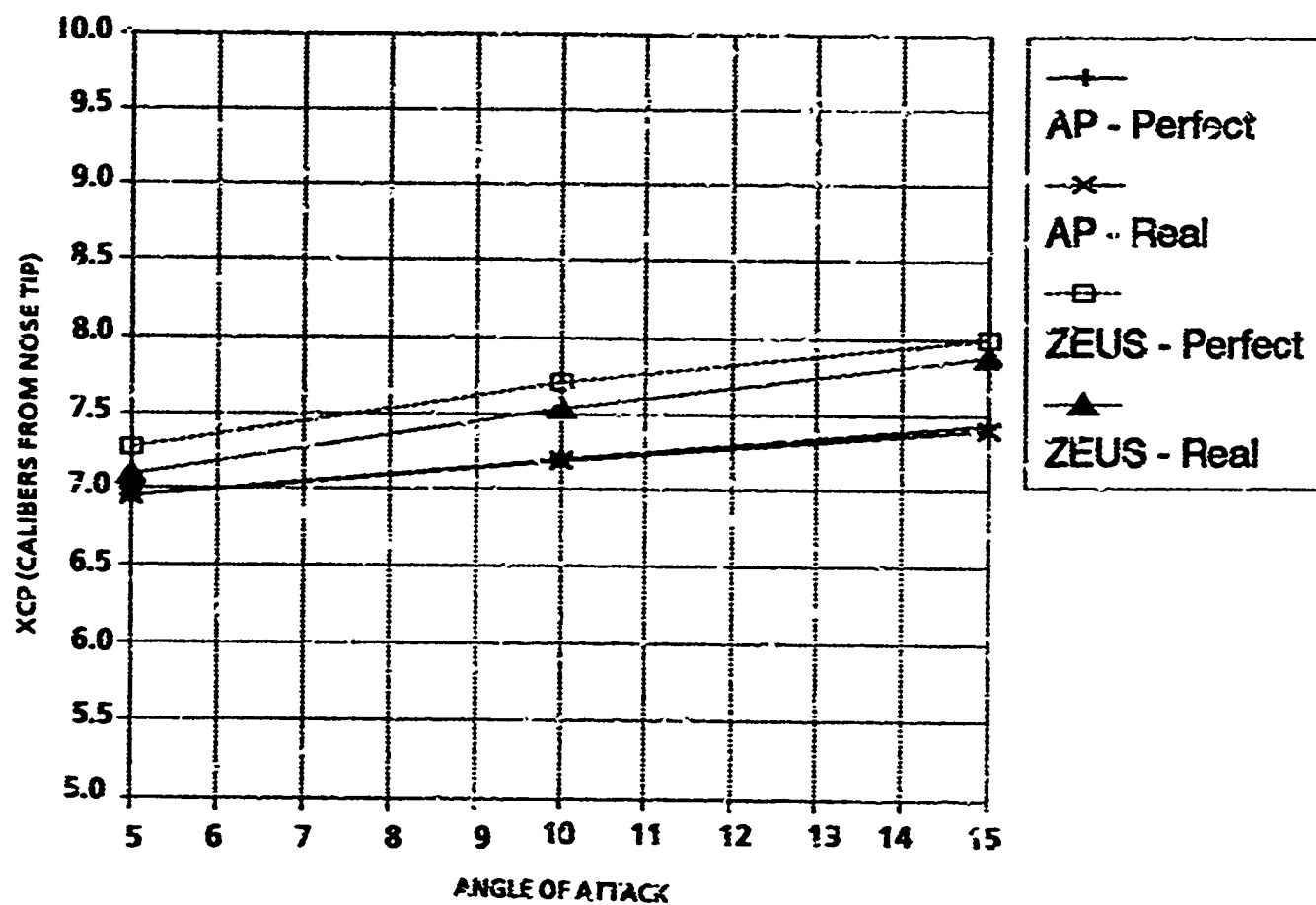


FIGURE 31(c). CENTER OF PRESSURE OF A 20-PERCENT BLUNT VON KARMAN OGIVE-CYLINDER-FIN CONFIGURATION ($M_\infty = 15$)

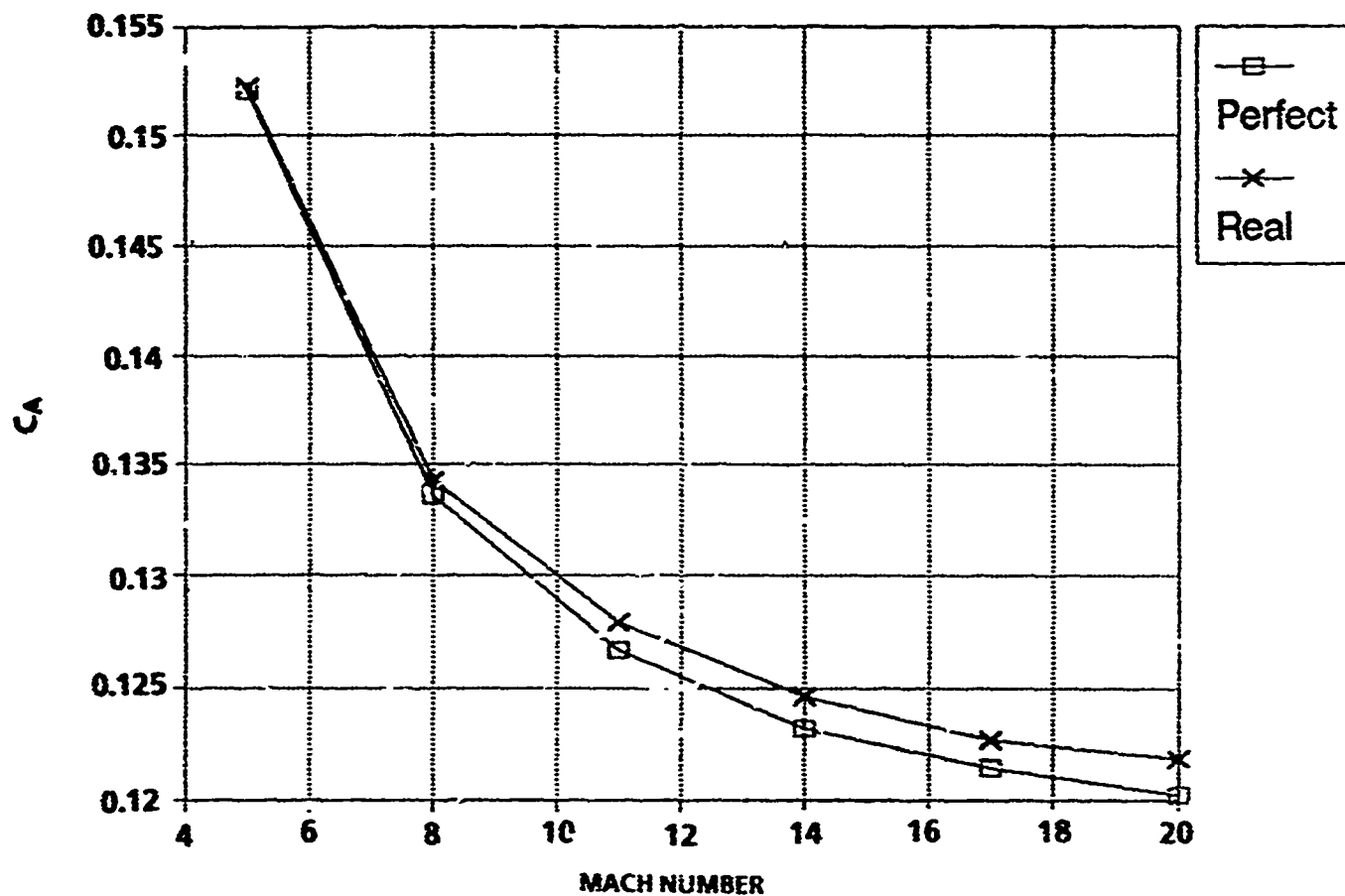


FIGURE 31(d). AXIAL WAVE DRAG COEFFICIENT FOR A 20-PERCENT BLUNT VON KARMAN OGIVE-CYLINDER-FIN CONFIGURATION ($\alpha = 5^\circ$)

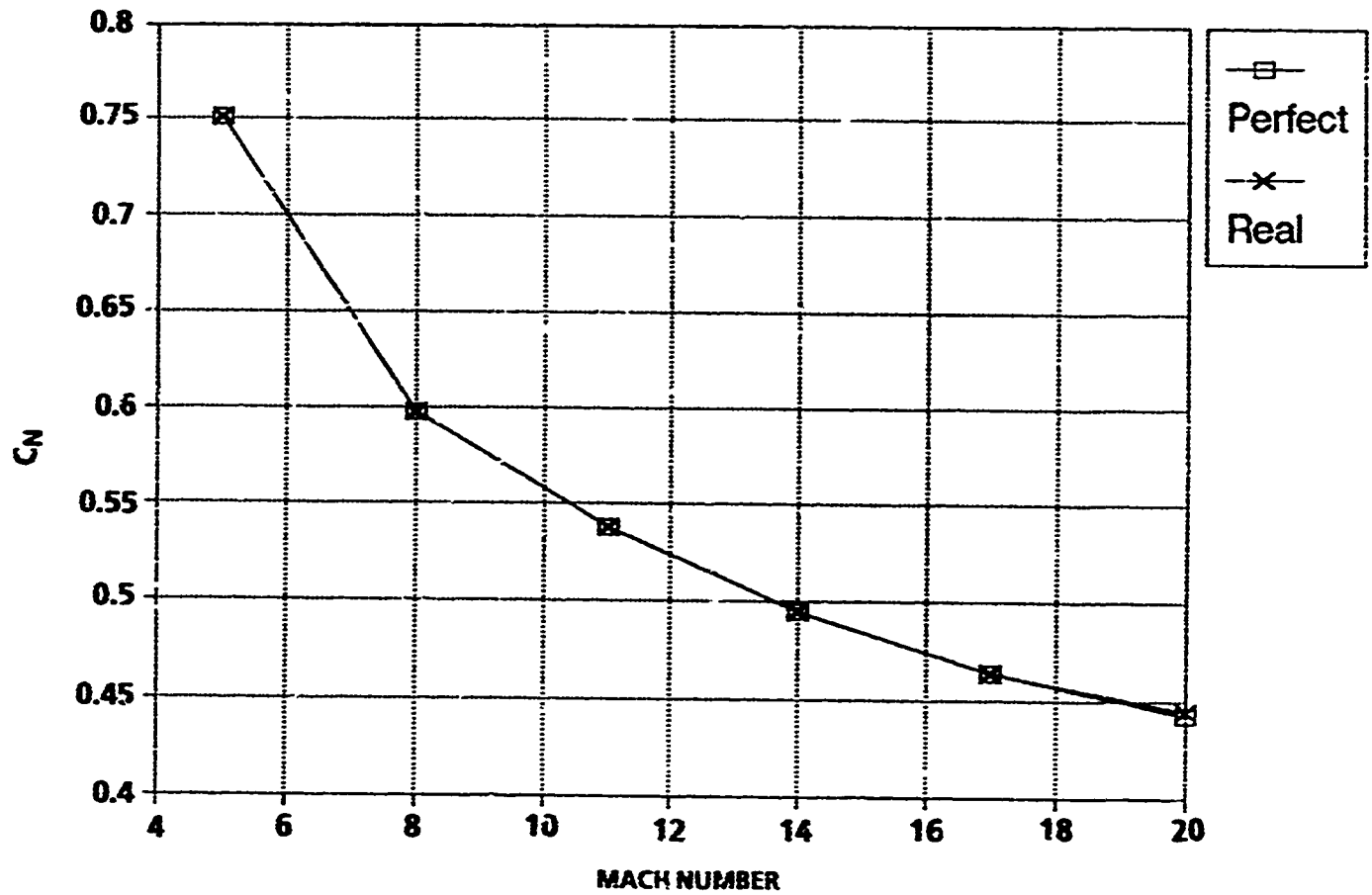


FIGURE 31(e). NORMAL FORCE COEFFICIENT FOR A 20-PERCENT BLUNT VON KARMAN OGIVE-CYLINDER-FIN CONFIGURATION ($\alpha = 5^\circ$)

4. SUMMARY

New methods have been developed to compute inviscid surface pressures and temperatures for both perfect and equilibrium chemically reacting flows on both pointed and blunt bodies of revolution. These new methods include an improved Shock-expansion Theory, an improved MNT, and an improved method for angle-of-attack effects. Comparison of these approximate engineering techniques to exact inviscid computations using a full Euler code showed the following:

1. Agreement on the critical windward plane inviscid temperatures generally of 4 percent or better.
2. Agreement of inviscid surface temperatures of 10 percent or better.
3. Agreement of axial wave drag and normal force of 10 percent, and center of pressure 8 percent of body length. For the body alone, wave drag estimates are generally within 5 percent of exact Euler computations.

A new real gas formulation for pressure gradient behind a corner was derived. However, in implementing this into the SOSET it was found to be of little value. This is because at high Mach numbers the exponential decay term used in the SOSET becomes positive requiring SOSET to revert back to either GSET or TCT. It was shown that neither of these theories was best for all cases and, as a result, a user input to allow a choice of which method to use was considered the best alternative for use of the traditional SOSET.

With the new technology developed, the NAVSWC aeroprediction code can now be used to give engineering estimates of inviscid surface temperature for any Mach number of interest. These approximate temperatures can then be used as inputs for more detailed heat transfer analysis.

5. REFERENCES

1. Moore, F. G., *Computational Aerodynamics at NAVSWC: Past, Present, and Future*, NAVSWC TR 90-569, October 1990.
2. Devan, L., *Aerodynamics of Tactical Weapons to Mach Number 8 and Angle of Attack 180°: Part I, Theory and Application*, NSWC TR 80-346, October 1980.
3. Devan, L., and Mason, L., *Aerodynamics of Tactical Weapons to Mach Number 8 and Angle of Attack 180°: Part II, Computer Program and Users Guide*, NSWC TR 81-358, September 1981.
4. Devan, L., Mason, L., and Moore, F. G., *Aerodynamics of Tactical Weapons to Mach Number 8 and Angle of Attack 180°*, AIAA Paper No. 82-0250, 20th Aerospace Sciences Meeting, Orlando, FL.
5. Vincenti, W. G., and Kruger, C. H., *Introduction to Physical Gas Dynamics*, John Wiley and Sons, Inc., New York, 1965.
6. Jones, J. B., and Hawkins, G. A., *Engineering Thermodynamics*, John Wiley and Sons, Inc., New York, 1960.
7. Liepmann, H. W., and Roshko, A., *Elements of Gasdynamics*, John Wiley and Sons, Inc., New York, 1957.
8. Anderson, J. D., *Modern Compressible Flow*, McGraw-Hill Book Company, 1982.
9. Truitt, R. W., *Hypersonic Aerodynamics*, The Ronald Press Company, New York, 1959.
10. Hayes, W. D., and Probstein, R. F., *Hypersonic Flow Theory*, Academic Press, New York, 1966.
11. Hilsenrath, J., Klein, M., and Wolley, H. W., *Tables of Thermodynamic Properties of Air Including Dissociation and Ionization from 1500°K to 15000°K*, AEDC TR-59-20.
12. Lees, Lester, *Hypersonic Flow*, Inst. Aero. Science, Preprint No. 554, 1955.
13. Ames Research Staff, *Equations, Tables, and Charts for Compressible Flow*, NACA TR 1135, 1953.
14. Eggers, A. J., Syvertson, C. A., and Kraus, S., *A Study of Inviscid Flow About Airfoils at High Supersonic Speeds*, NACA Report 1123, 1953.

15. Eggers, A. J., and Savin, R. C., *A Unified Two-Dimensional Approach to the Calculation of Three-Dimensional Hypersonic Flows, with Application to Bodies of Revolution*, NACA Report 1249, 1955.
16. Eggers, A. J., and Savin, R. C., *Approximate Methods for Calculating the Flow About Nonlifting Bodies of Revolution at High Supersonic Airspeeds*, NACA TN 2579, 1951.
17. Savin, R. C., *Application of the Generalized Shock Expansion Method to Inclined Bodies of Revolution Traveling at High Supersonic Airspeeds*, NACA TN 3349, 1955.
18. Taylor, G. I., and MacCall, J. W., *The Air Pressure on a Cone Moving at High Speed*, Proc. Royal Society (London) Ser. A., Vol. 139, 1933, pp. 278-311.
19. Syvertson, C. A., and Dennis, D. H., *A Second-Order Shock Expansion Method Applicable to Bodies of Revolution Near Zero Lift*, NACA TR 1323, 1957.
20. Jackson, C. M., Sawyer, W. C., and Smith, R. S., *A Method for Determining Surface Pressures on Blunt Bodies of Revolution at Small Angles of Attack in Supersonic Flow*, NASA TN P-4865, 1968.
21. DeJarnette, F. R., and Jones, K. M., *Development of a Computer Program to Calculate Aerodynamic Characteristics of Bodies and Wing-Body Combinations*, NSWC/DL TR-3829, April 1978.
22. DeJarnette, F. R., and Ford, C. P., *A New Method for Calculating Surface Pressures on Bodies at an Angle of Attack in Supersonic Flow*, Proceedings of the 11th Navy Symposium on Aeroballistics, Vol. II, August 22-24, 1978, pp. 199-231.
23. DeJarnette, F. R., Ford, C. P., and Young, D. E., *A New Method for Calculating Surface Pressures on Bodies at an Angle of Attack in Supersonic Flow*, AIAA Paper No. 79-1552, AIAA 12th Fluid and Plasma Dynamics Conference, Williamsburg, VA, July 1974.
24. Wittliff, Charles E., and Curtis, James T., *Normal Shock Wave Parameters in Equilibrium Air*, Cornell Aero Lab. Report CAL-III, November 1961.
25. Marrone, P. V., *Normal Shock Waves in Air: Equilibrium Composition and Flow Parameters for Velocities from 26,000 to 50,000 ft/sec*, CAL Report No. AG-1729-A-2, August 1962.
26. Heims, Steve, *Prandtl-Meyer Expansion of Chemically Reacting Gases in Local Chemical and Thermodynamic Equilibrium*, NACA TN 4230, March 1958.

27. Moeckel, W. E., *Oblique-shock Relations at Hypersonic Speeds for Air in Chemical Equilibrium*, NACA TN 3895, January 1957.
28. Wardlaw, A. B., Baltakis, F. P., Solomon, J. M., and Hackerman, L. B., *An Inviscid Computational Method for Tactical Missile Configurations*, NSWC TR 81-457, December 1981.
29. Wardlaw, A. B., Friolo, F. J., Solomon, J. M., and Baltakis, F. P., *Inviscid Multiple Zone Calculations for Supersonic Tactical Missiles*, AIAA Paper 84-2099, 1984.
30. Moore, F. G., *Body Alone Aerodynamics of Guided and Unguided Projectiles at Subsonic, Transonic, and Supersonic Mach Numbers*, NWL TR-3796, November 1972.
31. Moore, F. G., and McKerly, B., *Aerodynamics of Guided and Unguided Weapons: Part I -- Theory and Application*, NWL TR-3018, December 1973.
32. Moore, F. G., and Swanson, R., *Aerodynamics of Tactical Weapons to Mach Number 3 and Angle of Attack 15 Degrees: Part I -- Theory and Application*, NSWC TR-3584, February 1977.
33. Anderson, J. A., *Hypersonic and High Temperature Gas Dynamics*, McGraw-Hill Series in Aeronautical and Aerospace Engineering, 1989.
34. Tannehill, J. C., and Muge, P. H., *Improved Curve Fits for the Thermodynamic Properties of Equilibrium Air Suitable for Numerical Computation Using Time-Dependent or Shock-Capturing Methods*, NASA CR-2470, 1974.
35. Srinivasan, S., Tannehill, J., and Weilmuenster, K., *Simplified Curve Fits for the Thermodynamic Properties of Equilibrium Air*, Report ISU-ERI-AMES 86401, Eng. Research Institute, Iowa State University, Ames, IA, June 1986.
36. DeJarnette, F. R., Ford, C. P., Young, D. E., "Calculation of Pressure on Bodies at Low Angles of Attack in Supersonic Flow," *JSR Article No. 79-1552R*, Vol. 17, No. 6, November-December 1980.
37. Hudgins, Henry E., Jr., *Supersonic Flow About Right Circular Cones at Zero Yaw in Air at Chemical Equilibrium, Part I -- Correlation of Flow Properties*, TM 1493, Picatinny Arsenal, August 1965.
38. Jones, D. J., *Numerical Solutions of the Flow Field for Conical Bodies in a Supersonic Stream*, National Research Council of Canada Report LR-507, July 1968.

39. Van Driest, E. R., "Turbulent Boundary Layer in Compressible Fluids," *JAS*, Vol. 18, No. 3, pp. 145-160, 216.
40. Allen, J. H., and Perkins, E. W., *Characteristics of Flow Over Inclined Bodies of Revolution*, NACA RM A50L07, Moffett Field, CA, 1965.
41. Wardlaw, Andrew, and Baltakis, Frank, *ZEUSBL: Integral Boundary Layer Procedure for Tactical Missiles*, NAVSWC technical report in preparation.
42. Armistead, Michael, and McInville, R. M., *A User's Guide to the BLZEUS Aeroheating Analysis Code*, NAVSWC technical note in preparation.
43. Hender, D. R., *A Miniature Version of the JA70 Aerodynamic Heating Computer Program*, H 800 (MINIVER), McDonnell Douglas MDC G0462, (COSMIC PROGRAM 3 MFS-21951), June 1970.
44. Truit, R. W., *Fundamentals of Aerodynamic Heating*, The Ronald Press, New York, Copyright 1960.
45. Rubesin, M. W., and Johnson, A. H., "A Critical Review of Skin-Friction and Heat Transfer Solutions of the Laminar Boundary Layer of a Flat Plate," *Trans. of the ASME*, Vol. 71, No. 4, pp. 383-388, May 1949.
46. Eckert, E. R. G., "Engineering Relations for Heat Transfer and Friction in High Velocity Laminar and Turbulent Boundary-Layer Flow Over Surfaces with Constant Pressure and Temperature," *Trans. of the ASME*, Vol. 78, No. 6, p. 1273, August 1956.
47. Priolo, F. J., and Wardlaw, A. B., Jr., "High-temperature Effects for Missile-type Bodies Using the Euler Solver, ZEUS," AIAA Paper No. 91-3259, presented at 1991 AIAA Applied Aerodynamics Conference, Baltimore, Maryland, September 1991.
48. Morrison, A. M., Solomon, J. M., Ciment, M., and Ferguson, R. E., "Handbook of Inviscid Sphere-cone Flow Fields and Pressure Distributions: Volume I," NSWC/WOL/TR 75-45, December 1975.

6. SYMBOLS AND DEFINITIONS

a	speed of sound (ft/sec)
b	distance between body surface and streamline
C_1, C_2	left and right running characteristic coordinates
C_{f_w}	local skin friction coefficient
C_h	heat transfer coefficient
C_p	pressure coefficient
C_p, C_v	specific heats at constant pressure and volume
e	internal energy (ft ² /sec ²)
H	total enthalpy (ft ² /sec ²)
h	specific enthalpy (ft ² /sec ²) and altitude (ft)
h_{a_w}	adiabatic wall enthalpy
k	Kelvin temperature (deg)
M	Mach number
p	pressure (lb/ft ²)
Pr	Prandtl number
q	heat flux
q_w	heat flux at wall
R	gas constant [for air $R = 1716 \text{ (ft-lb) / (slug-°R) }$]
R_n	Reynolds number
r_c	recovery factor
S	entropy (ft-lb) / (slug-°R)
s, n, t	streamline coordinate system

T	temperature (degrees Kelvin or Rankine)
T_p	temperature of a perfect gas
T_R	temperature of a real gas
t	time
U_1, U_2	velocity (ft/sec)
V	total velocity
V_r, V_θ	velocity along and normal to a conical ray
V_{max}	maximum velocity
x, r, ϕ	cylindrical coordinate system with $\phi = 0 =$ leeward plane
x, y, z	rectangular coordinate system
Z	compressibility factor ($= 1$ for a perfect gas)
α	angle of attack (deg)
β	$\sqrt{M^2 - 1}$
γ	ratio of specific heats (C_p / C_v)
δ_{eq}	angle used in Newtonian Theory ($=$ angle between velocity vector and local body slope)
θ	local body slope
θ_c, θ_s	cone half-angle and shock angle, respectively
λ	$\rho V^2 / \beta$
μ	Mach angle, $\mu = \sin^{-1} (1 / M)$
μ_1	coefficient of viscosity
ν	Prandtl-Meyer angle (deg)
ρ	density (slugs/ft ³)

σ	shock wave angle (deg)
η, η_1	exponent used in Second-order Shock-expansion Theory

Subscripts

a_w	adiabatic wall
c	cone
d	dissociation energy
e	electronic excitation energy
f	frozen flow
L	local conditions
m	match point
o	total and reference
r	rotational energy
s	stagnation conditions
t	translation energy
v	vibration energy
∞	freestream conditions

Superscripts

*	reference conditions
---	----------------------

APPENDIX A

DETERMINATION OF ANGLE δ USED IN NEWTONIAN THEORY

DETERMINATION OF ANGLE δ USED IN NEWTONIAN THEORY

Refer to the nomenclature of Figure A-1.

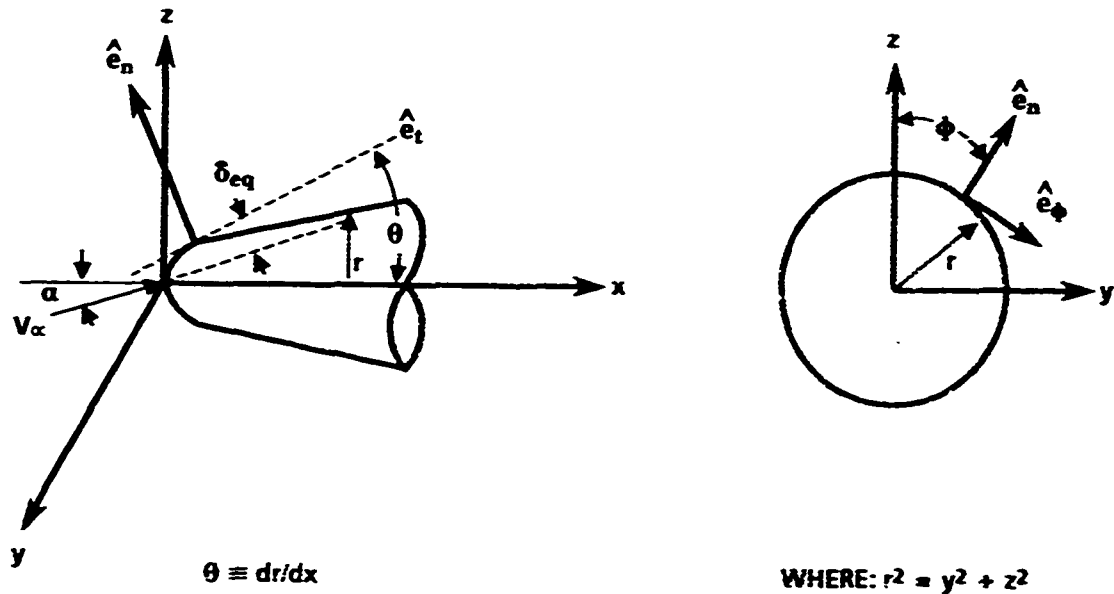


FIGURE A-1. NOMENCLATURE USED FOR DETERMINATION OF ANGLE δ_{eq}

Note that from the definition of the dot product of two vectors, one can write

$$\vec{V}_x \cdot \hat{e}_n = |\vec{V}_x| |\hat{e}_n| \cos(90 + \delta_{eq}) = -|\vec{V}_x| |\hat{e}_n| \sin(\delta_{eq}) \quad (A-1)$$

Also

$$\vec{V}_x = (V_x \cos \alpha) \hat{i} + (V_x \sin \alpha) \hat{k} \quad (A-2)$$

and

$$\hat{e}_n = -\sin \theta \hat{i} + (\sin \phi \cos \theta) \hat{j} + (\cos \phi \cos \theta) \hat{k} \quad (A-3)$$

$$\hat{e}_t = \cos \theta \hat{i} + \sin \theta \sin \phi \hat{j} + \sin \theta \cos \phi \hat{k} \quad (A-4)$$

$$\hat{e}_\phi = \cos \phi \hat{j} - \sin \phi \hat{k} \quad (A-5)$$

Substituting Equations (A-2) and (A-3) into Equation (A-1) and performing the indicated operations, one obtains:

$$\sin \delta_{eq} = \sin \theta \cos \alpha - \sin \alpha \cos \phi \cos \theta \quad (A-6)$$

This is the angle that is used for a general three-dimensional (3-D) point on a blunt surface at angle of attack in the Newtonian Theory. Here $\phi = 0$ is the leeward plane and $\phi = 180$ is the windward plane. If the reverse is true (as many references use), the negative sign of Equation (A-6) becomes positive.

APPENDIX B

**PRESSURE DISTRIBUTION ON A SPHERE
IN HYPERSONIC FLOW**

PRESSURE DISTRIBUTION ON A SPHERE IN HYPERSONIC FLOW

The Modified Newtonian pressure distribution has been used by numerous investigators to predict pressure distributions on blunt-nosed bodies in hypersonic flow. A close examination of this method for a sphere showed that for $M_\infty > 3.5$ it overpredicts pressures for $x/R_N < 0.5625$ and underpredicts pressures for most of the region beyond $x/R_N = 0.5625$. Here, x is the axial coordinate with $x=0$ at the stagnation point, and R_N is the radius of the sphere. However, the Modified Newtonian method predicts the correct pressure at $x/R_N = 0.5625$ for all $3.5 < M_\infty \leq 30$. Figure B-1 shows these features for $M_\infty = 3.5$ and 5, but they hold also for the higher Mach numbers.

A second feature of the Modified Newtonian (MN) method is that at $x/R_N = 0.5625$ the ratio

$$\frac{dp}{d\delta_{eq}} \bigg/ \left| p \frac{dp}{d\delta_{eq}} \right|_{MN}^{\frac{1}{2}}$$

varies very little with M_∞ . The value of

$$\frac{dp}{d\delta_{eq}}$$

was obtained numerically from CFD data in Reference B-1. The angle of δ_{eq} is the inclination of the surface with respect to the axis of the sphere, where $\delta_{eq} = \pi/2$ at the stagnation point. Table B-1 shows the numerical values.

TABLE B-1. VALUES OF PRESSURE GRADIENT PARAMETER AS FUNCTION OF MACH NUMBER

M_∞	$\frac{dp}{d\delta_{eq}} \bigg/ \left p \frac{dp}{d\delta_{eq}} \right _{MN}^{\frac{1}{2}} \text{ at } x/R_N = 0.5625$
3.5	1.469
5.0	1.519
10.0	1.516
20.0	1.523
30.0	1.524

B-1 Morrison, A. M., Solomon, J. M., Ciment, M., and Ferguson, R. E., *Handbook of Inviscid Sphere Cone Flowfields and Pressure Distributions: Vol. I*, NSWC/WOL TR 75-45, December 1975.

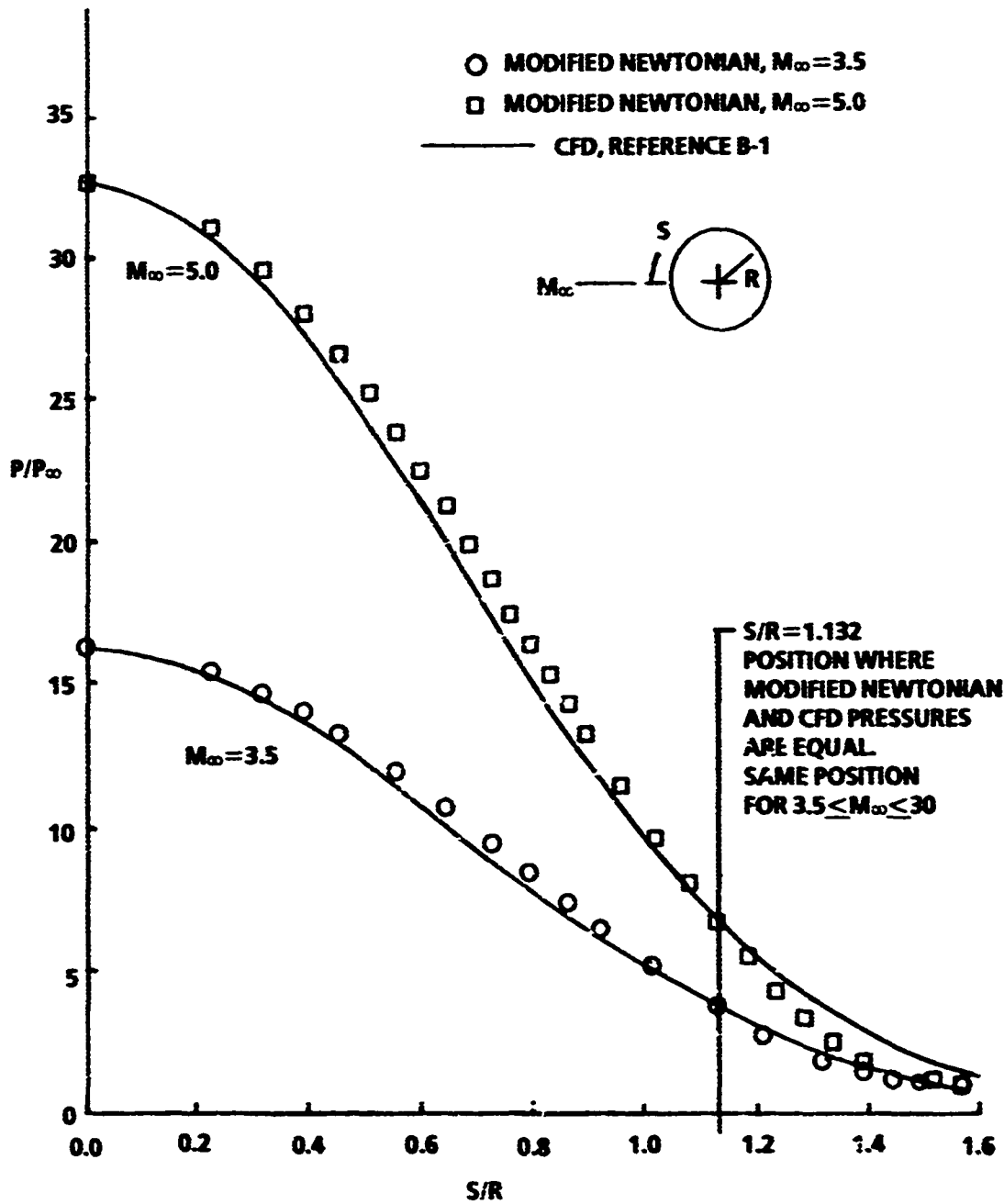


FIGURE B-1. PRESSURE ON A SPHERE

Thus, the position $x/R_N = 0.5625$ will be called the match point since the pressure is Modified Newtonian pressure and the pressure gradient can be calculated from the ratio

$$\frac{dp}{d\delta_{eq}} \bigg/ \left[p \frac{dp}{d\delta_{eq}} \right]_{MN}^{\frac{1}{2}}$$

It has been determined that using a numerical value of 1.5 for this ratio for all $M_\infty > 3.5$ gives accurate results.

For the region $0 \leq x/R_N < 0.5625$, a more accurate prediction of the pressure can be calculated from the equation

$$\Delta C_p = k \cos^m \delta_{eq} (\cos \delta_{eq} - \cos (\delta_{eq})_M) \quad (B-1)$$

where

$$\Delta C_p = (C_p)_{MN} - C_p$$

and $(\delta_{eq})_M = 25.95$, which is the value of δ_{eq} at $x/R_N = 0.5625$. Both k and m are constants to be determined. Note that Equation (B-1) gives $\Delta C_p = 0$ at both $x/R_N = 0$ and $x/R_N = 0.5625$. In addition, it gives $d(\Delta C_p) / d\delta_{eq} = 0$ at $x/R_N = 0$. It now remains to determine expressions for k and m .

The derivative of Equation (B-1) is

$$\frac{d(\Delta C_p)}{d\delta_{eq}} = k \sin \delta_{eq} \cos^{m-1} \delta_{eq} \left[(m+1) \cos \delta_{eq} - m \cos (\delta_{eq})_M \right] \quad (B-2)$$

Apply Equation (B-2) at the match point, $x/R_N = 0.5625$

$$\frac{d(\Delta C_p)}{d\delta_{eq}} = \left(\frac{dC_p}{d\delta_{eq}} \right)_{MN} - \frac{dC_p}{d\delta_{eq}} = -k \sin (\delta_{eq})_M \cos^m (\delta_{eq})_M \quad (B-3)$$

Now at the match point, the derivative

$$\frac{dC_p}{d\delta_{eq}}$$

can be calculated from the ratio given earlier; i.e.,

$$\frac{dp}{d\delta_{eq}} = 1.5 \left[p \frac{dp}{d\delta_{eq}} \right]_{MN}^{\frac{1}{2}}$$

which can also be written as

$$\frac{dC_p}{d\delta_{eq}} = 1.5 \left[\left(C_p + \frac{2}{\gamma M_\infty^2} \right) \frac{dC_p}{d\delta_{eq}} \right]_{MN}^{\frac{1}{2}} \quad (B-4)$$

where

$$(C_p)_{MN} = C_{p_{stag}} \sin^2 \delta_{eq} \quad (B-5)$$

Equation (B-4) can be used in Equation (B-3) but that only gives one equation for the two unknowns, k and m . Thus, an additional equation is needed.

A third feature of Modified Newtonian pressures is obtained by observing that the data in Reference B-1 show that ΔC_p is a maximum at $x/R_N = 0.25$ for all $M_\infty > 3.5$. Thus, Equation (B-2) can be used to get

$$\frac{d(\Delta C_p)}{d\delta_{eq}} = 0 = k \sin \delta_{eq} \cos^{m-1} \delta_{eq} \left[(m+1) \cos \delta_{eq} - m \cos(\delta_{eq})_M \right] \quad (B-6)$$

Apply this equation at $x/R_N = 0.25$ to obtain

$$m = \left(\frac{\cos \delta_{eq}}{\cos(\delta_{eq})_M - \cos \delta_{eq}} \right)_{x/R_N=0.25} = 2.78 \quad (B-7)$$

Finally, substitute Equation (B-4) into (B-3) and apply at the match point ($x/R_N = 0.5625$, $(\delta_{eq})_M = 25^\circ$, 5°) to get

$$k = \frac{-\left(\frac{dC_p}{d\delta_{eq}} \right)_{MN} + 1.5 \left[\left(C_p + \frac{2}{\gamma M_\infty^2} \right) \frac{dC_p}{d\delta_{eq}} \right]_{MN}^{\frac{1}{2}}}{\sin(\delta_{eq})_M \cos^m(\delta_{eq})_M} \quad (B-8)$$

All terms on the right side can be calculated for a given M_∞ . Substituting for the parameters of Equation (B-8) at the match point where $(\delta_{eq})_M = 25.95^\circ$, one obtains

$$k = -2.416 C_{p_c} + 4.606 \left[0.1597 C_{p_c}^2 + \frac{1.124}{M_\infty^2} C_{p_c} \right]^{\frac{1}{2}} \quad (B-9)$$

With m and k determined, an accurate C_p can be calculated from Equation (B-1) for $x/R_N \leq 0.5625$.

This method has been applied to a sphere for $3.5 \leq M_\infty \leq 30$. The results are compared to CFD results from Reference B-1 for $x/R_N \leq 0.5625$. At $M_\infty = 3.5$ the maximum error in pressure is 3 percent at $x/R_N = 0.25$. For $M_\infty > 3.5$, the maximum error is less than 1 percent and in most cases less than 0.5 percent. In contrast, the Modified Newtonian pressures had maximum errors from 7 to 10 percent. Equation (B-1) can be used for x/R_N up to about 0.7 with errors less than 3 percent. A better prediction for $x/R_N > 0.5625$ can be obtained by using the second-order shock-expansion method.

The new method gives a much more accurate prediction of surface pressures on a sphere in hypersonic flow than Modified Newtonian Theory. The additional computational effort is negligible for even the smallest PCs. Results of this new technique are shown in the Results and Discussion section of this report.

APPENDIX C

**COMPUTATION OF PROPERTIES ACROSS SHOCK WAVES
IN FROZEN AND EQUILIBRIUM CHEMICALLY
REACTING FLOWS**

COMPUTATION OF PROPERTIES ACROSS SHOCK WAVES IN FROZEN AND EQUILIBRIUM CHEMICALLY REACTING FLOWS

To compute the flow over 2-D or 3-D configurations using the Shock-Expansion Theory requires an initial starting solution. This solution is provided by computing the flow field variables across a normal (in the case of a blunt-nose body or blunt-leading-edge wing) or oblique shock for sharp-nosed bodies or wing leading edges. If the flow is low enough in Mach number so that real gas effects are negligible or if one is only interested in approximate prediction of forces and moments, a perfect gas can be assumed and the shock wave relations of Reference C-1 can be used directly. This last situation results from the fact that real gas effects have a fairly small effect on pressure (usually less than 10 percent) but can have a large effect on density and temperature. Since we are interested in temperature profiles along the body as inputs for structural analysis, we must consider both normal and oblique shock wave computations in real gases.

NORMAL SHOCK WAVES

The conservation of mass, momentum, and energy -- Equations (43), (44), and (45) of the main text of this report—for steady ($\partial/\partial t = 0$), adiabatic ($q = 0$) flow with no body forces ($f = 0$), reduce to the following for flow across a normal shock wave (see Figure C-1):

$$\rho_1 \bar{U}_1 = \rho_2 U_2 \quad (C-1)$$

$$p_1 + \rho_1 U_1^2 = p_2 + \rho_2 U_2^2 \quad (C-2)$$

$$h_1 + \frac{U_1^2}{2} = h_2 + \frac{U_2^2}{2} \quad (C-3)$$

Solving Equations (C-2) and (C-3) for p_2 and h_2 , while using Equation (C-1), there is obtained

$$p_2 = p_1 + \rho_1 U_1^2 (1 - \rho_1 / \rho_2) \quad (C-4)$$

$$h_2 = h_1 + U_1^2 / 2 [1 - (\rho_1 / \rho_2)^2] \quad (C-5)$$

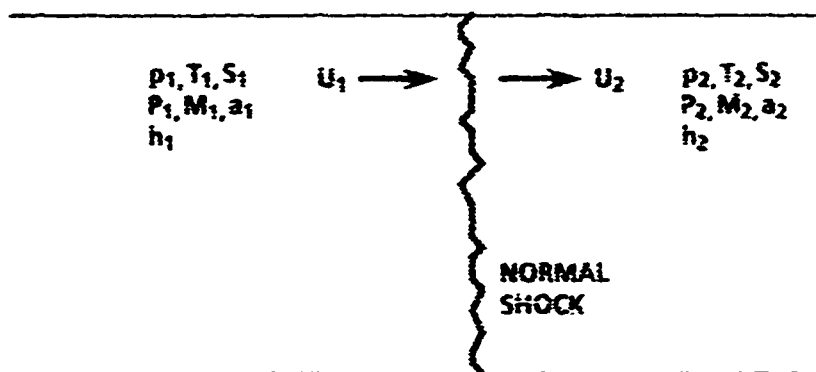


FIGURE C-1. NORMAL SHOCK WAVE FLOW

Note that all terms on the right-hand side of Equations (C-4) and (C-5) are known except for p_2 . To solve Equations (C-4) and (C-5), one guesses a value of p_1 / p_2 . A value of 0 or 0.1 is adequate. Equations (C-4) and (C-5) are then solved for p_2 and h_2 . Knowing p_2 and h_2 , a new value of p_2 is computed from the equilibrium chemistry model discussed in the Simplified Procedures for Air section (section 2.3.2). New values of p_2 and h_2 are then computed and, once again, new values of p_2 computed from the equilibrium chemistry model. This process is repeated until the change in p_2 is small and within the desired accuracy for convergence. This then defines the correct values of p_2 , h_2 , and ρ_2 behind the shock. T_2 , a_2 can be computed from section 2.3.2 once e_2 is computed from Equation (67). The compressibility factor Z is defined as:

$$Z = \frac{p}{\rho R T} \quad (C-6)$$

For a perfect or thermally perfect gas, Z is one but for a real gas that undergoes chemical reactions, Z represents the level of dissociation that takes place. Since R is the universal gas constant and p , ρ , and T are computed by Equations (C-4) and (C-5) and Section 2.3.2, Z is known. Also

$$U_2 = (\rho_1 / \rho_2) U_1 \quad (C-7)$$

$$\gamma_2 = a^2 \rho / p \quad (C-8)$$

$$M_2 = U_2 / a_2 \quad (C-9)$$

The Normal Shock Solution for Equilibrium Air is given in References C-2 and C-3. Figure C-2 gives T_2/T_1 as a function of freestream pressure and velocity. Note the large difference between the perfect and real gas temperatures as temperature increases and as atmospheric pressures decrease (higher altitudes).

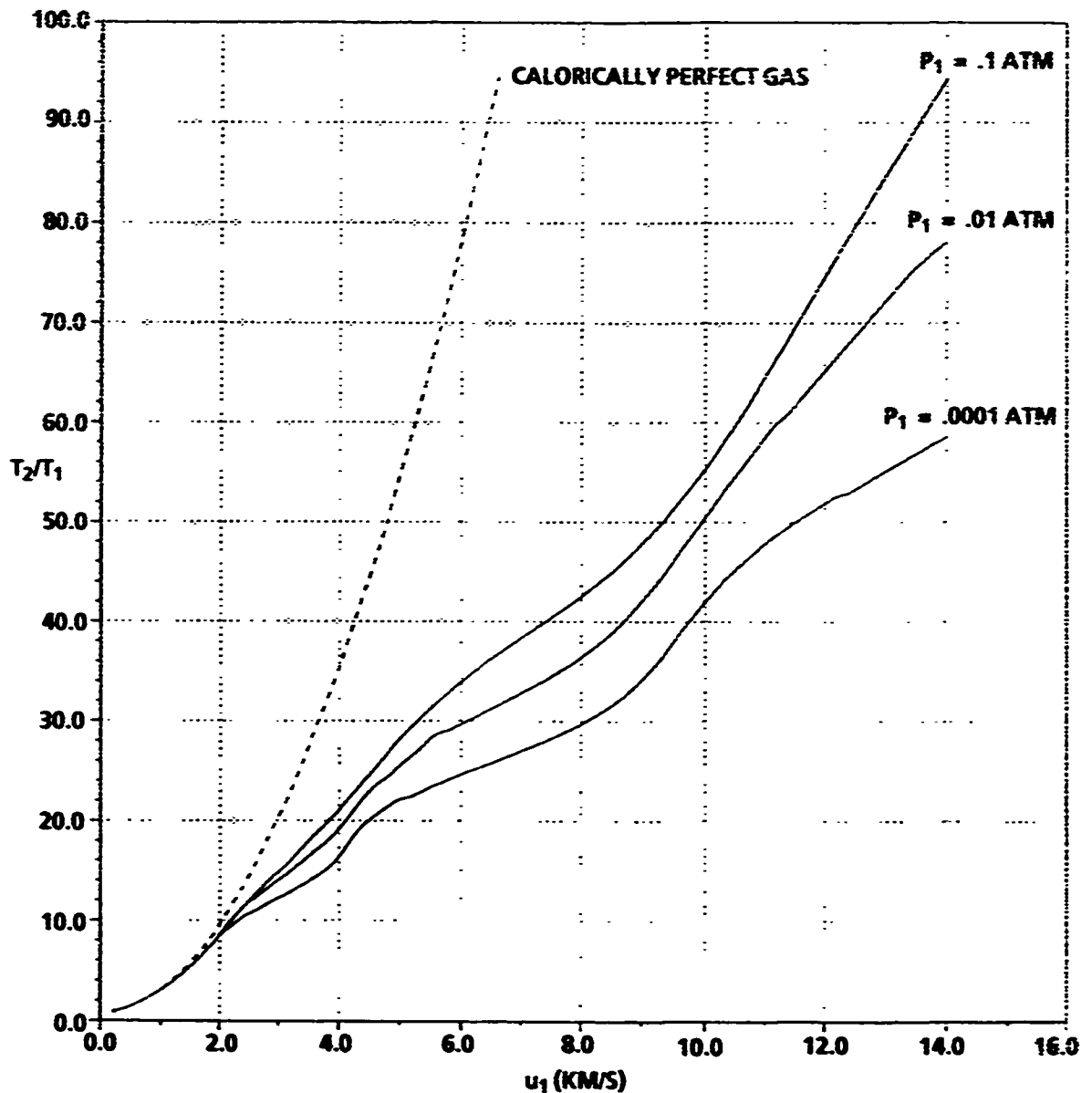


FIGURE C-2. INFLUENCE OF FREESTREAM PRESSURE AND VELOCITY ON NORMAL SHOCK TEMPERATURE FOR EQUILIBRIUM AIR ($T_1 = 225^\circ\text{K}$)

For the flow field over a blunt body, the properties vary between the shock and body. Hence, frozen flow would consist of computing real gas properties immediately behind the shock and then treating the flow field as a perfect gas thereafter, with constant values of $\gamma = \gamma_f$ and compressibility factor $Z = Z_f$. Equilibrium chemically reacting flow would allow different values of these parameters as a function of distance between the body and shock. However, if one is only interested in properties along the body surface from a method such as Modified Newtonian combined with SOSET, only the stagnation streamline that wets the body surface needs to be examined. Reference C-2 showed that, along the stagnation streamline, γ and Z change very little. Hence, effectively the flow is frozen at values that exist behind the shock (within 1 or 2 percent) between the shock and body stagnation point. This assumption will be made in the present work.

OBLIQUE SHOCK WAVES: 2-D OR WEDGE FLOWS

Examining Figure C-3, it soon becomes clear that one can use the previous normal shock relations (C-1) through (C-5) to solve for flow parameters behind an oblique shock if the U_1 and U_2 components of flow velocity normal to the shock wave are replaced with their equivalent components normal to the oblique shock wave. That is

$$U_{n_1} = U_1 \sin \sigma \quad (C-10)$$

$$U_{n_2} = U_2 \sin(\sigma - \theta) \quad (C-11)$$

Here, θ is the flow direction which, for attached flow on a wedge, is constant and equal to the wedge angle. Equations (C-1), (C-4), and (C-5) now become, with these substitutions

$$\rho_1 U_1 \sin \sigma = \rho_2 U_2 \sin(\sigma - \theta) \quad (C-12)$$

$$p_2 = p_1 + \rho_1 U_1^2 \sin^2 \sigma (1 - \rho_1 / \rho_2) \quad (C-13)$$

$$h_2 = h_1 + \frac{U_1^2 \sin^2 \sigma}{2} [1 - (\rho_1 / \rho_2)^2] \quad (C-14)$$

Also, since $U_{t_1} = U_{t_2}$ from the conservation of momentum, then

$$U_1 \cos \sigma = U_2 \cos(\sigma - \theta)$$

or

$$\frac{U_1}{U_2} = \frac{\cos(\sigma - \theta)}{\cos(\sigma)} \quad (C-15)$$

Combining Equation (C-15) with Equation (C-12), there is obtained

$$\frac{p_1}{p_2} = \frac{\tan(\sigma - \theta)}{\tan \sigma} \quad (C-16)$$

Expanding $\tan(\sigma - \theta)$ using a trigonometric identity, going through some algebraic manipulation, and taking the weak shock solution, one obtains

$$\tan \sigma = (p_2/p_1 - 1)/(2 \tan \theta) - \sqrt{\left(1 - \frac{p_2}{p_1}\right)^2 \frac{1}{4 \tan^2 \theta} - \frac{p_2}{p_1}} \quad (C-17)$$

$U_{t_1} = U_{t_2}$ FROM CONSERVATION OF MOMENTUM
 $\therefore U_{N_1} = U_1 \sin \sigma ; U_{N_2} = U_2 \sin(\sigma - \theta)$

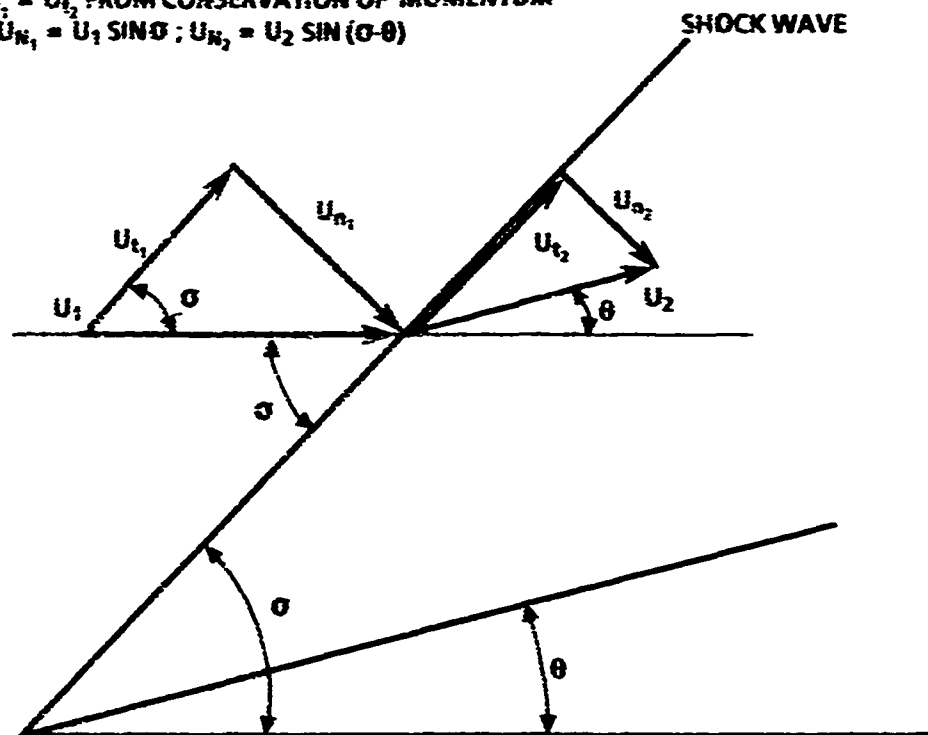


FIGURE C-3. OBLIQUE SHOCK GEOMETRY FOR A WEDGE

To solve for the flow field properties, a value of p_1/p_2 is once again guessed. The shock angle is computed from Equation (C-17). With this value of σ and p_1/p_2 known, p_2 and h_2 are computed from Equations (C-13) and (C-14). A new value of p_2 is computed from the process of Section 2.3.2 and an iteration takes place until successive changes in p_2 are within some error bound. This defines the values of σ , p_2 , p_2 , and h_2 behind the shock. T_2 and "a" are then computed from Section 2.3.2 and Z , U_2 from Equations (C-6), (C-7) and (C-15). Local Mach number and isentropic exponent γ are then computed from Equations (C-8) and (C-9).

It should be pointed out that the isentropic exponent, defined as

$$\gamma = \left[\frac{\partial(\ln p)}{\partial(\ln \rho)} \right]_s$$

is the same as the gamma of Equation (C-8). This is different than the "equivalent" gamma defined in Reference C-4 as

$$\bar{\gamma} = \frac{h}{e}$$

Here the word equivalent in quotes is used because $\gamma = \bar{\gamma}$ for a perfect gas. However, for a real gas where dissociation is present, the isentropic exponent used in true speed of sound computations is different than the "equivalent" gamma.

Since the body is a wedge, the flow properties behind the straight shock are constant throughout the flow field. Hence, the pressure p_2 is also the pressure on the surface which can be used to compute forces and moments. Also, Frozen and Equilibrium Chemically Reacting Flows give the same results since all properties are constant between the body and shock. Figure C-4 gives the results of the shock angle versus wedge half angle at an altitude of 100K ft for two velocities for a perfect and real gas (either frozen or equilibrium chemically reacting). Note the small change between the perfect gas and real gas at small flow deflections and Mach numbers. Figure C-5 is an example of the shock waves for a particular case where the conditions are such to show a large difference between perfect and real gas computations. This same simplified flow field does not hold true if the body is axisymmetric as will be discussed shortly.

Figures C-6 through C-8 show the temperature, density, and pressure for the same 100K altitude condition at two velocities as a function of wedge angle. Note the major effect of real gases is in the temperature and density at higher velocities and large wedge angles. The pressure is only affected slightly.

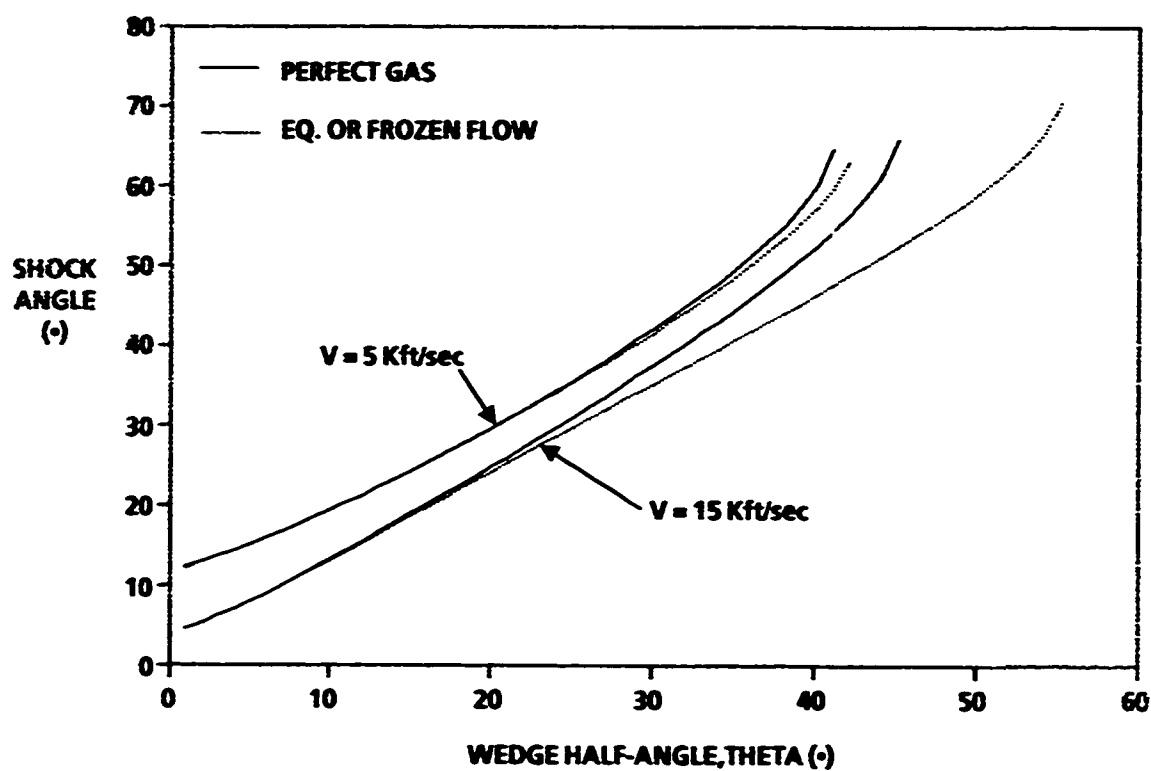


FIGURE C-4. DEFLECTION ANGLE/WAVE ANGLE VELOCITY DIAGRAM FOR OBLIQUE SHOCKS (ALTITUDE = 100k ft)

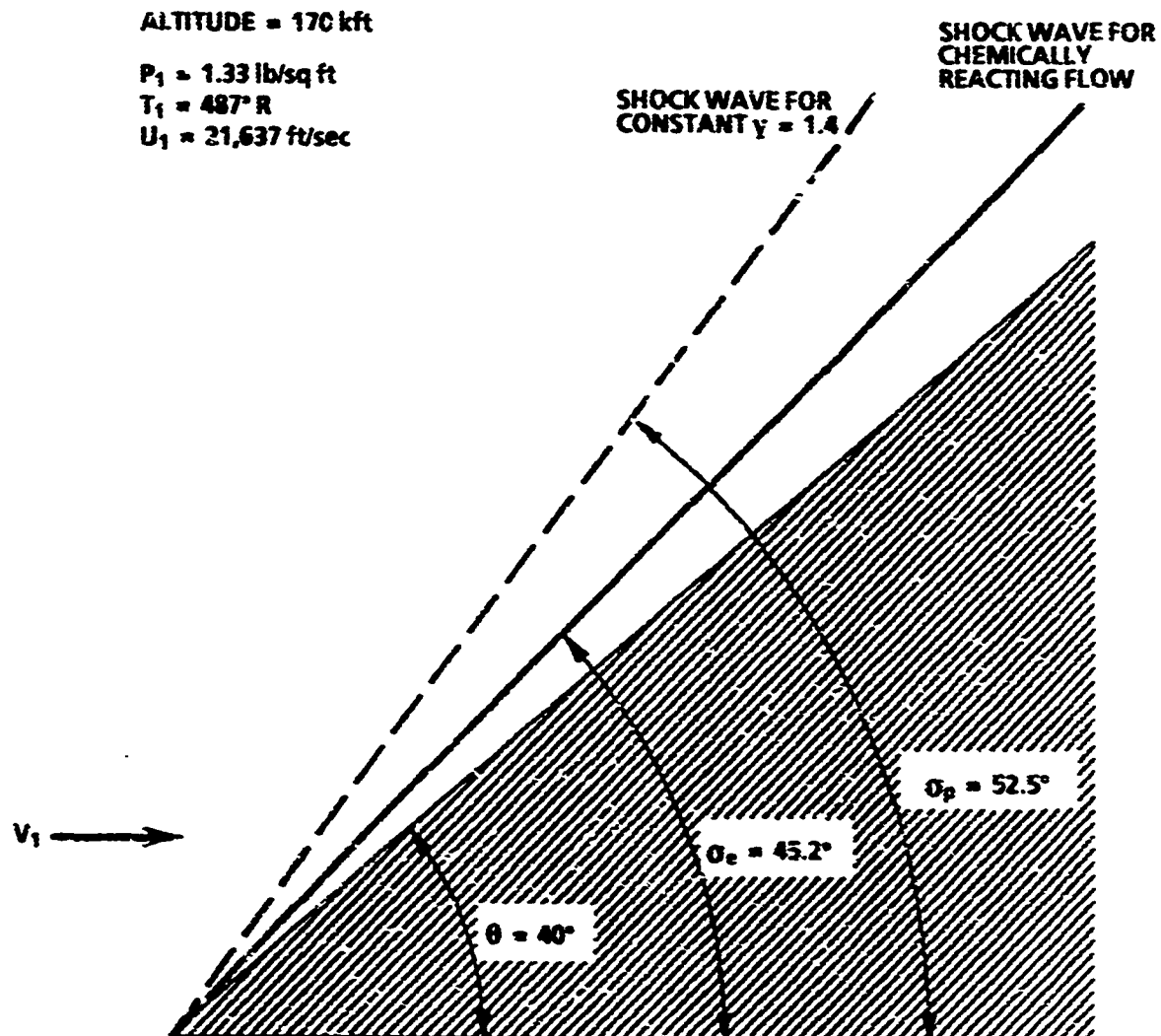


FIGURE C-5. COMPARISON OF OBLIQUE SHOCK WAVES FOR A CALORICALLY PERFECT GAS VERSUS AN EQUILIBRIUM CHEMICALLY REACTING GAS

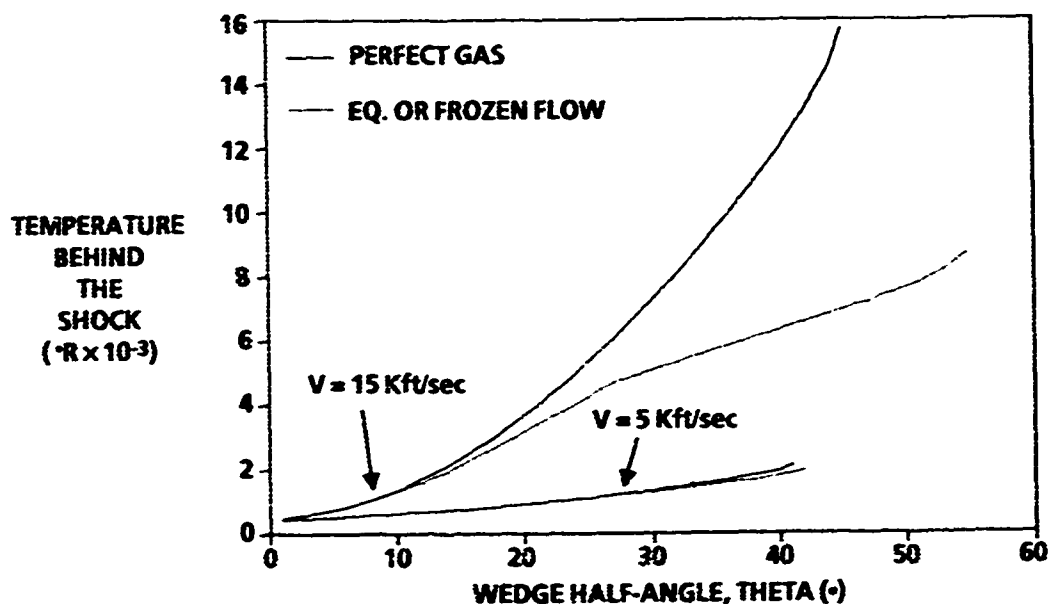


FIGURE C-6. TEMPERATURE IN THE SHOCK LAYER FOR A WEDGE (ALTITUDE = 100k ft)

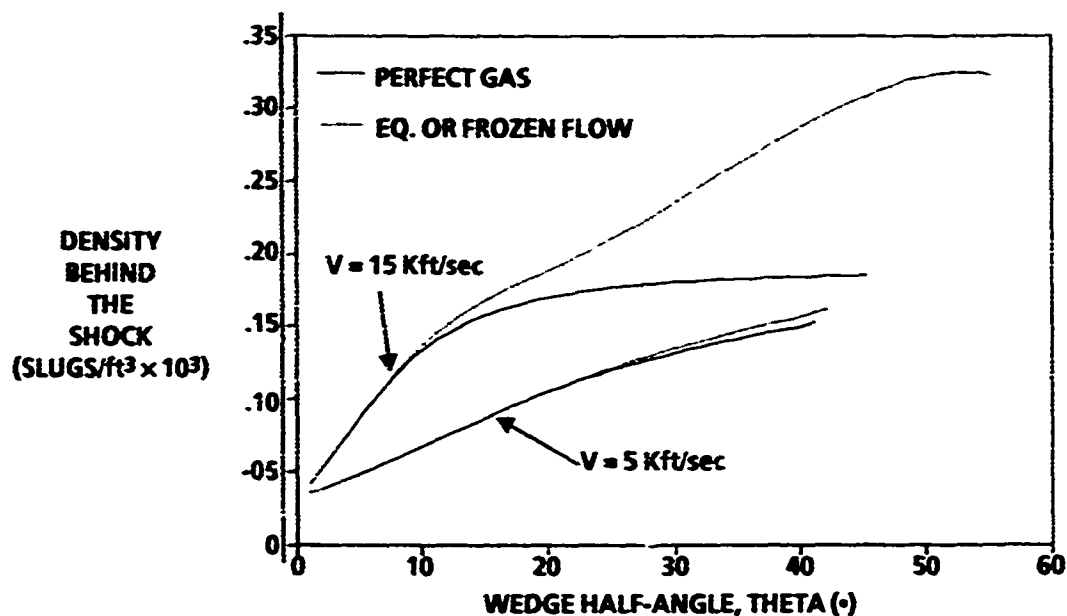


FIGURE C-7. DENSITY IN THE SHOCK LAYER FOR A WEDGE (ALTITUDE = 100k ft)

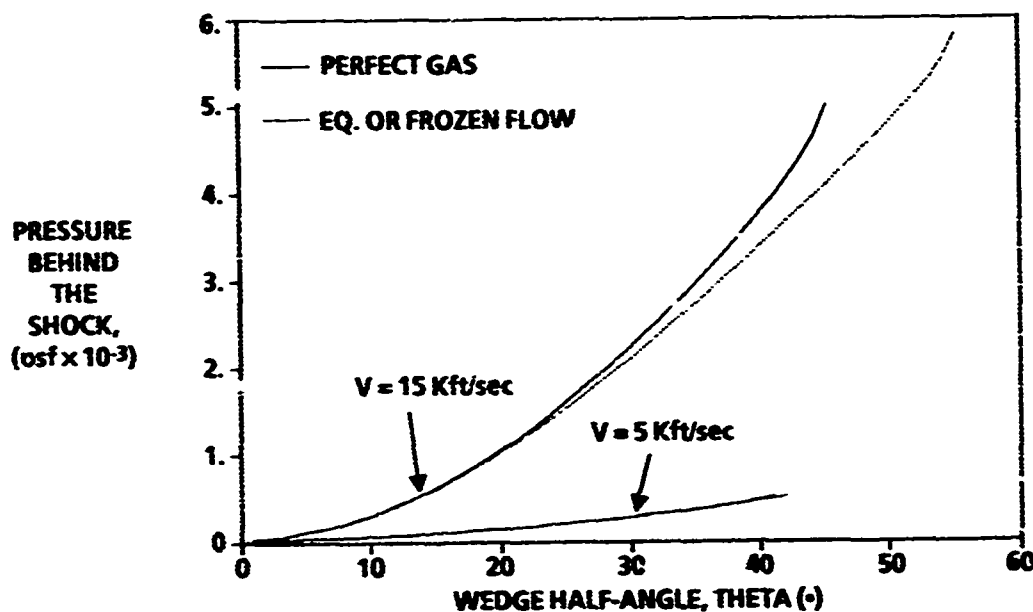


FIGURE C-8. PRESSURE IN THE SHOCK LAYER FOR A WEDGE
(ALTITUDE = 100k ft)

OBLIQUE SHOCK WAVES: AXISYMMETRIC CONICAL FLOWS

The flow field between the shock and conical surface is not constant here as was the case with the wedge. However, flow properties are constant along rays emanating from the conical tip for a perfect, frozen, or equilibrium chemically reacting gas. Furthermore, the entropy is constant throughout the flow field between the shock and body for these flow types. The continuity and momentum equations in spherical coordinates for this type of flow become C-5

$$\frac{dp}{d\theta} = -\rho V_\theta \left(\frac{a^2}{V_\theta^2 - a^2} \right) \left(\dot{V}_r + V_\theta \cot \theta \right) \quad (C-18)$$

$$\frac{dV_r}{d\theta} = V_\theta \quad (C-19)$$

$$\frac{dV_\theta}{d\theta} = \left(\frac{a^2}{V_\theta^2 - a^2} \right) \left(2V_r + V_\theta \cot \theta - \frac{V_\theta^2 V_r}{a^2} \right) \quad (C-20)$$

Figure C-9 shows the geometry and nomenclature used. These equations represent a set of three first-order ordinary differential equations for five unknowns. The remaining two equations come from high-temperature thermodynamic properties

$$\rho = \rho(p, S) \quad (C-21)$$

$$a = a(p, S) \quad (C-22)$$

Perfect Gas

For a perfect gas, Equations (C-21) and (C-22) are replaced by

$$a^2 = \left(\frac{\gamma - 1}{2} \right) \left[V_{\infty}^2 - V_r^2 - \left(\frac{dV_r}{d\theta} \right)^2 \right] \quad (C-23)$$

$$r = \frac{\gamma P}{a^2} \quad (C-24)$$

Substituting Equations (C-23) and (C-24) into Equations (C-18) through (C-20) and performing the algebra, one arrives at Equation (30) of section 2.2.2. The discussion on the solution of this equation was also given.

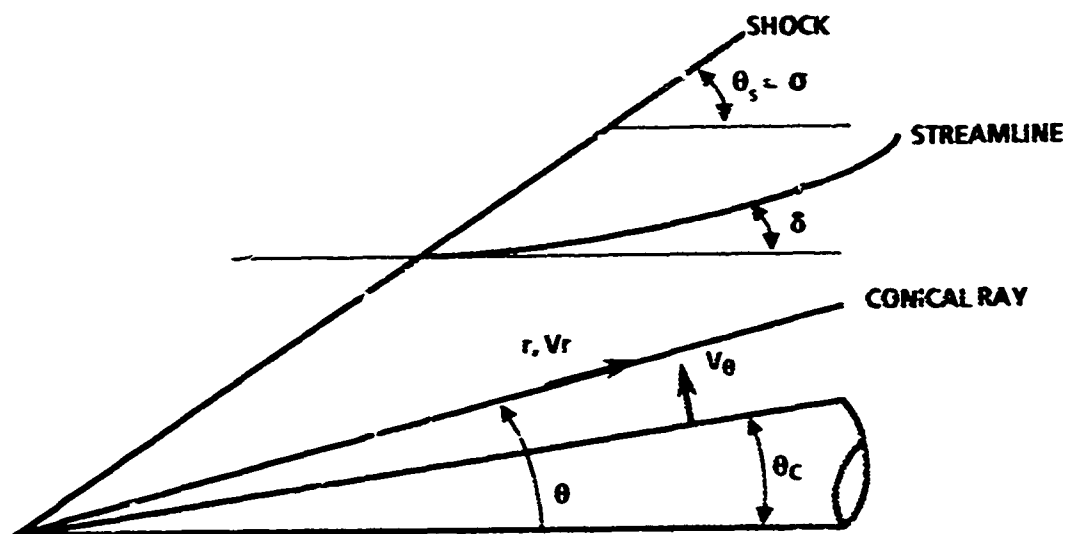


FIGURE C-9. OBLIQUE SHOCK GEOMETRY FOR A CONE
(SPHERICAL COORDINATES)

Frozen Flow

For frozen flow, the gas is allowed to change chemical composition across the shock instantaneously, and the values of γ and Z are no longer constant across the shock. Also, since the flow angle behind the shock is not constant and equal to the cone angle, as was the case for a wedge, Equation (C-17) is not the most appropriate equation to use in the solution process since this involves three unknowns. Using Equations (C-13) and (C-14) instead requires only a double iteration to solve Equations (C-18) through (C-20) from the body to the shock. The solution proceeds as follows:

1. Guess values of σ and p_1/p_2 . Perfect gas values are adequate.
2. Solve Equations (C-13) and (C-14) for p_2, h_2 .
3. Solve the appropriate form of Equation (73) for a new value of p_2 [i.e., $p_2 = p_2(p_2, h_2)$ or $p_2 = p_2(p_2, S)$ if S is given from blunt body flow].
4. Repeat steps 2 and 3 until successive changes in p_2 are within some acceptable tolerance. This defines the values of p_2, p_2, h_2 behind the shock of guessed angle σ .
5. Calculate values of " a " and T behind the shock from the appropriate thermodynamic curve fit equations and a value of $Z = Z_f$ and $\gamma = \gamma_f$ from

$$Z_f = \frac{p_2}{\rho_2 R T_2}$$

and

$$\gamma_f = \frac{a^2}{\frac{p_2}{\rho_2}}$$

The values of γ_f and Z_f are fixed at these values for the solution of Equations (C-18) through (C-20).

(Recall from the wedge flow computations that the values of $\bar{\gamma}$ and γ are different. The question arises as to which to use for frozen flow. The answer is that either can be used or, for that matter, other options for frozen flow could be used. However, to be consistent with the use of total temperature, pressure, and density relationships along the body where the flow is in fact isentropic and the isentropic exponent γ is used, the isentropic exponent γ is the one that will be used for frozen flow computations.)

6. Define initial values of V_r and V_θ behind the shock from the momentum and energy equations. That is

$$(V_r)_2 = V_1 \cos \sigma \quad (C-25)$$

$$(V_\theta)_2 = - \left[V_{\max}^2 - 2 h_2 - (V_r)_2^2 \right]^{\frac{1}{2}} \quad (C-26)$$

7. Numerically integrate Equations (C-18) through (C-20) from the shock to the body where $\theta = \theta_c$ using Fourth-Order Runge Kutta. During the integration, new values of p , V_r , V_θ are computed at each $\Delta\theta$ interval. At each interval, new values of a^2 and ρ must be computed based on the values of p , V_θ , V_r . These new values are

$$a^2 = \left(\frac{\gamma_f - 1}{2} \right) (V_{\max}^2 - V_r^2 - V_\theta^2) \quad (C-27)$$

$$\rho = \frac{\gamma_f p}{a^2} \quad (C-28)$$

8. At the body, check the value of V_θ . If it is not zero, guess a new value of σ .
9. Repeat steps 1 through 8 until V_θ is zero to some acceptable tolerance. Once this has occurred, the entire flow field between the shock and body is defined. Only the values of properties at the body surface are saved as they are all that will be used in the Shock Expansion Theory.
10. Calculate the entropy behind the shock from the appropriate thermofit equation. This value of entropy will be used later in the shock expansion theory. If entropy values are known from the blunt body stagnation solution, this step can be omitted.

Equilibrium Chemically Reacting Flow

For equilibrium chemically reacting flows, the computation process illustrated for frozen flows is used with two exceptions:

- i. The values γ and Z are allowed to vary between the body and shock.
2. The values of " a " and " ρ " at each point in the computation process are computed via thermofit Equation (73) based on the latest computed value of " p " and the value of " S " which is constant behind the shock. That is

$$\begin{aligned} a &= a(p, S) \\ \rho &= \rho(p, S) \end{aligned} \quad (C-29)$$

Both of these relations are given in Reference C-6 and they replace the equations for p and a in the frozen flow computations discussed previously.

Knowing the values of V_θ , V_r , S , p , a , and ρ during the solution process of Equations (C-18) through (C-20), the remaining thermodynamic properties can be computed as follows:

$$h = \left(V_{\max}^2 - V_\theta^2 - V_r^2 \right) / 2 \quad (C-30)$$

$$e = h - p / \rho \quad (C-31)$$

$$M = \frac{\left[V_\theta^2 + V_r^2 \right]^{1/2}}{a} \quad (C-32)$$

$$T = T(p, S) \quad (C-33)$$

$$Z = \frac{p}{\rho R T} \quad (C-34)$$

$$\gamma = h/e; \gamma = \frac{a^2 \rho}{p} \quad (C-35)$$

To illustrate the effects of real gas computations on conical shapes, Figures C-10 through C-13 have been prepared. These figures duplicate the results of Reference C-5 within numerical accuracy. Results here are similar to those of the wedge case presented previously except the frozen and chemical equilibrium cases are not the same. The trends of decreased shock angle, higher temperatures, lower densities, and near constant pressures of real gases compared to perfect gases holds true for the cone also. These trends will not be true for PME flows considered next in Appendix C.

Before proceeding to discuss PME flows, discussion of a problem that occurred in the solution of equilibrium chemically reacting flows over cones using the curve fits of Reference C-6 will be given. Since entropy is constant between the shock and body for a wedge or cone and is constant along streamlines for equilibrium flows, it seemed natural to use this as one of the independent variables [see Equation (C-29)]. However, when attempting to compute the entropy from internal energy and density, it was found that slight discontinuities (or jumps) occurred in the entropy values between various segments of the curve fits in Reference C-6. These jumps and attempts at smoothing the solution are illustrated in Figure C-14. Unfortunately, when both the actual and smoothed values of entropy were used in the solution of the equations for a cone [(C-18), (C-19), (C-20), and (C-29)], discontinuities occurred in the density and temperature at the cone surface. An example of the cone surface density is given in Figure C-15 (curve labeled $\rho = \rho(p, S)$). Note that the smoothed

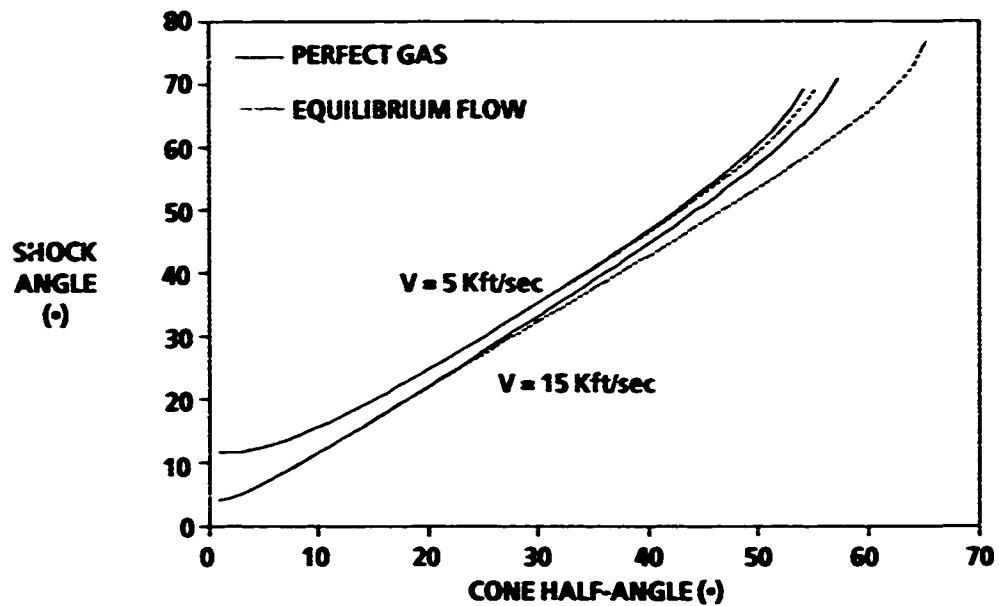


FIGURE C-10. EFFECT OF FREESTREAM VELOCITY AND CONE ANGLE ON CONE SHOCK WAVE ANGLE ($H = 100k$ ft)

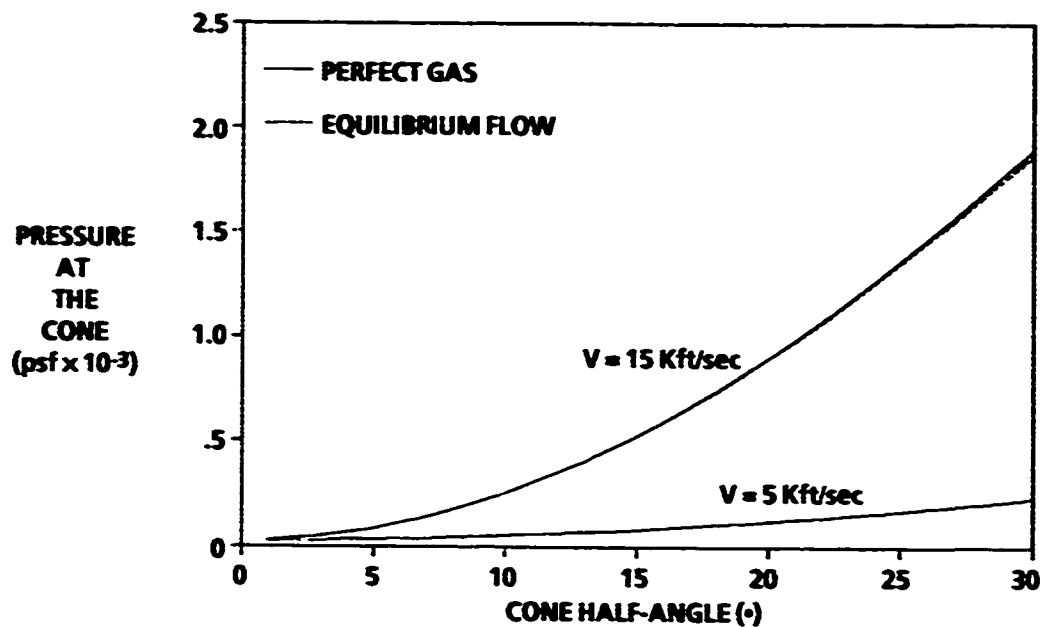


FIGURE C-11. EFFECT OF FREESTREAM VELOCITY AND CONE HALF-ANGLE ON CONE SURFACE PRESSURE ($H = 100k$ ft)

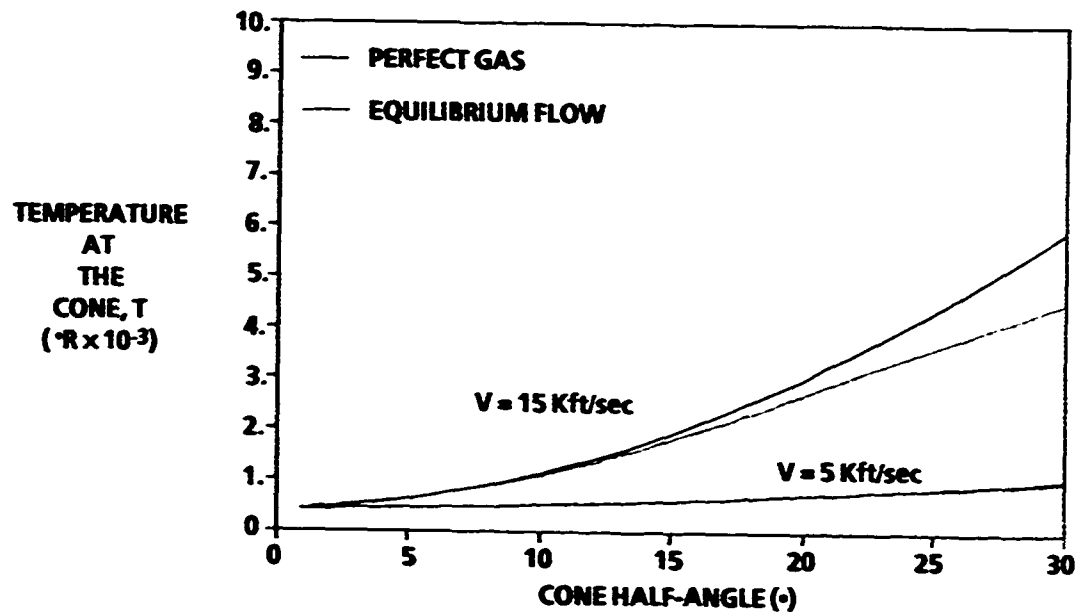


FIGURE C-12. EFFECT OF FREESTREAM VELOCITY AND CONE ANGLE ON CONE SURFACE TEMPERATURE ($H = 100\text{k ft}$)

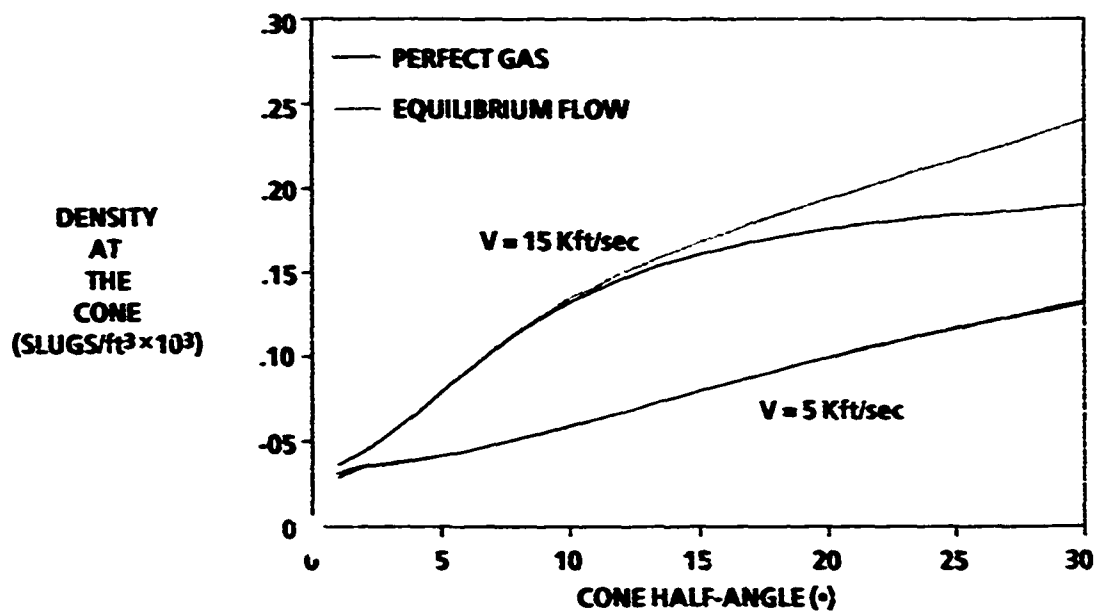


FIGURE C-13. EFFECT OF FREESTREAM VELOCITY AND CONE ANGLE ON CONE SURFACE DENSITY ($H = 100\text{k ft}$)

values show some improvement over the unsmoothed entropy values but both results deviate too much from the solution of Reference C-5 (up to 10 percent).

To get around this problem, several other alternatives were investigated. The first of these was to solve the conical equations using the total enthalpy and locally computed values of p , V_r , and V_θ from Equations (C-18) to (C-20) to solve for intermediate values of enthalpy from Equation (C-30). Internal energy could be computed using Equation C-31 and then density and speed of sound could be updated with $\rho(h, p)$ and $a(e, \rho)$. Using this approach, the results labeled $\rho(h, p)$ of Figure C-15 were obtained. These results agree almost identically to those of Hudgins.C-5 However, they still do not use one of the key parameters that will be needed downstream in the computation process: the constancy of entropy along the body surface.

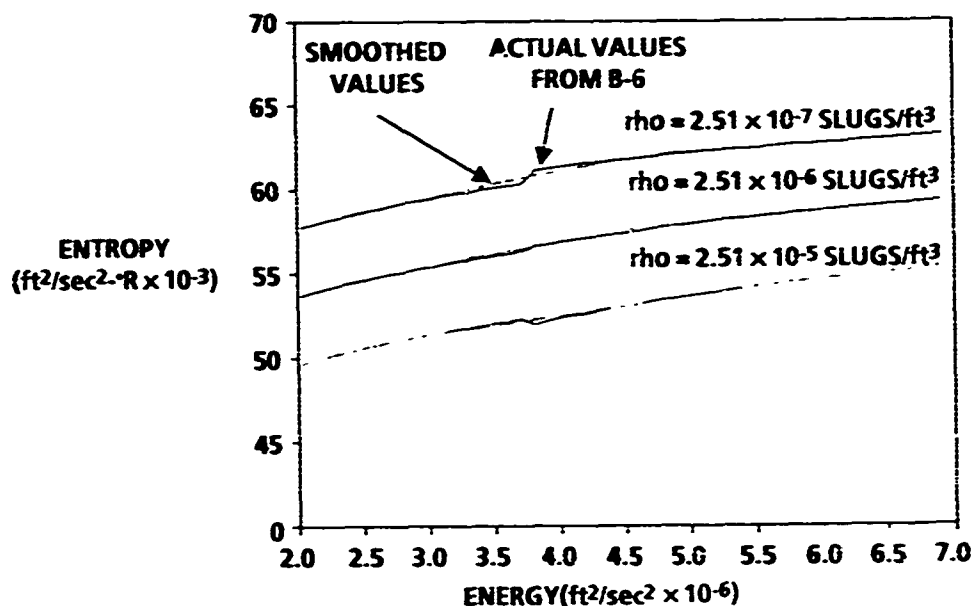


FIGURE C-14. ENTROPY VERSUS ENERGY FOR CONSTANT VALUES OF DENSITY

A final attempt was made to use entropy. The approach was to solve the conical flow equations (C-18) through (C-20) with conditions behind the shock determined as previously discussed.

Behind the shock, internal energy was found from Equation (C-31). Entropy was found from Equation 73 where $S = S(e, p)$. Using this value of S and p , a new value of e was computed from $e = e(p, S)$. This value of e was compared to the previous value of e . If the two did not agree to some desired accuracy, a new value of S was guessed and an iteration took place until the two values of e agreed. This then

was the value of S that was held constant in the wedge or cone flows and along the body surface ($S = S_I$). Using this approach to determine S_I , Equations (C-18) through (C-20) were solved in conjunction with (C-29). These results are shown in Figure C-15 as $\rho(p, S_I)$ where S_I refers to the value of entropy found from iteration. These results are very close to those where density is computed from $\rho = \rho(h, p)$ up to cone half-angles of 20° . The largest error up to cone half-angles of 30° is about 4 percent and for cone angles less than 20° is less than 1 percent. This then is the approach chosen to compute entropy that will be used throughout the flow field computations. Figures C-16 through C-18 show the comparison of the various cone solutions on surface pressure, temperature, and density for two velocities. Note that if one were interested in pressure only, any of the approaches are adequate. However, to get the most correct value of temperature that is needed for aerothermal analysis, the approach of iterating to find entropy appears to give results closer to the correct solution.

The only explanation that can be offered for this discrepancy is the fact that the curve fits are stated to be accurate to within 2 percent. The curve fits are formulated basically independent of each other. On the other hand, by using results from other curve fits to force a more correct value of entropy to be computed requires more consistency in the conservation laws and thermodynamic properties. The approach of iterating to find entropy takes a little more computer time. However, for the work herein where entropy will be held constant along the body surface and hence only computed once, the computational time is insignificant.

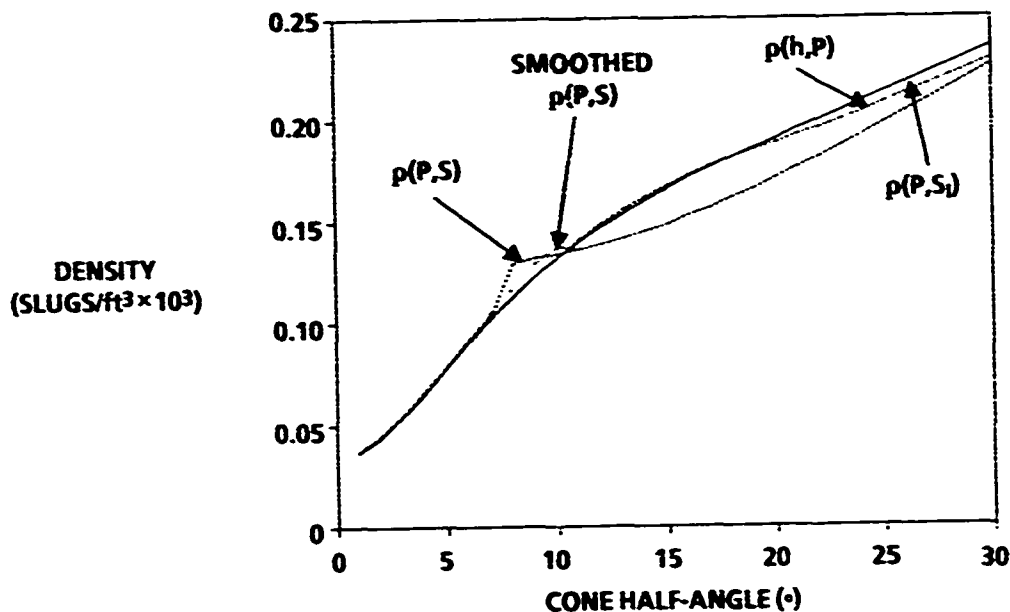


FIGURE C-15. COMPARISON OF DENSITY AT THE CONE SURFACE USING VARIOUS WAYS OF UPDATING DENSITY IN FLOW FIELD SOLUTION ($h = 100$ k ft)

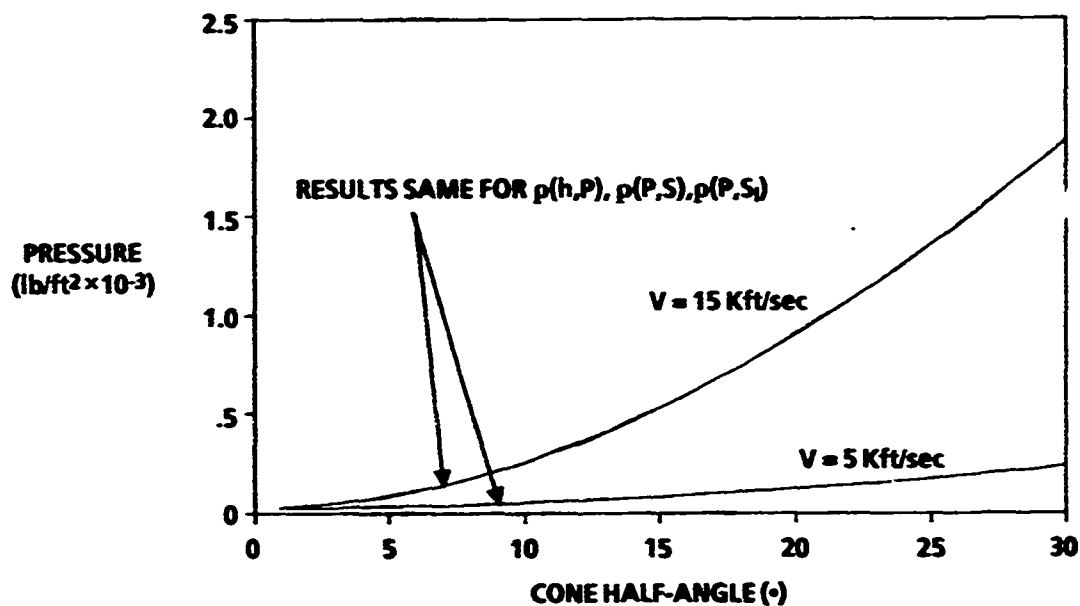


FIGURE C-16. CONE SURFACE PRESSURE COMPUTED WITH VARIOUS WAYS OF IMPLEMENTING REAL GAS EFFECTS ($h = 100k$ ft)

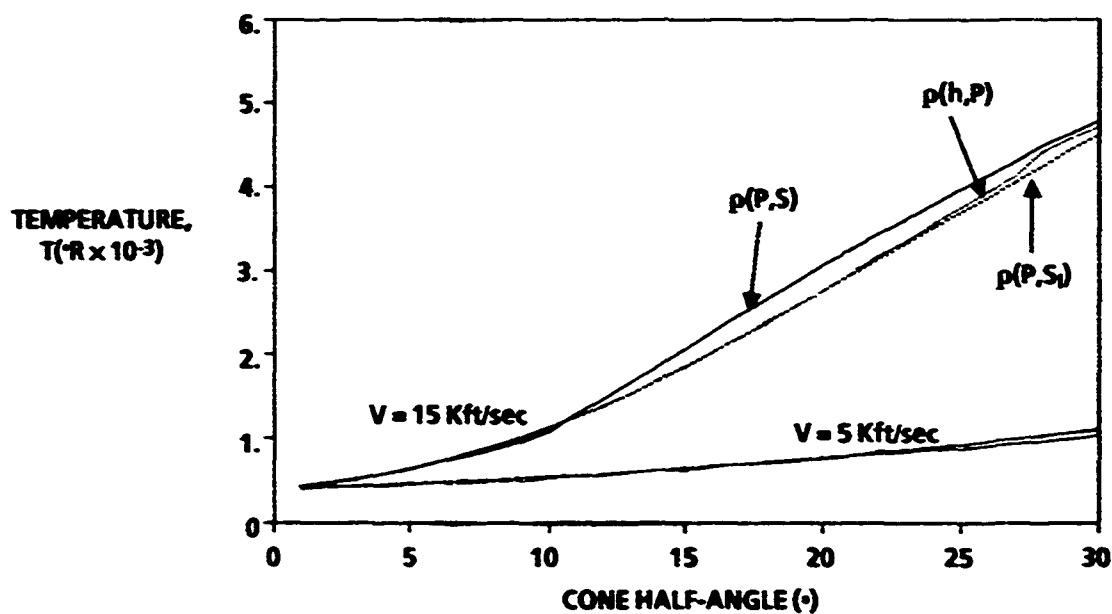


FIGURE C-17. CONE SURFACE TEMPERATURE COMPUTED WITH VARIOUS WAYS OF IMPLEMENTING REAL GAS EFFECTS ($h = 100k$ ft)

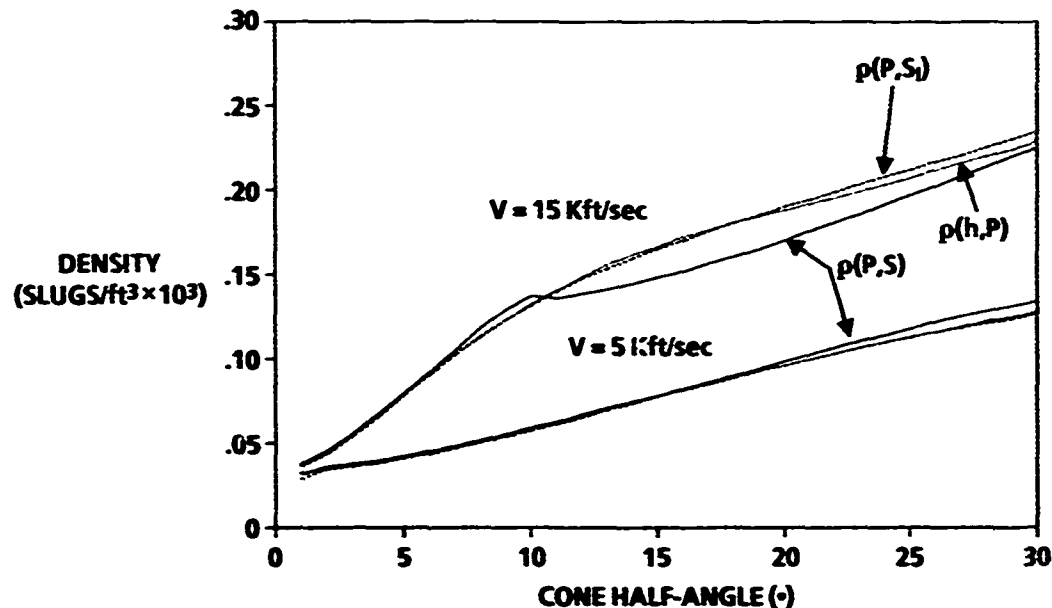


FIGURE C-18. CONE SURFACE DENSITY COMPUTED WITH VARIOUS WAYS OF IMPLEMENTING REAL GAS EFFECTS ($h = 100k$ ft)

REFERENCES

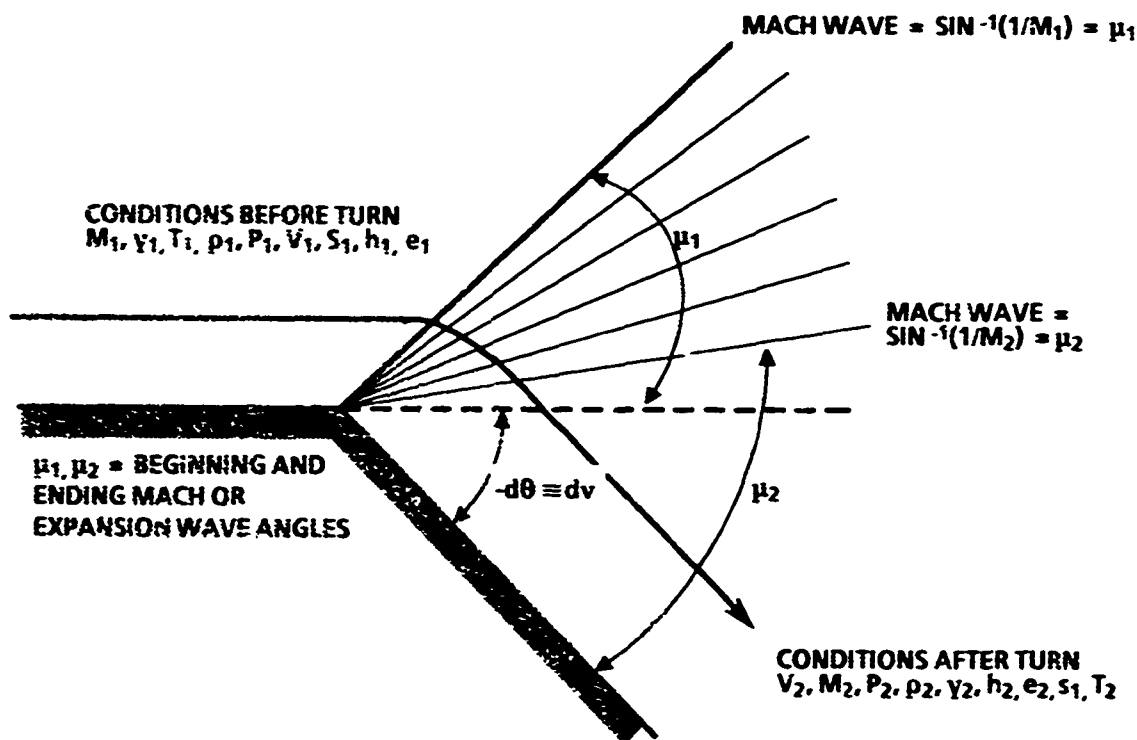
- C-1. Ames Research Staff, *Equations, Tables, and Charts for Compressible Flow*, NACA TR 1135, 1953.
- C-2. Wittliff, Charles E., and Curtis, James T., *Normal Shock Wave Parameters in Equilibrium Air*, Cornell Aero Lab. Report CAL-III, November 1961.
- C-3. Marrone, P. V., *Normal Shock Waves in Air: Equilibrium Composition and Flow Parameters for Velocities from 26,000 to 50,000 ft/sec*, CAL Report No. AG-1729-A-2, August 1962.
- C-4. Tannehill, J. C., and Mugge, P. H., *Improved Curve Fits for the Thermodynamic Properties of Equilibrium Air Suitable for Numerical Computation Using Time-Dependent or Shock-Capturing Methods*, NASA CR-2170, 1974.

- C-5. Hudgins, Henry E., Jr., *Supersonic Flow About Right Circular Cones at Zero Yaw in Air at Chemical Equilibrium, Part I -- Correlation of Flow Properties*, TM 1493, Picatinny Arsenal, August 1965.
- C-6. Srinivasan, S., Tannehill, J., and Weilmuenster, K., *Simplified Curve Fits for the Thermodynamic Properties of Equilibrium Air*, Report ISU-ERI-AMES 86401, Eng. Research Institute, Iowa State University, Ames, IA, June 1986.

APPENDIX D

**COMPUTATION OF PROPERTIES ACROSS EXPANSION WAVES
IN FROZEN AND EQUILIBRIUM CHEMICALLY
REACTING FLOWS**

The PME consists of an isentropic turning of a streamline from its initial conditions at state 1 to its final conditions at state 2 (see Figure D-1). Note that, while this is an isentropic process (for equilibrium air), this process applies from streamline to streamline, and each streamline can have different conditions. Referring to Figure D-1, this means that we do not necessarily have constant conditions in the entire flow field leading up to the turn. Indeed, in general, they are not. However, on the body surface, since it is considered a streamline, the flow is isentropic so long as nonequilibrium conditions do not occur. The Mach waves are actually characteristic lines along which no flow information is transmitted upstream. Of course, as conditions from streamline to streamline change, the Mach lines or characteristics will curve to accommodate these changes. If conditions ahead of the turn are constant throughout the flow field, the characteristics will be straight.



D-3

Another important feature is that the velocity parallel or tangential to the Mach line will be constant on either side. This comes from the conservation of mass and momentum equations used in derivation of the equations for flow across shock waves. This result is independent of type of flow (i.e., shock or expansion wave). Looking at an incremental change in the velocity as the flow turns around a corner, we can derive the equations for P.M. flows. Referring to the bottom sketch of Figure D-2, we can write the following from geometry:

$$d V_n \cos \mu = (V + d V) (-d \theta) = -V d \theta \quad (D-1)$$

$$\sin \mu = \frac{d V}{d V_n} \quad (D-2)$$

The figure shows μ_1 but the process applies to any portion of the expansion, so the subscripts have been dropped in the analysis. Substituting (D-2) into (D-1), we get

$$d V \frac{\cos \mu}{\sin \mu} = -V d \theta$$

or

$$-d \theta = \cot \mu \frac{d V}{V} \quad (D-3)$$

But, since

$$\sin \mu = \frac{1}{M},$$

then

$$\cot \mu = \sqrt{M^2 - 1}$$

Equation (D-3) becomes

$$-d \theta = \sqrt{M^2 - 1} \frac{d V}{V} \quad (D-4)$$

From the adiabatic energy equation, one can write

$$H = \text{Const} = h + \frac{V^2}{2} \quad (D-5)$$

Differentiating (D-5), solving for dV/V , we obtain

$$\frac{d V}{V} = \frac{d (H - h)}{2 (H - h)} \quad (D-6)$$

Also

$$M = \frac{V}{a} = \frac{\sqrt{2(H-h)}}{a} \quad (D-7)$$

Substituting Equations (D-6) and (D-7) into (D-4), the general equation for PME flows is obtained

$$-d\theta = \frac{1}{2(H-h)} \left[\frac{2(H-h)}{a^2} - 1 \right]^{\frac{1}{2}} d(H-h) \quad (D-8)$$

This equation is quite general as the only assumption is isentropic flow along a streamline. It, therefore, could apply to an isentropic expansion or compression and to perfect, frozen, or equilibrium chemically reacting flows.

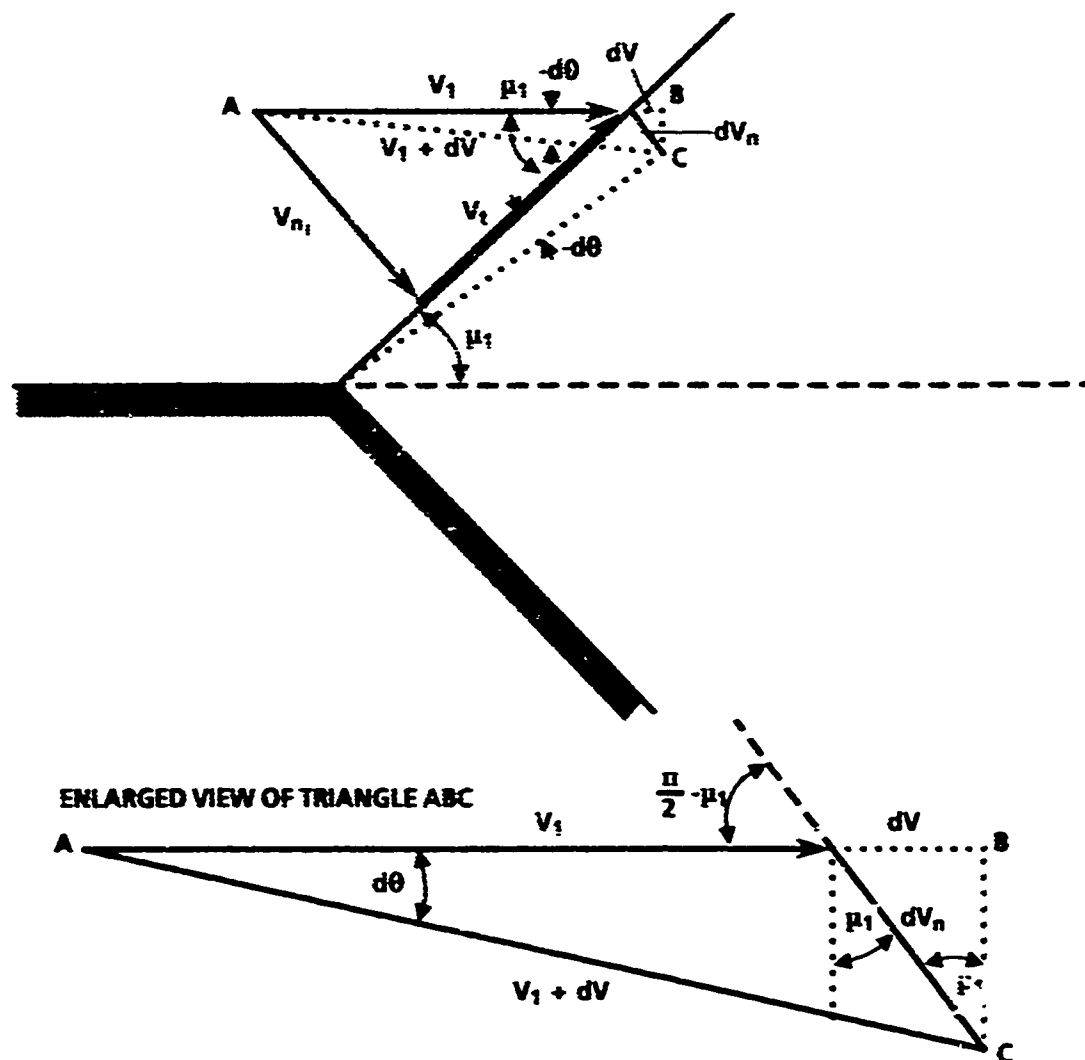


FIGURE D-2. GEOMETRY USED IN DERIVATION OF PRANDTL-MEYER EQUATION

PERFECT GAS FLOW

If we assume a perfect gas, then the specific heats are constant (\bar{C}_p , \bar{C}_v) and $Z = 1$. Thus, $h = \bar{C}_p T$ and $a^2 = \gamma R T$. With these substitutions, Equation (D-8) becomes

$$-d\theta = -\frac{1}{2(T_0 - T)} \left[\frac{2}{(\gamma - 1)} \left(\frac{T_0}{T} - 1 \right) - 1 \right]^{\frac{1}{2}} d(T_0 - T) \quad (D-9)$$

But since

$$\frac{T_0}{T} = 1 + \frac{\gamma - 1}{2} M^2$$

Equation (D-9) can be rewritten in the form

$$-d\theta = \frac{\sqrt{M^2 - 1}}{1 + \frac{\gamma - 1}{2} M^2} \frac{dM}{M} \quad (D-10)$$

In integral form, this becomes

$$-\int_{\theta_1}^{\theta_2} d\theta = \int_{M_1}^{M_2} \frac{\sqrt{M^2 - 1}}{1 + \frac{\gamma - 1}{2} M^2} \frac{dM}{M} \quad (D-11)$$

If $\theta = \theta^*$ is defined as the flow angle that corresponds to $M = 1$, Equation (D-11) can be rewritten as

$$-\int_{\theta^*}^{\theta_2} d\theta - \int_{\theta_1}^{\theta^*} d\theta = \int_1^{M_2} F(\gamma, M) dM + \int_{M_1}^1 F(\gamma, M) dM \quad (D-12)$$

where

$$F(\gamma, M) = \frac{\sqrt{M^2 - 1}}{\left[1 + \frac{\gamma - 1}{2} M^2 \right] M}$$

The integrals of Equation (D-12) can be integrated by the method of partial fractions to obtain:

$$v(M) = \int_1^M F(M, \gamma) dM = \sqrt{\frac{\gamma+1}{\gamma-1}} \tan^{-1} \left[\frac{\gamma-1}{\gamma+1} (M^2 - 1) \right]^{\frac{1}{2}} - \tan^{-1} \left[M^2 - 1 \right]^{\frac{1}{2}} \quad (D-13)$$

Substituting into Equation (D-12), there is obtained

$$-\theta_2 + \theta_1 = \Delta\theta = +v(M_2) - v(M_1) \quad (D-14)$$

$\Delta\theta$ and M_1 are known quantities so $v(M_1)$ can be computed from Equation (D-13). $v(M_2)$ is then computed from Equation (D-14), from which M_2 is solved for in a numerical iteration process by Equation (D-13). Knowing M_2 and the fact that the flow along the streamline is isentropic, all the other flow field properties can be computed by the total pressure, density, and temperature relationships which are constant. That is

$$T_2 = T_1 \left(1 + \frac{\gamma-1}{2} M_1^2 \right) / \left(1 + \frac{\gamma-1}{2} M_2^2 \right) \quad (D-15)$$

$$p_2 = p_1 \left(1 + \frac{\gamma-1}{2} M_1^2 \right)^{\frac{\gamma}{\gamma-1}} / \left(1 + \frac{\gamma-1}{2} M_2^2 \right)^{\frac{\gamma}{\gamma-1}} \quad (D-16)$$

$$\rho_2 = p_2 / RT_2 \quad (D-17)$$

Also, from the adiabatic energy relations we have

$$h_2 = \bar{C}_p T_2 \quad (D-18)$$

$$e_2 = \bar{C}_v T_2 \quad (D-19)$$

$$a_2 = \sqrt{\frac{\gamma p_2}{\rho_2}} \quad (D-20)$$

$$H = \bar{C}_p T_0 \quad (D-21)$$

$$V_2 = \sqrt{2(H - h_2)} \quad (D-22)$$

FROZEN FLOW

If the flow is frozen, the conditions behind the shock for a normal shock on a blunt body will be taken. These conditions come from the normal shock real gas computations.

For wedge or cone flows (sharp or pointed bodies), the conditions behind an oblique shock can be used. Again these results come from real gas computations for oblique shock waves in Appendix B. Hence, the initial conditions for frozen flow on blunt or pointed bodies or blunt or sharp wings are known. This gives values of

$$\gamma_f, Z_f$$

which are properties of the gas and its chemical states.

The rest of the flow can then be solved similar to a perfect gas. That is, Equations (D-13) through (D-16) are solved where frozen values of γ_f are used for γ .

Equations (D-17) through (D-22) are replaced with

$$\rho_2 = p_2 / (R Z T_2)$$

$$a_2 = \sqrt{\frac{\gamma_f p_2}{\rho_2}}$$

$$V_2 = M_2 a_2$$

$$h_2 = \frac{V_{\max}^2 - V_2^2}{2}$$

$$e_2 = h_2 - p_2 / \rho_2$$

EQUILIBRIUM CHEMICALLY REACTING FLOW

For the case of chemically reacting flows where the ratio of specific heats and compressibility factor can change as the flow expands around the surface, one can no longer assume a perfect gas and integrate Equation (D-8) in closed form. Equation (D-8) must be solved through numerical integration. In differential equation form, Equation (D-8) becomes

$$\frac{d(H-h)}{d\theta} + \frac{2(H-h)}{\left| \frac{2(H-h)}{a^2} - 1 \right|^2} = 0 \quad (D-23)$$

Once again, Fourth-order Runge Kutta or other appropriate numerical integration schemes can be used. The $\Delta\theta$ interval ($\theta_2 - \theta_1$) is divided into a given number of equally-spaced intervals. The initial values of H , h , θ_1 , θ_2 (defined), a , M , p , ρ , S , etc. are known. These all come from the conditions behind a normal shock or oblique shock. Of course, the conditions behind the shock must be taken to the surface of the body and, in the case of a blunt body or leading edge, taken to the point where the PME process begins. For a blunt body, this process is discussed in the Modified Newtonian Theory section of the text and in the discussion of wedges and cones in Appendix B.

One positive aspect about using the Fourth-order Runge Kutta integration routine (as opposed to Simpson's rule or some other integration process where h_2 is required) is the fact that no initial guess of h_2 is necessary nor any follow-on iteration to correct this guess based on the boundary conditions. Unfortunately, while Equation (D-23) is given in a very straightforward manner for integration, $a(h, S)$ is not available from either Reference D-6 or D-7. Informal communication with Tannehill also revealed that this particular thermofit equation still had not been developed. As a result, either a resort to tables^{D-8} must be used for $a(h, S)$ or Equation (D-23) must be put in a form compatible with the thermofit equations of References D-6 and D-7. Since the thermofit equation process is much faster than table look-up procedures, and at only a small sacrifice in accuracy, two different alternatives were investigated for solving Equation (D-23).

The first approach uses the Prandtl-Meyer Equation D-4; that is

$$\frac{dV}{d\theta} = \frac{-V}{\sqrt{M^2 - 1}} = \frac{-V}{\sqrt{\frac{V^2}{a^2} - 1}} \quad (D-24)$$

From the one-dimensional momentum equation

$$dV = - \frac{dp}{\rho V} \quad (D-25)$$

so that substituting Equation (D-25) into (D-24) one obtains

$$\frac{dp}{d\theta} = \frac{pV^2}{\sqrt{\frac{V^2}{z^2} - 1}} \quad (D-26)$$

To solve Equation (D-26), one knows initial values of p , θ , $\Delta\theta$, ρ , a , and V . Equation (D-26) is integrated using again Fourth-order Runge Kutta to obtain a value of p at the next integration interval. Knowing p and the fact that entropy is constant, updated values of

$$\left. \begin{aligned} \rho &= \rho(p, S) \\ a &= a(p, S) \\ e &= e(p, S) \end{aligned} \right\} \quad (D-27)$$

can be computed from the thermofit equations of Reference D-7. Then

$$h = e + p/\rho$$

and

$$V = \sqrt{2(H-h)} \quad (D-28)$$

(D-27) and (D-28) are then used along with (D-26) in the integration.

A second method investigated involved the simultaneous solution of Equations (D-24) and (D-26). That is, knowing initial values of V and a , Equation (D-24) was solved to obtain an updated value of V . This new value of V plus initial values of p , ρ , and a were used to solve for p at the next integration step. Using p and S , ρ and a were updated using Equation (D-27). Equations (D-24) and (D-26) were then solved at the next integration step. Figures D-3 and D-4 give the results of these two approaches for pressure and temperature (referred to on the figures as methods 1 and 2) and compares these results to Heims^{D-5} for equilibrium flow. It should be pointed out that Heims^{D-5} used table look-up procedures for the real gas properties so his results should be close to exact. Note that the method 1 approach of only integrating one differential equation gives more accurate results compared to Heims^{D-5}. Hence, this is the approach used herein for integrating the PME for equilibrium flow.

Figures D-5 through D-8 give pressure, temperature, density, and Mach number for perfect, equilibrium, and frozen flow cases. The initial conditions for the expansion were the same as those on Figures D-3 and D-4; that is, $T_1 = 5140^\circ$, $M_1 = 1$, and $p_1 = 1.2$ atm. It is quite interesting to note that while pressure is not affected to any appreciable extent in a compression process compared to perfect gas computations, it increases in an expansion process of equilibrium versus perfect gas computations (see Figure D-5). Also, the equilibrium temperature increases in an

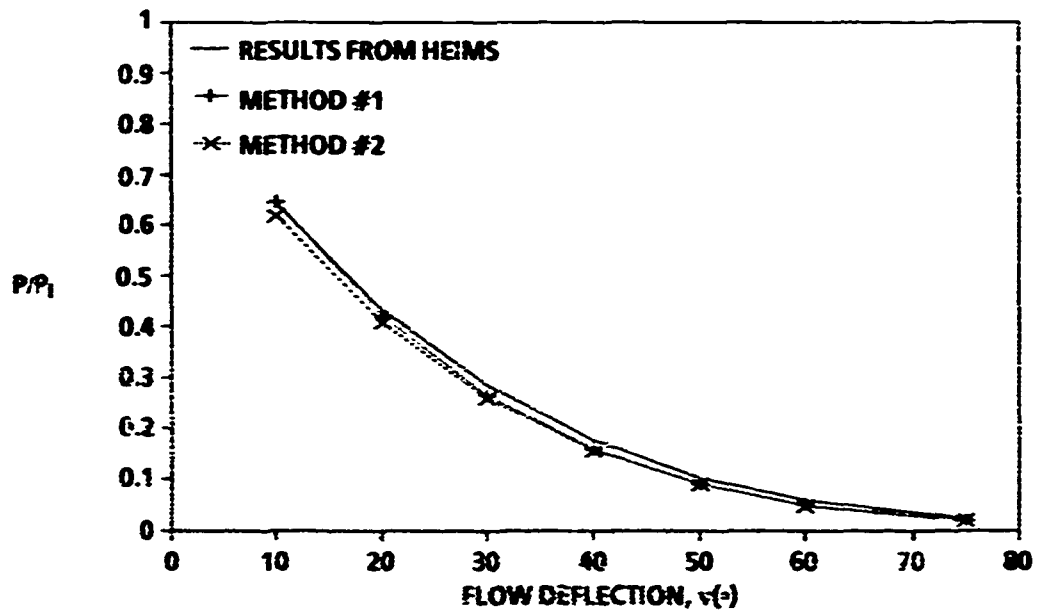


FIGURE D-3. PRESSURE COMPARISON OF INTEGRATION TECHNIQUES FOR PME OF EQUILIBRIUM FLOW ($M_1 = 1.0$, $T_1 = 6140^{\circ}\text{K}$, $p_1 = 1.2 \text{ atm}$)

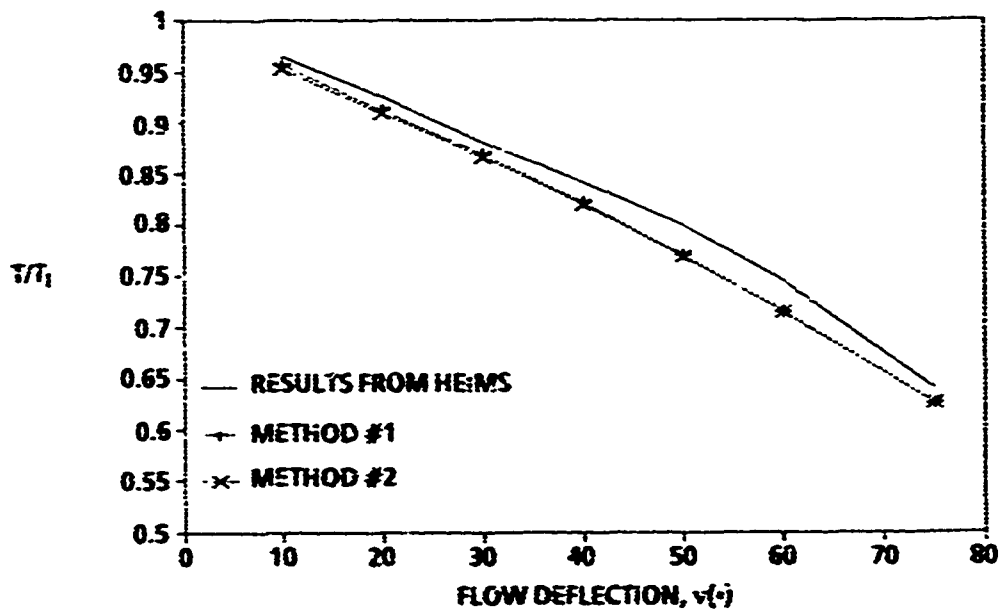


FIGURE D-4. TEMPERATURE COMPARISON OF INTEGRATION TECHNIQUES FOR PME OF EQUILIBRIUM FLOW ($M_1 = 1.0$, $T_1 = 6140^{\circ}\text{K}$, $p_1 = 1.2 \text{ atm}$)

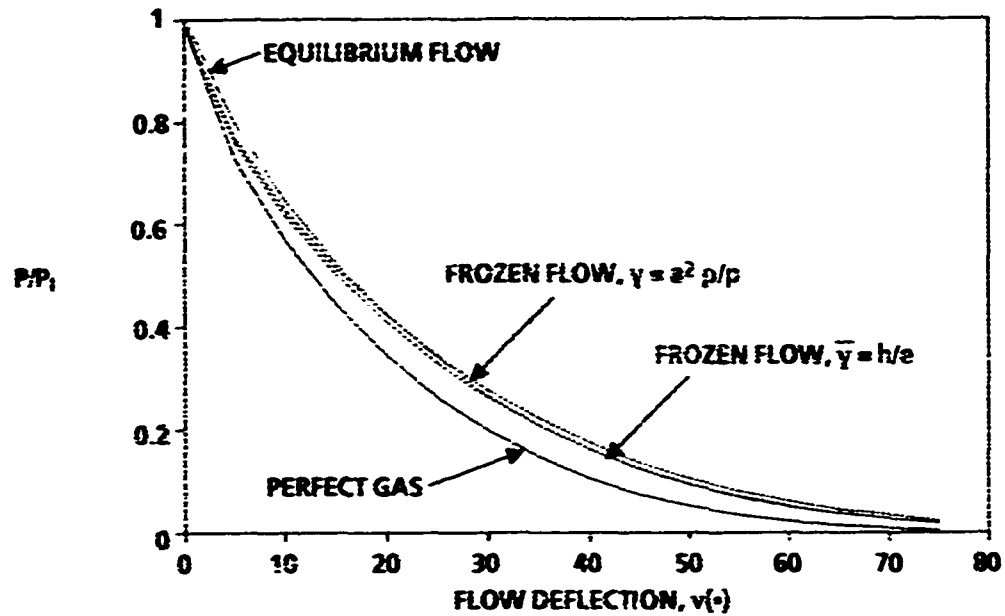


FIGURE D-5. PERFECT, FROZEN, EQUILIBRIUM PME: PRESSURE VERSUS FLOW DEFLECTION ANGLE ($M_1 = 1.0$, $T_1 = 6140^\circ\text{K}$, $p_1 = 1.2 \text{ atm}$)

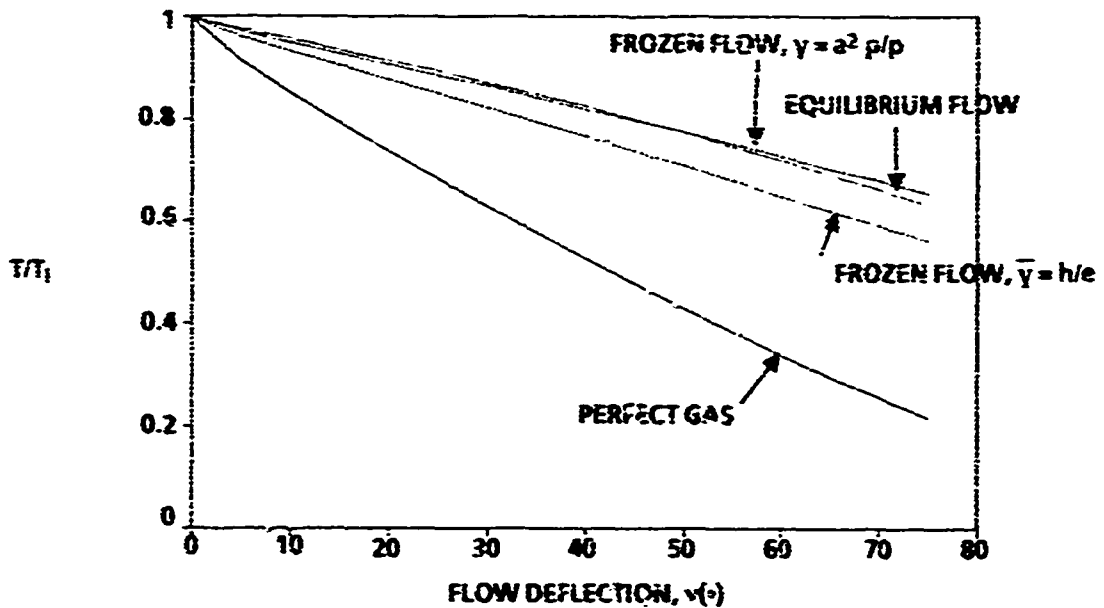


FIGURE D-6. PERFECT, FROZEN, EQUILIBRIUM PME: TEMPERATURE VERSUS FLOW DEFLECTION ANGLE ($M_1 = 1.0$, $T_1 = 6140^\circ\text{K}$, $p_1 = 1.2 \text{ atm}$)

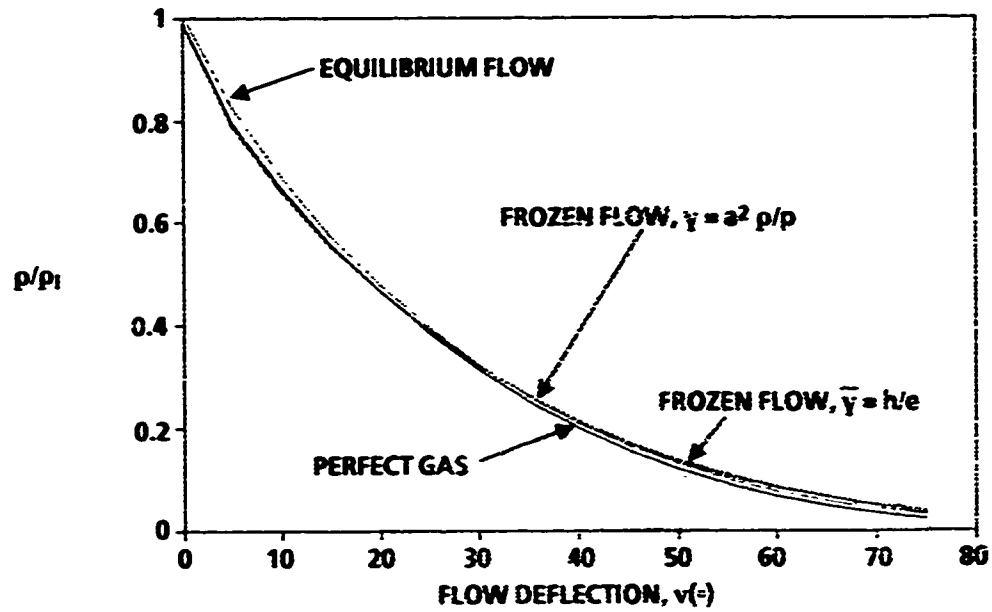


FIGURE D-7. PERFECT, FROZEN, EQUILIBRIUM PME: DENSITY VERSUS FLOW DEFLECTION ANGLE ($M_1 = 1.0$, $T_1 = 6140^\circ\text{K}$, $p_1 = 1.2 \text{ atm}$)

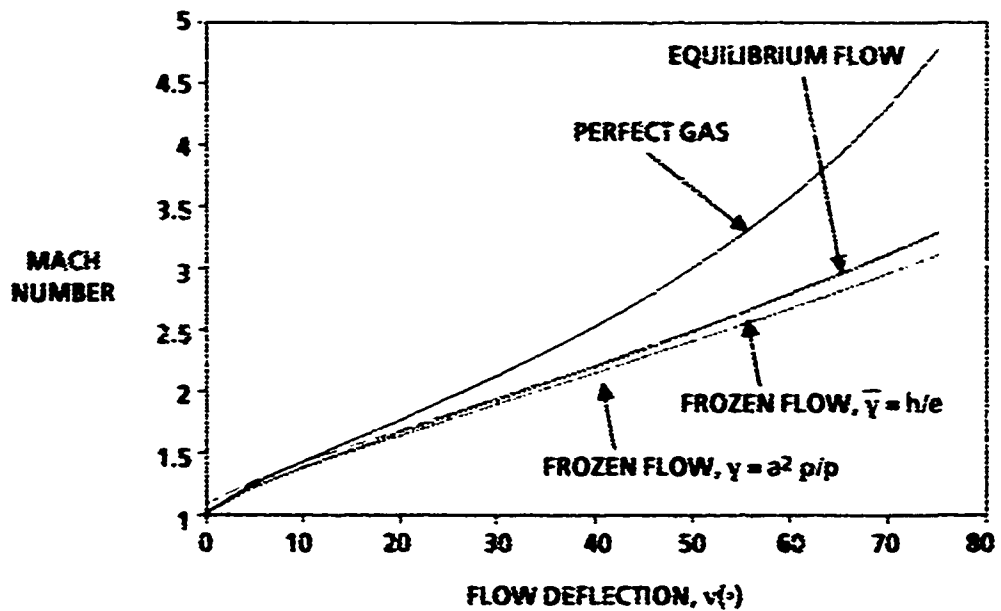


FIGURE D-8. PERFECT, FROZEN, EQUILIBRIUM PME: MACH NUMBER VERSUS FLOW DEFLECTION ANGLE ($M_1 = 1.0$, $T_1 = 6140^\circ\text{K}$, $p_1 = 1.2 \text{ atm}$)

expansion as opposed to decreasing in a compression compared to perfect gas computations (see Figure D-6). Note that density of equilibrium flows versus perfect gas is nearly constant for an expansion (Figure D-7), whereas it increases for an equilibrium compression compared to a perfect gas. Finally, Mach number decreases for an equilibrium expansion compared to a perfect gas (Figure D-8). Frozen flow cases are also shown on Figures D-5 through D-8 where the gas conditions that exist at the initial condition state are held constant throughout the expansion process. Two values of the initial state are held fixed corresponding to the isentropic exponent ($\gamma = a^2 \rho / p$) and the so-called "equivalent" gamma ($\bar{\gamma} = h/e$). Note that for the expansion process there is very little difference between the two, which indicates that for this set of initial conditions both values of gamma are about the same. This may not necessarily be the case, however, had the frozen flow values of $\bar{\gamma}$ and γ been those that existed behind a normal shock on a blunt body.

REFERENCES

- D-1. Moore, F. G., *Computational Aerodynamics at NAVSWC: Past, Present, and Future*, NAVSWC TR 90-569, October 1990.
- D-2. Truitt, R. W., *Hypersonic Aerodynamics*, The Ronald Press Company, New York, 1959.
- D-3. Hayes, W. D., and Probstein, R. F., *Hypersonic Flow Theory*, Academic Press, New York, 1966.
- D-4. Owczarek, J. A., *Fundamentals of Gas Dynamics*, International Textbook Company, Scranton, PA, 1964.
- D-5. Heims, Steve, *Prandtl-Meyer Expansion of Chemically Reacting Gases in Local Chemical and Thermodynamic Equilibrium*, NACA TN 4230, March 1958.
- D-6. Tannehill, J. C., and Mugge, P. H., *Improved Curve Fits for the Thermodynamic Properties of Equilibrium Air Suitable for Numerical Computation Using Time-Dependent or Shock-Capturing Methods*, NASA CR-2470, 1974.
- D-7. Srinivasan, S., Tannehill, J., and Weilmuenster, K., *Simplified Curve Fits for the Thermodynamic Properties of Equilibrium Air*, Report ISU-ERI-AMES 86401, Eng. Research Institute, Iowa State University, Ames, IA, June 1986.
- D-8. Hilsenrath, J., Klein, M., and Wooley, H. W., *Tables of Thermodynamic Properties of Air Including Dissociation and Ionization from 1500°K to 15000°K*, AEDC TR-59-20.

APPENDIX E

**DERIVATION OF CHARACTERISTIC COMPATIBILITY
CONDITIONS IN STREAMLINE COORDINATES**

DERIVATION OF CHARACTERISTIC COMPATIBILITY CONDITIONS IN STREAMLINE COORDINATES

Our equations of motion in vector form are as follows:

Continuity

$$\nabla \cdot (\rho \vec{V}) = 0 \quad (E-1)$$

Momentum

$$\rho \frac{D \vec{V}}{Dt} = -\nabla p$$

or for steady flow

$$\rho \vec{V} \cdot \nabla \vec{V} = \nabla p \quad (E-2)$$

Energy

$$\frac{V^2}{2} + h = H_t = \text{constant} \quad (E-3)$$

State

$$h = h(p, \rho) \quad (E-4)$$

$$a = a(p, \rho)$$

We would like to first transform these equations to the intrinsic or streamline coordinate system. In streamline coordinates, s is along the body, which is a streamline, and n is normal to it. Also

$$\vec{V} = V \hat{e}_s \quad (E-5)$$

Substituting (E-5) into (E-1) and (E-2) there is obtained

$$(\rho V) \nabla \cdot \hat{e}_s + \hat{e}_s \cdot \nabla (\rho V) = 0 \quad (E-6)$$

and

$$V^2(\hat{e}_s \cdot \nabla) \hat{e}_s + V \hat{e}_s (\hat{e}_s \cdot \nabla) V = -\frac{\nabla p}{\rho} \quad (E-7)$$

Take the dot product of Equation (E-7) with \hat{e}_n to obtain

$$V^2 \hat{e}_n \cdot \left[(\hat{e}_s \cdot \nabla) \hat{e}_s \right] = -\frac{1}{\rho} \hat{e}_n \cdot \nabla p \quad (E-8)$$

Using the vector identities

$$(\hat{e}_s \cdot \nabla) \hat{e}_s = \nabla \times \hat{e}_s \times \hat{e}_s$$

$$\hat{e}_n \cdot (\text{curl } \hat{e}_s \times \hat{e}_s) = \text{curl } \hat{e}_s \cdot (\hat{e}_s \times \hat{e}_n)$$

and the fact that $\hat{e}_s \times \hat{e}_n = \hat{e}_t$, Equation E-8 becomes

$$\hat{e}_t \cdot (\nabla \times \hat{e}_s) + \frac{1}{\rho V^2} \hat{e}_n \cdot \nabla p \quad (E-9)$$

Also, for equilibrium flow, entropy is conserved along streamlines, which requires

$$\hat{e}_s \cdot \nabla p = a^2 \hat{e}_s \cdot \nabla \rho \quad (E-10)$$

Substituting Equation (E-10) into the continuity Equation (6) and expanding there is obtained

$$(\hat{e}_s \cdot \nabla) V = -\frac{V}{\rho a^2} \hat{e}_s \cdot \nabla p - V(\nabla \cdot \hat{e}_s) \quad (E-11)$$

But from the momentum Equation (E-7), after taking the dot product with \hat{e}_s , one obtains

$$\hat{e}_s \cdot \nabla V = -\frac{1}{\rho V} (\hat{e}_s \cdot \nabla p) \quad (E-12)$$

Substituting (E-12) into (E-11), and performing the algebra, one obtains

$$\frac{\rho^2}{\rho V^2} \hat{e}_s \cdot \nabla p + \nabla \cdot \hat{e}_s = 0 \quad (E-13)$$

where

$$\beta^2 = M^2 - 1$$

The next step in the transformation of the equations of motion (E-1) and (E-2) into streamline coordinates is to relate the unit vectors \hat{e}_s and \hat{e}_n to those in the cylindrical coordinates \hat{e}_x and \hat{e}_r . To do this, simply rotate the \hat{e}_x, \hat{e}_r axis through an angle θ to the \hat{e}_s, \hat{e}_n plane. This gives

$$\hat{e}_s = \cos \theta \hat{e}_x + \sin \theta \hat{e}_r \quad (\text{E-14})$$

$$\hat{e}_n = (-\sin \theta) \hat{e}_x + \cos \theta \hat{e}_r \quad (\text{E-15})$$

The vector operators in cylindrical coordinates are

$$\nabla = \frac{\partial}{\partial x} \hat{e}_x + \frac{\partial}{\partial r} \hat{e}_r \quad (\text{E-16})$$

$$\nabla \cdot \vec{A} = \frac{1}{r} \left[\frac{\partial(rA_x)}{\partial x} + \frac{\partial(rA_r)}{\partial r} \right] \quad (\text{E-17})$$

$$\nabla \times \vec{A} = \frac{1}{r} \begin{bmatrix} \hat{e}_x & \hat{e}_r & r\hat{e}_\phi \\ \frac{\partial}{\partial x} & \frac{\partial}{\partial r} & \frac{\partial}{\partial \phi} \\ A_1 & A_2 & rA_3 \end{bmatrix}$$

For axisymmetric flow

$$\frac{\partial}{\partial \phi} = A_3 = 0$$

so that

$$\nabla \times \vec{A} = \hat{e}_\phi \left(\frac{\partial A_2}{\partial x} - \frac{\partial A_1}{\partial r} \right) \quad (\text{E-18})$$

Now in general $x = x(s, n)$ and $r = r(s, n)$. Thus, using the chain rule, one can write

$$\left(\frac{\partial}{\partial x} \right) = \frac{\partial}{\partial s} \left(\frac{\partial s}{\partial x} \right) + \frac{\partial}{\partial n} \left(\frac{\partial n}{\partial x} \right) \quad (\text{E-19})$$

$$\left(\frac{\partial}{\partial r} \right) = \frac{\partial}{\partial s} \left(\frac{\partial s}{\partial r} \right) + \frac{\partial}{\partial n} \left(\frac{\partial n}{\partial r} \right) \quad (\text{E-20})$$

Using Equations (E-14) and (E-15), Equations (E-19) and (E-20) become

$$\frac{\partial}{\partial x} = \cos \theta \frac{\partial}{\partial s} - \sin \theta \frac{\partial}{\partial n} \quad (\text{E-21})$$

$$\frac{\partial}{\partial r} = \sin \theta \frac{\partial}{\partial s} + \cos \theta \frac{\partial}{\partial n} \quad (\text{E-22})$$

Now substituting Equations (E-14), (E-16), and (E-17) into the continuity equation (E-13), one obtains

$$\begin{aligned} \frac{\beta^2}{\rho V^2} \left\{ \left[(\cos \theta) \hat{e}_x + (\sin \theta) \hat{e}_r \right] \cdot \left[\hat{e}_x \frac{\partial}{\partial x} + \hat{e}_r \frac{\partial}{\partial r} \right] \right\} p \\ + \frac{1}{r} \frac{\partial}{\partial x} (r \cos \theta) + \frac{1}{r} \frac{\partial}{\partial r} (r \sin \theta) = 0 \end{aligned} \quad (\text{E-23})$$

Now substituting Equations (E-21) and (E-22) into (E-23), performing the algebra, there is obtained

$$\frac{\beta^2}{\rho V^2} \frac{\partial p}{\partial s} + \frac{\partial \theta}{\partial n} = \frac{-\sin \theta}{r} \quad (\text{E-24})$$

This then is the continuity equation in streamline coordinates in terms of the dependent variables p and θ .

For the momentum equation (E-9), where

$$\hat{e}_t = \hat{e}_\phi$$

substitute Equations (E-18), (E-15), (E-16) and perform the dot product to obtain

$$\frac{\partial}{\partial x} (\sin \theta) - \frac{\partial}{\partial r} (\cos \theta) + \frac{1}{\rho V^2} \left[-\sin \theta \frac{\partial p}{\partial x} + \cos \theta \frac{\partial p}{\partial r} \right] = 0 \quad (\text{E-25})$$

Finally, substitute the relations (E-21) and (E-22) into (E-25) and perform the algebra to get the final form of the n momentum equation

$$\frac{1}{\rho V^2} \frac{\partial p}{\partial n} + \frac{\partial \theta}{\partial s} = 0 \quad (\text{E-26})$$

Equations (E-24), (E-26), and (E-10) are the continuity and momentum equations in streamline coordinates. They, in conjunction with (E-3) and (E-4) allow a complete solution of the flow field for axisymmetric bodies at zero angle of attack in steady, inviscid, adiabatic flow of an equilibrium chemically reacting fluid.

The next step in the derivation of the characteristic compatibility relations is to put the equations in a form for solution of the partial derivatives. It will then become obvious as to why the equations were put in the form of streamline coordinates before the compatibility equations were derived. In essence, this allowed reduction of one variable since in streamline coordinates the velocity is along the streamline, whereas in rectangular or cylindrical coordinates the velocity has components along the respective axes. Also, the entropy is constant along the streamline, simplifying the energy equation.

Repeating the equations for our mathematical model for convenience, we have

$$\frac{\beta^2}{\rho V^2} \frac{\partial p}{\partial s} + \frac{\partial \theta}{\partial n} = \frac{-\sin \theta}{r} \quad (\text{E-24})$$

$$\frac{1}{\rho V^2} \frac{\partial p}{\partial n} + \frac{\partial \theta}{\partial s} = 0 \quad (\text{E-26})$$

Also, we can write

$$dp = \frac{\partial p}{\partial s} ds + \frac{\partial p}{\partial n} dn \quad (\text{E-27})$$

$$d\theta = \frac{\partial \theta}{\partial s} ds + \frac{\partial \theta}{\partial n} dn \quad (\text{E-28})$$

Putting Equations (E-24), (E-26), and (E-28) in symbolic determinant form one has

$\frac{\partial p}{\partial s}$	$\frac{\partial p}{\partial n}$	$\frac{\partial \theta}{\partial s}$	$\frac{\partial \theta}{\partial n}$	=
$\frac{\beta^2}{\rho V^2}$	0	0	1	$\frac{-\sin \theta}{r}$
0	$\frac{1}{\rho V^2}$	1	0	0
ds	dn	0	0	dp
0	0	ds	dn	dθ

One can then solve for any one of the partial derivatives through a simple determinant process. For example

$$\frac{\partial \theta}{\partial s} = \frac{N}{D}$$

where $N =$

$$\begin{bmatrix} \frac{\beta^2}{\rho V^2} & 0 & \frac{-\sin \theta}{r} & 1 \\ 0 & \frac{1}{\rho V^2} & 0 & 0 \\ ds & dn & dp & 0 \\ 0 & 0 & d\theta & dn \end{bmatrix}$$

(E-29)

and

$$D = \begin{bmatrix} \frac{\beta^2}{\rho V^2} & 0 & 0 & 1 \\ 0 & \frac{1}{\rho V^2} & 1 & 0 \\ ds & dn & 0 & 0 \\ 0 & 0 & ds & dn \end{bmatrix} \quad (E-30)$$

The characteristic curves are defined as those lines along which the derivatives of fluid properties might be discontinuous. To determine these curves requires the denominator, Equation (E-30), to go to zero. Performing this operation and carrying out the algebra one obtains the result

$$\frac{dn}{ds} = \pm \frac{1}{\beta} = \pm \frac{1}{\sqrt{M^2 - 1}} = \pm \tan \mu \quad (E-31)$$

This says that along lines, called characteristic lines (which are also equal to Mach lines because the lines make the angle μ with respect to the streamline), the derivatives of flow properties may be discontinuous.

Now in order for the derivatives to exist, if the denominator is zero, then the numerator must also be equal to zero. Setting Equation (E-29) to zero and carrying out the math, one obtains the so-called compatibility condition

$$d\theta ds + dn dp \left(\frac{\beta^2}{\rho V^2} \right) + dn ds \left(\frac{\sin \theta}{r} \right) = 0 \quad (E-32)$$

Substituting (E-31) into (E-32), recognizing that the projections onto the s axes of the C_1 and C_2 coordinates are

$$ds = dC_1 \cos \mu + dC_2 \cos \mu$$

then one obtains

$$\frac{\beta}{\rho V^2} \frac{dp}{dC_1} + \frac{d\theta}{dC_1} = \frac{-\sin\theta \sin\mu}{r} \quad (E-33)$$

$$\frac{\beta}{\rho V^2} \frac{dp}{dC_2} - \frac{d\theta}{dC_2} = \frac{-\sin\theta \sin\mu}{r} \quad (E-34)$$

Here C_1 is called the left running and C_2 the right running characteristic corresponding to the plus and minus signs of Equation (E-31), respectively.

Note that along the characteristic lines, the partial differential equations (E-1) and (E-2) have been reduced to two first-order ordinary differential equations. This is the major advantage of the method of characteristics as it always reduces the equations of motion by one dimension when solved along the characteristic lines or surfaces.

DISTRIBUTION

	<u>Copies</u>		<u>Copies</u>
ATTN CODE 20 (P SELWYN)	1	ATTN W C SAWYER	1
CODE 21 (E ZIMET)	1	B HENDERSON	1
CODE 213 (D SIEGEL)	1	D MILLER	1
CHIEF OF NAVAL RESEARCH		J ALLEN	1
OFFICE OF NAVAL TECHNOLOGY		V ZOBY	1
800 N QUINCY ST BCT #1		H HAMILTON	1
ARLINGTON VA 22217-5000		C CREWS	1
		TECHNICAL LIBRARY	2
ATTN CODE 106P (W LUKENS)	1	NASA LANGLEY RESEARCH CENTER	
CODE 1132 F (S LEKOUDIS)	1	HAMPTON VA 23365	
CODE 12 (A WOOD)	1		
CODE 121 (R HANSEN)	1	ATTN TECHNICAL LIBRARY	1
CODE 1215 (J FEIN)	1	COMMANDER	
CHIEF OF NAVAL RESEARCH		NAVAL SEA SYSTEMS COMMAND	
OFFICE OF NAVAL RESEARCH		WASHINGTON DC 20362-5101	
800 N QUINCY ST BCT #1			
ARLINGTON VA 22217-5000		ATTN TECHNICAL LIBRARY	1
		COMMANDER	
ATTN CODE 3591 (C PORTER)	1	NAVAL AIR SYSTEMS COMMAND	
CODE 3592 (L STRUTZ)	1	WASHINGTON DC 20361	
TECHNICAL LIBRARY	1		
COMMANDER		ATTN J ROM	1
NAVAL WEAPONS CENTER		G COOPER	1
CHINA LAKE CA 93555-6001		TECHNICAL LIBRARY	1
		COMMANDER	
ATTN BILL WALKER	1	PACIFIC MISSILE TEST CENTER	
COMMANDING GENERAL		POINT MUGU CA 93041	
U.S. ARMY MISSILE COMMAND			
REDSTONE ARSENAL AL 35809		ATTN T C TAI	1
		M J MALIA	1
ATTN TECHNICAL LIBRARY	1	TECHNICAL LIBRARY	1
AFATL (ADLRA) (DLGC)		COMMANDER	
EGLIN AFB FL 32542-5000		NAVAL SHIP RESEARCH AND	
		DEVELOPMENT CENTER	
ATTN TECHNICAL LIBRARY	2	WASHINGTON DC 20034	
M TAUBER	1		
NASA AMES RESEARCH CENTER		ATTN TECHNICAL LIBRARY	1
MOFFETT CA 94035-1099		SUPERINTENDENT	
		U.S. NAVAL POSTGRADUATE SCHOOL	
ATTN C SCOTT	1	MONTEREY CA 93943-5000	
D CURRY	1		
NASA JOHNSON SPACE CENTER			
HOUSTON TX 77058			

DISTRIBUTION (CONTINUED)

	<u>Copies</u>		<u>Copies</u>
ATTN S GREENHALGH	1	ATTN A LOEB	1
C REITZ	1	H HUDGINS	1
TECHNICAL LIBRARY	1	G FRIEDMAN	1
COMMANDING OFFICER		TECHNICAL LIBRARY	1
NAVAL AIR DEVELOPMENT CENTER		COMMANDING GENERAL	
WARMINSTER PA 18974		ARRADCOM	
		PICTINNY ARSENAL	
		DOVER NJ 07801	
ATTN HEAD WEAPONS DEPT	1		
HEAD SCIENCE DEPT	1	ATTN TECHNICAL LIBRARY	1
TECHNICAL LIBRARY	1	COMMANDING OFFICER	
SUPERINTENDENT		HARRY DIAMOND LABORATORIES	
U.S. NAVAL ACADEMY		WASHINGTON DC 20013	
ANNAPOLIS MD 21402			
ATTN J B CHALK	1	ATTN J USSELTON	1
TECHNICAL LIBRARY	1	W B BAKER JR	1
OFFICER IN CHARGE		TECHNICAL LIBRARY	1
NAVAL INTELLIGENCE SUPPORT CENTER		ARNOLD ENGINEERING DEVELOPMENT	
4301 SUTTLAND RD		CENTER USAF	
WASHINGTON DC 20390		TULLAHOMA TN 37389	
ATTN TECHNICAL LIBRARY	1	ATTN K COBB	1
COMMANDING OFFICER		E SEARS	1
NAVAL ORDNANCE STATION		L E LIJEWSKI	1
INDIAN HEAD MD 20640		TECHNICAL LIBRARY	1
		COMMANDING OFFICER	
		AIR FORCE ARMAMENT LABORATORY	
		EGLIN AIR FORCE BASE FL 32542	
ATTN TECHNICAL LIBRARY	1		
DIRECTOR DEVELOPMENT CENTER		ATTN TECHNICAL LIBRARY	1
MARINE CORPS DEVELOPMENT AND		USAF ACADEMY	
EDUCATION COMMAND		COLORADO SPRINGS CO 80912	
QUANTICO VA 22134			
ATTN C H MURPHY	1	ATTN G KURYLOWICH	1
R. McCOY	1	D SHEREDA	1
W STUREK	1	J JENKINS	1
C NIETUBICZ	1	TECHNICAL LIBRARY	1
TECHNICAL LIBRARY	1	COMMANDING OFFICER	
COMMANDING GENERAL		AFSC	
BALLISTIC RESEARCH LABORATORY		WRIGHT-PATTERSON AFB OH 45433	
ABERDEEN PROVING GROUND MD 21005			
		ATTN W BOYLE	1
		NORTHROP SERVICES INC	
		HUNTSVILLE AL 35810	

DISTRIBUTION (CONTINUED)

	<u>Copies</u>		<u>Copies</u>
ATTN TECHNICAL LIBRARY ADVANCE RESEARCH PROJECTS AGENCY DEPARTMENT OF DEFENSE WASHINGTON DC 20305	1	ATTN P MURAD SCIENCE APPLICATIONS INC 680 E SWEDESFORD RD WAYNE PA 19087	1
ATTN TECHNICAL LIBRARY NASA WASHINGTON DC 20546	1	ATTN F PRILLMAN W B BROOKS R STANCIL VOUGHT CORPORATION PO BOX 5907 DALLAS TX 75222	1 1 1
ATTN CODE 30 (CAPT CHILDERS) CHIEF OF NAVAL RESEARCH NAVY SDI 2211 JEFFERSON DAVIS HWG ROOM 810 CP5 ALEXANDRIA VA 22217	1	ATTN TECHNICAL LIBRARY HUGHES AIRCRAFT CORPORATION CANOGA PARK CA 91304	1
ATTN CODE TNC (BLACKLEDGE) CDR AL KOREJO DIRECTOR INTERCEPTOR TECHNOLOGY STRATEGIC DEFENSE INITIATIVE ORG THE PENTAGON WASHINGTON DC 20350	1 1	ATTN R LaFARGE R EISLER TECHNICAL LIBRARY SANDIA LABORATORIES ALBUQUERQUE NM 87115	1 1 1
ATTN SFAE-SD-ASP SFAE-SD-HED DEPUTY COMMANDER US ARMY STRATEGIC DEFENSE COMMAND PO BOX 1500 HUNTSVILLE AL 35807-3501	1 1	ATTN TECHNICAL LIBRARY MARTIN MARIETTA AEROSPACE PO BOX 5837 ORLANDO FL 32895	1
ATTN PROF J A SCHETZ VIRGINIA POLYTECHNIC AND STATE UNIVERSITY DEPT OF AEROSPACE ENGINEERING BLACKSBURG VA 24060	1	ATTN TECHNICAL LIBRARY BUSINESS AND TECH SYSTEMS INC SUITE 406 AEROSPACE BLDG 10210 GREENBELT RD SEABROOK MD 20601	1
ATTN PROF F R DeJARNETTE NORTH CAROLINA STATE UNIVERSITY DEPT OF MECHANICAL AND AEROSPACE ENGINEERING BOX 7921 RALEIGH NC 27695	3	ATTN D G MILLER TECHNICAL LIBRARY LAWRENCE LIVERMORE LAB EARTH SCIENCES DIVISION UNIVERSITY OF CALIFORNIA LIVERMORE CA 94550	1
		ATTN B CMILIAN CALSPAN ADVANCED TECHNOLOGY CENTER PO BOX 400 BUFFALO NY 14225	1

DISTRIBUTION (CONTINUED)

	<u>Copies</u>		<u>Copies</u>
ATTN S SOPCZAK	1	ATTN H G KNOCHE	1
TECHNICAL LIBRARY	1	DR GREGORIOUS	1
HONEYWELL INC		MESSERSCHMIDT-BOLKOW-BLOHM	
600 SECOND ST		GMBH	
MINNEAPOLIS MN 55343		UNTERNEHMENSBEREICH APPARATE	
		MUNCHEN 80-POSTFACH 801149	
ATTN H T PONSFORD	1	BAYERN FED REP OF GERMANY (DFR)	
PACIFICA TECHNOLOGY			
PO BOX 148			
DEL MAR CA 92014		ATTN J M WU	1
		C BALASUBRAMAYAN	1
		TECHNICAL LIBRARY	1
ATTN J E RACHNER	1	THE UNIVERSITY OF TENNESSEE	
TECHNICAL LIBRARY	1	SPACE INSTITUTE	
ROCKWELL INTERNATIONAL		TULLAHOMA TN 37388	
MISSILE SYSTEMS DIVISION			
4300 E FIFTH AVE			
PO BOX 1259		ATTN R NELSON	1
COLUMBUS OH 43216		TECHNICAL LIBRARY	1
		UNIVERSITY OF NOTRE DAME	
ATTN R WYRICK	1	DEPARTMENT OF AEROSPACE AND	
BOEING COMPUTER SERVICES INC		MECHANICAL ENGINEERING	
PO BOX 24346		BOX 537	
SEATTLE WA 98124		NOTRE DAME IN 46556	
ATTN G H RAPP	1	ATTN E LUCERO	1
MOTOROLA INC		L TISSERAND	1
MISSILE SYSTEMS OPERATIONS		TECHNICAL LIBRARY	1
8201 E McDOWELL RD		APPLIED PHYSICS LABORATORY	
PO BOX 1417		THE JOHNS HOPKINS UNIVERSITY	
SCOTTSDALE AZ 85252		JOHNS HOPKINS RD	
		LAUREL MD 20810	
ATTN L M SHEPPARD	1	ATTN D P FORSMO	1
K D THOMSON	1	TECHNICAL LIBRARY	1
TECHNICAL LIBRARY	1	RAYTHEON COMPANY	
WEAPONS SYSTEMS RESEARCH LAB		MISSILE SYSTEMS DIVISION	
GPO BOX 2151 ADELAIDE SA 5001		HARTWELL RD	
SALISBURY SA AUSTRALIA		BEDFORD MS 01730	

DISTRIBUTION (CONTINUED)

	<u>Copies</u>		<u>Copies</u>
ATTN J XERIKOS	1	ATTN S PEARLSING	1
N CAMPBELL	1	P GIRAGOSIAN	1
TECHNICAL LIBRARY	1	RAYTHECN COMPANY	
McDONNELL-DOUGLAS		SPENCER LABORATORY	
ASTRONAUTICS CO (WEST)		BOX SL7162	
5301 BOLSA AVE		BURLINGTON MS 01803	
HUNTINGTON BEACH CA 92647			
ATTN J WILLIAMS	1	DEFENSE TECHNICAL INFORMATION CENTER	12
S VUKELICH	1	CAMERON STATION	
J FIVEL	1	ALEXANDRIA VA 22314	
TECHNICAL LIBRARY	1		
McDONNELL-DOUGLAS		ATTN GIFT AND EXCHANGE DIVISION	4
ASTRONAUTICS CO (EAST)		LIBRARY OF CONGRESS	
BOX 516		WASHINGTON DC 20390	
ST LOUIS MO 53166			
ATTN D ANDREWS	1	GIDEP OPERATIONS OFFICE	
TECHNICAL LIBRARY	1	CORONA CA 91720	1
LOCKHEED MISSILES AND SPACE COMPANY INC		DEFENSE PRINTING SERVICE	
PO BOX 1103		WASHINGTON NAVY YARD	
HUNTSVILLE AL 35807		WASHINGTON DC 20374	
ATTN L E ERICSSON	1	INTERNAL DISTRIBUTION	
P REDING	1	C	1
TECHNICAL LIBRARY	1	D	1
LOCKHEED MISSILES AND SPACE COMPANY INC		D1	1
PO BOX 504		D2	1
SUNNYVALE CA 94086		D4	1
		E	1
ATTN TECHNICAL LIBRARY	1	E211 (GREEN)	1
NIELSEN ENGINEERING AND RESEARCH INC		S231	3
510 CLYDE AVE		E232	2
MOUNTAIN VIEW CA 95043		E32 (GIDEP)	1
		F	1
ATTN R WHYTE	1	G	1
GENERAL ELECTRIC CO		G01	1
ARMAMENT SYSTEMS DEPT		G02	1
BURLINGTON VT 05401		G06	1
		G07	10
		G10	1

DISTRIBUTION (CONTINUED)

	<u>Copies</u>
G205	1
G20	1
G21	1
G23	1
G23 (ARMISTEAD)	3
G23 (DEVAN)	1
G23 (HARDY)	1
G23 (McINVILLE)	1
G23 (ROWLES)	1
G23 (WEISEL)	1
G301	1
G40	1
G60	1
G70	1
H	1
H13	1
K	1
K10	1
K195	1
K20	1
K204	1
N	1
R	1
R44	1
R44 (WARDLAW)	1
R44 (PRIGLO)	1
R44 (SHIEH)	1
U	1

REPORT DOCUMENTATION PAGE			Form Approved GSA No. 0704-0186	
<small>Public reporting burden for this collection of information is estimated to average 1 hour per response, including the time for reviewing instructions, searching existing data sources, gathering and maintaining the data needed, and completing and reviewing the collection of information. Send comments regarding this burden estimate or any other aspect of this collection of information, including suggestions for reducing this burden, to Washington Headquarters Services, Directorate for Information Operations and Reports, 1215 Jefferson Davis Highway, Suite 1204, Arlington, VA 22202-4302, and to the Office of Management and Budget, Paperwork Reduction Project (0704-0186), Washington, DC 20503.</small>				
1. AGENCY USE ONLY (Leave blank)	2. REPORT DATE February 1992	3. REPORT TYPE AND DATES COVERED Final		
4. TITLE AND SUBTITLE Second-order Shock-expansion Theory Extended to Include Real Gas Effects		5. FUNDING NUMBERS		
6. AUTHOR(S) Frank G. Moore, Michael A. Armistead, Steve H. Rowles Fred R. DeJarnette				
7. PERFORMING ORGANIZATION NAME(S) AND ADDRESS(ES) Naval Surface Warfare Center (G07) Dahlgren, VA 22448-5000		8. PERFORMING ORGANIZATION REPORT NUMBER NAVSWC TR 90-683		
9. SPONSORING/MONITORING AGENCY NAME(S) AND Surface-launched Weaponry Technology Program (G06) Office of Naval Technology—ONT-213		10. SPONSORING/MONITORING AGENCY REPORT NUMBER		
11. SUPPLEMENTARY NOTES				
12a. DISTRIBUTION/AVAILABILITY Approved for public release; distribution is unlimited.		12b. DISTRIBUTION CODE		
13. ABSTRACT (Maximum 200 words) <p>New methods have been developed to compute inviscid surface pressures and temperatures for both perfect and equilibrium chemically reacting flows on both pointed and blunt bodies of revolution. These new methods include an improved Shock-expansion Theory, an improved Modified Newtonian Theory (MNT), and an improved method for angle-of-attack effects. Comparison of these approximate engineering techniques to exact inviscid computations using a full Euler code showed that these new methods gave very good agreement of surface temperature and pressures as well as forces and moments. Incorporation of this new technology into the NAVSWC aeroprediction code will allow the code to be used for engineering estimates of inviscid surface temperature at high Mach numbers. These approximate temperatures can then be used as inputs to perform heat transfer analysis.</p>				
14. SUBJECT TERMS Second-order Shock-expansion, Perfect and Real Gases, Modified Newtonian Theory, Chemical Species Composition		15. NUMBER OF PAGES 173		
		16. PRICE CODE		
17. SECURITY CLASSIFICATION OF REPORT UNCLASSIFIED	18. SECURITY CLASSIFICATION OF THIS PAGE UNCLASSIFIED	19. SECURITY CLASSIFICATION OF ABSTRACT UNCLASSIFIED	20. LIMITATION OF ABSTRACT UL	